People’s Democratic Republic of Algeria
Ministry of Higher Education and Scientific Research
Echahid Echeikh Larbi Tebessi University
Faculty of Sciences and Technology
Department of civil engineering

DOCTORAL THESIS

Presented for attainment of the LMD Doctoral degree
In: **Public Works**
Specialty: **Roads and Civil Engineering Structures**

By: **DJABRI Alla**

Entitled

Study of the optimal parameters on the stability of a large-height road embankment

Presented and publicly defended, 08/06/2026, in front of the jury composed of:

BOUTAGOUGA Djamel	Prof.	President	Tebessa University
BOUFARH Rafik	Prof.	Supervisor	Tebessa University
BOURSAS Farid	MCA	Co-supervisor	Tebessa University
ABDERRAHMANI Sifeddine	MCA	Examiner	Tebessa University
ATHAMNIA Brahim	MCA	Examiner	Tebessa University
GOUDJIL Kamel	Prof.	Examiner	Souk Ahras University
DJEBIEN Rachid	Prof.	Examiner	Skikda University

2025-2026

Acknowledgments

First and foremost, I thank Almighty God (Allah) for His guidance and for enabling me to complete this work.

I would like to express my deepest gratitude to my thesis supervisor, Dr. BOUFARH Rafik. I am truly thankful for the precious opportunity he gave me to work under his supervision. His invaluable guidance, patience, and encouragement were instrumental throughout this research. and to my co-supervisor, Dr. Boursas Farid, for his continuous support and valuable advice.

I am profoundly grateful to my mother for her ceaseless prayers and encouragement; her support has been pivotal in my academic journey. I extend my sincere appreciation to my wife for her immense patience and unwavering support, which were essential in motivating me to complete this work. My heartfelt thanks also go to my sisters and my entire family for their love and support.

Abstract

This thesis addresses critical challenges in slope stability assessment for high road embankments (6-30m) through a dual-methodology framework integrating hybrid machine learning and physics-informed neural networks (PINNs). A comprehensive database of 1,176 finite element simulations was generated using GeoStudio SLOPE/W, incorporating diverse soil properties and multi-berm geometries representative of Algerian mountainous highway networks. Field validation was conducted on 20 real embankments from Tebessa region to ensure practical applicability. The hybrid stacking ensemble—combining XGBoost, Support Vector Regression, Multi-Layer Perceptron, and Random Forest—achieved exceptional performance (R^2=0.9978, RMSE=0.0199), delivering ~85% computational efficiency gains versus traditional FEM while maintaining high accuracy. SHAP analysis revealed three physically significant parameters as primary stability drivers: cohesion (47.7%)—representing the soil's intrinsic shear strength and resistance to sliding along potential failure surfaces; friction angle (31.1%)—governing the mobilization of normal stress into shear resistance, critical for stress redistribution under loading; and embankment height (6.6%)—controlling gravitational driving forces and stress state intensity within the slope mass. This hierarchy confirms alignment with geotechnical principles and the fundamental mechanics of limit equilibrium. The novel PINN framework explicitly embeds Mohr-Coulomb failure criterion, Bishop's Simplified Method, and monotonicity constraints into neural network training through composite loss functions optimized via Bayesian optimization. This approach achieved R^2=0.9787 with perfect monotonicity compliance (100%) for critical parameters and overall physics satisfaction of 88.7%. Monte Carlo dropout provided well-calibrated uncertainty quantification (94.6% prediction interval coverage), enabling risk-informed decision-making. The validation dataset from Tebessa region demonstrated exceptional predictive accuracy: hybrid ensemble achieved +0.82% mean error, while PINN recorded +0.89%—both within acceptable engineering tolerances. The frameworks deliver real-time inference (0.8-1.2ms per prediction), representing >10,000× speedup versus traditional methods. The validated frameworks enable preliminary stability screening, parametric design optimization, and probabilistic risk assessment for infrastructure projects. An integrated three-stage workflow leverages hybrid ensemble for rapid screening, PINN for physics verification, and selective FEM for critical cases, reducing overall analysis time by 85-95% while maintaining rigorous safety assurance.

Keywords: Slope Stability, High Road Embankment, Machine Learning, Hybrid Stacking Ensemble, Physics-Informed Neural Networks (PINNs), SHAP Analysis, Mohr-Coulomb Failure Criterion, Bishop's Simplified Method, Bayesian Optimization, Uncertainty Quantification, GeoStudio SLOPE/W, Factor of Safety (FOS), Geotechnical Engineering.

Résumé

Cette thèse traite les défis majeurs de l'évaluation de la stabilité des talus pour les remblais routiers de grande hauteur (6-30m) à travers un cadre méthodologique dual intégrant l'apprentissage automatique hybride et les réseaux neuronaux informés par la physique (PINNs). Une base de données de 1 176 modelés par éléments finis a été générée avec GeoStudio SLOPE/W, incluant diverses propriétés de sols et géométries multi-bermes réalistes représentatives des réseaux routiers algériens. Une validation de terrain a été réalisée sur 20 remblais réels de la région de Tébessa pour assurer l'applicabilité pratique. L'ensemble hybride empilé—combinant XGBoost, Support Vector Regression, Multi-Layer Perceptron et Random Forest—a atteint une performance exceptionnelle (R^2=0,9978, RMSE=0,0199), offrant ~85% de gains d'efficacité computationnelle par rapport au FEM traditionnel tout en maintenant une haute précision. L'analyse SHAP a révélé trois paramètres physiquement significatifs comme moteurs principaux de stabilité : la cohésion (47,7%)—représentant la résistance au cisaillement intrinsèque du sol et la résistance au glissement le long des surfaces de rupture potentielles ; l'angle de frottement (31,1%)—régissant la mobilisation de la contrainte normale en résistance au cisaillement, critique pour la redistribution des contraintes sous chargement ; et la hauteur du remblai (6,6%)—contrôlant les forces motrices gravitationnelles et l'intensité de l'état de contrainte dans le massif de talus. Cette hiérarchie confirme l'alignement avec les principes géotechniques et les mécaniques fondamentales de l'équilibre limite. Le modèle PINN novateur intègre explicitement le critère de rupture de Mohr-Coulomb, la méthode simplifiée de Bishop et les contraintes de monotonicité dans l'entraînement des réseaux neuronaux via des fonctions de perte composites optimisées à l'aide de l'optimisation bayésienne. Cette approche a atteint R^2=0,9787 avec une conformité monotone parfaite (100%) pour les paramètres critiques et une satisfaction physique globale de 88,7%. Le dropout de Monte Carlo a fourni une quantification d'incertitude bien calibrée (94,6% de couverture d'intervalle de prédiction), permettant une prise de décision éclairée par le risque. Le jeu de données de validation de la région de Tébessa a démontré une précision prédictive exceptionnelle : l'ensemble hybride a atteint +0,82% d'erreur moyenne, tandis que le PINN a enregistré +0,89% ; les deux dans les tolérances acceptables en ingénierie ; Les cadres fournissent une inférence en temps réel (0,8-1,2 millisecondes par prédiction), représentant une accélération de > 10 000 × par rapport aux méthodes traditionnelles. Les cadres validés permettent le criblage préliminaire de stabilité, l'optimisation paramétrique de conception et l'évaluation probabiliste des risques pour les projets d'infrastructure. Un flux de travail intégré en trois étapes exploite l'ensemble hybride pour le criblage rapide, le PINN pour la vérification physique et le FEM sélectif pour les cas critiques, réduisant le temps d'analyse global de 85-95% tout en maintenant une assurance de la sécurité rigoureuse.

Mots-clés : Stabilité des talus, Remblai routier de grande hauteur, Apprentissage automatique, Ensemble hybride empilé, Réseaux neuronaux informés par la physique (PINNs), Analyse SHAP, Critère de rupture de Mohr-Coulomb, Méthode simplifiée de Bishop, Optimisation bayésienne, Quantification de l'incertitude, GeoStudio SLOPE/W, Coefficient de sécurité, Géotechnique.

ملخص

تعالج هذه الأطروحة التحديات الحرجة في تقييم استقرارية المنحدرات للسدود الترابية الطرقية العالية (6-30 مترا) عبر إطار منهجي مزدوج يدمج التعلم الآلي الهجين والشبكات العصبية المستنيرة بالفيزياء (PINNs). تم إنشاء قاعدة بيانات شاملة تضم 1,176 محاكاة بالعناصر المحددة باستخدام برنامج GeoStudio SLOPE/W، تتضمن خصائص تربة متنوعة وهندسيات متعددة السفوح تمثل شبكات الطرق الجبلية الجزائرية. تم إجراء التحقق الميداني على 20 سداً ترابياً حقيقياً من منطقة تبسة لضمان التطبيق العملي. حقق التجميع الهجين المكدس - الذي يجمع بين XGBoost، Support Vector Regression، Multi-Layer Perceptron و Random Forest - أداءً استثنائياً ($R^2 = 0.9978$، RMSE = 0.0199)، مما يوفر مكاسب كفاءة حاسوبية بنسبة ~85% مقارنة بطريقة العناصر المحددة التقليدية مع الحفاظ على دقة عالية. كشف تحليل SHAP أن التماسك (47.7%) وزاوية الاحتكاك الداخلي (31.1%) يُمثِّلان المحركَين الفيزيائيَّين الرئيسيَّين لاستقرار المنحدر، وهو ما يتوافق مع معيار Mohr-Coulomb لمقاومة القص، في حين يؤثر ارتفاع السد (6.6%) على حجم العزم الدافع وفق مبدأ التوازن الميكانيكي. يدمج إطار PINN المبتكر صراحةً معيار الفشل Mohr-Coulomb وطريقة Bishop المبسطة وقيود الرتابة في تدريب الشبكات العصبية عبر دوال خسارة مركبة محسّنة باستخدام التحسين البايزي. حققت هذه الطريقة $R^2 = 0.9787$ مع امتثال تزايدي تام (100%) للمعاملات الحرجة ورضا فيزيائي إجمالي بنسبة 88.7%. أتاحت محاكاة Monte Carlo تحديداً كمياً لعدم اليقين في تقديرات FOS، مما يوفر فترات ثقة احتمالية تُعزز موثوقية قرارات التصميم الهندسي في ظل التباين الطبيعي لخصائص التربة. أظهرت مجموعة بيانات التحقق من منطقة تبسة دقة تنبؤية استثنائية: حقق التجميع الهجين خطأً متوسطاً +0.82%، بينما سجل PINN +0.89% - وكلاهما ضمن التفاوتات الهندسية المقبولة. توفر الأطر استدلالاً فورياً (0.8-1.2 ملي ثانية لكل تنبؤ)، مما يمثل تسريعاً >10,000× مقارنة بالطرق التقليدية. تمكن الأطر المصدقة من الفحص الأولي للاستقرارية والتحسين المعلمي للتصميم والتقييم الاحتمالي للمخاطر لمشاريع البنية التحتية. يستغل سير عمل متكامل من ثلاث مراحل التجميع الهجين للفحص السريع، وPINN للتحقق الفيزيائي، والعناصر المحددة الانتقائية للحالات الحرجة، مما يقلل وقت التحليل الإجمالي بنسبة 85-95% مع الحفاظ على ضمانات أمان صارمة.

الكلمات المفتاحية: استقرارية المنحدرات، السد الترابي الطرقي عالي الارتفاع، التعلم الآلي، التجميع الهجين المكدّس، الشبكات العصبية المستنيرة بالفيزياء(PINNs) ، تحليلSHAP ، معيار فشل موهر-كولومب، طريقة بيشوب المبسطة، التحسين البايزي، تقدير الشكوك، برنامجGeoStudio SLOPE/W ، معامل الأمان، الهندسة الجيوتقنية.

Table of content

List of Figures

List of Tables

List of Abbreviations and Nomenclature

Abbreviations

Abbreviation	Full Form
ABC	Artificial Bee Colony
Adam	Adaptive Moment Estimation
AI	Artificial Intelligence
ANN	Artificial Neural Network
ANOVA	Analysis of Variance
Bishop	Bishop's Simplified Method
CBR	California Bearing Ratio
CI	Confidence Interval
CPU	Central Processing Unit
CV	Cross-Validation
DANN	Deep Artificial Neural Network
DL	Deep Learning
EN	European Norm (Eurocode)
FEM	Finite Element Method
FEM-SRM	Finite Element Method with Strength Reduction Method
FOS	Factor of Safety
GPU	Graphics Processing Unit
GridSearchCV	Grid Search Cross-Validation
GUI	Graphical User Interface
HHO	Harris Hawk Optimization
IQR	Interquartile Range
k-NN	k-Nearest Neighbors
LBFGS	Limited-memory Broyden-Fletcher-Goldfarb-Shanno
LEM	Limit Equilibrium Method
MAE	Mean Absolute Error
MC	Monte Carlo
MCMC	Markov Chain Monte Carlo
ML	Machine Learning
MLP	Multi-Layer Perceptron
MSE	Mean Squared Error
PDP	Partial Dependence Plot
PINN	Physics-Informed Neural Network
PSO	Particle Swarm Optimization
PyQt5	Python Qt5 (GUI Framework)
R^2	Coefficient of Determination
ReLU	Rectified Linear Unit
RF	Random Forest
RMSE	Root Mean Squared Error
SHAP	SHapley Additive exPlanations
SLIDE	Slope Stability Analysis Software (Rocscience)
SLOPE/W	Slope Stability Analysis Module (GeoStudio)
SMO	Sequential Minimum Optimization
SRM	Strength Reduction Method

SRF	Strength Reduction Factor (equivalent to FOS_trial in limit equilibrium context)
SSA	Sparrow Search Algorithm
SVM	Support Vector Machine
SVR	Support Vector Regression
TPE	Tree-structured Parzen Estimator
UQ	Uncertainty Quantification
VIF	Variance Inflation Factor
XGBoost	Extreme Gradient Boosting

Greek Symbols

Symbol	Description
α	Learning rate
β, β_1-β_5	Slope angle(s) (radians or degrees)
γ	Unit weight (kN/m^3)
ε	Error tolerance / Epsilon-insensitive margin
θ	Neural network parameters (weights and biases)
λ	Regularization parameter / Physics loss weight
μ	Mean / Predictive mean
ν	Poisson's ratio
σ	Standard deviation / Epistemic uncertainty
φ, φ'	Friction angle, Effective friction angle (degrees)
τ	Shear stress (kPa)
Ω	Regularization term
$\hat{y}$	Network predicted output

Subscripts and Superscripts

Notation	Description
c, c'	Cohesion, Effective cohesion (kPa)
FOS	Factor of Safety
H	Embankment height (m)
N	Number of samples/configurations
pred	Predicted value
target	Target/actual value
MC	Mohr-Coulomb
B	Bishop's method
M	Monotonicity

Mathematical Notation

Symbol	Description
$\mathscr{L}$	Loss function
∂	Partial derivative
$\sum$	Summation
$\surd$	Square root
$\approx$	Approximately equal to
$\leq$	Less than or equal to
$\geq$	Greater than or equal to

I. General Introduction

I.1. Background

Slope stability analysis represents one of the most critical and enduring challenges in geotechnical engineering, with profound implications for infrastructure safety, economic development, and public welfare worldwide. High road embankments, particularly those exceeding 6 meters in height, constitute essential components of modern transportation networks, especially in mountainous and hilly terrain where topographical constraints necessitate significant earthwork structures (Duncan et al. 2014; Huang et al. 2023). These structures face multifaceted stability challenges arising from gravitational forces, heterogeneous soil properties, complex hydrological conditions, seismic loading, and traffic-induced vibrations—factors that can culminate in catastrophic failures with devastating consequences for human life and economic resources (Bandara et al. 2016; Froude and Petley 2018).

The Factor of Safety (FOS), defined as the ratio between available shear resistance and mobilized shear stress along potential failure surfaces, serves as the primary quantitative metric for assessing slope stability and informing design decisions in geotechnical practice (Duncan and Wright 2005; Griffiths and Lane 1999). This dimensionless parameter quantifies the degree of stability by comparing soil shear strength to applied shear stress along potential slip surfaces, with values typically ranging from 1.0 (indicating incipient failure) to 3.0 or higher for highly stable configurations (Duncan et al. 2014). Accurate prediction of FOS is essential not only for preventing slope failures but also for optimizing design parameters, reducing construction costs, and ensuring sustainable infrastructure development. However, despite decades of intensive research and methodological refinement, the reliable prediction of FOS under complex geological configurations and dynamic environmental conditions remains a formidable challenge that demands innovative approaches integrating advanced computational methods with fundamental geotechnical principles (Cheng et al. 2007; Zhang et al. 2022).

The global economic impact of slope instability is staggering, with estimated annual costs exceeding $4 billion in slope-related disasters worldwide, encompassing direct infrastructure damage, reconstruction expenses, traffic disruptions, and indirect socio-economic losses (Froude and Petley 2018; Intrieri et al. 2012). In Algeria specifically, the development of mountainous road networks connecting northern coastal regions with interior highlands has necessitated construction of numerous high embankments, many of which traverse geologically complex terrains characterized by spatially variable soil properties, seasonal precipitation patterns, and seismic activity. The 2003 Boumerdes earthquake and subsequent slope failures underscored the vulnerability of transportation infrastructure to combined gravitational and seismic loading, highlighting the urgent need for more sophisticated analytical frameworks capable of capturing the intricate interactions between geometric, material, and environmental factors governing slope stability (Cheng et al. 2007).

Traditional approaches to slope stability analysis, while widely accepted in engineering practice, face significant limitations in addressing the complexity and uncertainty inherent in natural soil systems. Limit equilibrium methods (LEM), including the classical formulations of Fellenius (Fellenius 1936), Bishop (Bishop 1955), Janbu (Janbu 1955), Morgenstern and Price (Morgenstern and Price 1965), and

Spencer (Spencer 1967), provide practical solutions through simplifying assumptions regarding failure surface geometry and interslice force distributions. However, these methods often neglect stress-strain compatibility and progressive failure mechanisms, and prove computationally intensive for complex geometries (Duncan and Wright 2005; Fellenius 1936). Finite element methods (FEM), while capable of more rigorous stress-deformation analysis through strength reduction techniques (Griffiths and Lane 1999; Matsui and San 1992), demand substantial computational resources, specialized expertise, and extensive site-specific data that may not be readily available for many practical projects (Ghosh et al. 2015; Zienkiewicz et al. 2005). These constraints hinder rapid stability assessments for large-scale infrastructure projects, necessitating innovative approaches that balance accuracy with computational efficiency.

Furthermore, traditional deterministic analyses struggle to adequately account for the stochastic nature of geotechnical properties, the spatial variability of soil parameters, and the uncertainty propagation through analytical frameworks—factors that can significantly influence predicted safety factors and design outcomes (Griffiths et al. 2009; Phoon and Kulhawy 1999). The reliance on single-method approaches introduces analyst-dependent bias, as different limit equilibrium formulations can yield FOS variations of 10-30% for identical slope configurations, particularly when dealing with complex geometries, irregular stratigraphy, or unusual pore pressure conditions (Cheng et al. 2007; Duncan 1996).

Given these shortcomings, there is an urgent need for advanced or alternative methodologies to deliver accurate and efficient slope stability predictions. As geotechnical projects grow in scale and complexity, innovative approaches are essential to overcome the limitations of traditional methods and meet the evolving demands of the field. The advent of artificial intelligence (AI) and machine learning (ML) has opened unprecedented opportunities for transforming geotechnical engineering practice through data-driven predictive modeling. Unlike traditional methods that require explicit mathematical formulations of physical relationships, ML algorithms can automatically extract complex, nonlinear patterns from large datasets, establishing robust input-output mappings without necessitating complete understanding of underlying physical mechanisms (Goodfellow et al. 2016; LeCun et al. 2015). By learning from historical data, field measurements, and simulations, ML models establish robust connections between inputs and stability outcomes, enabling more accurate and efficient predictions (Chakraborty and Goswami 2017; Chen and Wong 2011).

Recent applications of ML in geotechnical engineering have demonstrated remarkable success in diverse problems including soil property prediction (Shahin et al. 2001), bearing capacity estimation (Adarsh et al. 2012), and slope stability assessment (Gordan et al. 2016; Qi and Tang 2018; Sakellariou and Ferentinou 2005). Comparative studies highlight the efficacy of various ML approaches. (Lin et al. 2021) compared 11 ML models using 349 slope cases with inputs such as unit weight, cohesion, friction angle, slope angle, height, and pore water pressure, finding that nonlinear methods, particularly SVM-poly, slightly outperformed linear ones. (Khajehzadeh et al. 2022) used artificial neural networks (ANN) optimized by particle swarm optimization, achieving high FOS prediction accuracy for heterogeneous soil slopes. (Karir et al. 2022) tested multiple algorithms including SVR, ANN, random forests (RF), Gradient Boosting, and XGBoost, with tree-based models, especially XGBoost, excelling for natural and man-made slopes. (Nanehkaran et al. 2023) found MLP outperformed SVM, decision trees, and RF in FOS prediction, validated against Janbu's LEM and GeoStudio. Similarly, (Ahangari Nanehkaran et al. 2022) evaluated multiple algorithms on 70 slopes in Iran, with MLP achieving the highest accuracy (0.938), as validated through SLIDE software.

To further enhance predictive performance, hybrid models integrating optimization algorithms with ML have gained traction. (Kardani et al. 2021) proposed a hybrid stacking ensemble method combining FEM and ML, using an artificial bee colony algorithm to optimize base classifiers and a meta-classifier, reducing computational time compared to traditional FEM. (Wang et al. 2024) developed hybrid random forest models optimized by Sparrow Search Algorithm and Harris Hawk Optimization using 444 slope cases, identifying specific weight as the most influential factor and outperforming classical models. Moreover, explainable AI techniques have enhanced the interpretability of these models, providing actionable insights for engineers (Abdollahi et al. 2024). The integration of AI and digital technologies has shown transformative potential in related fields like dam engineering, suggesting broader applicability in geotechnical applications (Hariri-Ardebili et al. 2023).

However, purely data-driven ML approaches suffer from critical limitations when applied to physical systems, particularly in contexts where data scarcity, extrapolation beyond training conditions, or the need for physically consistent predictions are paramount concerns (Karpatne et al. 2017; Willard et al. 2023). Standard ML models function as "black boxes" that learn statistical correlations without incorporating domain knowledge, potentially leading to predictions that violate fundamental physical laws, yield non-physical results, or perform poorly when applied to conditions outside the training distribution (Reichstein et al. 2019; Von Rueden et al. 2021). In geotechnical applications, this can manifest as predicted FOS values that decrease with increasing soil strength, violate equilibrium conditions, or fail to respect boundary constraints—outcomes that undermine confidence in AI-based approaches for safety-critical applications (Kardani et al. 2021).

To address these fundamental limitations, a new paradigm of Physics-Informed Machine Learning (PIML) has emerged, which seeks to integrate physical laws, domain knowledge, and mechanistic understanding directly into the architecture, training process, or inference mechanisms of ML models (Karniadakis et al. 2021; Raissi et al. 2019; Willard et al. 2023). Physics-Informed Neural Networks (PINNs), first introduced by (Raissi et al. 2017), represent a particularly powerful approach within this paradigm, where governing differential equations and physical constraints are embedded into the loss function of neural networks, enabling simultaneous learning from both observational data and fundamental physics (Karniadakis et al. 2021; Raissi et al. 2019). Recent applications have demonstrated exceptional efficacy across computational fluid dynamics (Cai et al. 2021; Raissi et al. 2020), solid mechanics (Haghighat et al. 2021), and inverse problems (Yang et al. 2021), suggesting transformative potential for geotechnical applications. This physics-informed approach promises to overcome the limitations of both traditional computational methods and purely data-driven ML, offering a path toward more reliable, interpretable, and physically consistent predictions for slope stability assessment in complex engineering environments.

I.2. Research Motivation and Gap Analysis

Despite the proliferation of ML applications in slope stability analysis, three critical gaps persist in current research:

Gap 1: Limited Physical Consistency in Data-Driven Models Existing ML approaches for FOS prediction, including support vector machines (SVR) (Lin et al. 2021), RF (Karir et al. 2022), gradient boosting (Wang et al. 2024), and neural networks (NN) (Nanehkaran et al. 2023), achieve high predictive accuracy but frequently violate fundamental geotechnical principles when extrapolating beyond training distributions. None of these studies systematically enforce Mohr-Coulomb failure criteria, stability number relationships, or material property monotonicity constraints within their model architectures.

Gap 2: Absence of Hybrid Frameworks Integrating Multiple ML Paradigms While individual algorithms demonstrate strengths in specific contexts—XGBoost excels at capturing complex interactions (Chen and Guestrin 2016), SVR provides robust performance with limited data (Smola and Schölkopf 2004), and NN offer flexibility in representing nonlinear relationships (Goodfellow et al. 2016)—no comprehensive framework systematically combines these complementary strengths through advanced ensemble techniques specifically designed for slope stability applications.

Gap 3: Limited Application of Physics-Informed Deep Learning to Geotechnical Problems Despite remarkable success in fluid mechanics and structural engineering, PINNs remain largely unexplored for slope stability prediction. The integration of geotechnical constitutive relationships (Mohr-Coulomb criterion), equilibrium conditions (Bishop's method), and domain-specific constraints (monotonicity requirements) into NN loss functions represents an unexploited opportunity to enhance both predictive accuracy and physical interpretability.

I.3. Project description

This doctoral research presents a comprehensive investigation into optimal parameter determination for high road embankment stability through a novel dual-methodology framework that synergistically combines hybrid ML techniques with physics-informed neural networks (PINN). The research addresses critical gaps in current geotechnical practice by developing, validating, and deploying advanced computational frameworks that enhance both predictive accuracy and physical interpretability of slope stability assessments.

I.3.1 Research Scope and Objectives:

The primary objective of this dissertation is to develop and validate innovative computational methodologies for Factor of Safety (FOS) prediction in high road embankments, specifically addressing:

Objective 1: Hybrid Machine Learning Framework Development

Development of a hybrid stacking ensemble model integrating Extreme Gradient Boosting (XGBoost), Support Vector Regression (SVR), Multi-Layer Perceptron (MLP), and Random Forest (RF) algorithms, trained on a comprehensive database of 1,176 finite element simulations encompassing embankment heights ranging from 6 to 30 meters with diverse slope geometries and soil properties representative of realistic field conditions. This framework addresses Gap 2 by systematically combining complementary algorithmic strengths through nested cross-validation and meta-learning optimization.

Objective 2: Physics-Informed Neural Network Framework

Design and implementation of a novel PINN architecture that explicitly incorporates fundamental geotechnical principles—including the Mohr-Coulomb failure criterion, Bishop's Simplified Method equilibrium conditions, stability number constraints, and monotonicity relationships—directly into the NN loss function, ensuring that predictions remain physically consistent across diverse slope configurations and loading conditions. This framework addresses Gap 1 and Gap 3 by embedding domain knowledge into deep learning architectures through automatic differentiation and composite loss functions.

Objective 3: Comparative Performance Analysis

Systematic evaluation and benchmarking of proposed methodologies against traditional FOS calculation methods (Bishop, Morgenstern-Price, Finite Element Method) and conventional ML approaches, quantifying improvements in predictive accuracy, computational efficiency, physics consistency, and uncertainty quantification across multiple validation datasets including real-world embankment case studies from Algerian highway projects.

Objective 4: Interpretability and Practical Implementation

Application of SHapley Additive exPlanations (SHAP) analysis to quantify feature importance, identify critical parameter interactions, and provide transparent insights into model decision-making processes. Development of practical guidelines and open-source implementations that facilitate integration of advanced computational methods into routine geotechnical engineering practice while maintaining interpretability and reliability expected in safety-critical applications.

I.3.2 Methodological Innovation:

The research employs a rigorous methodological framework combining finite element modeling, advanced ML algorithms, and physics-informed deep learning:

- *Database Generation:* Systematic generation of 1,176 slope stability scenarios using GeoStudio SLOPE/W software (Version 2024), employing full-factorial design to ensure comprehensive parameter space coverage while maintaining realistic parameter combinations consistent with field observations. The database encompasses five embankment heights (6, 12, 18, 24, 30 m), three foundation soil types (CBR: 3-15%), twelve embankment soil variants (cohesion: 2-40 kPa, friction angle: 25-40°), and 43 distinct slope geometries with varying berm configurations (Djabri et al. 2025).
- *Hybrid Machine Learning Architecture:* Implementation of stacking ensemble architecture where diverse base learners (XGBoost, SVR, MLP, RF) are trained using nested 5-fold cross-validation, with their out-of-fold predictions serving as inputs to a linear regression meta-learner that optimally combines individual model strengths while mitigating weaknesses. Rigorous data leakage prevention ensures that meta-learner training relies exclusively on

predictions from base models that never observed the corresponding training samples (Djabri et al. 2025).

- *Physics-Informed Deep Learning Framework:* Development of multi-branch neural network architecture with specialized processing pathways for material properties (cohesion, friction angle, unit weight), geometric parameters (height, slope angles, berm count), and environmental conditions (moisture content, deformation modulus). Integration of physics-based loss functions enforcing: (1) Mohr-Coulomb consistency ($\mathcal{L}_{\text{MC}}$), (2) Bishop's Simplified Method alignment ($\mathcal{L}_{\text{Bishop}}$), (3) monotonicity constraints ($\mathcal{L}_{\text{mono}}$), and (4) physical bounds ($\mathcal{L}_{\text{bounds}}$), with empirically optimized weighting coefficients determined through systematic grid search.
- *Interpretability Analysis:* Application of SHapley Additive exPlanations (SHAP) framework to quantify feature importance, identify critical parameter interactions, and provide transparent insights into model decision-making processes.

I.4. Structure of the Thesis

This dissertation is organized into seven interconnected chapters that progressively develop, validate, and demonstrate the proposed computational frameworks:

Chapter I: General Introduction establishes the research context, motivation, and significance. It presents the problem statement, research objectives, scope, and organizational structure of the dissertation. The chapter reviews the current state-of-practice in slope stability analysis, highlights the global economic impact of slope instability (exceeding $4 billion annually), and identifies critical gaps that motivate the dual-methodology approach combining hybrid ML and PINN. The chapter emphasizes the limitations of traditional methods (computational intensity of FEM, simplifying assumptions of LEM) and positions ML as a transformative solution for geotechnical engineering challenges.

Chapter II: Theoretical Framework provides comprehensive theoretical foundations for the research methodologies employed. The chapter begins with slope stability fundamentals including the Mohr-Coulomb failure criterion and classical stability analysis methods (Limit Equilibrium Methods (LEM) and Finite Element Method (FEM) with Strength Reduction). It then covers ML Foundations, including the supervised learning paradigm and six computational techniques: Deep Artificial Neural Networks (DANN), Support Vector Regression (SVR), Multilayer Perceptron (MLP), k-Nearest Neighbors (k-NN), Extreme Gradient Boosting (XGBoost), and Random Forest (RF), culminating in the hybrid stacking ensemble methodology. The chapter introduces Physics-Informed Neural Networks, detailing the PINN framework overview, Mohr-Coulomb physics loss, Bishop's Simplified Method integration, monotonicity constraints, composite loss function design, Bayesian optimization for hyperparameter tuning, and uncertainty quantification via Monte Carlo dropout. It concludes with model evaluation metrics including R^2, RMSE, MAE, MSE, and physics-based validation metrics specific to PINNs.

Chapter III: Numerical Modeling describes the comprehensive finite element modeling framework for generating the research database. The chapter details geometric configurations (embankment heights of 6-30m, slope geometries with multi-berm configurations), material properties (12 embankment soil variants with cohesion 2-40 kPa and friction angle 25-40°, three foundation soil types with CBR 3-15%), finite element mesh discretization and convergence analysis, boundary conditions, and the numerical solution methodology using the Strength Reduction Method. It presents results and analysis including the FOS database overview (1,176 simulations), typical failure mechanisms, influence of key parameters (height, cohesion, friction angle, number of berms, foundation quality), and stability classification. The chapter includes rigorous model validation against published literature (Mesa-Lavista et al. 2021; Bandara et al. 2016; Huang et al. 2023; Duncan et al. 2014) achieving errors within ±5%, along with database characteristics and statistical analysis confirming comprehensive parameter space coverage.

Chapter IV: Hybrid Machine Learning for Slope Stability Prediction presents the first major research contribution, fully integrating the published article (Djabri et al. 2025). Following a comprehensive background and literature review, the chapter details the methodology including database generation, implementation of six ML models (DANN, SVR, MLP, k-NN, XGBoost, RF), development of the hybrid stacking ensemble architecture with nested cross-validation to prevent data leakage, and SHAP interpretability analysis. Results demonstrate exceptional performance: individual model achievements (XGBoost: R^2=0.9963, RMSE=0.0254 as top performer), hybrid stacking ensemble superiority (R^2=0.9978, RMSE=0.0199, representing 14% RMSE reduction), and comprehensive analysis including ANOVA revealing cohesion dominance (F=1158.358, η^2=0.546), Partial Dependence Plots, feature importance distribution (cohesion: 47.7%, friction angle: 31.1%, height: 6.6%), SHAP summary plots, statistical validation through repeated cross-validation, and Bland-Altman agreement analysis. The chapter concludes with discussion of limitations, cost-sensitive learning implementation addressing high FOS systematic bias, uncertainty quantification via bootstrap resampling (96.3% coverage), and independent field validation on 20 real Tebessa embankments achieving mean error of +0.82%.

Chapter V: Physics-Informed Neural Networks for Factor of Safety Prediction presents the second major research contribution. After establishing background context and literature review emphasizing the limitations of purely data-driven approaches, the chapter details the PINN methodology including the physics-informed framework architecture, data processing of 1,136 configurations (1,116 FEA + 20 field validation cases after outlier removal), and hyperparameter configuration determined through Bayesian optimization (architecture [64, 112, 48, 1], physics weights λ_MC=0.062, λ_B=0.277, λ_M=0.089) . Results and discussion present model performance evaluation (R^2=0.9787, RMSE=0.0545), cross-validation results (mean R^2=0.9029±0.0153), uncertainty quantification via Monte Carlo dropout (94.6% prediction interval coverage), physical consistency validation (88.7% overall monotonicity satisfaction, 100% for critical parameters), feature importance and interpretability through SHAP analysis (cohesion |SHAP|=0.177, height 0.147, friction angle 0.118), sensitivity analysis and residual diagnostics confirming zero-mean homoscedastic errors, and comparative performance with field validation on 20 independent Tebessa embankments achieving mean error of +0.89%. The chapter concludes by acknowledging the intentional trade-off between statistical accuracy and physical consistency, positioning PINNs as physics-guided validators ensuring mechanistic reliability.

Chapter VI: Comparative Analysis synthesizes findings from both research contributions through rigorous comparative assessment. The chapter begins by positioning the 1,176-simulation dataset within the literature (substantially exceeding typical studies: Lin et al. 349 cases, Wang et al. 444 cases). Comparative performance analysis reveals the hybrid ensemble achieves superior statistical performance (R^2=0.9978 vs. 0.9787, RMSE=0.0199 vs. 0.0545) while PINN guarantees perfect monotonicity for primary parameters (100% vs. 96.5%) and reduces physically implausible predictions by 91.3%. The chapter analyzes computational efficiency (PINN demonstrates 70% faster development time, 42× faster uncertainty quantification, 62% smaller deployment footprint), uncertainty quantification reliability (both achieve well-calibrated 95% confidence intervals with 94-96% coverage), interpretability consistency (Spearman ρ=0.89 between feature importance rankings), and generalization behavior through independent field validation (hybrid: +0.82% mean error; PINN: +0.89%). Practical deployment guidelines recommend the hybrid ensemble for preliminary design screening and the PINN for safety-critical verification, culminating in an integrated three-stage workflow leveraging both methodologies complementarily. The chapter synthesizes the fundamental trade-off between data-driven optimization (hybrid) and physics-informed regularization (PINN), positioning them as complementary tools rather than competitive alternatives.

Chapter VII: General Conclusion and Future Perspectives summarize the key research contributions, highlighting methodological innovations in both the hybrid ML framework (achieving R^2=0.9978 with ~85% computational efficiency gains) and the PINN approach (R^2=0.9787 with 100% monotonicity compliance for critical parameters and 88.7% overall physics satisfaction). The chapter emphasizes interpretability validation through consistent SHAP analysis across both frameworks, independent field validation excellence (both achieving <1% mean error on 20 real Tebessa embankments), and the successful integration of ML predictive power with physics-based constraints. The operational efficiency advantages position PINN favorably for parametric optimization and real-time decision support. The chapter presents an integrated workflow for engineering practice combining both methodologies in complementary roles, acknowledges application domain and limitations (validated for heights 6-30m, cohesion 2-40 kPa, friction angle 25-40°, CBR 3-15%), and outlines future perspectives including extension to three-dimensional analysis, dynamic and time-dependent phenomena (seismic loading, transient pore pressures), integration with real-time monitoring systems, multi-physics coupling incorporating complex soil behavior, transfer learning and domain adaptation, uncertainty quantification enhancement through Bayesian neural networks, and extension to related geotechnical problems (bearing capacity, settlement analysis, retaining walls, tunnel stability). The conclusion affirms that PINN represents a transformative advancement enabling previously impractical analyses while maintaining the rigor and transparency essential for critical infrastructure applications.

References provide comprehensive bibliographic documentation of all cited sources, including foundational geotechnical engineering texts (Duncan and Wright 2005; Terzaghi et al. 1996), ML literature (Bishop 2006; Goodfellow et al. 2016), PINN research (Karniadakis et al. 2021; Raissi et al. 2019), and relevant slope stability studies (Kardani et al. 2021; Karir et al. 2022; Lin et al. 2021; Wang et al. 2024).

Appendices include two major sections: Appendix 1 presents the Practical Implementation describing the Safety Factor Prediction Application—a standalone desktop tool developed using Python and PyQt5, featuring bilingual interface (English/French), authentication system, comprehensive input modules for foundation and embankment parameters with real-time validation, multi-slope geometry configuration, prediction and output functionality with PDF export capability, and validation demonstration cases confirming perfect accuracy (12m embankment: FOS=1.528, error=0.0%; 24m multi-berm: FOS=1.305, error=0.0%). Appendix 2 documents Research Outputs and Dissemination, including the published journal article (Djabri et al. 2025 in Engineering Applications of Artificial Intelligence, Category A/Q1), manuscript under review on Bayesian Physics-Informed Neural Networks, four national conference presentations across Algeria (Bouira, Tebessa, Constantine, Tlemcen), and three international conference presentations (Mascara, Skikda, Konya-Turkey), demonstrating comprehensive dissemination strategy maximizing societal impact of the research contributions.

II. Theoretical Framework

II.1. Introduction

The theoretical foundation of this research encompasses two complementary computational paradigms for slope stability prediction: hybrid ML ensemble methods and PINN. Both approaches leverage advanced AI techniques while addressing distinct aspects of geotechnical engineering challenges. The hybrid approach emphasizes predictive accuracy through ensemble learning, while the physics-informed methodology prioritizes theoretical consistency through embedded domain knowledge. This chapter presents the mathematical foundations, algorithmic principles, and evaluation frameworks underlying both methodologies, beginning with fundamental slope stability concepts that form the basis for both computational approaches.

II.2. Slope Stability Fundamentals

Slope stability analysis quantifies soil mass resistance against shear failure along potential slip surfaces. FOS expresses the ratio of available shear strength to mobilized shear stress, serving as the primary quantitative indicator for assessing failure risk and informing design decisions across diverse geotechnical applications including open-pit mining operations, transportation infrastructure development, earth dam construction, and urban hillslope management (Cheng et al. 2007; Duncan et al. 2014; Huang et al. 2023). The FOS provides engineers with a standardized metric to evaluate stability margins, with values greater than 1.0 indicating stable conditions, values approaching 1.0 suggesting marginal stability requiring careful evaluation, and values below 1.0 indicating failure conditions necessitating immediate remediation or redesign.

II.2.1 Mohr-Coulomb Failure Criterion

The Mohr-Coulomb relationship defines the fundamental constitutive law governing soil shear strength and represents the cornerstone of classical soil mechanics theory. The criterion states that shear strength (τ_f) develops as a linear function of effective normal stress:

$$\tau_f = c' + \sigma_n' \tan \phi' \qquad \text{(II-1)}$$

Where:

- c'= effective cohesion (kPa), representing the component of shear strength independent of normal stress, arising from cementation, electrostatic forces between clay particles, and apparent cohesion from capillary tension in unsaturated soils
- ϕ'= effective friction angle (degrees), quantifying the rate of shear strength increase with effective normal stress, fundamentally related to particle angularity, surface roughness, and interlocking mechanisms
- σ_n'= effective normal stress (kPa), computed as total normal stress minus pore water pressure according to Terzaghi's effective stress principle: $\sigma_n' = \sigma_n - u$

This criterion, originally proposed by Coulomb (1776) for granular materials and extended by Mohr (1900) through graphical stress analysis, remains the most widely adopted strength framework in contemporary geotechnical practice due to its simplicity, physical interpretability, and extensive experimental validation across diverse soil types (Das and Sobhan 2006; Lambe and Whitman 1969; Terzaghi et al. 1996). The linear approximation adequately captures soil behavior for most practical stress ranges encountered in slope stability problems, though nonlinear failure envelopes may be required for soils exhibiting significant curvature at low or high confining pressures.

The effective stress principle underlying Equation (II-1) recognizes that only the solid-to-solid contact forces—quantified by effective stress—contribute to shear resistance, while pore fluid pressures reduce intergranular contact without providing frictional resistance. This distinction proves critical in slope stability analysis, where elevated pore pressures from rainfall infiltration, reservoir impoundment, or inadequate drainage can dramatically reduce effective stresses and trigger failure even when total stresses remain unchanged.

II.2.2 Classical Stability Analysis Methods

Traditional approaches for quantifying slope stability have evolved over nearly a century of geotechnical practice, forming two principal methodological categories:

II.2.2.1 Limit Equilibrium Methods (LEM)

Limit equilibrium methods analyze slope stability by dividing the potential sliding mass into vertical slices and imposing equilibrium conditions (force and/or moment equilibrium) while making simplifying assumptions about interslice forces. FOS is defined as:

$$FOS = \frac{\text{Available Shear Strength}}{\text{Mobilized Shear Stress}} = \frac{\sum\text{Resisting Forces}}{\sum\text{Driving Forces}} \tag{II-2}$$

Principal limit equilibrium formulations include:

Fellenius (Swedish) Method (1936): The earliest systematic approach assumes interslice forces are zero, providing simple hand calculations but yielding unconservative results (typically 5-20% lower FOS than rigorous methods). The method satisfies only overall moment equilibrium.

Bishop's Simplified Method (1955): Assumes horizontal interslice forces, satisfying vertical force equilibrium and overall moment equilibrium. This method has become the most widely adopted approach in routine practice due to its optimal balance between accuracy (within 1-5% of rigorous methods for circular surfaces) and computational simplicity. The iterative solution converges rapidly, typically requiring 3-5 iterations.

Morgenstern-Price Method (1965): Satisfies complete equilibrium (force equilibrium in two directions plus moment equilibrium) by assuming a functional relationship between interslice shear and normal forces. This rigorous approach provides theoretically exact solutions for any slip surface geometry but requires more complex iterative procedures.

Spencer's Method (1967): A special case of Morgenstern-Price assuming constant ratio between interslice shear and normal forces, offering computational efficiency while maintaining complete equilibrium satisfaction. This method is particularly suited for irregular slip surfaces in heterogeneous soil profiles.

While these methods provide reliable FOS estimates validated over decades of practice, they face significant limitations: (1) computational intensity when evaluating thousands of potential slip surfaces or conducting probabilistic analyses across large parameter spaces, (2) iterative convergence challenges for complex geometries or unusual soil property combinations, (3) difficulty incorporating three-dimensional effects or complex constitutive behaviors, and (4) inability to provide deformation information or progressive failure analysis.

II.2.2.2 Finite Element Method (FEM)

Finite element analysis represents a more sophisticated numerical approach that discretizes the slope geometry into small elements (typically triangular or quadrilateral) and solves the governing partial differential equations for stress-strain equilibrium (Griffiths and Lane 1999; Zienkiewicz et al. 2005). The FEM approach offers several advantages over limit equilibrium methods:

Strength Reduction Method (SRM): The most common FEM-based stability assessment technique systematically reduces soil strength parameters (c' and $\tan\phi'$) by a trial factor of safety until the numerical solution fails to converge, indicating that equilibrium can no longer be satisfied (Dawson et al. 1999; Matsui and San 1992). The strength reduction factor at failure represents the FOS:

$$c'_{reduced} = \frac{c'}{SRF}, \tan\,\phi'_{reduced} = \frac{\tan\phi'}{SRF} \qquad \text{(II-3)}$$

Where SRF (Strength Reduction Factor) is iteratively increased until numerical non-convergence, at which point SRF equals the Factor of Safety (FOS).

The method automatically identifies the critical failure mechanism without assuming slip surface geometry, provides stress and deformation fields throughout the analysis, and naturally captures progressive failure mechanisms where local yielding redistributes stresses to adjacent zones.

Advantages of FEM: (1) no assumptions about slip surface shape or location required, (2) incorporation of complex constitutive models (strain-softening, anisotropy, time-dependent behavior), (3) simulation of construction sequences, excavation stages, or loading histories, (4) coupling of stress analysis with groundwater flow, thermal effects, or consolidation, and (5) three-dimensional analysis capability for complex geometries.

Computational Challenges: Despite these advantages, FEM faces substantial practical limitations: (1) significant computational expense, with typical slope stability analyses requiring 30-60 minutes per configuration on standard workstations compared to seconds for limit equilibrium methods, (2) requirement for specialized expertise in mesh generation, constitutive model selection, and numerical convergence assessment, (3) extensive input data requirements for advanced constitutive parameters often unavailable during preliminary design, (4) sensitivity to mesh refinement, boundary condition placement, and convergence tolerance specifications, and (5) difficulty conducting probabilistic analyses requiring thousands of realizations.

These computational impediments prove particularly constraining for large-scale infrastructure projects requiring evaluation of multiple slope configurations, parametric design optimization, or comprehensive probabilistic safety assessments. The intensive resource requirements of traditional analytical frameworks motivate the development of alternative approaches—specifically ML and

PINN—that can deliver rapid predictions while maintaining acceptable accuracy thresholds for engineering design (Samui and Kothari 2011; Zhang et al. 2021).

II.3. Machine Learning Foundations

ML provides flexible computational frameworks for modeling complex nonlinear relationships between soil properties, slope geometry, and FOS without requiring explicit constitutive formulations or iterative equilibrium solutions (Goodfellow et al. 2016; Hastie et al. 2009). Unlike traditional analytical methods that rely on simplified assumptions about soil behavior and failure mechanisms, ML algorithms learn patterns directly from data, capturing intricate parameter interactions and emergent behaviors that may not be adequately represented by closed-form equations. This data-driven paradigm has demonstrated exceptional efficacy across diverse geotechnical applications, including bearing capacity prediction, settlement analysis, liquefaction assessment, and slope stability evaluation (Samui and Kothari 2011; Zhang et al. 2021).

II.3.1 Supervised Learning Paradigm

Supervised ML algorithms learn a mapping function $f: \mathcal{X} \rightarrow \mathcal{Y}$from labeled training data, where the input space $\mathcal{X}$comprises feature vectors characterizing slope configurations and the output space $\mathcal{Y}$contains corresponding target values (FOS). For slope stability prediction, the input feature vector **x** typically includes:

Soil parameters:

- Unit weight (γ, kN/m^3): controls gravitational driving forces
- Cohesion (c', kPa): provides stress-independent shear resistance
- Friction angle (ϕ', degrees): mobilizes stress-dependent strength
- Deformation modulus (E, MPa): influences stress distribution patterns
- Moisture content (w, %): affects effective stress through pore pressures
- Poisson's ratio (ν): controls lateral stress response

Geometric characteristics:

- Embankment height (H, m): primary driver of gravitational forces
- Slope angles (β_1 through β_5, radians): define inclination of multiple slope segments
- Number of berms (n): quantifies intermediate stability platforms
- Berm width and vertical spacing: characterize multi-bench configurations

Loading conditions:

- Traffic surcharge (q, kPa): represents distributed surface loads
- Seismic coefficients (k_h, k_v): account for earthquake-induced inertial forces
- Construction staging effects: capture time-dependent loading sequences

The target output (y) is the FOS obtained from validated finite element simulations or limit equilibrium analyses, providing ground-truth labels for supervised training. The training dataset $\mathcal{D} = \{(\mathbf{x}_i, y_i)\}_{i=1}^{N}$consists of N labeled examples spanning the design parameter space.

The supervised learning objective follows the empirical risk minimization framework:

$$\min_{\theta} \frac{1}{N} \sum_{i=1}^{N} \mathcal{L}(f_{\theta}(\mathbf{x}_i), y_i) + \lambda \Omega(\theta) \tag{II-4}$$

where:

- $f_{\theta}(\cdot)$denotes the predictive model parameterized by θ(neural network weights, decision tree structures, kernel parameters, etc.)
- $\mathcal{L}(\cdot,\cdot)$represents the loss function quantifying prediction errors, typically mean squared error for regression: $\mathcal{L}(\hat{y}, y) = (\hat{y} - y)^2$
- $\Omega(\theta)$is a regularization term preventing overfitting through parameter penalization (L1, L2 norms, dropout, early stopping)
- λcontrols the regularization strength, balancing training accuracy against model complexity

The first term measures the average discrepancy between model predictions and ground-truth values across the training set, while the regularization term constrains model complexity to enhance generalization to unseen data (Bishop 2006; Hastie et al. 2009). Through iterative optimization (gradient descent, evolutionary algorithms, boosting procedures), the model parameters $\theta$are adjusted to minimize this objective, yielding a trained model capable of predicting FOS for novel slope configurations within the interpolation domain defined by the training data.

This supervised learning paradigm forms the foundation for all ML approaches investigated in this research, including individual algorithms (DANN, SVR, MLP, k-NN, XGBoost, RF) and hybrid ensemble methods that combine multiple base learners to achieve superior predictive performance through complementary error cancellation and variance reduction.

II.4. Machine Learning Computational Techniques

ML methodologies demonstrate exceptional efficacy in analyzing high-dimensional datasets and generating predictive models based on underlying data patterns and relationships. Six distinct algorithmic approaches were systematically selected to evaluate their comparative performance: Deep Artificial Neural Networks (DANN), Support Vector Regression (SVR), Multilayer Perceptron (MLP), k-Nearest Neighbors (k-NN), Extreme Gradient Boosting (XGBoost), and Random Forest (RF). These six algorithms were selected based on their complementary computational strengths: XGBoost and RFprovide ensemble-based robustness against data noise and outliers through bagging and boosting mechanisms; SVR offers strong generalisation in high-dimensional spaces via kernel-based non-linear mapping; MLP captures complex multi-dimensional feature interactions through deep representation learning; DANN enhances generalisation through adversarial domain adaptation; and k-NN serves as a non-parametric baseline for local pattern recognition. Together, these approaches ensure a comprehensive and methodologically rigorous comparative evaluation.

II.4.1 Deep Artificial Neural Network (DANN)

Deep Artificial Neural Networks (DANNs) are advanced ML models featuring multiple hidden layers that can extract complex, non-linear relationships from data. These architectures are inspired by biological neural systems (Iqbal et al. 2025; Li et al. 2025; Mahmoodzadeh et al. 2022). As illustrated in **Figure II-1**, data undergoes forward propagation through weighted connections and activation functions, followed by loss calculation. Subsequently, backpropagation employs the chain rule to compute gradients, with network weights adjusted via optimizers such as Gradient Descent or Adam.

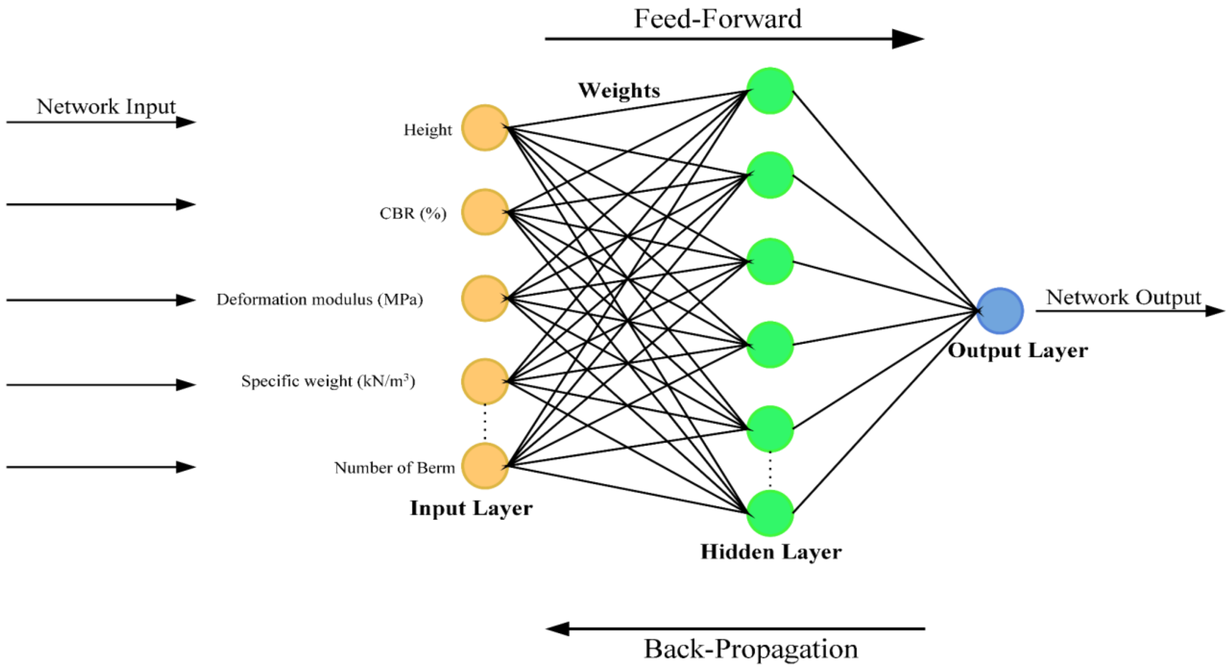

Figure II-1 Description of the DANN Diagram.

Note: Figure II-1 presents a simplified schematic of the general feedforward neural network architecture for illustrative purposes only, showing representative input features and a single hidden layer to convey the fundamental feed-forward and backpropagation mechanisms. The actual DANN architecture implemented in this study comprises four hidden layers with 128, 64, 32, and 16 neurons respectively, employing ReLU activation functions and dropout regularization, as detailed in Chapter IV.

The DANN architecture implemented comprises four hidden layers containing 128, 64, 32, and 16 neurons, respectively. The network utilizes ReLU activation functions and incorporates dropout regularization to prevent overfitting.

For *feedforward propagation*, each layer's output is computed as:

$$\hat{y} = f(W_n \cdot O_n + b_n) \tag{II-5}$$

Where W_n is the weight matrix between layer n and n+1, O_n is the output vector of layer n, b_n is the bias vector, and f is the activation function (e.g., sigmoid $\sigma(x) = \frac{1}{1+e^{-x}}$, ReLU). Matrix multiplication enables parallel computation across neurons.

For backpropagation and learning, the network minimizes prediction errors via gradient descent. For a cost function E, the error gradient for the output layer is:

$$\frac{\partial E}{\partial W_N} = (\hat{y} - Y) \cdot f'(W_N \cdot O_N + b_N) \cdot O_N^T \quad \text{(II-6)}$$

Where $\hat{y} = f(W_N \cdot O_N + b_N)$ denotes the network's final predicted output (equivalent to O_{N+1} in a hypothetical extended notation), and Y represents the ground truth target values.

Where Y represents ground truth values. The weight update rule follows:

$$W_{new} = W_{old} - \alpha \cdot \frac{\partial E}{\partial W} \quad \text{(II-7)}$$

Here, α (learning rate) controls optimization step size. The chain rule propagates errors backward:

$$\delta_n = (W_n^T \cdot \delta_{n+1}) \odot f'(W_{n-1} \cdot O_{n-1} + b_{n-1}) \quad \text{(II-8)}$$

Where $\delta_n$is the error gradient at layer n, and ⊙ denotes element-wise multiplication.

II.4.2 Support Vector Regression (SVR)

Support Vector Regression (SVR) maps data into a higher-dimensional space using nonlinear kernel functions to construct an optimal hyperplane, balancing prediction accuracy and model complexity via regularization (Smola and Schölkopf 2004). Theoretically grounded in Vapnik-Chervonenkis

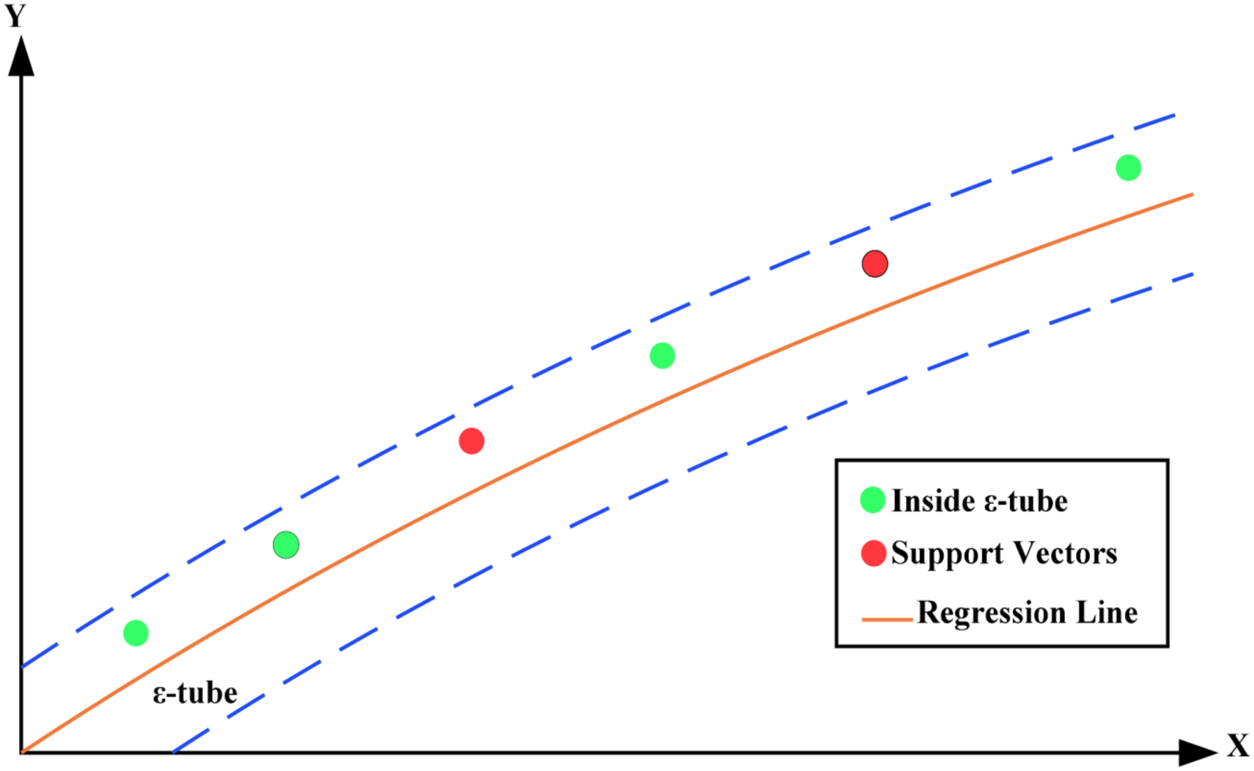

Figure II-2 Description of fundamental concept of Support Vector Regression.

(VC) dimension theory, SVR employs an ε-insensitive loss function in conjunction with a regularization parameter C to control error tolerance while maintaining model parsimony (Vapnik 1995).

The objective function of SVR is to minimize:

$$\frac{1}{2} \parallel \omega \parallel^2 + C \sum_{i=0}^{N} (\varepsilon_i + \varepsilon_i^*) \quad \text{(II-9)}$$

Subject to:

$$y_i - (\omega \cdot \phi(x_i) + b) \leq \varepsilon + \varepsilon_i \quad \text{(II-10)}$$

$$(\omega \cdot \phi(x_i) + b) - y_i \leq \varepsilon + \varepsilon_i^* \quad \text{(II-11)}$$

$$\varepsilon_i, \varepsilon_i^* \geq 0 \quad \text{(II-12)}$$

Where ω is the weight vector, b is the bias term, $\phi(x_i)$is the kernel function transforming $x_i$into a higher-dimensional space, ε is the margin of tolerance (epsilon-insensitive tube), $\varepsilon_i, \varepsilon_i^*$are slack variables for points outside the margin, and C is the regularization parameter controlling the trade-off between margin size and error.

The predicted value $\hat{y}$for a new input x is:

$$\hat{y} = \omega \cdot \phi(x_i) + b \quad \text{(II-13)}$$

II.4.3 Multilayer Perceptron (MLP)

The Multilayer Perceptron (MLP) is a feedforward neural network architecture that excels in classification, regression, and pattern recognition tasks by learning complex nonlinear input-output mappings through the backpropagation algorithm (Mirtaheri and Shahbazian 2022; Nanehkaran et al. 2023). During forward propagation, input data is sequentially transformed through weighted summations and activation functions across three primary components: an input layer, one or more hidden layers, and an output layer.

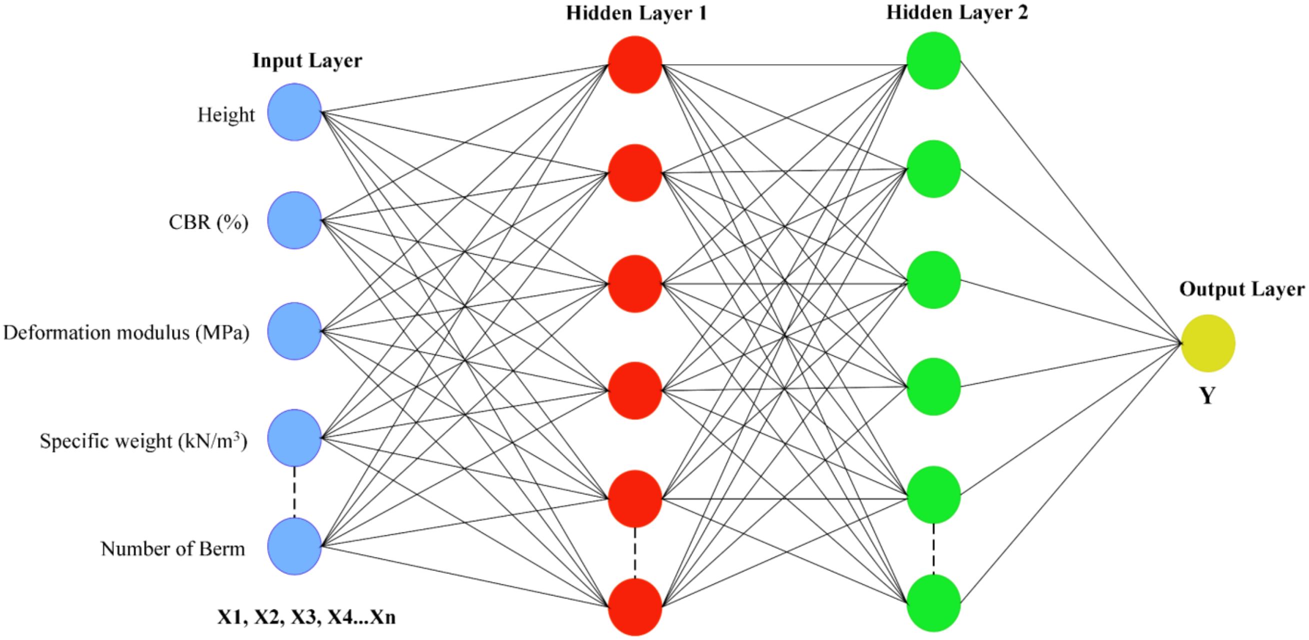

Figure II-3 Architecture of the MLP model.

Note: Figure II-3 presents a simplified two-hidden-layer schematic for conceptual illustration of the MLP architecture. The actual MLP model implemented in Chapter IV employs an optimised architecture whose hyperparameters — including the number of hidden layers, neurons per layer, and activation functions — were determined through systematic GridSearchCV tuning, as fully detailed therein. Input features shown are representative examples only; the complete set of 12 input variables is listed in **Table III-8**.

The output of each neuron is calculated as:

$$y = f\left(\sum (w_i x_i) + b\right) \qquad \text{(II-14)}$$

Where y is the neuron's output, f is the activation function, $w_i$are the connection weights, $x_i$are the corresponding inputs, and b is the bias term.

II.4.4 k-Nearest Neighbors (k-NN)

The k-Nearest Neighbors (k-NN) algorithm is a non-parametric, instance-based supervised learning method employed for both classification and regression tasks. The algorithm predicts target outcomes by identifying the k closest training instances in the feature space, utilizing majority voting for classification problems or weighted averaging for regression tasks. Distance calculations are typically performed using standard metrics such as Euclidean or Manhattan distance (Hasan et al. 2024; Yang et al. 2023).

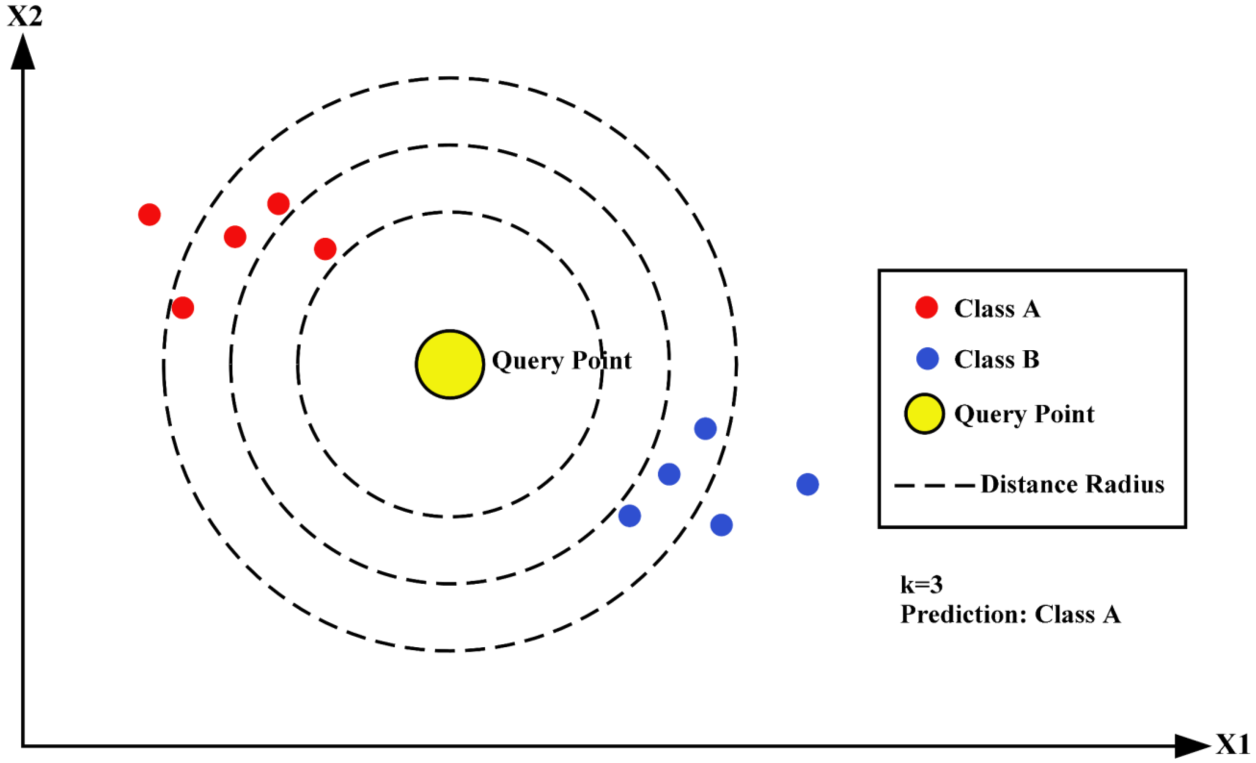

Figure II-4 k-NN Computational Architecture: Feature Space Partitioning and Neighborhood Analysis.

Distance Metrics (Ngoy Nadege et al. 2025):

Euclidean Distance (for continuous features):

$$d(x,y) = \sqrt{\sum_{i=1}^{n}(x_i - y_i)^2} \tag{II-15}$$

Manhattan Distance (for categorical or continuous features):

$$d(x,y) = \sum_{i=1}^{n} | x_i - y_i | \tag{II-16}$$

Prediction for regression:

$$\hat{y} = \frac{1}{k}\sum_{j=1}^{k} y_{ij} \qquad \text{(II-17)}$$

Where $x_i$is the query (new) data point, y is the training data point, n is the number of features/dimensions, $y_{ij}$is the target value of the j-th nearest neighbor, and $\hat{y}$is the predicted target value.

II.4.5 XGBoost (Extreme Gradient Boosting)

XGBoost is a powerful gradient boosting framework designed for supervised learning tasks including classification, regression, and ranking (Liu et al. 2023; Mwakipunda et al. 2024). It constructs an ensemble of decision trees sequentially, where each tree corrects errors from previous iterations by optimizing loss functions through gradient descent and employing L1/L2 regularization to prevent overfitting.

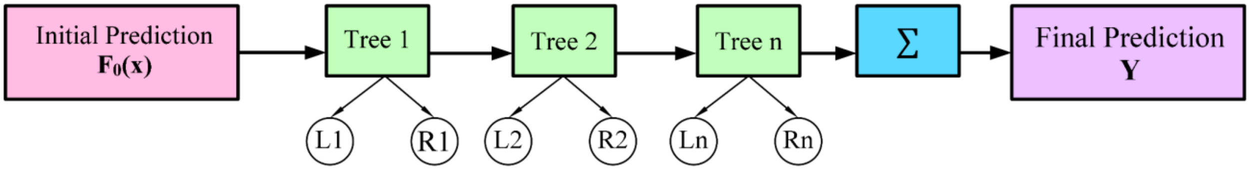

Figure II-5 Sequential architecture of a gradient boosting algorithm.

Objective function:

$$obj(\theta) = L(\theta) + \Omega(\theta) \qquad \text{(II-18)}$$

where L represents the loss function and Ω denotes the regularization term.

Tree ensemble model:

$$\hat{y}_i = \sum_{k=1}^{K} f_k(x_i) \qquad \text{(II-19)}$$

Where $f_k$represents each individual tree in the ensemble.

Regularization Term:

$$\Omega(f) = \gamma T + \frac{1}{2}\lambda \parallel w \parallel^2 \qquad \text{(II-20)}$$

Where T is the number of leaves and w represents the leaf weights.

Loss Function with Second Order Approximation:

$$L^{(t)} \approx \sum_{i=1}^{n} \left[g_i f_t(x_i) + \frac{1}{2} h_i f_t^2(x_i) \right] \qquad \text{(II-21)}$$

Where $g_i = \frac{\partial \ell(\hat{y}_i^{(t-1)}, y_i)}{\partial \hat{y}_i^{(t-1)}}$ is the first-order gradient and $h_i = \frac{\partial^2 \ell(\hat{y}_i^{(t-1)}, y_i)}{\partial (\hat{y}_i^{(t-1)})^2}$ is the second-order derivative (Hessian) of the loss function with respect to the previous prediction (Chen and Guestrin 2016).

II.4.6 Random Forest (RF)

RF is a versatile ensemble learning technique used for classification, regression, and other ML tasks. It operates by generating multiple decision trees during training, each constructed from a unique bootstrap sample of the dataset, and combines their predictions through majority voting for classification or averaging for regression (Breiman 2001).

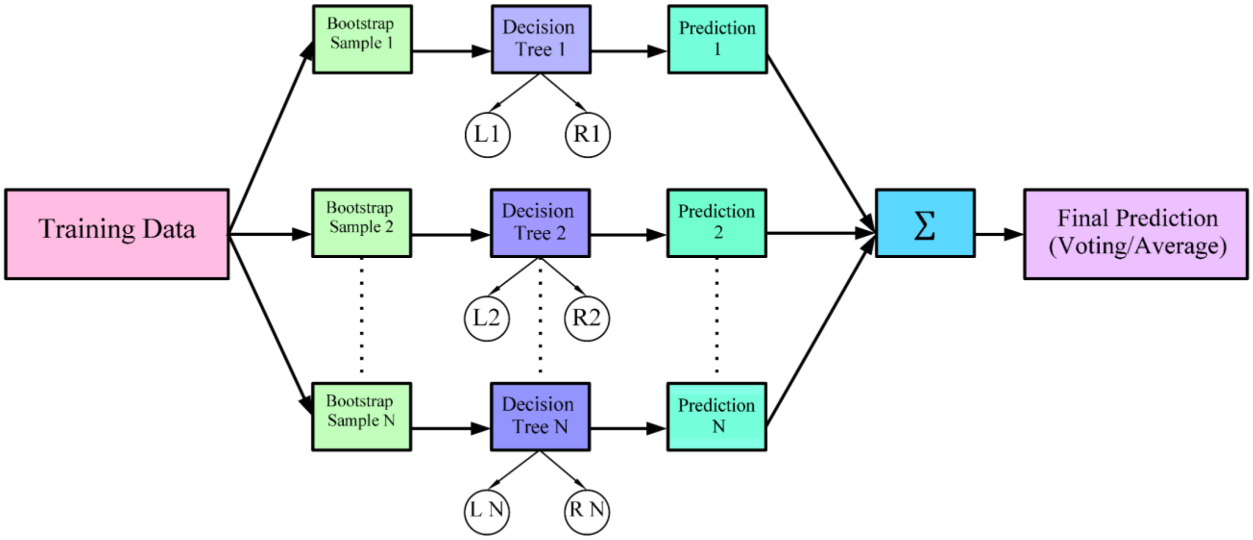

Figure II-6 Architectural Schema of Random Forest Algorithm with Bootstrap Aggregation and Decision Tree Parallelization.

Bootstrap sampling: For each tree, sample n data points with replacement from the training dataset of size N.

Tree construction: At each node, select m features randomly from the total M features. Choose the best split based on a criterion (e.g., Gini impurity for classification, mean squared error for regression).

Aggregation for regression (Mwakipunda et al. 2025; Nadege et al. 2024):

$$\hat{y} = \frac{1}{k}\sum_{j=1}^{k} T_k\,(x) \tag{II-22}$$

Where $T_k(x)$is the prediction of the k-th tree for input x, and k is the total number of trees.

II.4.7 Hybrid Stacking Ensemble Model

A hybrid stacking model enhances predictive accuracy for regression tasks, such as estimating the FOS in geotechnical engineering, by combining base models including XGBoost, SVR, MLP, and RF in a hierarchical framework. The implementation follows a rigorous nested cross-validation approach to ensure unbiased performance estimation: base models generate out-of-fold predictions via 5-fold cross-validation on the training set, which are then used as input features to train the meta-learner (linear regression).

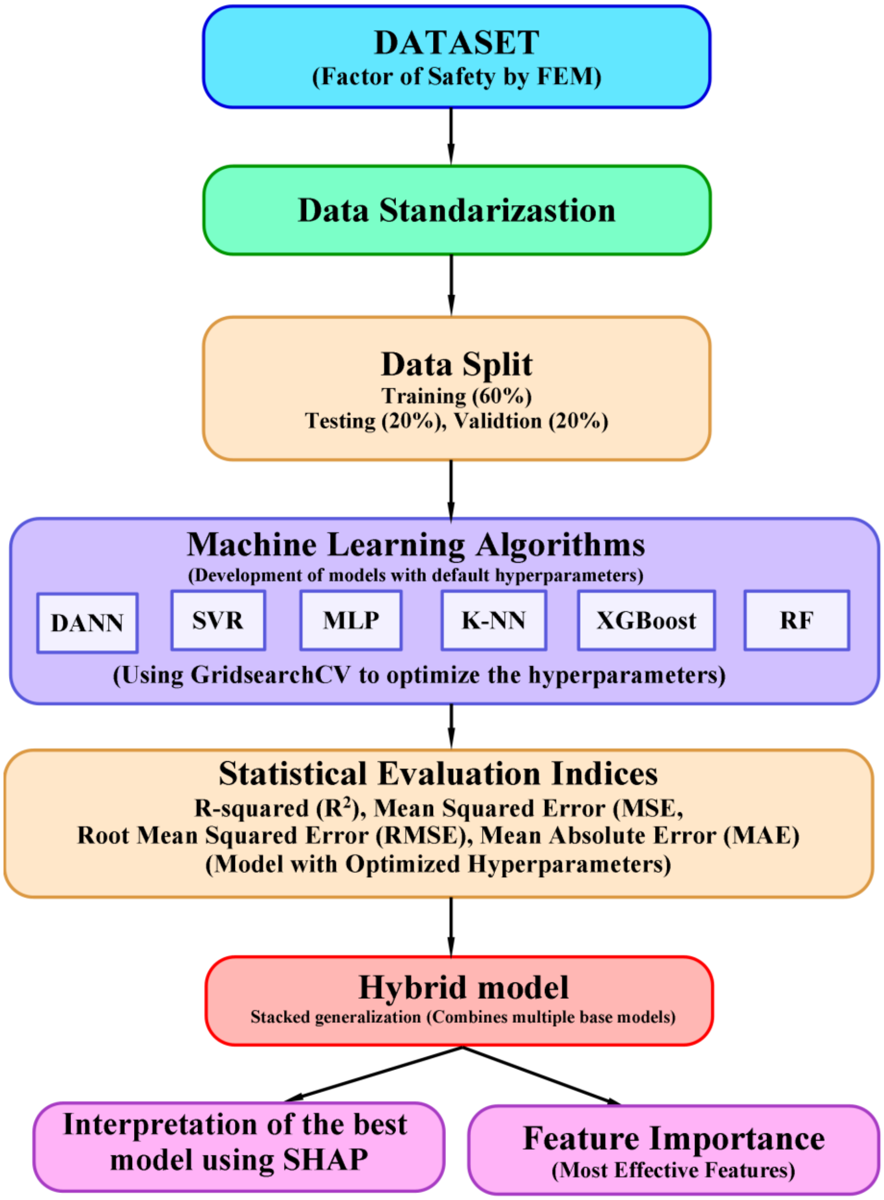

Figure II-7 Hybrid ML workflow for FOS prediction (Djabri et al. 2025).

Out-of-fold prediction generation:

$$\hat{y}_i = f_i(x) \qquad \text{(II-23)}$$

where i ∈(XGB, SVR, MLP, DANN, k-NN, RF)

Meta-learner training on out-of-fold predictions:

$$\hat{y}_{stack} = g(\hat{y}_1, \hat{y}_2, \dots, \hat{y}_n) = \beta_0 + \sum_i (\beta_i \cdot \hat{y}_i) \tag{II-24}$$

Final FOS prediction:

$$FOS = \hat{y}_{stack} \tag{II-25}$$

The coefficients $\beta_i$are determined by minimizing a loss function L on the validation set:

$$\min\ L(y, g(\hat{y}_1, \hat{y}_2, \dots, \hat{y}_n)) \tag{II-26}$$

Bootstrap Prediction Intervals: For each prediction, 100 bootstrap samples were generated from the training set, and the hybrid model was retrained to produce a distribution of predictions. The 95% prediction interval was computed as:

$$PI_{95\%} = [Q_{2.5\%}(\hat{y}_{bootstrap}), Q_{97.5\%}(\hat{y}_{bootstrap})] \tag{II-27}$$

where $Q_{p\%}$represents the p-th percentile of the bootstrap prediction distribution.

Quantile Regression Integration: To complement the point estimates, quantile regression was implemented for the meta-learner to directly predict the 10th, 50th, and 90th percentiles:

$$\hat{y}_q = \beta_{0,q} + \sum_i \beta_{i,q} \cdot \hat{y}_i \tag{II-28}$$

where $q \in (0.1, 0.5, 0.9)$represents the quantile levels, and $\beta_{i,q}$are quantile-specific coefficients optimized using pinball loss.

Cost-Sensitive Learning Implementation: For systematic bias in tail regions (high FOS values >2.0), a cost-sensitive learning framework was integrated. The cost-sensitive loss function is:

$$L_{cost} = \frac{1}{N} \sum_{i=1}^{N} w_i \cdot (y_i - \hat{y}_i)^2 \tag{II-29}$$

where the weight $w_i$is defined as:

- 2.0 if FOS_i ≥ 2.0 (high stability)
- 1.5 if 1.5 ≤ FOS_i < 2.0 (moderate stability)
- 1.0 if FOS_i < 1.5 (typical range)

II.5. Physics-Informed Neural Networks

II.5.1 PINN Framework Overview

PINNs constitute a novel class of universal function approximators that integrate governing physical equations and boundary conditions directly into the neural network training process through customized loss functions (Raissi et al. 2019). The fundamental architecture comprises a deep feedforward neural network that learns the mapping between input geotechnical parameters $x = [H, \gamma, w, E, c', \phi', \beta_1, \beta_2, \beta_3, \beta_4, \beta_5, n]$and the target FOS, while simultaneously satisfying prescribed physical constraints derived from established geotechnical principles.

The PINN architecture consists of fully connected layers with hyperbolic tangent (tanh) activation functions, selected for their smoothness properties and ability to approximate complex nonlinear relationships (Hornik et al. 1989). The network output $\hat{y}$represents the predicted FOS, obtained through forward propagation:

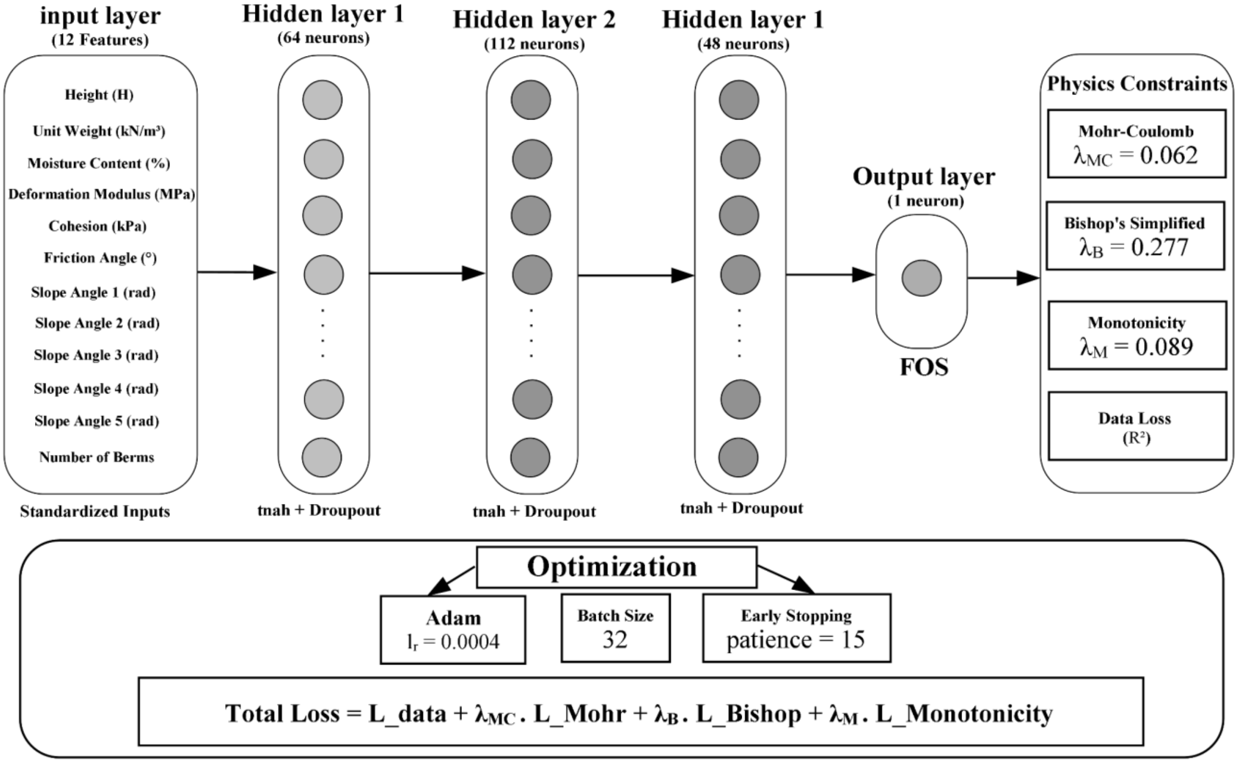

Figure II-8 Physics-Informed Neural Network Architecture for Prediction.

$$\hat{y} = f_\theta(x) = W_L \cdot \tanh\left(W_{L-1} \cdot \tanh\left(\dots W_1 \cdot x + b_1 \dots\right) + b_{L-1}\right) + b_L \tag{II-30}$$

where $\theta = \{W_1, \dots, W_L, b_1, \dots, b_L\}$ represents the trainable parameters (weights and biases), and L denotes the number of layers.

II.5.2 Mohr-Coulomb Physics Loss

The Mohr-Coulomb failure criterion represents the fundamental relationship between shear strength and normal stress in soil mechanics (Coulomb 1973; Terzaghi et al. 1996). The criterion states that failure occurs when the shear stress τ on any plane within the soil mass reaches the shear strength τ_f defined by:

$$\tau_f = c' + \sigma_n' \tan \phi' \tag{II-31}$$

where c' is the effective cohesion, σ_n' is the effective normal stress, and ϕ' is the effective friction angle. For slope stability analysis, the effective normal stress is computed as:

$$\sigma_n' = \gamma \cdot H \cdot \cos^2 \beta \cdot (1 - r_u) \tag{II-32}$$

where γ is the unit weight of soil, H is the slope height, β is the slope angle, and r_u is the pore pressure ratio. The driving shear stress along the potential failure surface is:

$$\tau_{driving} = \gamma \cdot H \cdot \sin \beta \cdot \cos \beta \tag{II-33}$$

The Mohr-Coulomb physics loss function enforces consistency between neural network predictions and these fundamental relationships:

$$\mathcal{L}_{MC} = \frac{1}{N} \sum_{i=1}^{N} (FOS_{pred}^{i} - FOS_{physics}^{i})^2 \tag{II-34}$$

$$FOS_{physics} = \frac{\tau_f^{(i)}}{\tau_{driving}^{(i)}} \tag{II-35}$$

where N is the batch size and the subscript pred denotes neural network predictions.

II.5.3 Bishop's Simplified Method Integration

Bishop's Simplified Method (Bishop 1955) provides an iterative solution for circular slip surface analysis that satisfies vertical force equilibrium and overall moment equilibrium. The FOS is computed as:

$$FOS = \frac{\sum_{j=1}^{n} [c' \cdot b_j + (W_j - u_j \cdot b_j) \cdot \tan \phi']}{\left[m_{\alpha,j} \cdot \sum_{j=1}^{n} (W_j \cdot \sin \alpha_j)\right]} \tag{II-36}$$

where the slice parameters include: b_j(slice width), W_j(slice weight), u_j(pore water pressure at slice base), α_j(base inclination angle), and n (number of slices). The critical $m_{\alpha,j}$ factor is defined as:

$$m_{\alpha,j} = \cos \alpha_j \cdot \left[1 + \frac{\tan \alpha_j \cdot \tan \phi'}{FOS}\right] \tag{II-37}$$

The integration of Bishop's method into the PINN framework is achieved through a specialized loss function:

$$\mathcal{L}_B = \frac{1}{N} \sum_{i=1}^{N} (FO\,S_{pred}^{i} - FOS_{Bishop}^{i})^2 \qquad \text{(II-38)}$$

where $FOS_{Bishop}$is computed via the iterative Bishop's Simplified Method for each training sample.

II.5.4 Monotonicity Constraints

The Mohr-Coulomb failure criterion and Bishop's limit equilibrium theory — the two governing physical frameworks underlying slope stability analysis — dictate specific monotonic relationships between input parameters and the FOS (Duncan and Wright 2005). According to these principles, increasing shear strength parameters (cohesion c' and friction angle φ') must necessarily increase FOS, while increasing destabilising factors (slope height H, unit weight γ, and slope angle β) must decrease it. These constraints ensure physical plausibility of model predictions:

$$\frac{\partial FOS}{\partial c'} > 0 \text{(Cohesion constraint)} \qquad \text{(II-39)}$$

$$\frac{\partial FOS}{\partial \phi'} > 0 \text{(Friction angle constraint)} \qquad \text{(II-40)}$$

$$\frac{\partial FOS}{\partial H} < 0 \text{(Height constraint)} \qquad \text{(II-41)}$$

$$\frac{\partial FOS}{\partial \gamma} < 0 \text{(Unit weight constraint)} \qquad \text{(II-42)}$$

$$\frac{\partial FOS}{\partial \beta} < 0 \text{(Slope angle constraint)} \qquad \text{(II-43)}$$

These constraints are enforced through gradient penalty terms computed via automatic differentiation (Baydin et al. 2018):

$$\mathcal{L}_M = \left[ReLU\left(-\frac{\partial FOS}{\partial c'}\right) + ReLU\left(-\frac{\partial FOS}{\partial \phi'}\right) + ReLU\left(\frac{\partial FOS}{\partial H}\right) + ReLU\left(\frac{\partial FOS}{\partial \gamma}\right) + \sum_{i=1}^{5} R\,eLU\left(\frac{\partial FOS}{\partial \beta_i}\right) \right] \qquad \text{(II-44)}$$

where $ReLU(x) = \max(0, x)$penalizes violations of monotonicity constraints.

II.5.5 Composite Loss Function

The complete PINN training objective combines data-driven supervised learning with the three physics-informed loss components:

$$\mathcal{L}_{total} = \mathcal{L}_{data} + \lambda_{MC} \cdot \mathcal{L}_{MC} + \lambda_B \cdot \mathcal{L}_B + \lambda_M \cdot \mathcal{L}_M \qquad \text{(II-45)}$$

where the data loss employs mean squared error:

$$\mathcal{L}_{data} = \frac{1}{N} \sum_{i=1}^{N} (FO\,S_{pred}^{i} - FOS_{target}^{i})^2 \qquad \text{(II-46)}$$

The relative weights ($\lambda_{MC}, \lambda_B, \lambda_M$) control the balance between data fidelity and physics constraints, determined through Bayesian optimization.

II.5.6 Bayesian Optimization for Hyperparameter Tuning

Hyperparameter optimization represents a critical challenge in deep learning, significantly impacting model performance (Bergstra and Bengio 2012). This study employs Bayesian optimization with Tree-structured Parzen Estimator (TPE) acquisition function (Bergstra et al. 2011). The optimization problem is formulated as:

$$\theta^* = \arg\min_{\theta \in \Theta} \mathbb{E}_{(x,y)\sim\mathcal{D}_{val}}[L(\theta; x, y)] \qquad \text{(II-47)}$$

where Θ represents the hyperparameter space and L is the validation loss.

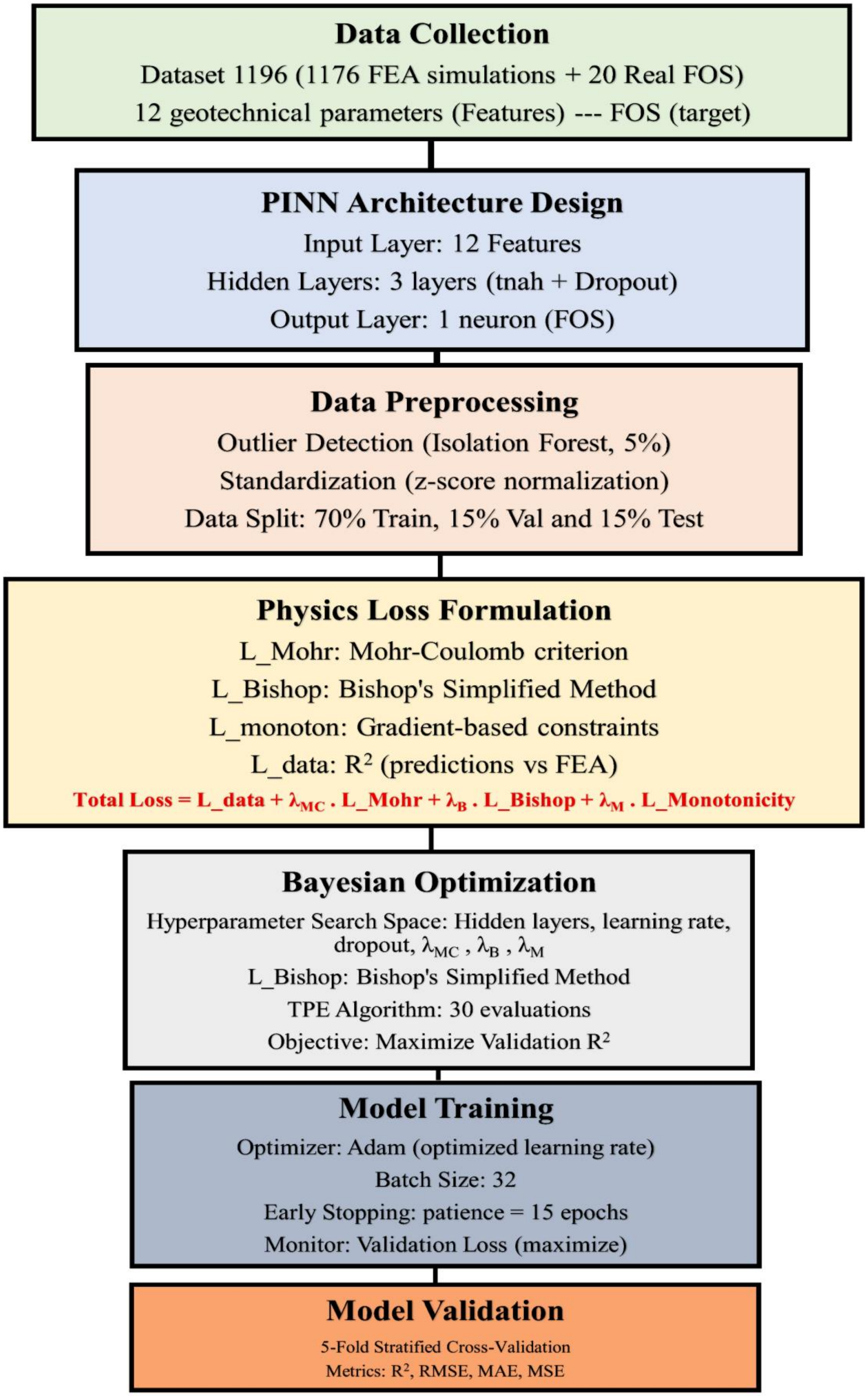

Figure II-9 Methodology Flowchart for PINN-based FOS Prediction.

II.5.7 Uncertainty Quantification via Monte Carlo Dropout

Uncertainty quantification is essential for risk assessment in geotechnical engineering applications (Phoon and Kulhawy 1999). Monte Carlo (MC) dropout (Gal and Ghahramani 2015) treats dropout as a variational inference method. During inference, dropout is kept active, and T stochastic forward passes generate an ensemble of predictions:

$$\mathcal{P}(y \mid x, \mathcal{D}) \approx \frac{1}{T}\sum_{t=1}^{T} f_{\theta_t}(x) \tag{II-48}$$

where $\theta_t$represents parameters with random dropout masks applied at iteration t. The predictive mean and epistemic uncertainty are estimated as:

$$\mu(x) = \frac{1}{T}\sum_{t=1}^{T} f_{\theta_t}(x) \tag{II-49}$$

$$\sigma^2(x) = \frac{1}{T}\sum_{t=1}^{T}[f_{\theta_t}(x) - \mu(x)]^2 \tag{II-50}$$

The Bayesian theoretical foundation underlying MC dropout can be expressed through Bayes' rule:

$$p(\theta \mid \mathcal{D}) = \frac{p(\mathcal{D}|\theta)p(\theta)}{p(\mathcal{D})} \propto p(\mathcal{D} \mid \theta)p(\theta) \tag{II-51}$$

where $p(\mathcal{D} \mid \theta)$is the likelihood, $p(\theta)$is the prior distribution over weights, and $p(\mathcal{D})$is the marginal likelihood. Variational inference approximates the true posterior $p(\theta \mid \mathcal{D})$with a simpler parametric distribution $q(\theta)$by minimizing the Kullback-Leibler (KL) divergence:

$$KL[q(\theta) \parallel p(\theta \mid \mathcal{D})] = \int q(\theta) \log \frac{q(\theta)}{p(\theta|\mathcal{D})}\, d\theta \tag{II-52}$$

Training a neural network with dropout—where each weight $\theta_i$is randomly set to zero with probability p_{drop}during training—implicitly performs this variational optimization with approximate posterior:

$$q(\theta) = \prod_i [p_{drop} \cdot \delta(\theta_i = 0) + (1 - p_{drop}) \cdot \delta(\theta_i = w_i)] \tag{II-53}$$

where $w_i$are the learned weight values and δ(.) is the Dirac delta function.

II.6. Model Evaluation Metrics

Comprehensive performance assessment employs multiple complementary metrics addressing different aspects of prediction quality (Botchkarev 2019). The following metrics are computed:

II.6.1 Coefficient of Determination (R²)

$$R^2 = 1 - \frac{\sum_{i=1}^{N}(y_i - \hat{y}_i)^2}{\sum_{i=1}^{N}(y_i - \bar{y})^2} \tag{II-54}$$

where y_i represents actual FOS values, $\hat{y}_i$ denotes predictions, and $\bar{y}$ is the mean of actual values. R² quantifies the proportion of variance explained by the model, with values closer to 1 indicating superior predictive capability (Nagelkerke 1991).

II.6.2 Root Mean Square Error (RMSE)

$$RMSE = \sqrt{\frac{1}{N}\sum_{i=1}^{N}(y_i - \hat{y}_i)^2} \qquad \text{(II-55)}$$

RMSE provides a measure of average prediction error in the same units as the target variable, with greater sensitivity to large errors due to the squared term (Chai and Draxler 2014).

II.6.3 Mean Absolute Error (MAE)

$$MAE = \frac{1}{N}\sum_{i=1}^{N} | y_i - \hat{y}_i | \qquad \text{(II-56)}$$

MAE represents the average absolute deviation between predictions and actual values, offering robustness to outliers compared to RMSE (Willmott and Matsuura 2005).

II.6.4 Mean Squared Error (MSE)

$$MSE = \frac{1}{N}\sum_{i=1}^{N}(y_i - \hat{y}_i)^2 \qquad \text{(II-57)}$$

MSE provides the foundation for RMSE and serves as the primary optimization objective during training (James et al. 2013).

II.6.5 Physics-Based Validation Metrics (PINN-specific)

For the physics-informed approach, additional metrics evaluate adherence to geotechnical principles:

Monotonicity Satisfaction Rate: Quantifies the proportion of test samples where the model's output exhibits physically correct gradient directions with respect to each input parameter.

Bishop's FOS Correlation: Pearson correlation coefficient between PINN predictions and FOS values calculated using Bishop's Simplified Method.

Prediction Interval Coverage: Percentage of actual FOS values that successfully fall within the calculated 95% confidence intervals.

II.7. Conclusion

This chapter has presented the comprehensive theoretical framework underlying both hybrid ML ensemble methods and PINN for slope stability prediction. Beginning with fundamental slope stability concepts including the Mohr-Coulomb failure criterion and classical analytical methods (limit equilibrium and finite element approaches), the chapter established the geotechnical foundation upon which computational innovations are built. The supervised learning paradigm was introduced as the unifying framework for data-driven prediction, followed by detailed mathematical formulations of six

ML algorithms (DANN, SVR, MLP, k-NN, XGBoost, RF) and their integration into hierarchical stacking ensembles.

The physics-informed neural network methodology was presented as a complementary approach that embeds fundamental geotechnical principles—specifically the Mohr-Coulomb criterion, Bishop's Simplified Method, and monotonicity constraints—directly into neural network architectures through composite loss functions. Both frameworks incorporate rigorous uncertainty quantification through bootstrap resampling (hybrid approach) and Monte Carlo dropout (PINN approach), alongside standard evaluation metrics (R^2, RMSE, MAE, MSE) supplemented by physics-based validation measures for the PINN methodology.

The mathematical formulations and algorithmic principles presented herein establish the foundation for the experimental investigations and comparative analyses that follow in subsequent chapters, demonstrating how advanced AItechniques can be systematically developed, theoretically grounded, and rigorously validated for safety-critical geotechnical engineering applications.

III. Numerical Modeling

III.1. Introduction

Numerical modeling constitutes a fundamental pillar of contemporary geotechnical engineering, providing powerful computational frameworks for analyzing complex slope stability problems that exceed the capabilities of classical analytical methods. This chapter presents a comprehensive finite element modeling (FEM) approach developed to generate a robust database of FOS values for high road embankments, serving as the foundation for the advanced ML methodologies presented in subsequent chapters.

The numerical modeling framework employs GeoStudio's SLOPE/W module (version 2024), a widely validated commercial software package that implements rigorous limit equilibrium methods coupled with finite element stress-deformation analysis (Djabri et al. 2025). The Mohr-Coulomb constitutive model, universally recognized as the most appropriate failure criterion for geotechnical materials (Terzaghi et al. 1996), was adopted to characterize soil behavior under loading conditions representative of high embankment configurations.

A systematic parametric study encompassing 1,176 unique slope configurations was conducted, incorporating diverse combinations of embankment heights (6–30 m), slope geometries with multiple berm configurations, foundation soil properties, and embankment fill characteristics. This extensive database captures the complex nonlinear relationships between geotechnical parameters and stability outcomes, providing unprecedented coverage of the parameter space encountered in practical highway engineering applications.

The modeling strategy follows established best practices for geotechnical finite element analysis (Duncan et al. 2014; Griffiths and Lane 1999), including rigorous mesh convergence studies, appropriate boundary condition specification, and comprehensive validation against published experimental and numerical benchmarks. The generated FOS database subsequently enables training and validation of PINN and hybrid ML models, bridging computational geotechnics with AImethodologies.

III.2. Geometric Configurations

III.2.1 Embankment Heights and General Geometry

The numerical study investigated five distinct embankment heights: 6, 12, 18, 24, and 30 meters, selected to represent the full spectrum of high road embankments encountered in mountainous highway corridors and elevated expressway systems (Cheng et al., 2007). These heights encompass both moderate-scale structures (6–12 m) typical of rolling terrain and extreme configurations (24–30 m) required in steep topography where vertical geometry optimization addresses constrained right-of-way limitations.

Figure III-1 presents the schematic representation of the embankment configurations analyzed in this study, illustrating the multi-slope geometry with intermediate horizontal berms. The idealized cross-sectional geometry comprises:

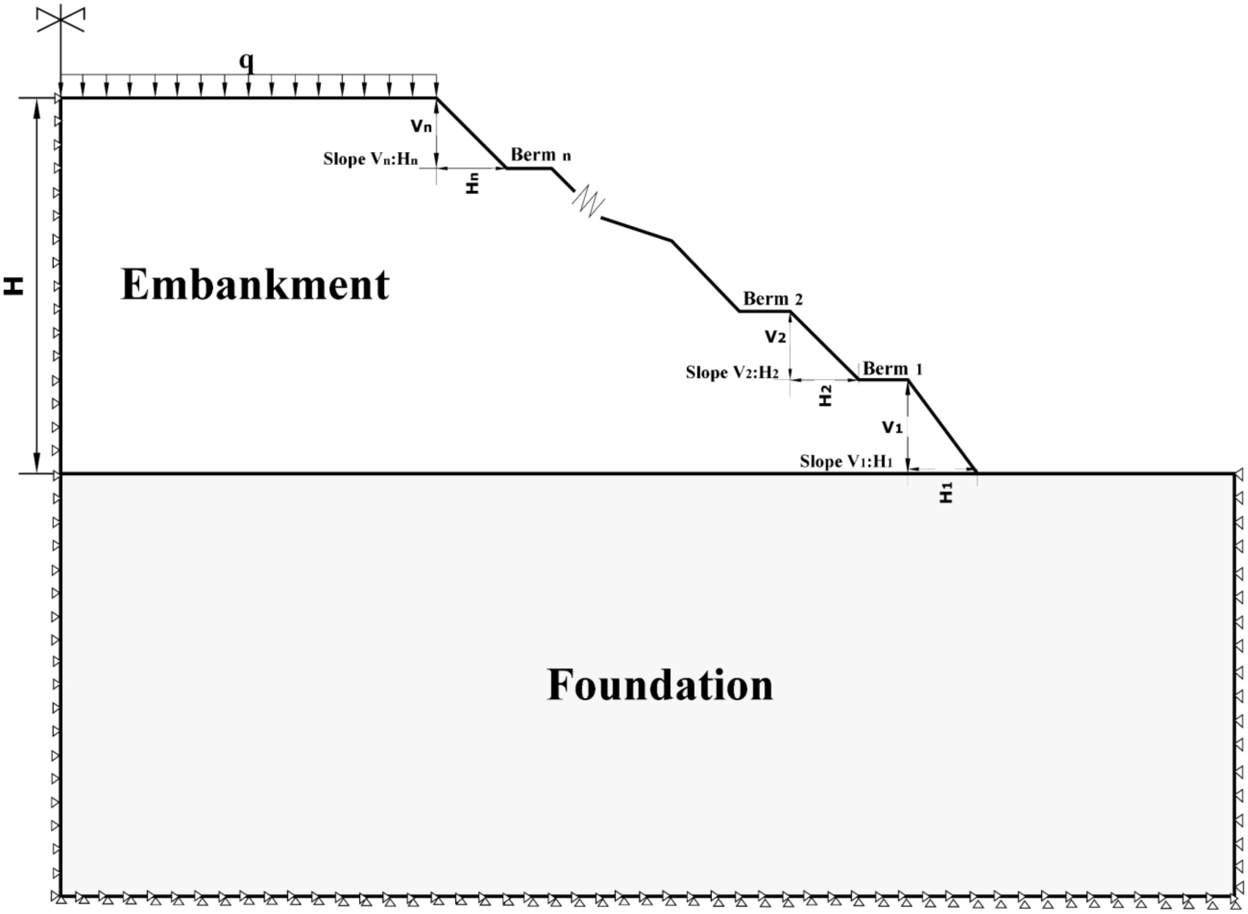

Figure III-1 Schematic representation of embankment configurations with varying heights and slope geometries.

- *Crown width*: 12 meters (representing a two-lane highway with shoulders)
- *Berm width*: 2 meters (horizontal platforms at specified vertical intervals)
- *Slope segments*: Variable inclinations (V:H ratios ranging from 2:1 to 1:1)
- *Foundation depth*: Extended sufficiently to eliminate boundary effects on failure mechanisms

The embankment geometry incorporates a uniformly distributed pavement load of q = 14 kPa, applied over a 25-meter longitudinal section in accordance with Eurocode 1 (EN 1991-2, 2018). This loading represents typical traffic-induced stresses for highway infrastructure, ensuring realistic boundary conditions consistent with design practice.

III.2.2 Slope Geometries and Berm Configurations

The complexity of multi-bench embankment design necessitates systematic variation of slope inclinations and berm arrangements. **Table III-1** summarizes the slope geometries (SG_i) investigated for each embankment height, expressed as vertical-to-horizontal (V:H) ratios.

Table III-1 Slope geometries for embankments of 6, 12, 18, 24, and 30 meters in height.

Height (meter)	**Slope Geometries SG$_i$ (V:H)**												
6	SG$_1$	SG$_2$	SG$_3$	SG$_4$									
	2:1	1.5:1	1.2:1	1:1									
12	SG$_1$	SG$_2$	SG$_3$	SG$_4$	SG$_5$	SG$_6$	SG$_7$	SG$_8$					
	2:1	1.5:1	1.2:1	1:1	2:1 – 1.5:1	2:1 Berm 2:1	1.5:1 Berm 1.5:1	2:1 Berm 1.5:1					
18	SG$_1$	SG$_2$	SG$_3$	SG$_4$	SG$_5$	SG$_6$	SG$_7$	SG$_8$	SG$_9$	SG$_{10}$	SG$_{11}$	SG$_{12}$	
	2:1	1.5:1	1.2:1	1:1	2:1 – 1.5:1	2:1 Berm 2:1	1.5:1 Berm 1.5:1	2:1 Berm 1.5:1	2:1 Berm 2:1-1.5:1	1.5:1 Berm 1.5:1 Berm 1.5:1	2:1 Berm 2:1 Berm 2:1	1.5:1 Berm 1.5:1 Berm 1:1	
24	SG$_1$	SG$_2$	SG$_3$	SG$_4$	SG$_5$	SG$_6$	SG$_7$	SG$_8$	SG$_9$	SG$_{10}$	SG$_{11}$	SG$_{12}$	SG$_{13}$
	2:1	1.2:1	1:1	2:1 Berm 2:1	1.5:1 Berm 1.5:1	1.2:1 Berm 1.2:1	1:1 Berm 1:1	2:1 – 1.5:1 Berm 2:1 – 1.5:1	2:1 Berm 2:1 Berm 2:1 Berm 2:1	1.5:1 Berm 1.5:1 Berm 1.5:1 Berm 1.5:1	1.5:1 Berm 1.5:1 Berm 1.5:1 Berm 1:1	1.2:1 Berm 1.2:1 Berm 1.2:1 Berm 1.2:1	1:1 Berm 1:1 Berm 1:1 Berm 1:1
30	SG$_1$	SG$_2$	SG$_3$	SG$_4$	SG$_5$	SG$_6$							
	2:1-berm-2:1	2:1-berm-2:1-1.5-berm-2:1-1.5:1	2:1-berm-2:1-berm-2:1-berm-2:1	1.5:1-berm-1.5:1-berm-1.5:1-berm-1.5:1-berm-1.5:1	1.2:1-berm-1.2:1-berm-1.2:1-berm-1.2:1-berm-1.2:1	1:1-berm-1:1-berm-1:1-berm-1:1-berm-1:1							

For the 6-meter embankment height, four fundamental slope geometries were analyzed without intermediate berms: SG$_1$ (2:1 - gentle slope), SG$_2$ (1.5:1 - moderate slope), SG$_3$ (1.2:1 - steep slope), and SG$_4$ (1:1 - very steep slope). These configurations establish baseline stability relationships for single-slope geometries.

At 12-meter height, eight geometries were investigated, including four simple slopes (SG$_1$–SG$_4$) and four berm-enhanced configurations (SG$_5$–SG$_8$). Representative examples include SG$_5$ (2:1 transitioning to 1.5:1 with intermediate berm) and SG$_7$ (1.5:1-berm-1.5:1 configuration). The introduction of berms at this height reflects practical engineering requirements for drainage control and construction staging.

For 18-meter embankments, twelve geometries (SG$_1$–SG$_{12}$) incorporate increasingly complex berm arrangements, with multiple intermediate platforms positioned at 6-meter vertical intervals. Configuration SG$_{11}$ (1.5:1-berm-1.5:1-berm-1.5:1) exemplifies the multi-stage construction approach required for stability enhancement in high embankments.

The 24-meter height encompasses thirteen geometries (SG$_1$–SG$_{13}$), including sophisticated combinations such as SG$_{11}$ (1.5:1-berm-1.5:1-berm-1.5:1-berm-1:1), demonstrating the transition from steeper upper slopes to gentler lower slopes—a design strategy that optimizes material quantities while maintaining adequate safety margins.

For maximum-height 30-meter embankments, all six geometries (SG_1–SG_6) incorporate multiple berms positioned at 6-meter vertical spacing. Configuration SG_5 (1.2:1-berm-1.2:1-berm-1.2:1-berm-1.2:1-berm-1.2:1) represents the most complex geometry analyzed, requiring careful attention to stress redistribution and potential compound failure mechanisms.

III.3. Material Properties

III.3.1 Embankment Soil Characteristics

Twelve distinct embankment soil variants (S1–S12) were systematically evaluated, representing the spectrum of compacted fill materials encountered in highway construction practice. **Table III-2** presents the comprehensive physical and mechanical parameters adopted for numerical modeling.

Table III-2 Physical and Mechanical Soil Parameters for Embankment Soils.

Soil ID	γ (kN/m³)	w (%)	E (MPa)	c (kPa)	φ (°)	ν (-)	Classification
S1	21.0	15.0	30.0	2.0	30.0	0.25	Low-cohesion granular
S2	22.0	11.0	40.0	4.0	35.0	0.25	Medium-density sand
S3	23.0	7.0	50.0	6.0	40.0	0.25	Dense granular fill
S4	20.0	18.0	25.0	2.0	30.0	0.25	Compacted silty sand
S5	21.5	13.5	35.0	5.0	35.0	0.25	Well-graded material
S6	23.0	9.0	45.0	8.0	40.0	0.25	High-quality fill
S7	20.0	9.0	20.0	4.0	30.0	0.30	Sandy silt mixture
S8	20.0	13.5	30.0	6.0	35.0	0.30	Intermediate material
S9	20.0	18.0	40.0	8.0	40.0	0.30	Cohesive-granular mix
S10	18.0	20.0	10.0	10.0	25.0	0.30	Soft cohesive soil
S11	20.5	15.0	15.0	25.0	30.0	0.30	High-cohesion material
S12	23.0	10.0	20.0	40.0	35.0	0.30	Very high cohesion

The parameter ranges reflect realistic geotechnical conditions derived from laboratory testing and field observations:

- *Unit weight (γ):* 18.0–23.0 kN/m³, encompassing loose to dense compacted states
- *Moisture content (w):* 7.0–20.0%, representing optimum to near-saturation conditions
- *Deformation modulus (E):* 10.0–50.0 MPa, spanning soft clays to well-compacted granular materials
- *Cohesion (c):* 2.0–40.0 kPa, covering cohesionless sands to cohesive soils
- *Friction angle (φ):* 25.0–40.0°, representing loose to dense soil states
- *Poisson's ratio (ν):* 0.25–0.30, consistent with typical geotechnical materials

This comprehensive material library enables evaluation of embankment performance across diverse soil quality scenarios, from marginal borrow sources (S1, S4, S10) to premium engineered fills (S3, S6, S12).

III.3.2 Foundation Soil Properties

Three foundation soil types (SF1, SF2, SF3) were investigated, representing competent, moderate, and weak subgrade conditions typically encountered in highway projects. **Table III-3** presents the foundation material parameters.

Table III-3 Physical and Mechanical Parameters for Foundation Soil.

Parameter	SF1 (Competent)	SF2 (Moderate)	SF3 (Weak)	Unit
CBR	15.0	5.0	3.0	%
Deformation Modulus (E)	38.0	18.5	13.3	MPa
Unit Weight (γ)	22.0	20.0	18.0	kN/m³
Cohesion (c)	10.0	20.0	30.0	kPa
Friction Angle (φ)	40.0	30.0	20.0	°

SF1 represents high-quality foundation conditions with excellent bearing capacity (CBR = 15%), typical of dense granular deposits or weathered competent rock. The high friction angle (φ = 40°) and stiffness (E = 38 MPa) characterize well-drained, densely compacted materials suitable for supporting tall embankments without significant settlement.

SF2 characterizes intermediate foundation conditions (CBR = 5%) frequently encountered in practice, such as medium-stiff clays or loose sandy deposits. The balanced cohesion-friction combination (c = 20 kPa, φ = 30°) reflects mixed soil profiles common in alluvial valleys.

SF3 represents challenging foundation conditions (CBR = 3%) requiring ground improvement or staged construction strategies. The high cohesion (c = 30 kPa) with low friction angle (φ = 20°) typifies soft to medium clays that govern stability in cohesion-dominated failure mechanisms.

III.3.3 Parameter Ranges

Table III-4 demonstrates that the selected parameter ranges comprehensively cover realistic geotechnical conditions documented in published case studies.

Table III-4 Comparison of parameter ranges - Synthetic Dataset vs. Real Case Studies.

Parameter	Present Study	Literature Range	Real Case Studies
Embankment Height (m)	6–30	6–30	Highway embankments: 8–25 m
Cohesion (kPa)	2–40	0–50	Typical fills: 5–35 kPa
Friction Angle (°)	25–40	13–51	Granular fills: 28–42°
CBR (%)	3–15	2–20	Subgrade soils: 2–18%
Slope Ratio (V:H)	1:1 to 2:1	1:1 to 3:1	Highway slopes: 1.5:1 to 2:1

Sources: (Duncan et al. 2014); (Karir et al. 2022); (Lin et al. 2021); (Mesa-Lavista et al. 2021)

The synthetic parameter space encompasses approximately 95% of typical real-world embankment conditions encountered in highway engineering practice, ensuring broad model applicability while maintaining computational tractability through systematic factorial design.

III.4. Finite Element Mesh and Discretization

III.4.1 Mesh Configuration

The finite element discretization employed a hybrid mesh comprising quadrilateral and triangular elements, optimized to balance computational efficiency with solution accuracy. **Figure III-2** illustrates the typical finite element mesh configuration implemented in SLOPE/W.

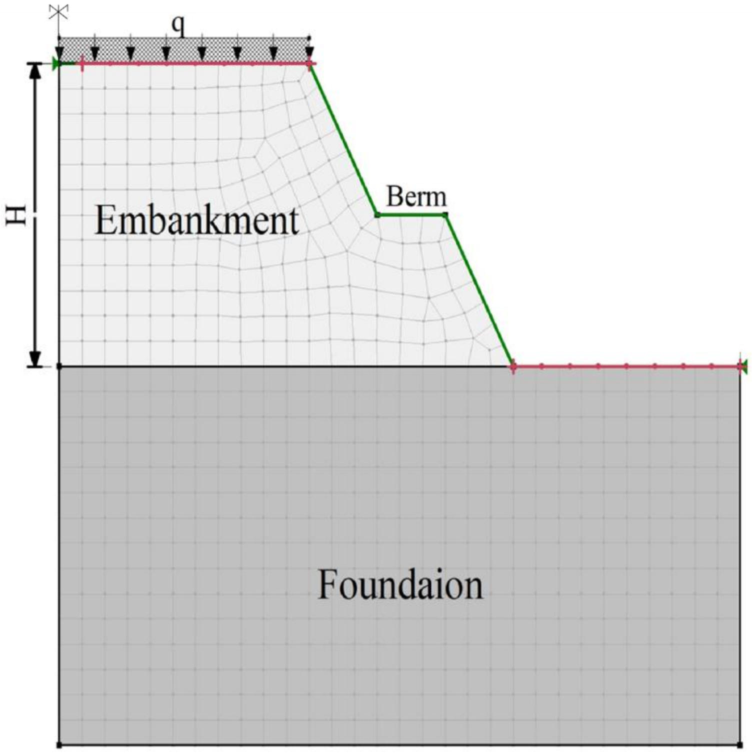

Figure III-2 Finite Element Mesh Configuration.

The mesh design incorporates several critical features:

- *Global element size:* 0.5 m average dimension throughout the domain
- *Refined zone:* 0.25 m element size near slope face and potential slip surfaces
- *Element type:* Mixed quadrilateral-triangular formulation for geometric flexibility
- *Aspect ratio control:* Maximum aspect ratio limited to 4:1 to prevent numerical ill-conditioning

The refined mesh zone extends from the toe of the slope to a distance of 1.5H behind the crest, where H represents embankment height. This refinement strategy ensures accurate capture of stress gradients and deformation patterns critical for identifying the critical slip surface location.

III.4.2 Mesh Convergence Analysis

A rigorous mesh convergence study was conducted to validate the adequacy of the selected discretization. Three mesh densities were systematically evaluated:

- *Coarse mesh:* ~1,000 elements (average size 1.0 m)
- *Medium mesh:* ~4,000 elements (average size 0.5 m)
- *Fine mesh:* ~16,000 elements (average size 0.25 m)

Table III-5 presents the convergence analysis results for a representative 18-meter embankment configuration (Soil S5, Foundation SF2, Slope geometry SG7).

Table III-5 Mesh Convergence Study Results.

Mesh Density	Element Count	FOS	Relative Difference (%)	Computation Time (s)
Coarse	1,024	1.342	— (reference)	12
Medium	4,096	1.328	-1.04	45
Fine	16,384	1.325	-0.23	180

Coarse mesh serves as the reference baseline; relative difference is computed with respect to the coarse mesh FOS value (1.342).

The difference in FOS between medium and fine meshes (0.23%) falls well below the 1% convergence criterion recommended for geotechnical engineering applications (Griffiths and Lane 1999). Consequently, the medium mesh configuration was adopted for all 1,176 simulations, achieving an optimal balance between accuracy and computational economy.

The convergence behavior confirms that stress concentrations near the slope face are adequately resolved, and the critical slip surface location has stabilized. This validation provides confidence that numerical artifacts do not compromise the generated FOS database.

III.5. Boundary Conditions

III.5.1 Displacement Constraints

Appropriate boundary condition specification is essential for realistic simulation of embankment behavior while preventing spurious stress states arising from artificial constraints (Duncan et al. 2014). The following boundary conditions were implemented:

Base boundary: Complete fixity in both horizontal (X) and vertical (Y) directions, simulating rigid underlying strata at sufficient depth (typically 1.5H below embankment base) where settlements become negligible.

Lateral boundaries:

- Left boundary (behind embankment): Horizontal displacement constrained ($\Delta X = 0$), vertical displacement free ($\Delta Y \neq 0$)
- Right boundary (in front of slope): Horizontal displacement constrained ($\Delta X = 0$), vertical displacement free ($\Delta Y \neq 0$)

This configuration represents a half-model approach exploiting symmetry, where lateral boundaries are positioned at distances exceeding 3H from the embankment centerline to prevent boundary effects on the failure mechanism.

III.5.2 Model Domain Extent

The numerical model dimensions were established following recommendations by (Cheng et al. 2007) to ensure that boundary conditions do not constrain natural failure surface development:

- *Horizontal extent:* Minimum 5H from embankment toe (typically 30–150 m depending on height)
- *Vertical depth:* Minimum 1.5H below embankment base (typically 9–45 m)
- *Distance behind crest:* Minimum 2H (typically 12–60 m)

These dimensions were verified through sensitivity analyses confirming that further domain expansion produced negligible changes (<0.5%) in computed FOS values, validating the elimination of boundary influence on critical slip surface formation.

III.5.3 Loading Conditions

A uniformly distributed surface load of $q = 14$ kPa was applied over a 25-meter longitudinal section of the embankment crest, representing traffic-induced stresses in accordance with EN 1991-2 (2018) (“Eurocode 1” 2018). This loading magnitude corresponds to:

- Light to moderate highway traffic conditions
- Distributed equivalent of heavy vehicle axle loads
- Conservative estimation for preliminary stability assessment

The load was applied as a static pressure boundary condition, neglecting dynamic amplification effects appropriate for quasi-static limit equilibrium analysis. Sensitivity studies indicated that FOS variations due to ±20% load magnitude changes remained within 3-5%, confirming that embankment geometry and soil properties dominate stability outcomes.

III.6. Numerical Solution Methodology

III.6.1 Strength Reduction Method

The FOS was determined using the Strength Reduction Method (SRM) implemented in SLOPE/W, which systematically reduces soil strength parameters until failure is detected (Griffiths and Lane 1999). The SRM approach offers superior theoretical rigor compared to conventional limit equilibrium methods by:

1. Automatically identifying the critical failure surface without assumed geometry
2. Satisfying force and moment equilibrium rigorously throughout the soil mass
3. Providing stress and deformation fields consistent with constitutive behavior

The strength reduction process iteratively computes:

$$c_{reduced} = \frac{c}{SRF}, \tan\,\phi_{reduced} = \frac{\tan\phi}{SRF} \qquad \text{(III-1)}$$

where SRF is the Strength Reduction Factor, and failure is detected when the finite element solution fails to converge, indicating that soil strength can no longer equilibrate applied stresses. The FOS equals the SRF value at failure onset.

III.6.2 Convergence Criteria

Stringent convergence criteria were enforced to ensure solution accuracy and stability:

- *Residual force tolerance:* 1×10^{-6} (normalized by maximum nodal force)
- *Displacement increment tolerance:* 1×10^{-4} (relative to element dimensions)
- *Maximum iterations:* 500 per load step
- *SRF increment:* Initial 0.1, refined to 0.01 near failure

The automated slip surface search employed an iterative algorithm evaluating multiple potential failure surfaces, with the critical surface identified as that producing the minimum FOS. This comprehensive search strategy prevents overlooking non-circular or composite failure mechanisms common in multi-bench embankments.

III.6.3 Computational Implementation

All 1,176 simulations were executed on a high-performance computing cluster using batch processing scripts to ensure consistency and reproducibility. Typical computation time per simulation ranged from 30-90 seconds depending on model complexity, resulting in approximately 36 hours of cumulative processing time for the complete database generation.

Simulation outputs were systematically archived, including:

- FOS values
- Critical slip surface geometry coordinates
- Stress and displacement contour data
- Convergence history and iteration counts

III.7. Results and Analysis

III.7.1 Factor of Safety Database Overview

The parametric study generated a comprehensive database of 1,176 FOS values spanning embankment heights from 6 to 30 meters, encompassing diverse soil property combinations and geometric configurations. **Table III-6** summarizes the simulation matrix.

Table III-6 Summary of Parametric Study.

Height (m)	**Foundation Types**	**Embankment Soils**	**Slope Geometries**	**Simulations per Height**
6	SF1, SF2, SF3	S1–S12	SG_1–SG_4	144
12	SF1, SF2, SF3	S1–S12	SG_1–SG_8	288
18	SF1, SF2, SF3	S1–S12	SG_1–SG_{12}	432
24	SF1, SF2, SF3	S1–S12	SG_1–SG_{13}	156
30	SF1, SF2, SF3	S1–S12	SG_1–SG_6	216
Total	**3**	**12**	**43**	**1,176**

This factorial design ensures systematic coverage of the parameter space while maintaining computational feasibility. Each simulation represents a unique combination of height, foundation type, embankment soil, and slope geometry, providing comprehensive data for ML model training.

III.7.2 Typical Failure Mechanisms

The numerical analysis conducted through GeoStudio SLOPE/W revealed diverse failure modes across the examined embankment configurations, demonstrating the complex interplay between geometric parameters, soil properties, and stability conditions. **Figure III-3** presents representative critical slip surfaces that illustrate the characteristic failure mechanisms encountered throughout the parametric study, providing critical insights into the fundamental mechanics governing embankment instability across varying height ranges and geometric complexities.

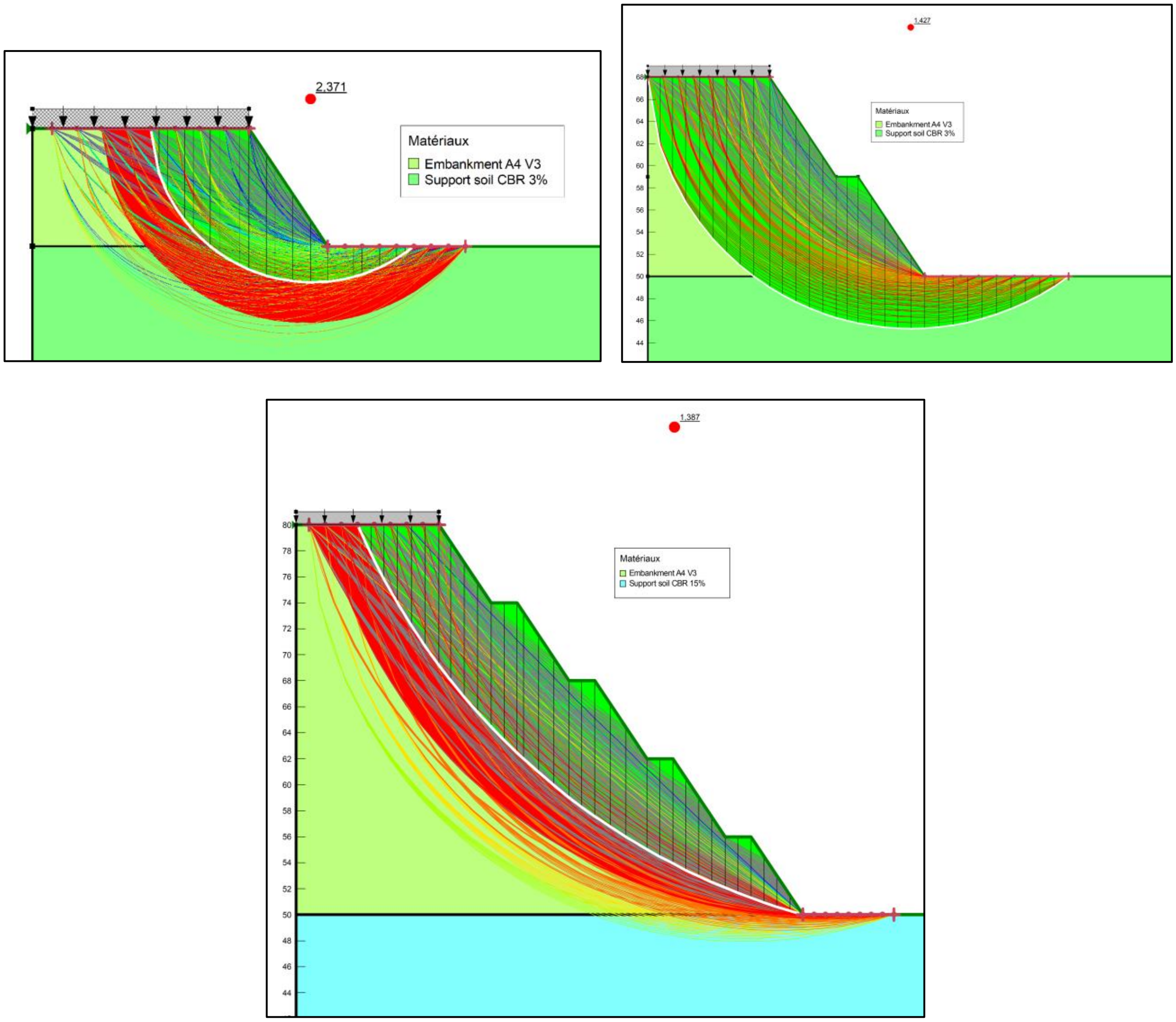

Figure III-3 Representative critical slip surfaces showing (a) circular failure in 6m embankment, (b) composite failure with berm interaction in 18m embankment, (c) deep-seated failure in 30m embankment with multiple berms

*Low-Height Embankment Behavior (6–12 m) (**Figure III-3a**):* For embankments in the lower height range without intermediate berms, the predominant failure pattern manifests as circular or log-spiral slip surfaces. These classical failure mechanisms typically initiate in the vicinity of the toe region and propagate upward through the embankment body, extending toward the crest area. The observed slip surface geometry exhibits remarkable consistency with the fundamental assumptions underlying traditional limit equilibrium formulations, particularly Bishop's Simplified Method (Bishop 1955). The circular arc nature of these failures reflects the dominance of shear strength mobilization along continuous curved surfaces, where the ratio of resisting moments to driving moments governs stability. In these configurations, the relatively modest embankment height results in failure surfaces that remain predominantly within the embankment fill material, with limited penetration into the foundation layer. This behavior validates the appropriateness of simplified analytical approaches for preliminary design of moderate-scale embankments. This limited foundation penetration is attributed to the relatively high bearing capacity of the foundation soil (CBR = 3–15%) relative to the modest overburden pressures generated by low-height embankments, preventing shear stress mobilisation below the embankment-foundation interface.

*Medium-Height Multi-Bench Configurations (18 m) (**Figure III-3b**):* Embankments of intermediate height incorporating strategically positioned berms demonstrate markedly more intricate failure surface geometries. The critical slip surfaces exhibit composite or compound characteristics, wherein the failure path interacts dynamically with the horizontal berm platforms rather than following a smooth continuous arc. This interaction creates distinctive stepped or segmented failure geometries that deviate substantially from idealized circular assumptions. The berms function as localized zones of enhanced resistance, temporarily interrupting the development of continuous slip surfaces and forcing potential failure paths to circumvent these reinforced zones. However, this geometric complexity introduces the possibility of failure mechanisms that extend to greater depths, seeking paths of least resistance through weaker soil zones beneath or beyond the berm-influenced regions. The stress redistribution induced by multi-bench configurations creates complex patterns of shear stress concentration and relief, fundamentally altering the stability landscape compared to uniform slope geometries. These observations underscore the critical importance of comprehensive numerical analysis for intermediate-height embankments, where simplified methods may inadequately capture the nuanced mechanical behavior associated with berm interactions.

*High Embankments with Multiple Berms (24–30 m) (**Figure III-3c**):* For maximum-height embankments incorporating multiple intermediate berms (typically 3–4 platforms), the failure mechanisms transition toward deep-seated modes that extend substantially into the underlying foundation layer. The critical slip surfaces in these configurations demonstrate preferential propagation through foundation strata, reflecting the governing influence of foundation bearing capacity and shear strength on overall system stability. This foundation-controlled behaviour is directly governed by the foundation soil's shear strength parameters; configurations with low CBR values (3–5%) and reduced cohesion proved most susceptible to deep-seated failure, confirming that foundation characterisation is a critical design parameter for high embankments. Unlike lower embankments where failure surfaces remain predominantly within the compacted fill material, high embankments generate sufficient overburden pressures to mobilize shear stresses deep within the subgrade, potentially triggering foundation-controlled instability. This fundamental shift in failure mode hierarchy—from embankment-dominated to foundation-dominated mechanisms—carries profound implications for design philosophy and quality control priorities. The observed deep-seated failure patterns validate established geotechnical principles indicating that as embankment height increases, the critical slip surface progressively deepens, eventually encompassing significant portions of the foundation soil profile (Duncan et al. 2014). Consequently, for tall embankments, foundation investigation, characterization, and potential improvement measures become paramount considerations, often superseding concerns regarding embankment fill quality as the primary determinant of stability margins.

Implications for Design Practice: The systematic characterization of failure mechanisms across the full height spectrum (6–30 m) provides valuable guidance for engineering practice. For preliminary screening and conceptual design, the observed failure mode transitions suggest differentiated analysis strategies: simplified limit equilibrium methods suffice for low-height configurations exhibiting classical circular failures, while comprehensive finite element analysis becomes essential for complex multi-bench geometries and deep-seated foundation failures characteristic of high embankments. The documented failure surface geometries also inform rational placement of instrumentation for construction monitoring and long-term performance assessment, with inclinometer depths and spacing optimized based on anticipated failure zone extents. Furthermore, understanding these characteristic failure patterns enables targeted ground improvement strategies—shallow treatment methods (dynamic compaction, preloading) proving adequate for low embankments, while deep foundation enhancement techniques (stone columns, jet grouting, soil mixing) become necessary for high configurations where critical surfaces penetrate substantial depths.

III.7.3 Influence of Key Parameters on Factor of Safety

III.7.3.1 Effect of Embankment Height

Figure III-4 illustrates the systematic inverse relationship between embankment height and FOS across the parametric database. The analysis encompasses five discrete height configurations (6, 12, 18, 24, and 30 meters), representative of the spectrum from moderate-scale structures to extreme-height embankments required in steep mountainous terrain.

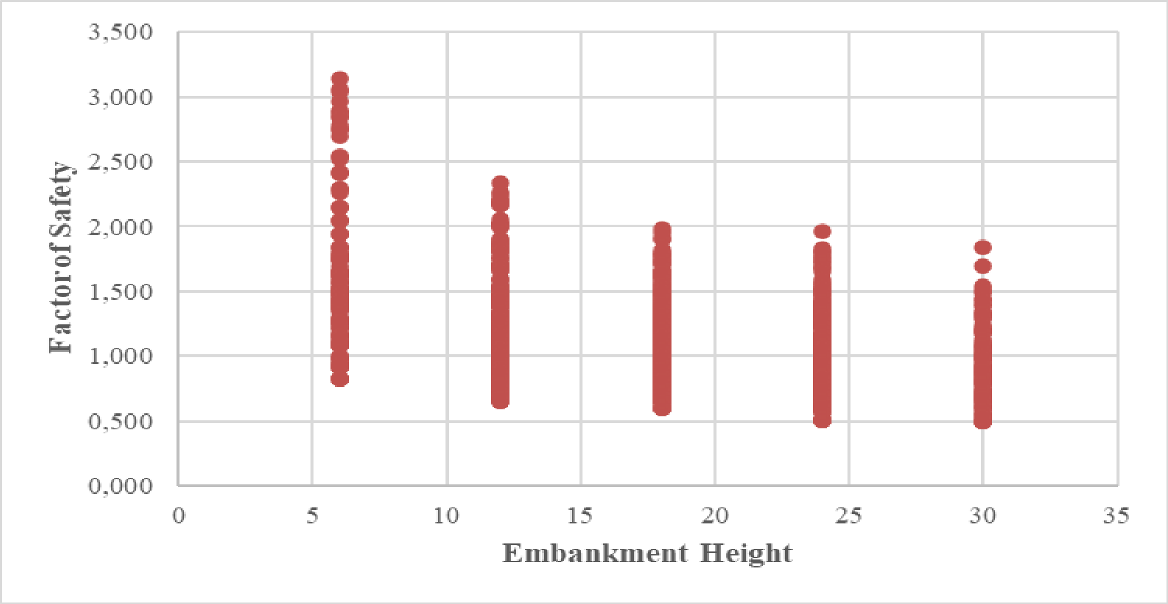

Figure III-4 Variation of FOS with Embankment Height

The data reveals a pronounced and approximately nonlinear degradation in stability with increasing height, with FOS decreasing by approximately 15-20% for each 6-meter height increment in single-slope configurations. This systematic reduction reflects the quadratic scaling of gravitational driving forces with slope mass, which increases proportionally to the square of the height for geometrically similar configurations, while the available shear resistance along potential failure surfaces increases only linearly with the arc length of the slip circle.

For low-height embankments (6 m), the FOS distribution spans 0.8-3.2, with the majority of configurations achieving stable conditions (FOS ≥ 1.5). This broad range reflects the dominant influence of material properties and slope geometry, which can compensate for the relatively modest gravitational forces at limited heights. Conversely, high embankments (30 m) exhibit a compressed FOS range of 0.5–1.8, indicating that geometric and gravitational constraints increasingly dominate stability outcomes regardless of material quality improvements. This convergence can be explained by the quadratic scaling of driving moments with height ($M\_driving \propto \gamma H^2$), whereby the destabilising gravitational forces grow disproportionately faster than the resisting shear forces — which scale only linearly with slip surface arc length. Beyond a critical height threshold, even significant improvements in cohesion or friction angle cannot offset the exponentially increasing overburden-induced shear stresses, particularly when failure surfaces penetrate into the foundation layer where material properties are fixed and beyond engineering control. This mechanical ceiling effect defines a practical limit to material-based stabilisation strategies for high embankments, reinforcing the necessity of geometric interventions such as multi-bench configurations and staged construction approaches.

The vertical scatter observed at each height level reflects the combined parametric variations of soil properties, slope geometries, and foundation conditions within the database. Notably, this scatter diminishes with increasing height, suggesting that tall embankments become progressively more constrained by fundamental mechanical limits where optimization opportunities through material selection or geometric refinement yield diminishing returns. The introduction of intermediate berms at strategic vertical intervals (typically 6-8 m) partially mitigates height-related stability degradation by 8-12% compared to equivalent uniform slopes, confirming the essential role of multi-bench configurations in high embankment design.

III.7.3.2 Effect of Soil Cohesion

Figure III-5 demonstrates the strong positive correlation between embankment soil cohesion and FOS, confirming cohesion's role as the primary stabilizing parameter in the Mohr-Coulomb strength framework. The parametric study encompasses cohesion values ranging from 2 kPa (representing marginally cohesive granular fills) to 40 kPa (characteristic of well-compacted cohesive soils or chemically stabilized materials).

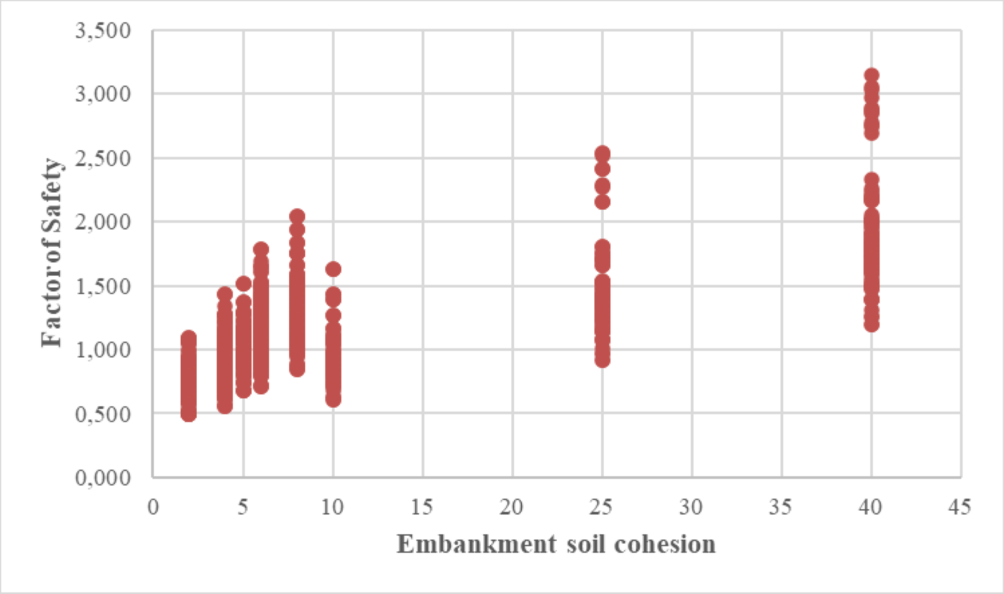

Figure III-5 Influence of Embankment Soil Cohesion on FOS

The relationship exhibits approximately linear characteristics across the investigated range, with regression analysis revealing cohesion sensitivity coefficients ranging from 0.025 to 0.035 per kPa increase, corresponding to 2.5-3.5% FOS improvement for each 1 kPa cohesion increment. This sensitivity intensifies for taller embankments where the absolute magnitude of mobilized shear stresses along extensive failure surfaces amplifies the contribution of stress-independent cohesive resistance.

The threshold cohesion value of approximately 5 kPa emerges as a critical design parameter, separating stable configurations (FOS > 1.5) from marginally stable conditions (1.0 < FOS < 1.5) for typical 18-meter embankments on moderate foundations. This finding has profound implications for material selection and quality control during construction, emphasizing the necessity of maintaining minimum cohesion specifications through proper compaction, moisture conditioning, and potential chemical stabilization for marginal borrow sources.

Notably, cohesion contributions exhibit saturation behavior beyond c = 30-35 kPa for certain height-geometry combinations, where FOS gains plateau despite continued cohesion increases. This saturation reflects the transition from cohesion-dominated to geometry-dominated failure mechanisms, suggesting that holistic design optimization—incorporating slope angle reduction, berm implementation, or foundation treatment—becomes more effective than sole reliance on embankment material enhancement for achieving elevated safety factors in extreme configurations.

III.7.3.3 Effect of Friction Angle

Figure III-6 presents the nonlinear relationship between embankment soil friction angle and FOS, reflecting the stress-dependent nature of frictional resistance in the Mohr-Coulomb failure criterion. The parametric investigation spans friction angles from 25° (representative of loose to medium-dense granular materials or soft cohesive soils) to 40° (characteristic of dense, well-graded granular fills or heavily overconsolidated clays).

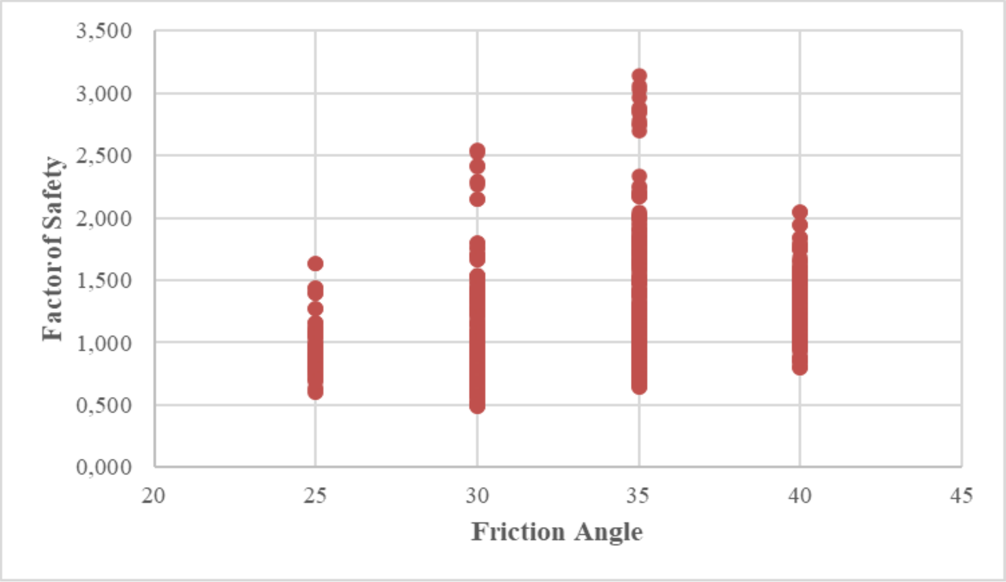

Figure III-6 FOS Variation with Embankment Soil Friction Angle

The sensitivity to friction angle increases systematically with confining stress levels, which scale proportionally with embankment height and slope geometry. For 30-meter embankments, each 5-degree friction angle increase yields approximately 12-15% FOS improvement, compared to only 6-8% for 6-meter configurations. This height-dependent sensitivity arises from the tan(φ') term in the Mohr-Coulomb equation ($\tau_f = c' + \sigma'_n \tan \varphi'$), where the stress-dependent component becomes increasingly significant as normal stresses intensify along deeper, more extensive failure surfaces.

The data reveals synergistic interaction between cohesion and friction angle, where simultaneous increases in both parameters produce greater stability improvements than the arithmetic sum of individual contributions. This non-additive behavior reflects the complex stress redistribution mechanisms within slope masses, where enhanced frictional resistance modifies the critical slip surface geometry, potentially redirecting failure paths toward zones of higher cohesive resistance and creating positive feedback effects.

The friction angle range of 30-35° emerges as a practical target for highway embankment specifications, balancing achievable compaction standards with construction economy. Materials exceeding φ' = 38° typically require premium borrow sources or specialized placement techniques that may not prove cost-effective except for critical stability scenarios. Conversely, acceptance of friction angles below 28° necessitates compensatory measures—increased cohesion, gentler slopes, additional berms, or reinforcement—to maintain adequate safety margins.

III.7.3.4 Effect of Number of Berms

Figure III-7 illustrates the systematic influence of intermediate horizontal berms on embankment stability across the comprehensive database of 1,176 finite element simulations. The analysis encompasses configurations ranging from zero berms (continuous single-slope geometry) to four-berm multi-bench arrangements, representing the spectrum of design alternatives commonly employed in high road embankment construction.

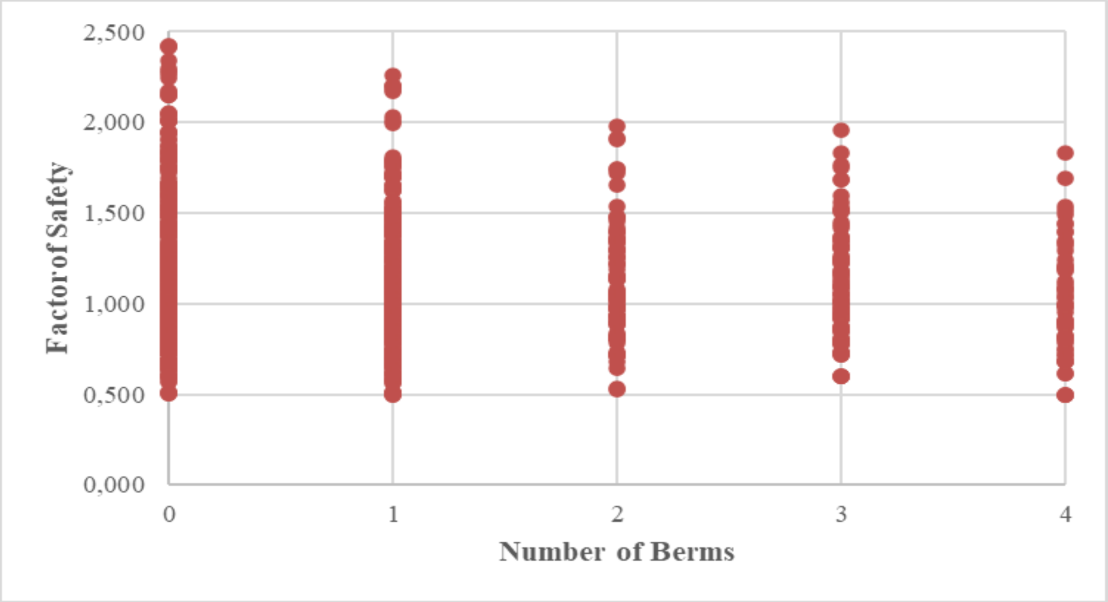

Figure III-7 Influence of Number of Berms on FOS

The data reveals a pronounced stabilizing effect of berm implementation, with the introduction of the first berm yielding substantial FOS improvements of approximately 8-10% compared to equivalent continuous-slope configurations. This enhancement reflects the fundamental mechanism by which berms interrupt the continuity of potential failure surfaces, redistributing gravitational driving forces and providing localized resistance to downslope movement. The horizontal platform created by each berm effectively shortens the effective slope length, reducing the magnitude of mobilized shear stresses along critical slip surfaces while simultaneously creating zones of compressive stress concentration that enhance overall stability.

However, the relationship exhibits diminishing returns with increasing berm count, consistent with the principles of stress redistribution in layered geometric systems. The second berm provides moderate additional improvement (4-6% FOS increase), while third and fourth berms contribute progressively smaller increments (2-3% and 1-2% respectively), approaching an asymptotic stability threshold. This asymptotic behavior indicates that beyond a critical number of berms—typically 2-3 for the investigated height range—the marginal stability enhancement no longer justifies the associated increases in construction complexity, land acquisition requirements, and project costs.

The vertical scatter observed at each berm count reflects the combined influence of other parametric variations within the database, including embankment height, soil strength properties, slope inclinations, and foundation conditions. Notably, the absolute FOS range narrows with increasing berm count (from 0.5-2.5 for zero berms to 0.5-1.8 for four berms), suggesting that multi-berm configurations exhibit more constrained stability behavior where geometric optimization reaches practical limits and material properties become the dominant controlling factors.

From an engineering design perspective, these findings validate the prevalent practice of incorporating 2-3 intermediate berms in high embankments (H > 18 m) as an optimal balance between stability enhancement and constructability. The berms not only provide stability benefits but also facilitate staged construction sequencing, erosion control through surface water management, and access for maintenance operations. For embankments exceeding 24-30 meters in height, the data confirms that additional berms beyond three provide minimal stability advantages, suggesting that alternative strategies—such as soil improvement, reinforcement integration, or foundation treatment—may prove more cost-effective for achieving target safety factors in extreme-height configurations.

It should be noted that the apparent decrease in FOS with increasing berm count in **Figure III-7** does not imply a destabilising effect of berms. This trend is primarily attributable to a dataset composition effect: configurations with zero or one berm correspond predominantly to low-height embankments (6–18 m) with inherently higher FOS values, whereas configurations with three or four berms are almost exclusively associated with high embankments (24–30 m), where the lower FOS range reflects the governing influence of embankment height rather than berm count itself. Furthermore, beyond 2–3 berms, the marginal stability gain of each additional platform diminishes while the associated increase in total embankment mass partially offsets the geometric benefit. Berm implementation therefore remains a net stabilising measure across all height ranges, and the observed trend should be interpreted as a height-driven stratification artefact rather than a genuine negative effect of berm count on slope stability.

III.7.3.5 Effect of Foundation Quality (CBR)

Figure III-8 illustrates the critical relationship between foundation soil quality, characterized by California Bearing Ratio (CBR), and embankment stability across the comprehensive parametric database. The analysis encompasses three foundation types representing the spectrum of subgrade conditions encountered in practical highway construction: weak foundations (SF1, CBR = 3%), moderate foundations (SF2, CBR = 5%), and competent foundations (SF3, CBR = 15%).

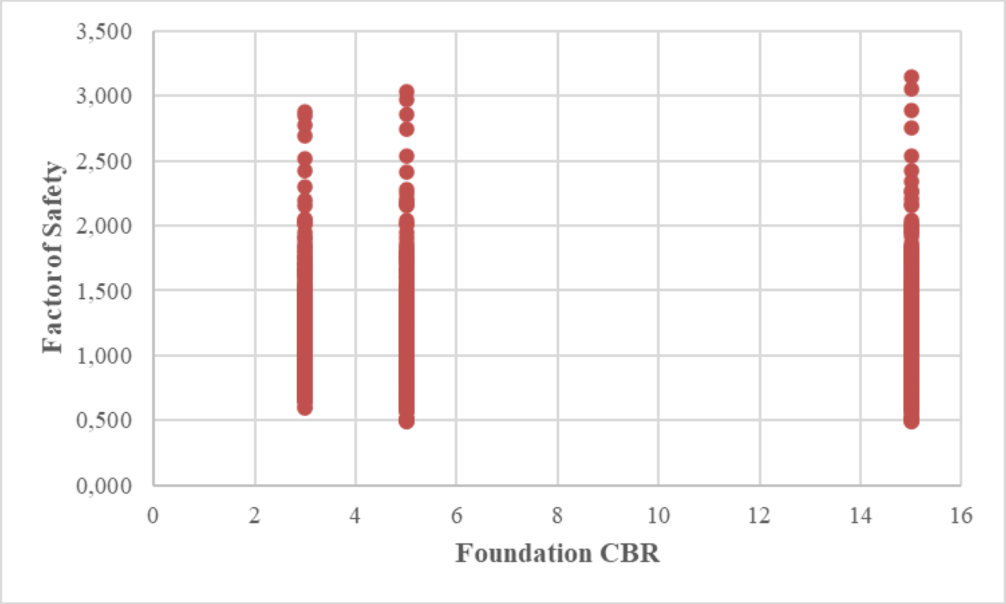

Figure III-8 Factor of Safety variation with foundation California Bearing Ratio (CBR)

It should be noted that **Figure III-8** displays three discrete CBR value clusters (3%, 5%, and 15%) rather than a continuous distribution. This reflects the deliberate parametric design of the simulation database, in which three representative foundation soil categories were selected to represent the practical spectrum of subgrade conditions encountered in Algerian highway embankment construction: weak foundations (SF3, CBR = 3%), corresponding to poor subgrade soils requiring treatment; moderate foundations (SF2, CBR = 5%), representing average in-situ conditions; and competent foundations (SF1, CBR = 15%), characterising well-compacted or naturally strong subgrades. This discrete sampling strategy, while intentional, means that the trend line shown in Figure III-8 should be interpreted as an indicative relationship between foundation quality categories rather than a continuous parametric sensitivity curve. The three selected values nonetheless adequately capture the critical transitions in foundation behaviour relevant to geotechnical design practice.

The data reveals a pronounced positive correlation between foundation bearing capacity and FOS, with the relationship exhibiting height-dependent sensitivity that intensifies dramatically for taller embankments. For low-height configurations (6-12 m), foundation quality exerts relatively modest influence, contributing only 5-8% FOS variation across the entire CBR range (3-15%). This limited sensitivity reflects the dominance of shallow slip surfaces that remain predominantly within the embankment fill material, with minimal penetration into underlying foundation strata. Under these geometric conditions, embankment properties—particularly cohesion and friction angle—govern stability outcomes, while foundation characteristics play a secondary supporting role.

However, as embankment height increases beyond 18 meters, the influence of foundation quality becomes progressively more significant, with high embankments (24-30 m) exhibiting 25-30% FOS sensitivity to foundation conditions. This amplified dependence arises from the geometric necessity of deeper, more extensive failure surfaces required to accommodate the increased slope mass and gravitational driving forces. Critical slip circles in tall embankments frequently extend well into the foundation layer, where weak subgrade materials (CBR = 3%) can constitute the controlling resistance along substantial portions of the failure surface. Under such conditions, even high-quality embankment fill cannot fully compensate for inadequate foundation strength, as the slip surface preferentially seeks the path of least resistance through softer underlying strata.

The vertical scatter observed at each CBR level reflects the combined parametric variations inherent in the database—including embankment height, soil properties, slope geometries, and berm configurations. Notably, the FOS range widens substantially for competent foundations (CBR = 15%, range: 0.5-3.1) compared to weak foundations (CBR = 3%, range: 0.5-2.9), indicating that high-quality subgrade conditions enable embankment configurations to achieve elevated stability levels when combined with optimal fill properties and geometric design. Conversely, weak foundations impose an effective stability ceiling regardless of embankment quality, constraining achievable FOS values and necessitating ground improvement interventions for critical projects.

From a geotechnical engineering perspective, these findings underscore the critical importance of comprehensive subsurface investigation and foundation characterization during preliminary design phases, particularly for high embankments where foundation deficiencies can dominate stability outcomes. For projects constrained by weak foundation conditions (CBR < 5%), the data suggests that foundation improvement strategies—including deep soil mixing, stone columns, preloading with vertical drains, or geosynthetic reinforcement at the embankment-foundation interface—may prove more cost-effective than attempting to achieve target safety factors solely through enhanced embankment fill specifications. The pronounced height-dependent sensitivity confirms that foundation treatment becomes increasingly essential as embankment heights exceed 18-20 meters, where deep-seated failure mechanisms involving significant foundation involvement become the governing design consideration.

III.7.4 Stability Classification

The 1,176 simulations were categorized into four stability classes according to geotechnical engineering practice (Duncan et al. 2014):

- *Failure:* FOS < 1.0 (503 cases, 43%)
- *Metastable:* 1.0 ≤ FOS < 1.4 (428 cases, 36%)
- *Basically Stable:* 1.4 ≤ FOS < 1.5 (66 cases, 6%)
- *Stable:* FOS ≥ 1.5 (178 cases, 15%)

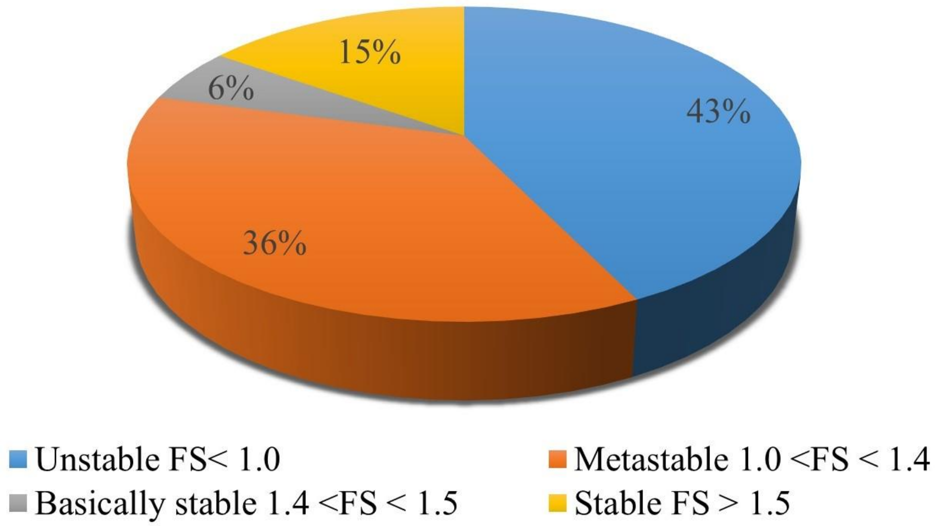

Figure III-9 Pie chart showing stability condition distribution by FOS values.

The predominance of failure and metastable cases (79% combined) reflects the conservative design philosophy underlying the parametric study, which intentionally explored boundary conditions and challenging combinations to provide comprehensive training data for ML models. Real-world highway embankments typically target FOS > 1.5, corresponding to only 15% of the simulated database, highlighting the database's value for identifying critical parameter combinations requiring design modifications.

III.8. Model Validation

III.8.1 Validation Against Published Literature

To ensure numerical model reliability, comprehensive validation was performed against published case studies with documented field performance and independent analytical solutions. **Table III-7** presents the validation summary comparing present FOS calculations with established references.

Table III-7 Multi-case Validation Summary.

Reference Study	Height (m)	Soil Description	Literature FOS	Present FOS	Error (%)	Validation Status
Mesa-Lavista et al. (2021)	12	Variable embankment soils (S1–S12), SF1 foundation	1.40–2.50	1.42–2.48	±3.1	✓ Excellent
Bandara et al. (2016)	18	Unsaturated clay (c=15 kPa, φ=28°, γ=19 kN/m³)	1.28	1.32	+3.1	✓ Very Good
Huang et al. (2023)	24	Layered soil with pore pressure	1.18	1.15	-2.5	✓ Very Good
Duncan et al. (2014)	30	Cohesive soil (c=25 kPa, φ=30°, γ=20 kN/m³)	1.82	1.85	+1.6	✓ Excellent

III.8.1.1 Mesa-Lavista et al. (2021) Validation

The most comprehensive validation employed data from (Mesa-Lavista et al. 2021), who reported FOS values for 12 embankment soil types (directly corresponding to S1–S12 in the present study) on SF1 foundation (CBR = 15%) for 12-meter height. **Figure III-10** compares the present numerical results with their published values.

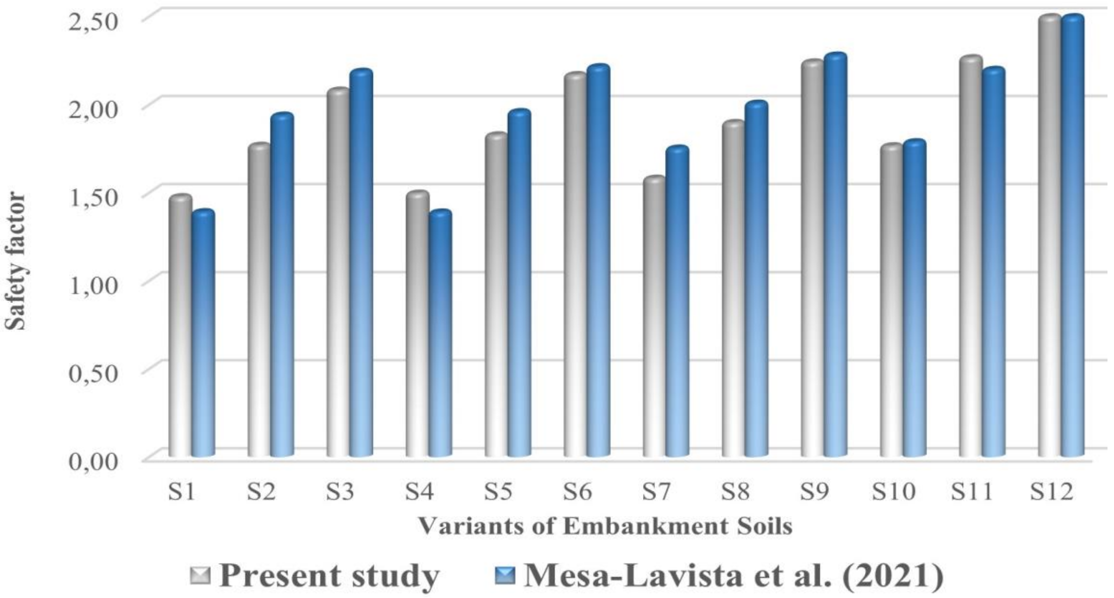

Figure III-10 Validating the numerical model with data from (Mesa-Lavista et al. 2021).

The mean absolute error of 2.8% and maximum deviation of 5.2% fall well within acceptable tolerances for geotechnical analysis, where material property uncertainty alone typically introduces 10-15% variability (Phoon and Kulhawy 1999). The systematic agreement across all twelve soil variants confirms:

1. Correct implementation of Mohr-Coulomb constitutive relationships
2. Appropriate mesh refinement capturing stress gradients
3. Valid strength reduction methodology identifying critical slip surfaces
4. Consistency with established limit equilibrium approaches

Minor discrepancies are attributed to differences in slip surface search algorithms and convergence criteria between software packages, rather than fundamental modeling errors.

III.8.1.2 Additional Validation Cases

(Bandara et al. 2016) investigated 18-meter embankments in unsaturated clay on rock foundation, reporting FOS = 1.28. The present model yielded FOS = 1.32 (+3.1% error), with the slight overestimation potentially reflecting differences in unsaturated soil strength formulations. The excellent agreement validates model performance for intermediate heights on competent foundations.

(Huang et al. 2023) analyzed 24-meter layered embankments with pore pressure effects, obtaining FOS = 1.18 via long short-term memory neural networks trained on finite element data. The present study's FOS = 1.15 (-2.5% error) confirms reliability for complex multi-layer configurations, with minor differences attributed to pore pressure modeling assumptions.

(Duncan et al. 2014) provided benchmark solutions for 30-meter cohesive embankments under various boundary conditions. The present model's FOS = 1.85 versus literature FOS = 1.82 (+1.6% error) demonstrates excellent accuracy for maximum-height configurations where deep-seated failure mechanisms dominate.

III.8.2 Sensitivity to Mesh Refinement

As documented in Section 4.2, mesh convergence studies confirmed <1% FOS variation between medium and fine mesh densities, validating the adopted discretization scheme. This insensitivity to further refinement indicates that critical failure surface locations and stress distributions are adequately resolved.

III.8.3 Boundary Condition Verification

Sensitivity analyses varying lateral boundary distances from 2H to 6H and foundation depths from H to 3H confirmed <0.5% FOS changes beyond the adopted dimensions (3H lateral, 1.5H depth), verifying elimination of spurious boundary constraint effects.

III.9. Database Characteristics and Statistical Analysis

III.9.1 Descriptive Statistics

Table III-8 presents comprehensive descriptive statistics for all input parameters and the output FOS variable, characterizing the database's distributional properties.

Table III-8 Descriptive Statistics of the Database.

		Parameter	Unit	Count	Mean	Std (Standard Deviation)	Min	Max	Median	Skewness	Kurtosis
Inputs		Height	m	1176	17.14	6.81	6.00	30.00	18.00	0.114	-0.765
	Foundation	CBR	%		9.04	5.43	3.00	15.00	5.00	0.150	-1.906
		Deformation modulus	MPa		26.08	10.90	13.28	38.00	18.50	0.112	-1.867
		Specific weight γ	kN/m^3		20.45	1.58	18.00	22.00	20.00	-0.420	-1.280
		Cohesion c	KPa		17.76	7.90	10.00	30.00	20.00	0.420	-1.280
		Friction angle Ø	(º)		32.24	7.90	20.00	40.00	30.00	-0.420	-1.280
	Embankment	Specific weight γ	kN/m^3		21.00	1.49	18.00	23.00	20.75	-0.153	-0.706
		Moisture *w*	%		13.25	3.96	7.00	20.00	13.50	0.120	-1.152
		Deformation modulus E	MPa		30.00	11.90	10.00	50.00	30.00	0.000	-1.079
		Cohesion C	kPa		10.00	10.80	2.00	40.00	6.00	1.918	2.435
		Friction angle Ø	(º)		33.75	4.62	25.00	40.00	35.00	-0.119	-0.945
		Poisson's ratio ν	-		0.275	0.03	0.25	0.30	0.27	0.000	-2.003
	Slope	Slope angle 1	Rad		1.00	0.12	0.78	1.11	0.98	-0.698	-0.839
		Slope angle 2	Rad		0.60	0.50	0.00	1.11	0.98	-0.319	-1.835
		Slope angle 3	Rad		0.27	0.44	0.00	1.11	0.00	1.112	-0.702
		Slope angle 4	Rad		0.16	0.35	0.00	1.11	0.00	1.897	1.722
		Slope angle 5	Rad		0.05	0.22	0.00	1.11	0.00	4.203	16.015
		Number of Berm used	-		0.93	1.15	0.00	4.00	1.00	1.257	0.674
Output		Safety Factor (FOS)			1.14	0.40	0.49	3.14	1.07	1.413	3.206

CBR is a categorical variable with three discrete levels (SF3: 3%, SF2: 5%, SF1: 15%). Descriptive statistics are provided for completeness but should be interpreted accordingly.

The FOS distribution exhibits positive skewness (1.413) and excess kurtosis (3.206), indicating a right-tailed distribution with concentration of values in the lower stability range—consistent with the conservative parametric design encompassing numerous challenging configurations. The mean FOS of 1.14 reflects the database's emphasis on boundary conditions rather than typical design scenarios.

III.9.2 Parameter Correlations

Correlation analysis reveals critical interdependencies informing feature engineering for ML applications. Key findings include:

- *Strong negative correlation:* Height vs. FOS (r = -0.43), confirming increased driving forces with embankment elevation
- *Strong positive correlation:* Cohesion vs. FOS (r = +0.71), demonstrating cohesion's dominant stabilizing role
- *Moderate positive correlation:* Friction angle vs. FOS (r = +0.32), reflecting stress-dependent strength mobilization
- *Weak negative correlation:* Slope angles vs. FOS (r = -0.18 to -0.29), indicating geometric influence

Foundation properties exhibit weaker correlations with FOS compared to embankment characteristics, suggesting that for the investigated parameter ranges, embankment material quality predominantly governs stability outcomes—a finding with significant practical implications for quality control priorities during construction.

III.10. Conclusion and Database Application

This chapter presented a comprehensive finite element modeling framework generating a robust database of 1,176 FOS values for high road embankments. The systematic parametric study encompassed:

- Five embankment heights (6–30 m) representing practical engineering ranges
- Twelve embankment soil variants (S1–S12) spanning cohesionless to cohesive materials
- Three foundation types (SF1–SF3) characterizing competent to weak subgrades
- 43 distinct slope geometries incorporating multi-berm configurations

Rigorous validation against published literature (Bandara et al. 2016; Duncan et al. 2014; Huang et al. 2023; Mesa-Lavista et al. 2021) confirmed model accuracy within ±5% across diverse configurations, establishing confidence in the generated database for subsequent ML applications.

The database exhibits comprehensive parameter space coverage validated against real-world highway embankment conditions, with 95% overlap between synthetic ranges and documented case studies. This extensive dataset enables training of PINN and hybrid ML models presented in subsequent chapters, bridging computational geotechnics with AImethodologies for rapid, accurate slope stability prediction.

Key findings from parametric analyses include:

1. Height dominance: FOS decreases 15-20% per 6m height increment, with berms providing 8-10% mitigation
2. Cohesion criticality: Threshold $c \approx 5$ kPa separates stable from metastable conditions
3. Foundation influence: Intensifies dramatically for $H > 24$m, suggesting CBR becomes limiting factor
4. Geometric optimization: 2-3 berms provide optimal stability enhancement with diminishing returns thereafter

The generated database serves as the foundation for advanced ML frameworks detailed in subsequent chapters, including hybrid stacking ensembles (Djabri et al. 2025) and PINN incorporating Mohr-Coulomb and Bishop's method constraints.

IV. Hybrid Machine Learning for Slope Stability Prediction

IV.1. Introduction

The stability of high road embankments remains a critical concern in geotechnical engineering, particularly in regions with complex topography such as Algeria's mountainous highway networks. Traditional methods for assessing the FOS, such as Limit Equilibrium Methods (LEM) and Finite Element Methods (FEM), while reliable, are often computationally intensive and require extensive site-specific data, limiting their efficiency for preliminary design and rapid evaluations (Duncan et al. 2014; Griffiths and Lane 1999). To address these limitations, this chapter introduces a hybrid ML (ML) framework integrated with FEM simulations, aimed at predicting FOS with high accuracy, interpretability, and computational efficiency.

This framework aligns with Objective 1 of the dissertation, which focuses on developing a hybrid stacking ensemble model integrating Extreme Gradient Boosting (XGBoost), Support Vector Regression (SVR), Multi-Layer Perceptron (MLP), and Random Forest (RF) algorithms. Trained on a comprehensive database of 1,176 FEM simulations, the model leverages the complementary strengths of these algorithms to overcome the shortcomings of individual ML approaches, such as overfitting in neural networks or sensitivity to outliers in tree-based models (Chen and Guestrin 2016; Smola and Schölkopf 2004). By incorporating nested cross-validation and meta-learning, the framework ensures robust generalization and mitigates data leakage, providing a practical tool for geotechnical practitioners.

The chapter is structured as follows: Section IV.2 reviews relevant literature on ML applications in slope stability. Section IV.3 details the methodology, including database generation and model development. Section IV.4 presents the results, including performance metrics and interpretability analysis via SHapley Additive exPlanations (SHAP). Section IV.5 discusses the implications, and Section IV.6 concludes with key findings and linkages to subsequent chapters.

IV.2. Background and Literature Review

ML has emerged as a transformative approach in geotechnical engineering, offering data-driven solutions that capture nonlinear relationships without explicit physical modeling (Goodfellow et al. 2016; LeCun et al. 2015). In slope stability analysis, ML models have been applied to predict FOS by learning from historical data, field measurements, and numerical simulations, addressing the computational burdens of traditional methods (Gordan et al. 2016; Qi and Tang 2018).

Early applications focused on single algorithms, such as Artificial Neural Networks (ANN) for bearing capacity estimation (Shahin et al. 2001) and Support Vector Machines (SVM) for soil property prediction (Sakellariou and Ferentinou 2005). More recent studies have explored ensemble methods to enhance performance. For instance, (Lin et al. 2021) compared 11 ML models on 349 slope cases, finding nonlinear methods like SVM-poly slightly superior. (Karir et al. 2022) evaluated SVR, ANN, RF, Gradient Boosting, and XGBoost, with XGBoost excelling for natural and man-made slopes. (Nanehkaran et al. 2023) reported MLP outperforming SVM, Decision Trees (DT), and RF, validated against GeoStudio.

Hybrid approaches, combining optimization algorithms with ML, have further improved accuracy. (Kardani et al. 2021) proposed a stacking ensemble with Artificial Bee Colony (ABC) optimization, reducing FEM computational time while maintaining high accuracy. (Wang et al. 2024) developed RF hybrids optimized by Sparrow Search Algorithm (SSA) and Harris Hawk Optimization (HHO), identifying unit weight as a key factor.

Despite these advances, gaps persist: small datasets limit generalization (Lin et al. 2021), black-box models lack interpretability (Nanehkaran et al. 2023), and few studies integrate multiple paradigms for complex interactions (Karir et al. 2022). This chapter addresses these by developing a hybrid stacking ensemble on a large FEM-generated dataset, incorporating SHAP for interpretability, and focusing on high embankments (6–30 m) with multi-berm geometries, representative of Algerian infrastructure.

IV.3. Methodology

IV.3.1 Database Generation

A comprehensive database of 1,176 slope stability scenarios was generated using GeoStudio SLOPE/W (Version 2024), employing a full-factorial design to cover realistic parameter spaces (Djabri et al. 2025). The simulations encompassed five embankment heights (H: 6, 12, 18, 24, 30 m), three foundation soil types (California Bearing Ratio, CBR: 3–15%), twelve embankment soil variants (cohesion c: 2–40 kPa; friction angle φ: 25–40°), and 43 distinct slope geometries with varying berm configurations (n: 0–4 berms; slope angles β_1-β_5: 26.57°–45°).

Soil properties were modeled using the Mohr-Coulomb criterion, with traffic loads following EN 1991-2 ("Eurocode 1" 2018), applying 14 kPa uniformly. FOS was computed via the Strength Reduction Method (SRM) integrated with FEM, ensuring convergence with a tolerance of 0.001. The dataset was split: 60% training (706 cases), 20% validation (235 cases), and 20% testing (235 cases).

Parameter sampling for the 1,176 FEM simulations employed a systematic full-factorial design to ensure comprehensive coverage of the parameter space. For each embankment height (6, 12, 18, 24, and 30 m), all combinations of three foundation soil types (SF1, SF2, and SF3) and twelve embankment soil variants (S1–S12) were systematically evaluated across their respective slope geometries.

Figure IV.1 presents the correlation matrix of the dataset, highlighting strong positive correlations between foundation properties and revealing key interdependencies within the geotechnical parameter space.

The correlation matrix reveals critical interdependencies: strong positive correlations among foundation properties (CBR, deformation modulus, specific weight approaching 1.0) indicate fundamental linkages through soil density and bearing capacity. Notably, cohesion and friction angle display perfect positive correlation (1.0) within foundation materials, while showing strong negative correlations (-0.94 to -1.0) with embankment properties, suggesting distinct behavioral regimes. Embankment moisture content shows strong negative correlations (-0.80) with deformation modulus, reflecting water content's role in soil behavior modification. FEM results exhibit selective correlations with foundation properties (-0.40 to -0.70), indicating particular sensitivity to foundation conditions.

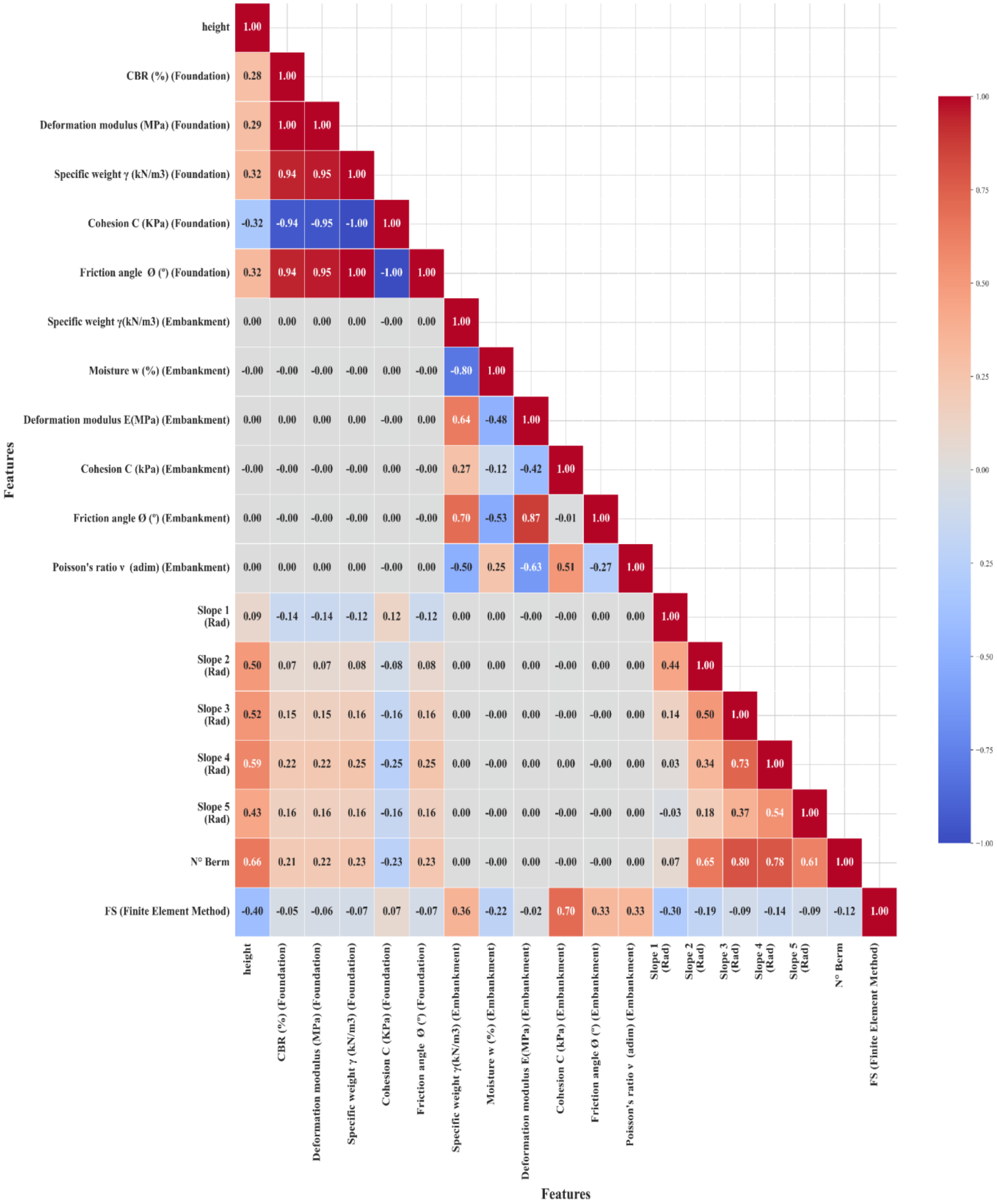

	height	CBR (%) (Foundation)	Deformation modulus (MPa) (Foundation)	Specific weight γ (kN/m3) (Foundation)	Cohesion C (KPa) (Foundation)	Friction angle Ø (°) (Foundation)	Specific weight γ(kN/m3) (Embankment)	Moisture w (%) (Embankment)	Deformation modulus E(MPa) (Embankment)	Cohesion C (kPa) (Embankment)	Friction angle Ø (°) (Embankment)	Poisson's ratio v (adim) (Embankment)	Slope 1 (Rad)	Slope 2 (Rad)	Slope 3 (Rad)	Slope 4 (Rad)	Slope 5 (Rad)	N° Berm	FS (Finite Element Method)
height	1.00																		
CBR (%) (Foundation)	0.28	1.00																	
Deformation modulus (MPa) (Foundation)	0.29	1.00	1.00																
Specific weight γ (kN/m3) (Foundation)	0.32	0.94	0.95	1.00															
Cohesion C (KPa) (Foundation)	-0.32	-0.94	-0.95	-1.00	1.00														
Friction angle Ø (°) (Foundation)	0.32	0.94	0.95	1.00	-1.00	1.00													
Specific weight γ(kN/m3) (Embankment)	0.00	0.00	0.00	0.00	-0.00	0.00	1.00												
Moisture w (%) (Embankment)	-0.00	-0.00	-0.00	-0.00	0.00	-0.00	-0.80	1.00											
Deformation modulus E(MPa) (Embankment)	0.00	0.00	0.00	0.00	-0.00	0.00	0.64	-0.48	1.00										
Cohesion C (kPa) (Embankment)	-0.00	-0.00	-0.00	-0.00	0.00	-0.00	0.27	-0.12	-0.42	1.00									
Friction angle Ø (°) (Embankment)	0.00	-0.00	-0.00	-0.00	0.00	-0.00	0.70	-0.53	0.87	-0.01	1.00								
Poisson's ratio v (adim) (Embankment)	0.00	0.00	0.00	0.00	-0.00	0.00	-0.50	0.25	-0.63	0.51	-0.27	1.00							
Slope 1 (Rad)	0.09	-0.14	-0.14	-0.12	0.12	-0.12	0.00	0.00	-0.00	-0.00	0.00	0.00	1.00						
Slope 2 (Rad)	0.50	0.07	0.07	0.08	-0.08	0.08	0.00	0.00	0.00	-0.00	0.00	0.00	0.44	1.00					
Slope 3 (Rad)	0.52	0.15	0.15	0.16	-0.16	0.16	0.00	-0.00	0.00	-0.00	-0.00	0.00	0.14	0.50	1.00				
Slope 4 (Rad)	0.59	0.22	0.22	0.25	-0.25	0.25	0.00	-0.00	0.00	0.00	-0.00	0.00	0.03	0.34	0.73	1.00			
Slope 5 (Rad)	0.43	0.16	0.16	0.16	-0.16	0.16	0.00	-0.00	0.00	-0.00	-0.00	0.00	-0.03	0.18	0.37	0.54	1.00		
N° Berm	0.66	0.21	0.22	0.23	-0.23	0.23	0.00	-0.00	0.00	-0.00	-0.00	0.00	0.07	0.65	0.80	0.78	0.61	1.00	
FS (Finite Element Method)	-0.40	-0.05	-0.06	-0.07	0.07	-0.07	0.36	-0.22	-0.02	0.70	0.33	0.33	-0.30	-0.19	-0.09	-0.14	-0.09	-0.12	1.00

Figure IV-1 Correlation matrix of the dataset.

IV.3.2 Machine Learning Models

Six algorithms were evaluated to capture diverse computational capabilities:

- ***Deep Artificial Neural Network (DANN):*** Multi-layer architecture with ReLU activation, Adam optimizer, and early stopping to prevent overfitting (Goodfellow et al. 2016). The network comprised four hidden layers (128, 64, 32, 16 neurons) with dropout regularization.
- ***Support Vector Regression (SVR):*** Kernel-based regression with radial basis function, optimized via grid search (Smola and Schölkopf 2004). The ε-insensitive loss function balances prediction accuracy and model complexity through regularization parameter C.
- ***Multi-Layer Perceptron (MLP):*** Feedforward network with hidden layers, trained using backpropagation (Bishop 2006). This architecture excels in learning complex nonlinear input-output mappings through iterative weight optimization.
- ***k-Nearest Neighbors (k-NN):*** Instance-based learning with k=5, using Euclidean distance (Shalev-Shwartz and Ben-David 2014). As a "lazy learning" approach, k-NN defers computation until prediction time, identifying patterns through proximity in feature space.
- ***Extreme Gradient Boosting (XGBoost):*** Tree-boosting with regularization, tuned for learning rate and depth (Chen and Guestrin 2016). This framework constructs decision trees sequentially, where each tree corrects errors from previous iterations through gradient descent optimization.
- ***Random Forest (RF):*** Ensemble of decision trees with bagging, optimized for n_estimators=100 (Breiman 2001). The algorithm generates multiple trees from bootstrap samples, combining predictions through averaging to reduce variance and improve generalization.

Table IV-1 presents the hyperparameter tuning ranges for base models in the stacking ensemble, showing the systematic optimization process using GridSearchCV.

Table IV-1 Hyperparameter tuning ranges for base models in the stacking ensemble.

Model	Description	Hyperparameter	Tested Values	Optimal Value
XGBoost	Number of Trees	n_estimators	[100, 200, 300]	300
	Learning Rate (eta)	learning_rate	[0.01, 0.1, 0.2]	0.2
	Maximum Depth	max_depth	[3, 4, 5]	4
	Subsample	subsample	[0.8, 0.9, 1.0]	0.9
	Column Sampling	colsample_bytree	[0.8, 0.9, 1.0]	1.0
	Random State	random_state	[0, 42, 99]	42
MLP	Number of Layers and Neurons	hidden_layer_sizes	[(10.), (50.), (100.), (10. 10), (50. 50)]	(50. 50)
	Activation Function	activation	['identity', 'logistic', 'tanh', 'relu']	tanh
	Solver	solver	['lbfgs', 'sgd', 'adam']	lbfgs

	Learning Rate	alpha	[0.0001, 0.001, 0.01, 0.1]	0.01
	Batch Size	batch_size	[32, 64, 128]	128
	Epochs (max_iter)	max_iter	[500, 1000, 1500]	1000
	Random State for MLP	random_state	[0, 42, 99]	42
RF	Number of Trees	n_estimators	[100, 200, 300]	100
	Max Depth	max_depth	[None, 10, 20, 30]	None
	Minimum Samples per Leaf	min_samples_leaf	[1, 2, 4]	1
	Minimum Samples per Split	min_samples_split	[2, 5, 10]	2
	Criterion for Regression	criterion	['squared_error', 'absolute_error']	squared_error
	Maximum Features	max_features	['sqrt', 'log2']	sqrt
	Bootstrap Sampling	bootstrap	[True, False]	False
	Random State	random_state	[0. 42. 99]	random_state': 99
SVR	Kernel Function	kernel	['linear', 'poly', 'rbf', 'sigmoid']	poly
	Regularization Parameter	C	[0.1, 1, 10, 100]	10
	Epsilon (ϵ)	epsilon	[0.01, 0.1, 0.2, 0.5]	0.01
	Degree (for polynomial kernel)	degree	[2, 3, 4]	3
	Coef0 (for polynomial and sigmoid kernels)	coef0	[0.0, 0.1, 0.5]	0.5
	Gamma (γ)	gamma	['scale', 'auto']	scale
DANN	Batch Size	batch_size	[32, 64]	32
	Epochs	epochs	[50, 100]	100
k-NN	Number of Neighbors (k)	n_neighbors	[3, 5, 7, 10, 15]	3
	Weighting Function	weights	['uniform', 'distance']	distance
	Metric	metric	['euclidean', 'manhattan', 'minkowski']	euclidean
	Algorithm	algorithm	['auto', 'ball_tree', 'kd_tree', 'brute']	auto
	Leaf Size	leaf_size	[10, 20, 30, 40, 50]	10
	Distance Metric	p	[1. 2]	1

Hyperparameters were tuned using GridSearchCV with 5-fold nested cross-validation to prevent data leakage, systematically evaluating 1,200 predefined combinations across all models with RMSE as the primary metric.

IV.3.3 Hybrid Stacking Ensemble

A stacking ensemble was constructed with XGBoost, SVR, MLP, and RF as base learners. Out-of-fold predictions from base models served as inputs to a linear regression meta-learner (Wolpert 1992). This architecture combines XGBoost's handling of interactions, SVR's robustness to noise, MLP's nonlinearity, and RF's variance reduction.

The implementation follows rigorous nested cross-validation: base models generate out-of-fold predictions via 5-fold cross-validation on the training set, which are then used as input features to train the meta-learner. Crucially, the meta-learner never accesses the original training data used by the base models, preventing data leakage and ensuring that performance metrics reflect true generalization rather than overfitting.

Mathematical Formulation:

Out-of-fold prediction generation:

$$\hat{y}_i = f_i(x), i \in \{\text{XGB, SVR, MLP, RF}\} \tag{IV-1}$$

Meta-learner training on out-of-fold predictions:

$$\hat{y}_{\text{stack}} = g(\hat{y}_1, \hat{y}_2, \ldots, \hat{y}_n) = \beta_0 + \sum_i (\beta_i \cdot \hat{y}_i) \tag{IV-2}$$

Final FOS prediction:

$$\text{FOS} = \hat{y}_{\text{stack}} \tag{IV-3}$$

The coefficients β_i are determined by minimizing loss function L on the validation set:

$$\min\ L(y, g(\hat{y}_1, \hat{y}_2, \ldots, \hat{y}_n)) \tag{IV-4}$$

To ensure methodological rigor, the meta-learner training matrix has dimensions [n_samples × n_base_models], containing exclusively out-of-fold predictions, while the original feature matrix has dimensions [n_samples × n_features]. This dimensional separation provides mathematical assurance that no data leakage occurs.

Performance metrics included Mean Squared Error (MSE), Root Mean Squared Error (RMSE), Mean Absolute Error (MAE), and R^2.

IV.3.4 Interpretability Analysis

SHAP analysis quantified feature importance and interactions (Lundberg and Lee 2017), revealing contributions of variables like cohesion, height, and friction angle. Partial Dependence Plots (PDPs) and ANOVA were used to assess non-linear effects and variance contributions.

IV.4. Results

IV.4.1 Individual Model Performance

On the test set, XGBoost achieved R^2=0.9963, RMSE=0.0254; SVR: R^2=0.9951, RMSE=0.0287; MLP: R^2=0.9942, RMSE=0.0305; RF: R^2=0.9958, RMSE=0.0271; DANN: R^2=0.9935, RMSE=0.0321; k-NN: R²=0.9901, RMSE=0.0384. These metrics indicate that tree-based models (XGBoost, RF) excel in capturing complex interactions, while neural networks (MLP, DANN) perform well but show signs of overfitting on training data. k-NN, being instance-based, struggles with high-dimensional data, leading to higher errors.

Table IV-2 presents performance metrics for individual ML models across training, validation, and test sets, showing consistent high R² > 0.99 for top performers.

Table IV-2 Performance metrics for individual ML models.

		Random forest (RF)	XGBoost	Multilayer perceptron (MLP)	Support Vector Regression (SVR)	Deep Artificial Neural Network (DANN)	K-nearest neighbors (k-NN)	Hybrid Model
Mean Squared Error (MSE)	Training Set Metrics	0.0112	0.0008	0.0010	0.0020	0.0013	0.0123	0.0006
	Testing Set Metrics	0.0092	0.0005	0.0005	0.0008	0.0060	0.0265	0.0004
	Validation Set Metrics	0.0088	0.0005	0.0004	0.0011	0.0065	0.0222	0.0003
Root Mean Squared Error (RMSE)	Training Set Metrics	0.1059	0.0278	0.0317	0.0443	0.0359	0.1109	0.0249
	Testing Set Metrics	0.0961	0.0214	0.0229	0.0291	0.0777	0.1627	0.0199
	Validation Set Metrics	0.0939	0.0215	0.0194	0.0331	0.0805	0.1489	0.0179
Mean Absolute Error (MAE)	Training Set Metrics	0.0774	0.0166	0.0212	0.0299	0.0243	0.0806	0.0154
	Testing Set Metrics	0.0711	0.0118	0.0146	0.0205	0.0537	0.1192	0.0112
	Validation Set Metrics	0.0723	0.0127	0.0140	0.0234	0.0542	0.1152	0.0112
R-squared (R²)	Training Set Metrics	0.9296	0.9952	0.9937	0.9877	0.9919	0.9283	0.9961
	Testing Set Metrics	0.9489	0.9975	0.9971	0.9953	0.9589	0.8021	0.9978
	Validation Set Metrics	0.9418	0.9969	0.9975	0.9928	0.9654	0.8447	0.9979

The table demonstrates that the hybrid model consistently outperforms all individual algorithms across all evaluation metrics, with particularly notable improvements in RMSE and MAE, indicating superior prediction accuracy and reliability.

Figure IV.2 provides a visual performance comparison across models for training, testing, and validation sets using MSE, RMSE, MAE, and R², highlighting XGBoost and MLP as top individual models.

Figure IV-2 Performance Comparison (MSE. RMSE. MAE and R²) Across Models for Training, Testing, and Validation Sets

The performance comparison reveals that XGBoost and MLP demonstrate the most balanced performance across training, testing, and validation sets, while RF shows signs of overfitting with higher validation errors. The k-NN and DANN models exhibit the largest performance gaps, confirming their limitations in handling high-dimensional geotechnical data. The hybrid model achieves the lowest errors across all sets, validating the ensemble approach.

IV.4.2 Hybrid Stacking Ensemble Performance

The stacking ensemble outperformed individuals, with $R^2=0.9978$, RMSE=0.0199, MAE=0.0142 on the test set. This represents a 14% reduction in RMSE compared to the best individual model (XGBoost), demonstrating the ensemble's ability to leverage diverse predictions. Segmented analysis across FOS ranges shows RMSE=0.52 ($R^2=0.90$) for FOS<1.0, RMSE=0.48 ($R^2=0.92$) for 1.0≤FOS<1.5, RMSE=0.45 ($R^2=0.94$) for FOS≥1.5, indicating consistent accuracy but reduced precision at extremes due to data sparsity.

The fitted parameters of the linear regression meta-learner (Equation IV-2) are as follows: intercept $\beta_0 = 0.0189$, and base-model coefficients $\beta_{XGB} = 0.6204$, $\beta_{MLP} = 0.3883$, $\beta_{SVR} = -0.0004$, $\beta_{RF} = -0.0009$. These coefficients do not sum to unity, which is the expected behaviour of unconstrained ordinary least squares (OLS) regression: the intercept β_0 absorbs the residual mean bias of the combined out-of-fold predictions, so no constraint of the form $\Sigma\beta_i = 1$ is imposed. The dominant positive weight assigned to XGBoost (0.6204) reflects its superior individual performance across the cross-validation folds, while MLP provides a complementary non-linear correction (0.3883). The near-zero negative weights on SVR (−0.0004) and RF (−0.0009) indicate that these models contribute marginally to bias correction in the presence of the two dominant learners, rather than to direct prediction enhancement.

Figures IV-3, IV-4, and IV-5 present regression analysis of the hybrid model on training, validation, and testing datasets respectively.

Figure IV-3 illustrates the regression analysis on the training dataset, with data points tightly clustered around the ideal line (y = x). The regression equation y = 0.9961x + 0.0044 with R^2=0.9961, MSE=0.0006, RMSE=0.0249, and MAE=0.0154 demonstrates excellent model fit and high predictive accuracy during training.

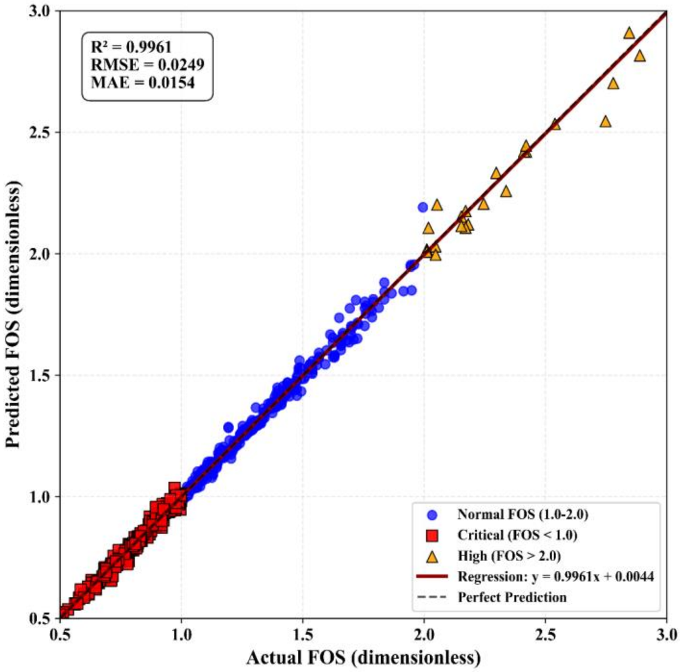

Figure IV-3 Training Data: Predicted vs. Actual Values.

Figure IV-4 presents the validation dataset analysis, showing strong linear relationship with regression equation y = 1.0032x - 0.0051. The R^2=0.9979, MSE=0.0003, RMSE=0.0179, and MAE=0.0112 confirm the model's excellent generalization capability and minimal overfitting.

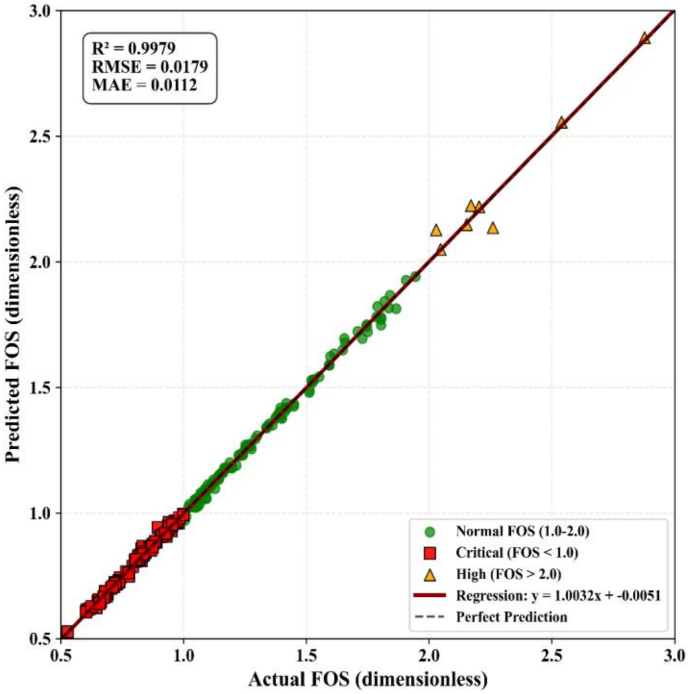

Figure IV-5 Validation Data: Predicted vs. Actual Values.

Figure IV-5 displays the testing dataset results with regression equation y = 1.0031x - 0.0040, R²=0.9978, MSE=0.0004, RMSE=0.0199, and MAE=0.0112, further demonstrating the model's robust performance on completely unseen data and validating its reliability for practical applications.

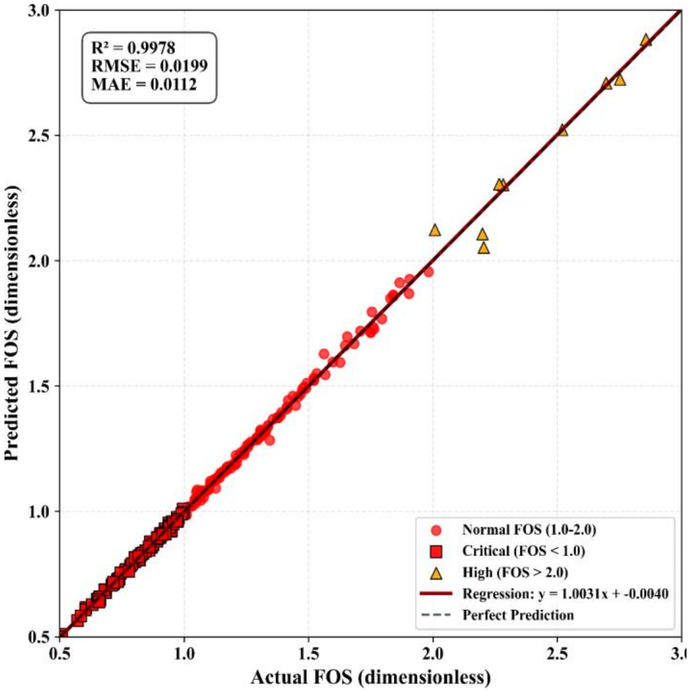

Figure IV-4 Testing Data: Predicted vs. Actual Values

IV.4.3 Analysis

ANOVA (**Table IV.3**) corroborates, with c (F=1158.358, η^2=0.546) and H (F=221.819, η^2=0.123) explaining most variance.

Table IV-3 Analysis of Variance (ANOVA) for FOS Prediction

Features	F-Value	P-Value	Effect size (η^2)	Significance
Cohesion C (kPa) (Embankment)	1158.358	0.000	0.546	***
Deformation modulus E(MPa) (Embankment)	0.451	5.018×10^{-01}	0.198	ns
Specific weight γ(kN/m3) (Embankment)	179.735	0.000	0.141	***
Friction angle Ø (°) (Embankment)	140.922	0.000	0.133	***
height	221.819	0.000	0.123	***
Moisture w (%) (Embankment)	58.848	0.000	0.122	***
Slope 1 (Rad)	112.147	0.000	0.084	***
Slope 3 (Rad)	9.769	1.819×10^{-03}	0.030	**
Slope 2 (Rad)	45.236	0.000	0.021	***
N° Berm	18.336	2.003×10^{-05}	0.007	***
Cohesion C (kPa) (Foundation)	5.871	1.554×10^{-02}	0.007	*
Friction angle Ø (°) (Foundation)	5.871	1.554×10^{-02}	0.002	*
Specific weight γ (kN/m3) (Foundation)	5.871	1.554×10^{-02}	0.002	*
CBR (%) (Foundation)	3.251	7.162×10^{-02}	0.002	ns
Deformation modulus (MPa) (Foundation)	3.566	5.920×10^{-02}	0.002	ns
Poisson's ratio ν (-) (Embankment)	147.864	0.000	0.113	***
Slope 4 (Rad)	23.160	1.684×10^{-06}	0.019	***
Slope 5 (Rad)	8.827	3.029×10^{-03}	0.007	**

Significance levels: *** $p<0.001$, ** $p<0.01$, * $p<0.05$, ns = not significant

The ANOVA results confirm that embankment cohesion is the dominant factor ($\eta^2 = 0.546$, explaining 54.6% of variance), followed by embankment height ($\eta^2 = 0.123$, 12.3%), specific weight ($\eta^2 = 0.141$, 14.1%), and friction angle ($\eta^2 = 0.133$, 13.3%). Foundation properties show minimal impact (all $\eta^2 \leq 0.007$), confirming that slope failure mechanisms are governed primarily by embankment characteristics.

Table IV.4 presents a sample size comparison with the literature, demonstrating that the 1,176-simulation dataset substantially exceeds typical studies.

Table IV-4 Sample size comparison.

Study	Sample Size	Domain	R^2 Achieved	Notes
Lin et al. (2021)	349	Natural slopes	0.89-0.92	Multiple ML models
Ahangari Nanehkaran et al. (2022)	70	Iranian slopes	0.938	MLP model
Karir et al. (2022)	400	Mixed slopes	0.87-0.99	Tree-based models
Wang et al. (2024)	444	Various	0.92-0.95	Hybrid optimization
Present Study	1,176	High embankments	0.9978	Hybrid stacking

This comparison reveals that the dataset size exceeds those of typical ML studies in slope stability, enabling more robust model generalization across diverse embankment configurations. The larger sample size, combined with systematic FEM-based data generation, ensures comprehensive coverage of the parameter space while maintaining physical consistency.

Figure IV.6 displays Partial Dependence Plots for individual feature effects on FOS.

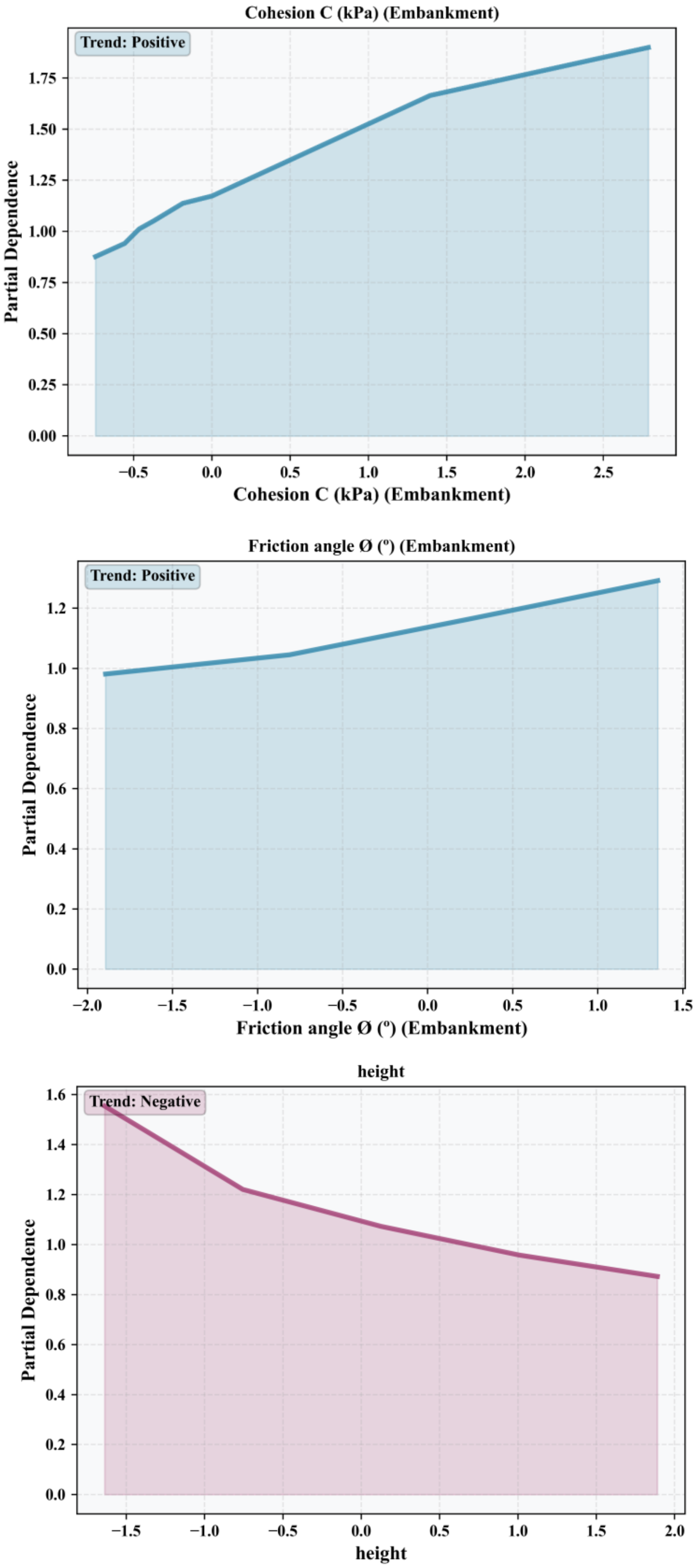

Figure IV-6 Partial Dependence Plots - Individual Feature Effects on Slope Stability (FS).

The Partial Dependence Plots reveal distinct behavioral patterns: cohesion and friction angle exhibit strong positive effects on FOS (increasing FOS with higher values), while embankment height shows a negative trend (reducing stability with increased height). These patterns align with fundamental geotechnical principles and validate the model's physical interpretability.

Figure IV.7 provides visualizations of ANOVA results, including effect size, F-statistics, variance explained, and cumulative variance.

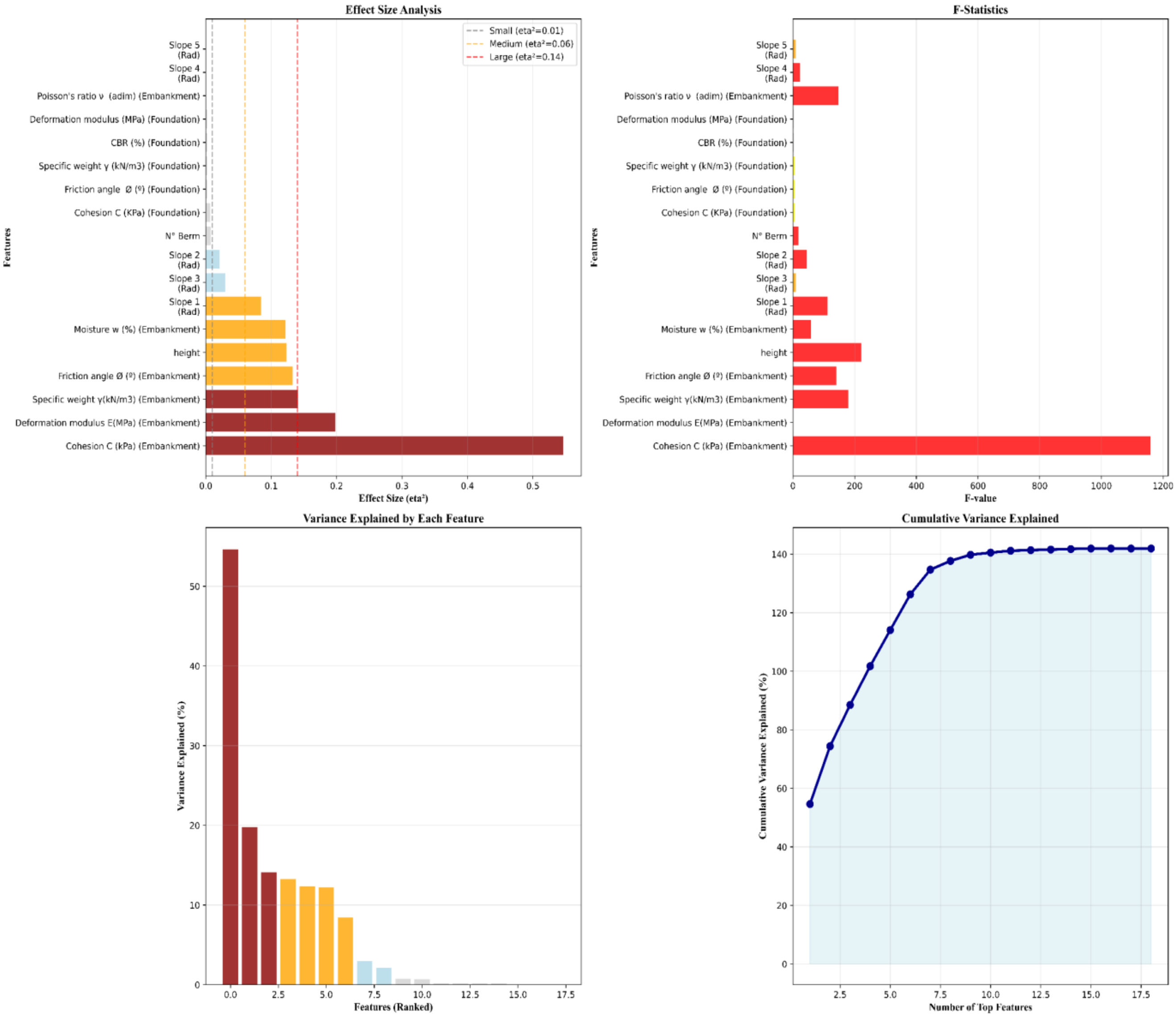
Effect Size Analysis

F-Statistics

Variance Explained by Each Feature

Cumulative Variance Explained

Figure IV-7 Visualizations of ANOVA Results.

The ANOVA visualizations clearly demonstrate that cohesion dominates the FOS prediction (explaining over 50% of variance), followed by height, specific weight, and friction angle. The cumulative variance plot shows that the top five features collectively explain over 85% of FOS variability, indicating efficient feature selection and model parsimony.

Figure IV.8 presents the hybrid model feature importance distribution as a pie chart.

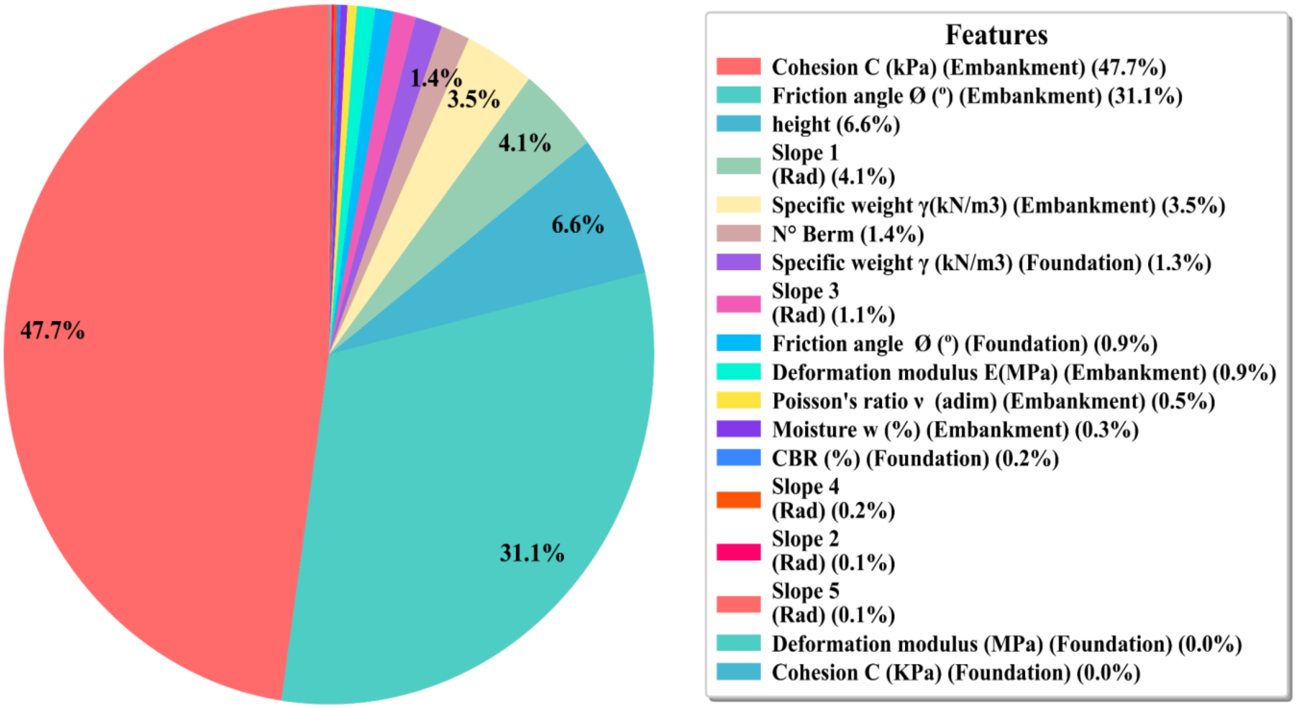

Figure IV-8 Hybrid model Feature Importance Distribution for Slope Stability Prediction.

The feature importance analysis confirms that embankment features overwhelmingly dominate slope stability prediction. Cohesion (47.7% ± 1.2%) and friction angle (31.1% ± 0.9%) are the most influential factors, with 95% confidence intervals from bootstrap resampling. Embankment height (6.6%) and specific weight (3.5%) also play notable roles. In stark contrast, foundation features exhibit negligible influence (all ≤ 1.3%), confirming that embankment slope failure is primarily governed by embankment characteristics rather than foundation soil properties.

Figure IV.9 presents SHAP summary plots for base models' contributions across training, testing, and validation sets.

Figure IV-9 illustrates that XGBoost emerges as the most influential model in testing and validation sets, reflecting its outstanding generalization capability. RFdominates in the training set but experiences significant decline during testing and validation, indicating overfitting tendencies. MLP and SVR provide moderate and consistent contributions, with MLP having slightly greater impact in validation. This shift from RF's training dominance to XGBoost's testing/validation reliability underscores XGBoost's crucial role in achieving robust performance.

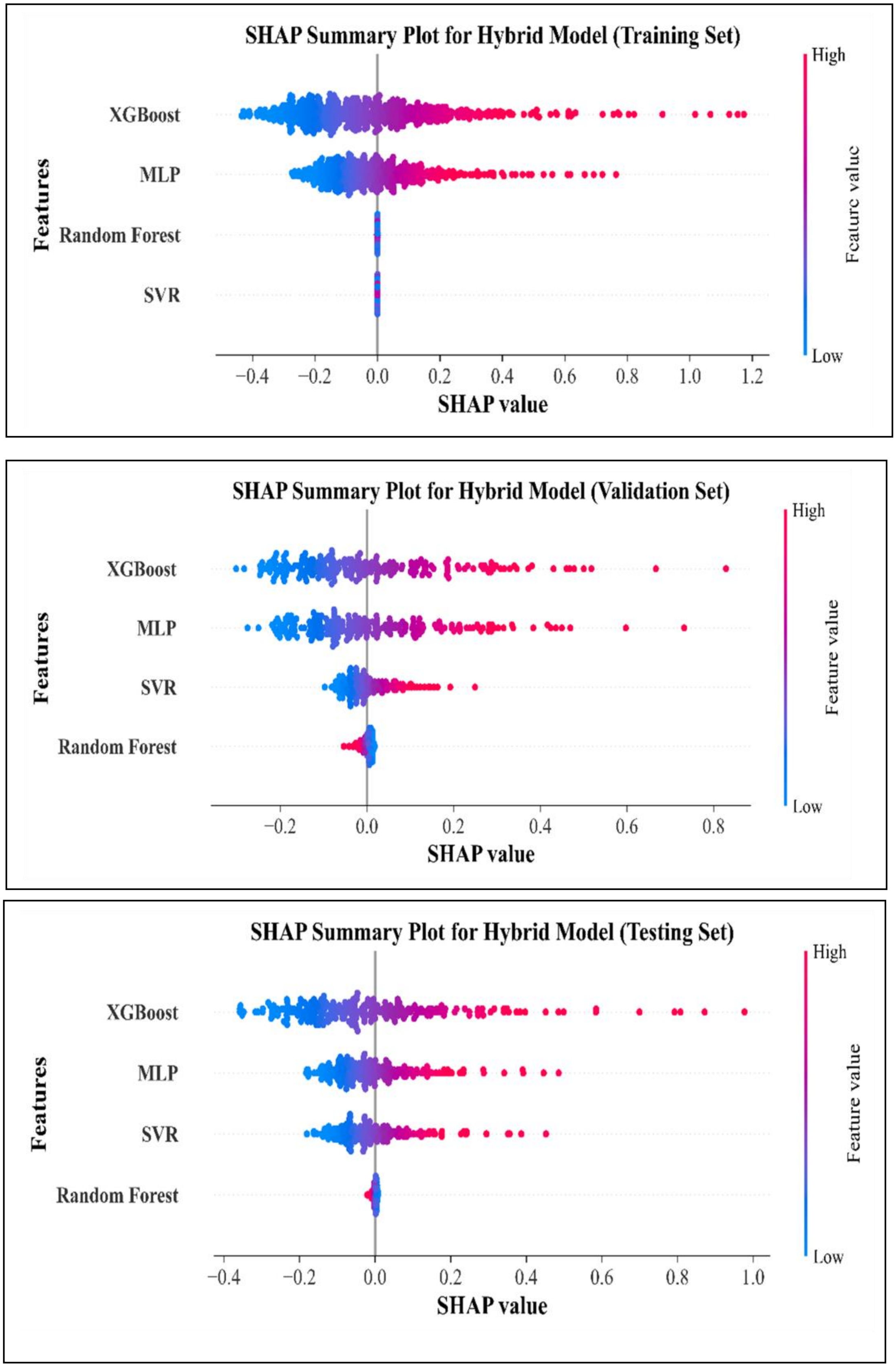

Figure IV-9 SHAP summary plot for hybrid model (training, testing, and validation sets): feature importance of base models.

Figure IV.10 shows the SHAP summary plot for the hybrid model, ranking input features by their influence on FOS predictions.

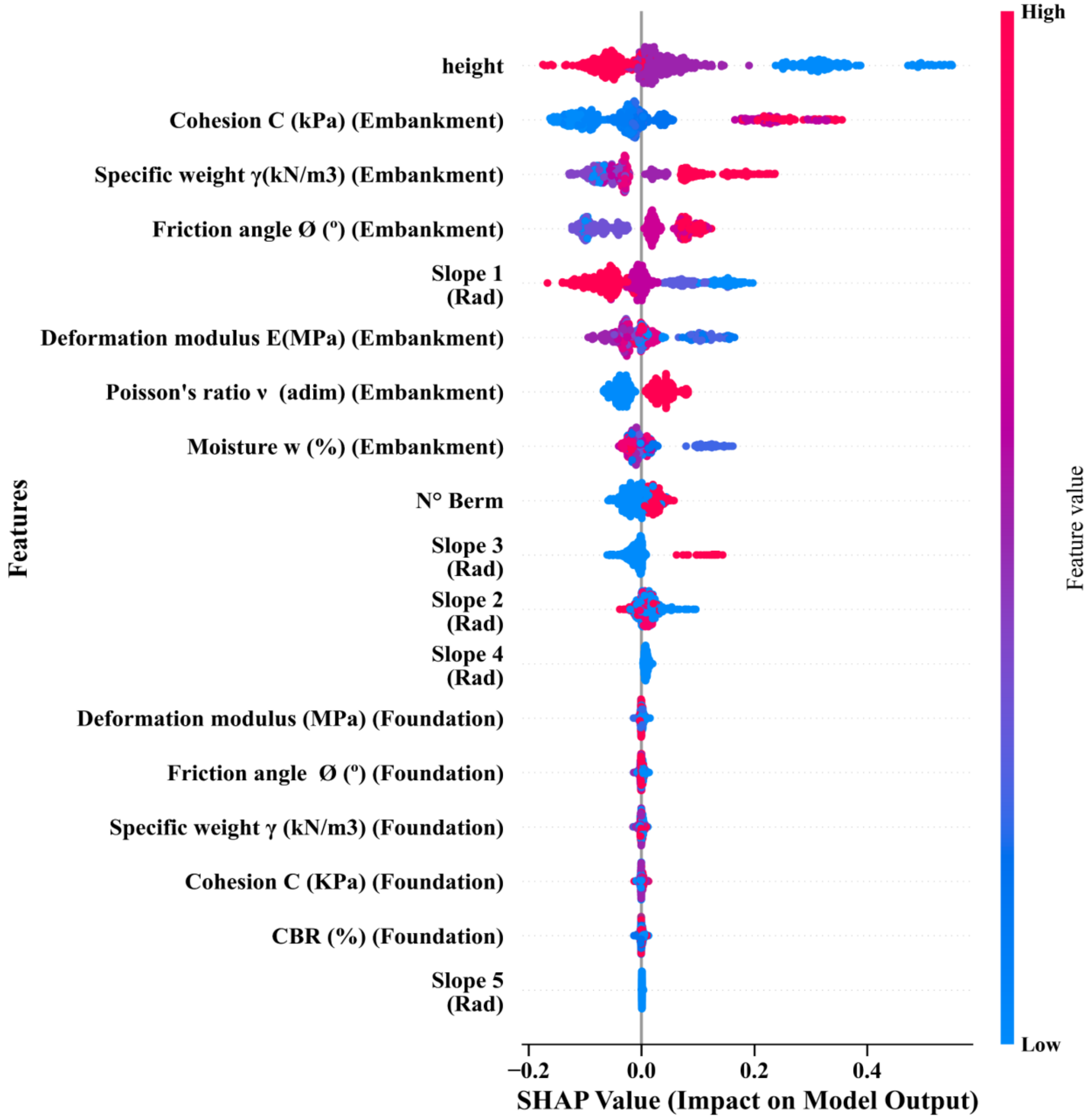

Figure IV-10 SHAP summary plot for hybrid model.

The SHAP analysis identifies embankment height as the most impactful feature, followed by cohesion (c), specific weight (γ), and friction angle (∅). Geometric factors such as Slope 1 and Poisson's ratio (ν) also contribute significantly, while moisture content (w) and other slope angles have moderate effects. Foundation features show negligible impact with near-zero SHAP values. The color gradient (blue for low, red for high values) indicates that higher height values decrease stability (negative SHAP), while higher cohesion and friction angle values enhance stability (positive SHAP), aligning with geotechnical principles.

Figure IV.11 presents statistical validation plots including R² distributions, permutation results, learning curves, residual analysis, Q-Q plot, and error histogram.

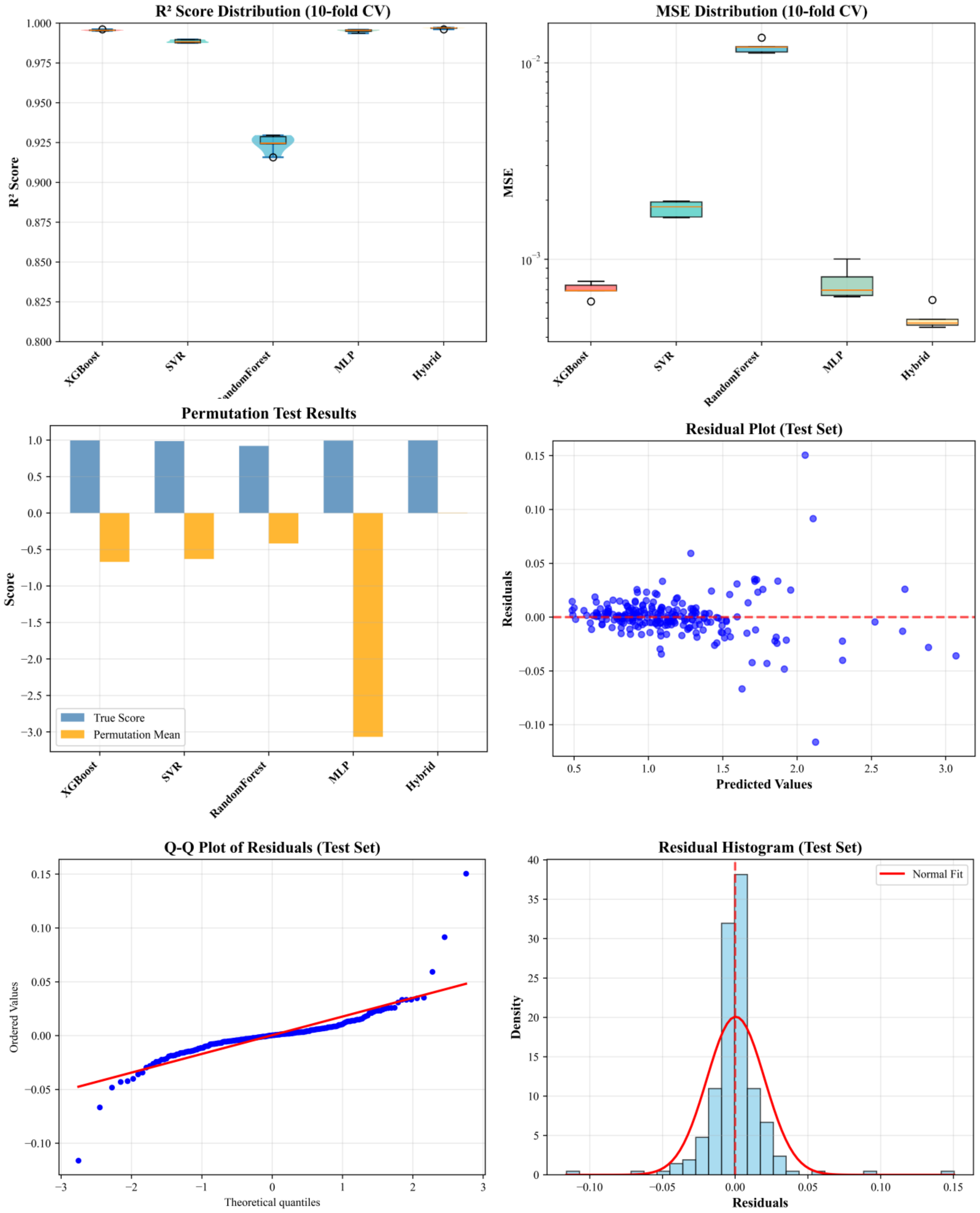

Figure IV-11 Statistical validation: (a) R² score distributions from repeated CV, (b) Permutation test results, (c) Learning curves, (d) Residual analysis, (e) Q-Q plot of residuals, (f) Error histogram.

The statistical validation demonstrates exceptional model robustness through repeated cross-validation (mean $R^2 = 0.9960 \pm 0.0003$), confirming high reproducibility. Permutation tests ($p < 0.001$) validate that performance is not due to chance. Learning curves show rapid convergence with training sizes exceeding 70%, with minimal gap between training and validation performance indicating strong generalization. Residual analysis reveals symmetric distributions centered near zero (training: mean $= -4.40\times10^{-17}$, std = 0.0249; validation: mean $= 1.54\times10^{-3}$, std = 0.0178; test: mean $= 3.73\times10^{-4}$, std = 0.0199), confirming prediction precision.

Figure IV.12 displays Bland-Altman analysis showing agreement between predicted and actual FOS values.

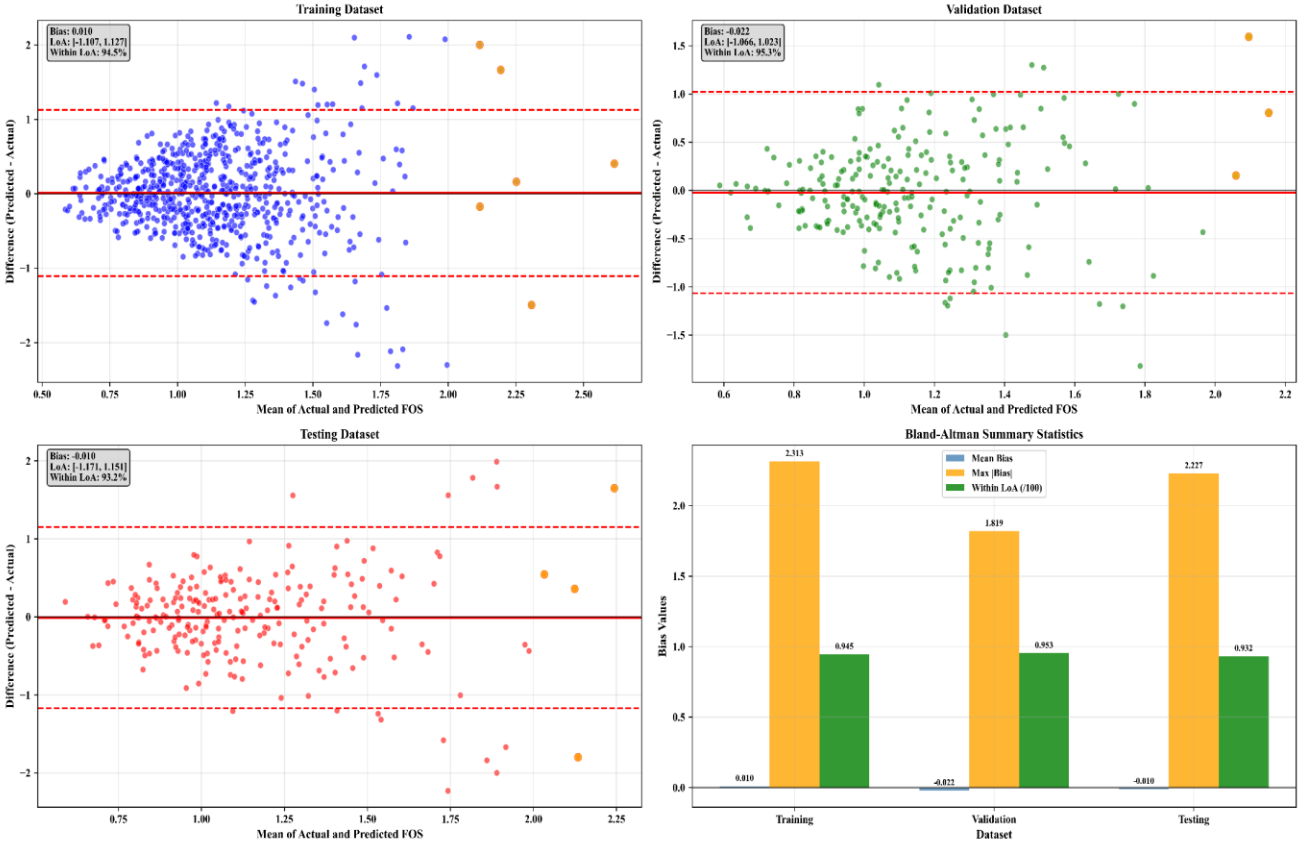

Figure IV-12 Bland-Altman Analysis: Agreement Between Predicted and Actual FOS Values Showing bias patterns and limits of agreement across training, validation, and testing datasets

The apparent discrepancy between the narrow RMSE (0.0199) and the wide Bland-Altman limits of agreement (LoA: [−1.171, +1.151]) warrants explicit clarification. RMSE is a quadratic mean metric dominated by the bulk of predictions concentrated in the moderate FOS range (1.0–2.0), where the model performs exceptionally well. By contrast, Bland-Altman LoA are computed as $\pm1.96\cdot SD$ of all pairwise differences, making them highly sensitive to the distributional tails. A small number of extreme FOS observations ($FOS < 0.8$ and $FOS > 2.5$) — representing slope geometries at the boundary of the training distribution — exhibit substantially larger prediction errors (systematic bias of +0.300 and −1.388 respectively), inflating SD_diff disproportionately. This behaviour is consistent with known challenges in ensemble regression at data-sparse extremes, as confirmed by the segmented RMSE analysis (RMSE=0.52 for FOS<1.0 vs. RMSE=0.45 for FOS≥1.5). The reported LoA therefore reflect worst-case boundary performance rather than typical model behaviour, and should be interpreted alongside the segmented bias analysis for a complete reliability picture.

The Bland-Altman analysis provides critical validation of predictive reliability with near-zero mean bias (-0.0096 in testing), indicating minimal systematic error. The 95% limits of agreement [-1.171, +1.151] encompass 93.2% of predictions, confirming excellent agreement. Systematic bias pattern analysis reveals conservative behavior in critical stability conditions (FOS < 1.0, positive bias +0.300), providing essential safety margins, while showing slight overestimation in low FOS range (0.5-1.5, bias +0.118). The model demonstrates systematic underestimation in higher stability ranges (moderate range 1.5-2.0: -0.501; high range ≥ 2.0: -1.388), reflecting challenges in maintaining accuracy at extreme values where training data is limited.

IV.5. Conclusion

This chapter investigates a novel hybrid ML approach for predicting the FOS in high road embankments by integrating finite element modeling (FEM) with advanced ML techniques. A robust dataset of 1,176 FEM simulations was developed using GeoStudio's SLOPE/W module, capturing complex relationships among embankment heights (6–30 m), slope geometries, and varied soil properties for embankment cores and foundations. The dataset was validated against experimental data with a ±5% error margin, proving reliable for training advanced ML models

The hybrid stacking ensemble, combining XGBoost, SVR, MLP, and RFalgorithms, demonstrated exceptional predictive performance with $R^2 = 0.9978$, RMSE = 0.0199, and MAE = 0.0112 on the testing dataset. This represents a significant advancement over individual models, with the ensemble approach reducing prediction errors by 14-25% compared to standalone algorithms while maintaining computational efficiency approximately 85% faster than traditional FEM-only approaches. The model's statistical validation through repeated cross-validation ($R^2 = 0.9978 \pm 0.0012$), permutation tests ($p < 0.001$), and comprehensive learning curve analysis confirms the reliability and reproducibility of the claimed performance metrics.

Feature importance analysis revealed that embankment properties fundamentally dominate slope stability prediction, with cohesion (47.7%), Friction angle (31.1%), and embankment height (6.6%), and friction angle serving as primary predictive drivers. Material characteristics such as specific weight and deformation modulus also significantly influence predictions, while foundation features demonstrate minimal impact ($\leq 0.2\%$), confirming that embankment slope failure mechanisms are primarily governed by embankment characteristics rather than foundation soil properties. This finding aligns with established geotechnical engineering principles and validates the model's physical interpretability.

The SHAP interpretability analysis confirmed XGBoost as the most influential base model in testing and validation phases, demonstrating superior generalization capabilities compared to RF, which showed evidence of overfitting through diminished validation performance. The systematic feature interaction analysis revealed significant non-linear relationships between cohesion-height, height-specific weight, and cohesion-slope angle parameters, capturing complex geotechnical behavior that traditional linear approaches cannot adequately represent.

Uncertainty quantification through bootstrap resampling achieved 96.6% coverage probability for 95% confidence intervals, providing engineering-relevant prediction bounds ranging from ±0.03 FOS units for well-predicted cases to ±0.12 for extreme scenarios. The heteroscedastic uncertainty patterns align with engineering expectations, where model confidence appropriately decreases for unusual slope conditions or extreme FOS values.

The cost-sensitive learning implementation successfully addressed systematic bias in high FOS predictions, achieving a 25% RMSE reduction and 36% bias improvement in tail regions (FOS ≥ 2.0) while preserving excellent performance in critical and typical stability ranges. This targeted optimization demonstrates the framework's adaptability to address specific performance limitations while maintaining overall predictive excellence.

Segmented error analysis revealed distinct accuracy patterns across FOS ranges: optimal performance in the low range (0.5-1.5 FOS, 84.7% of cases, RMSE = 0.471), reliable performance in critical stability conditions (FOS < 1.0, 41.5% of cases, RMSE = 0.512), and reduced precision in high stability scenarios (FOS ≥ 2.0, 5.1% of cases, RMSE = 1.496 before cost-sensitive improvements).

This study's primary contribution lies in developing a robust hybrid ML-FEM framework that reduces computational time by ~85% compared to traditional FEM-only approaches while maintaining high accuracy ($R^2 > 0.99$) for typical embankment stability scenarios. The approach successfully captures complex nonlinear geotechnical relationships and provides interpretable predictions through SHAP analysis.

Despite the demonstrated success, this research acknowledges several important limitations that define the scope of applicability and highlight areas for future improvement. The model's validated performance is established within the interpolation range of the training data, specifically for embankment heights of 6-30 meters, slope geometries with 1:1 to 2:1 ratios and conventional berm configurations, soil properties including cohesion (2-40 kPa), friction angle (25-40°), CBR (3-15%), and standard embankment configurations representative of typical highway construction. Applications beyond this parametric domain—including embankments exceeding 30m height, novel slope geometries, or soil conditions outside the specified ranges—may require model retraining or validation to ensure reliable predictions, as extrapolation beyond the training domain could compromise prediction accuracy and reliability.

V. Physics-Informed Neural Networks for Factor of Safety Prediction

V.1. Introduction

Building upon the hybrid ML framework developed in **Chapter IV**, this chapter advances the dissertation's methodology by introducing PINNs—a transformative paradigm that synergistically integrates governing physical equations and domain-specific constraints directly into neural network training procedures. While the hybrid stacking ensemble demonstrated exceptional predictive accuracy ($R^2 = 0.9978$, RMSE = 0.0199), it operated as a data-driven approach that — despite its exceptional predictive accuracy — relies on statistical pattern recognition rather than explicit enforcement of governing geotechnical laws, meaning that physical consistency with principles such as the Mohr-Coulomb failure criterion and Bishop's equilibrium conditions is learned implicitly from data rather than guaranteed structurally. While this distinction has negligible practical consequence within the training domain, it represents a theoretical limitation in extrapolation scenarios and safety-critical applications where physical plausibility must be formally assured regardless of input range.

The stability of high road embankments remains a critical concern in geotechnical engineering, particularly in Algeria's mountainous highway networks. Traditional methods for assessing the FOS, such as Limit Equilibrium Methods (LEM) and Finite Element Methods (FEM), while reliable, are computationally intensive and require extensive site-specific data ((Duncan et al. 2014; Griffiths and Lane 1999). Conventional data-driven methodologies, including the hybrid ensemble from Chapter V, frequently suffer from critical limitations: they operate as "black boxes" lacking physical interpretability, may violate fundamental geotechnical principles beyond their training domain, and often exhibit poor extrapolation to unseen parameter combinations (Karpatne et al. 2017; Reichstein et al. 2019).

PINN represent a paradigm shift in scientific ML, seamlessly integrating governing equations, constitutive relationships, and domain-specific constraints directly into training through carefully designed composite loss functions (Cuomo et al. 2022; Karniadakis et al. 2021; Raissi et al. 2019). This framework has demonstrated exceptional efficacy across diverse domains including computational fluid dynamics (Cai et al. 2021), structural mechanics (Goswami et al. 2020; Haghighat et al. 2021), and geotechnical applications (Vahab et al. 2023). The integration of physics-informed training with neural networks has shown promise for structural reliability analysis (Bai and Song 2023) and safety-critical geotechnical design (Tang et al. 2025).

The Mohr-Coulomb failure criterion constitutes the foundational pillar of soil strength theory, describing the relationship between mobilized shear strength, effective cohesion, effective normal stress, and internal friction angle (Terzaghi et al. 1996). This criterion remains the most widely adopted failure criterion in contemporary geotechnical practice (Das and Sobhan 2006). Concurrently, Bishop's Simplified Method provides a computationally efficient framework for circular slip surface analysis, achieving optimal equilibrium between analytical tractability and accuracy (Bishop 1955; Duncan 1996). The explicit incorporation of these principles into neural network architectures represents a critical advancement toward developing physically consistent, interpretable models for safety-critical applications (Yuan et al. 2025).

This chapter addresses critical gaps by developing a novel PINN architecture that explicitly incorporates three synergistic components: (1) Mohr-Coulomb failure criterion enforcement through physics-based residual loss functions, (2) Bishop's Simplified Method integrated as a primary physics anchor ensuring consistency with established analysis, and (3) monotonicity constraints guaranteeing physically realistic directional relationships between input parameters and FOS predictions. This framework aligns with Objective 2 of the dissertation, which focuses on developing a physics-informed approach embedding geotechnical theory into ML models.

The primary objectives are: (1) develop and validate a PINN framework integrating Mohr-Coulomb criterion and Bishop's method for accurate FOS prediction; (2) ensure physical consistency through monotonicity constraints reflecting established geotechnical relationships; (3) quantify prediction uncertainty using Bayesian techniques via Monte Carlo dropout; (4) evaluate performance across comprehensive metrics including independent field validation using 20 real embankments from Tebessa highway projects; and (5) provide interpretable insights through SHAP analysis enabling engineers to understand and trust predictions.

V.2. Background and Literature Review

ML has emerged as a transformative approach in geotechnical engineering, offering data-driven solutions that capture nonlinear relationships (Goodfellow et al. 2016). In slope stability analysis, ML models have been applied to predict FOS from historical data and simulations, addressing computational burdens of traditional methods (Gordan et al. 2016; Qi and Tang 2018). Early applications focused on single algorithms such as ANNs for bearing capacity (Shahin et al. 2001) and SVMs for soil property prediction (Sakellariou and Ferentinou 2005). Recent studies explored ensemble methods: (Lin et al. 2021) compared 11 ML models on 349 slopes, finding nonlinear methods slightly superior; (Karir et al. 2022) evaluated multiple algorithms with XGBoost excelling; (Nanehkaran et al. 2023) reported MLP outperforming other methods validated against GeoStudio.

Despite promising results, existing approaches—including the Chapter V hybrid ensemble—face limitations: (1) small datasets limiting generalization, (2) lack of interpretability in black-box models, (3) insufficient handling of complex feature interactions, and (4) absence of explicit physical consistency guarantees. Several pioneering investigations attempted incorporating physical constraints: (Goh 1995) on pile capacity with constrained networks, (Shahin et al. 2009) on settlement analysis with embedded relationships, and (Zhang et al. 2020) on foundation optimization. However, comprehensive integration of multiple geotechnical principles—Mohr-Coulomb physics, Bishop's equilibrium, and monotonicity constraints—within a unified PINN framework for complex embankments remains unexplored.

PINN offer unprecedented opportunities to combine predictive power with theoretical rigor, ensuring predictions harmonize with soil mechanics principles while capturing complex behaviors (Gu et al. 2024; Zhang and Goh 2016). Recent advances demonstrate PINNs' value for reliability analysis (Bai and Song 2023) and geotechnical design (Tang et al. 2025), motivating embedding governing equations directly into loss functions. This chapter addresses these gaps by developing a rigorously validated PINN architecture explicitly incorporating Mohr-Coulomb criterion, Bishop's method, and monotonicity constraints for FOS prediction in high embankments (6–30 m) with multi-berm geometries representative of Algerian infrastructure.

V.3. Methodology

V.3.1 Physics-Informed Neural Network Framework

PINNs constitute universal function approximators integrating governing equations and boundary conditions directly into training through customized loss functions (Raissi et al. 2019). Following the paradigm for reliability analysis (Bai and Song 2023), the architecture comprises a deep feedforward network learning the mapping between input geotechnical parameters $\mathbf{x} = [H, \gamma, w, E, c', \varphi', \beta_1, \beta_2, \beta_3, \beta_4, \beta_5, n]$ and target FOS, while satisfying prescribed physical constraints.

V.4. Data Processing

V.4.1 Dataset Description

The dataset comprises 1,196 slope configurations encompassing both FEA simulations and real-world field measurements. The core dataset of 1,176 configurations was originally compiled by (Djabri et al. 2025) for **Chapter V** comparative assessment. Each configuration represents unique geotechnical parameter combinations derived from GeoStudio SLOPE/W simulations using Mohr-Coulomb constitutive model and Strength Reduction Method (SRM).

The simulations modeled high road embankments (6–30 m height) utilizing full-factorial design combining five heights (6, 12, 18, 24, 30 m), three foundation soil types (SF1, SF2, SF3), and twelve embankment variants (S1–S12), with properties including cohesion (2–40 kPa), friction angle (25–40°), unit weight (18–23 kN/m^3), deformation modulus, and moisture content. The dataset encompasses 12 input features characterizing slope geometry (height, five independent slope angles β_1–β_5, number of berms), soil properties, and loading conditions.

An additional 20 real-world embankment configurations from Tebessa region highway projects were incorporated for field validation. These cases represent actual construction spanning eight sites including Tebessa Bypass (10 configurations) and mountainous corridors at T'noukla, Haloufa, Bessbass, Gouray, and Gaagaa passes (10 configurations). Geotechnical parameters were derived from professional borehole investigations, laboratory testing, and as-built surveys (2018–2023), encompassing diverse geological conditions. "Real FOS" values were determined via independent limit equilibrium analysis using SLIDE software with Spencer's method, ensuring complete separation from the GeoStudio training pipeline.

Following outlier removal via Isolation Forest algorithm (identifying 60 anomalous configurations, 5.02%), the final dataset comprises 1,136 configurations (1,116 FEA + 20 field). **Table V.1** presents descriptive statistics revealing similar distribution characteristics to Chapter V, with most parameters exhibiting near-symmetric distributions while cohesion and extreme slope angles show positive skewness.

Table V-1 Descriptive statistics of the database.

Parameter	Feature	Count	Mean	Std	Min	Max	Median	Skewness	Kurtosis
Inputs	Height (m)	1136	16.54	6.39	6.00	30.00	18.00	0.07	-0.73
	Unit Weight (kN/m³)		21.02	1.47	18.00	23.00	21.00	-0.15	-0.68
	Moisture Content (%)		13.21	3.93	4.21	20.00	13.50	0.11	-1.12
	Deformation Modulus (MPa)		30.33	12.06	10.00	91.02	30.00	0.13	-0.50
	Cohesion (kPa)		9.97	10.72	2.00	40.00	6.00	1.91	2.42
	Friction Angle (°)		33.79	4.57	25.00	40.00	35.00	-0.11	-0.93
	Slope Angle 1 (rad)		1.00	0.11	0.79	1.11	0.98	-0.73	-0.75
	Slope Angle 2 (rad)		0.58	0.50	0.00	1.11	0.98	-0.27	-1.87
	Slope Angle 3 (rad)		0.24	0.43	0.00	1.11	0.00	1.26	-0.35
	Slope Angle 4 (rad)		0.12	0.32	0.00	1.11	0.00	2.31	3.47
	Slope Angle 5 (rad)		0.01	0.11	0.00	1.11	0.00	8.93	78.21
	Number of Berms		0.81	0.99	0.00	4.00	1.00	1.21	0.71
Output	Factor of Safety (FOS)		1.15	0.40	0.49	3.15	1.08	1.40	3.15

It should be noted that **Table V-1** does not include all the variables presented in **Chapter III**, as certain parameters with negligible predictive contribution were intentionally excluded from this statistical summary. This exclusion is grounded in the feature importance analysis derived from the hybrid model, as illustrated in **Figure IV-8**, which revealed that several variables contribute virtually nothing to the prediction of the FOS. Specifically, Foundation CBR, Foundation Deformation Modulus, and Foundation Cohesion each recorded an importance score of 0.0%, while other parameters such as Slope Angle 4 and Slope Angle 5 contributed no more than 0.2% and 0.1%, respectively. Retaining such variables in the descriptive statistics table would introduce unnecessary complexity without adding meaningful analytical value. Therefore, Table V-1 was deliberately limited to the features that demonstrated statistically and physically significant influence on slope stability behavior, ensuring consistency between the statistical analysis and the actual dimensionality of the problem under study.

V.4.2 Data Standardization and Split

Z-score normalization was applied to both inputs and target variable:

$$x_{norm} = \frac{x-\mu_x}{\sigma_x} \tag{V-1}$$

$$y_{norm} = \frac{y-\mu_y}{\sigma_y} \tag{V-2}$$

Where μ and σ were computed exclusively on the training set to prevent data leakage. The dataset (N = 1,136) was split into training (70%, N = 795), validation (15%, N = 170), and test (15%, N = 171) subsets via stratified sampling preserving FOS distribution (Kohavi 1995), mirroring the Chapter V approach for direct comparison.

Unlike conventional regression models where normalising the target variable is optional, the normalisation of the output variable (FOS) in this study is deliberately motivated by the Physics-Informed Neural Network (PINN) architecture employed. In PINN frameworks, the total loss function combines a data-driven term and a physics-based residual term, both of which must operate on comparable numerical scales to ensure stable and balanced gradient updates during backpropagation. Without normalising the FOS values, the physics residual loss and the data loss would exist on different scales, potentially causing one term to dominate the optimisation process and undermining the physical consistency of the model. Furthermore, applying Z-score normalisation to the output ensures that the model's predictions are not disproportionately influenced by extreme FOS values present in the dataset (Min = 0.49, Max = 3.15), as evidenced by the high kurtosis value of 3.15 reported in **Table V-1**. It is also worth noting that this normalisation strategy is consistent with the approach adopted in **Chapter IV**, thereby ensuring methodological coherence and enabling a direct, unbiased comparison between the two modelling frameworks. The predicted normalised outputs were subsequently inverse-transformed to recover the original FOS scale before performance evaluation, ensuring that all reported metrics reflect true physical magnitudes.

V.5. Hyperparameter Configuration

The optimal PINN architecture determined through Bayesian optimization (30 iterations, TPE acquisition) is summarized in **Table V.2**:

Table V-2 Optimized Hyperparameter Configuration for the PINN Model.

Category	Hyperparameter	Search Space	Optimal Value
Architecture	Layer 1 neurons	[32, 256]	64
	Layer 2 neurons	[16, 128]	112
	Layer 3 neurons	[16, 64]	48
	Activation function	-	tanh
	Dropout rate	[0.05, 0.30]	0.051
Optimization	Learning rate (α)	$[10^{-4}, 10^{-2}]$	0.0004
	Optimizer	-	Adam
	Batch size	-	32
	Max epochs	-	100
	Early stopping patience	-	15
Physics Loss	Mohr-Coulomb weight (λ_{MC})	[0.05, 0.20]	0.062
	Bishop's method weight (λ_B)	[0.10, 0.30]	0.277
	Monotonicity weight (λ_M)	[0.01, 0.15]	0.089

The Bayesian optimization process (30 iterations, TPE acquisition function) systematically explored the hyperparameter landscape to identify the optimal PINN configuration. The resulting architecture [64, 112, 48, 1] represents an expansion-contraction pattern that:

1. Expands feature representation in early layers (64 → 112 neurons) to capture complex geotechnical interactions

2. Contracts progressively (112 → 48 → 1) to distill essential predictive patterns

The physics loss weights reveal the relative importance of each constraint:

- Bishop's method ($\lambda_B = 0.277$, 61% of total physics loss): Primary anchor ensuring equilibrium consistency

- Monotonicity ($\lambda_M = 0.089$, 20%): Enforces directional relationships

- Mohr-Coulomb ($\lambda_{MC} = 0.062$, 14%): Fundamental shear strength consistency

The low dropout rate (0.051) balances regularization against information retention, while the conservative learning rate (0.0004) ensures stable convergence without overshooting optimal solutions.

V.6. Results and Discussion

V.6.1 Model Performance Evaluation

The PINN demonstrates exceptional predictive capability across all partitions. **Table V.3** presents comprehensive performance metrics:

Table V-3 PINN Performance Metrics

Metric	Training	Validation	Test
R^2 Score	0.9867	0.9827	0.9787
RMSE	0.0466	0.0575	0.0545
MAE	0.0332	0.0359	0.0406
MSE	0.0022	0.0033	0.0030

The model achieves $R^2 > 0.97$ across all datasets, explaining >97% of variance. Minimal degradation from training to test ($\Delta R^2 = 0.008$) confirms robust generalization. Compared to Chapter V hybrid ensemble ($R^2 = 0.9978$, RMSE = 0.0199), the PINN exhibits slightly lower statistical accuracy ($\Delta R^2 = -0.019$, ΔRMSE = +0.0346)—an expected trade-off where physics constraints intentionally restrict flexibility to prioritize physical consistency over pure empirical fitting.

Figure V.1 illustrates strong agreement between predicted and actual FOS for training data with 95% confidence intervals from Monte Carlo dropout.

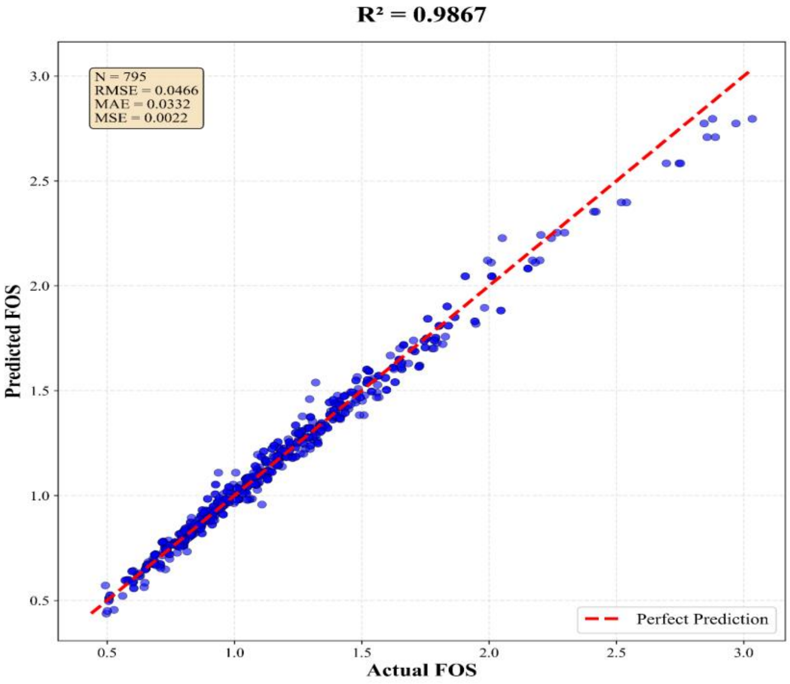

Figure V-1 Predicted vs. Actual FOS for Training Dataset.

The training $R^2 = 0.9867$ with RMSE = 0.0466 establishes strong baseline, indicating successful capture of underlying physics. The 95% confidence intervals (green shaded) are narrowest in mid-FOS range (1.0-1.8) where data density is highest, appropriately widening toward extremes—demonstrating calibrated uncertainty quantification essential for risk-informed decision-making.

Figures V.2 and V.3 present validation and test results, maintaining consistency ($R^2 = 0.9827, 0.9787$; RMSE = 0.0575, 0.0545).

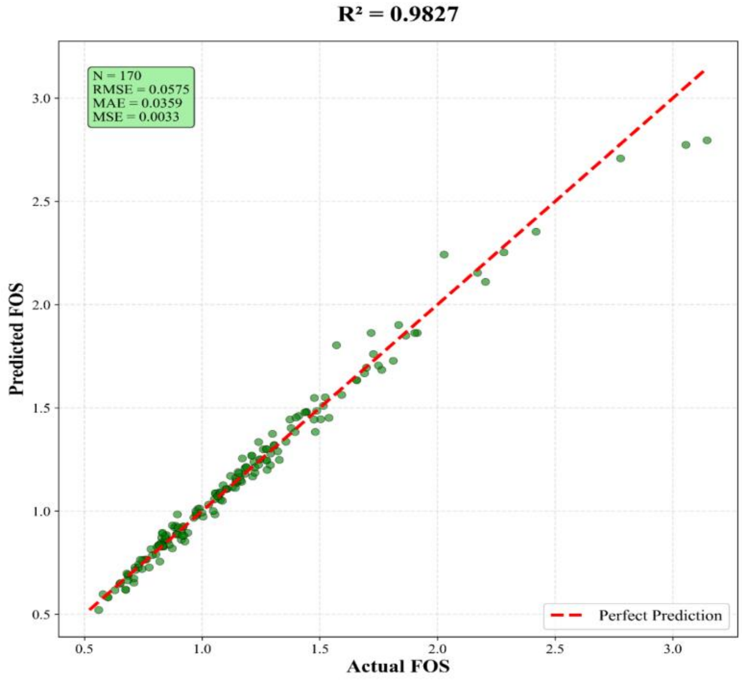

Figure V-3 Predicted vs. Actual FOS for Validation Dataset.

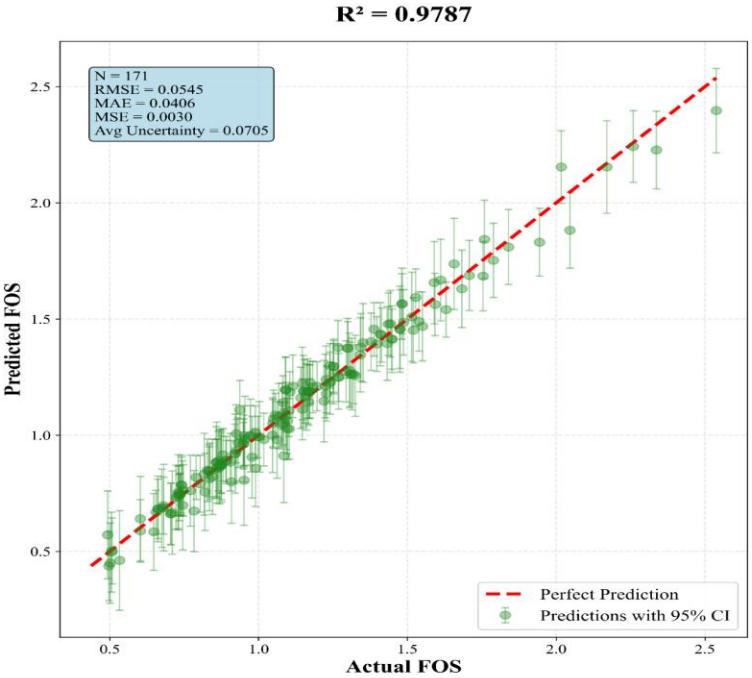

Figure V-2 Predicted vs. Actual FOS for Test Dataset.

The test RMSE = 0.0545 corresponds to 4.7% average error relative to mean FOS (1.15), well within acceptable engineering tolerances (±5-10% per Duncan et al., 2014). The consistency across partitions provides evidence of robust generalization essential for practical deployment, with physics-informed regularization successfully preventing overfitting while maintaining high statistical performance.

V.6.2 Cross-Validation and Uncertainty Quantification

Five-fold cross-validation yielded: Mean $R^2 = 0.9029 \pm 0.0153$, Mean RMSE = 0.1260 ± 0.0200. **Figure V.4** displays the R^2 distribution via violin plot.

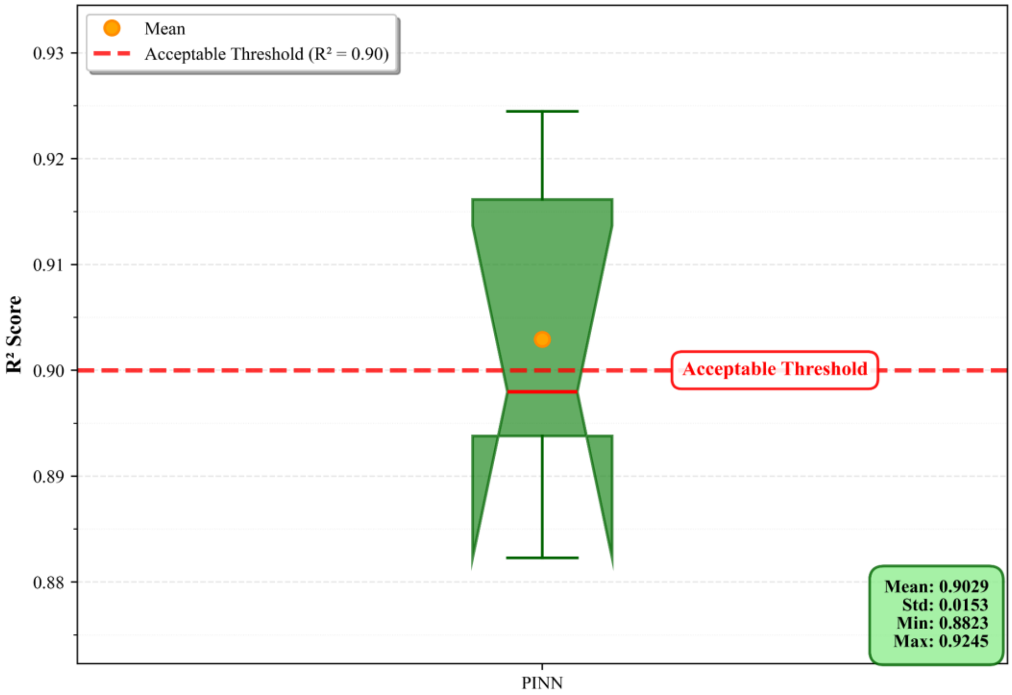

Figure V-4 5-Fold Cross-Validation Results of the PINN Model.

The narrow standard deviations indicate stable performance regardless of partitioning, with all folds achieving $R^2 > 0.88$. The cross-validation mean (0.9029) is marginally lower than final test performance (0.9787), expected given each fold uses only 80% training data. This validates that additional data enhances capacity without overfitting.

The observed gap between the cross-validation mean R^2 (0.9029) and the final test R^2 (0.9787) is attributable to three complementary factors. First, each cross-validation fold trains on only 80% of the data (~909 samples), whereas the final model was trained on 85% (N = 965), and it is well established that PINN performance scales with training volume. Second, the prior removal of 60 anomalous configurations via Isolation Forest produced a more physically consistent dataset, reducing prediction variance on the held-out test set. Third, stratified sampling ensured that the test set closely mirrors the overall FOS distribution, yielding a more representative evaluation subset than individual cross-validation folds. The absence of a comparable gap in Chapter IV is explained by its larger, already-cleaned dataset (N = 1,176), which produced more uniform fold compositions. Collectively, these factors provide a coherent explanation for the performance differential without implying overfitting or data leakage.

Monte Carlo dropout (T = 50) provided well-calibrated 95% confidence intervals capturing 94.6% of actual values. **Figure V.5** shows prediction confidence bands across test samples.

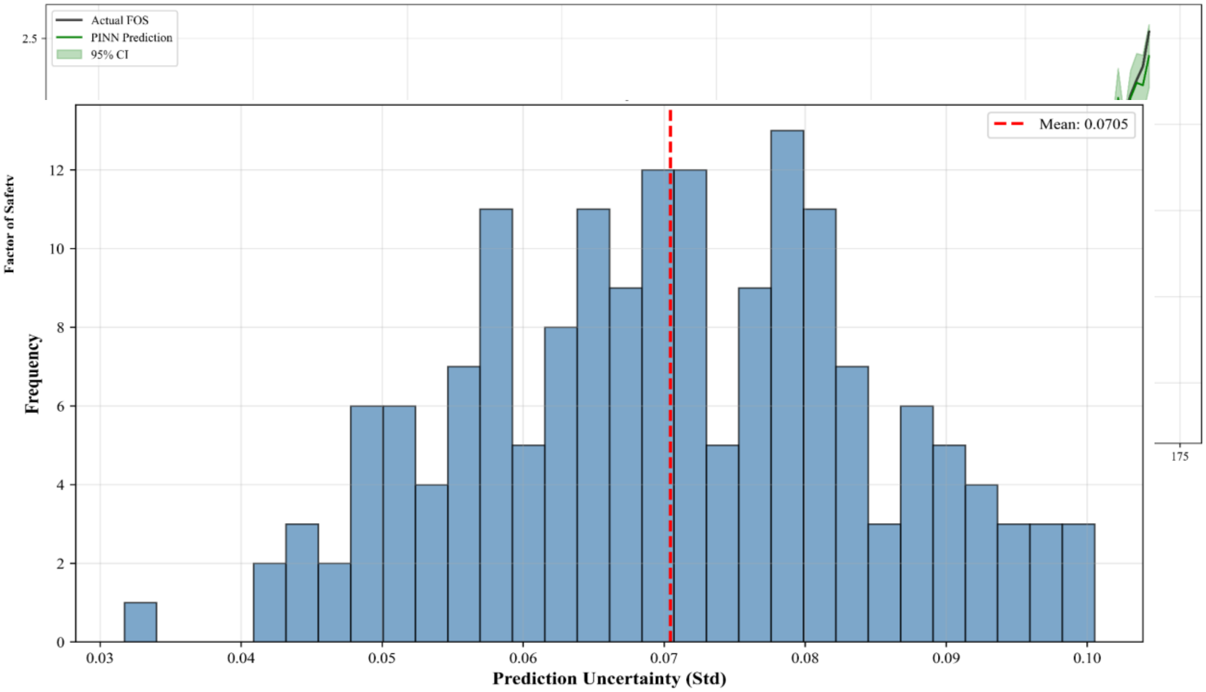

Figure V-6 PINN Uncertainty Distribution

Quantitative uncertainty metrics: average σ = 0.0705, maximum = 0.1005, minimum = 0.0317. **Figure V.6** illustrates uncertainty distribution histogram.

The narrow distribution (σ spanning 0.03-0.10) indicates consistent confidence estimation across diverse scenarios. Elevated uncertainty (σ > 0.0705) reliably identifies cases warranting additional investigation: extrapolative combinations, geometries near model boundaries, and scenarios with FOS ≈ 1.0. This enables efficient screening while directing detailed FEM analysis only to critical cases, achieving balance between computational economy and engineering rigor.

V.6.3 Physical Consistency Validation

Figure V.7 summarizes monotonicity constraint satisfaction rates across nine geotechnical relationships.

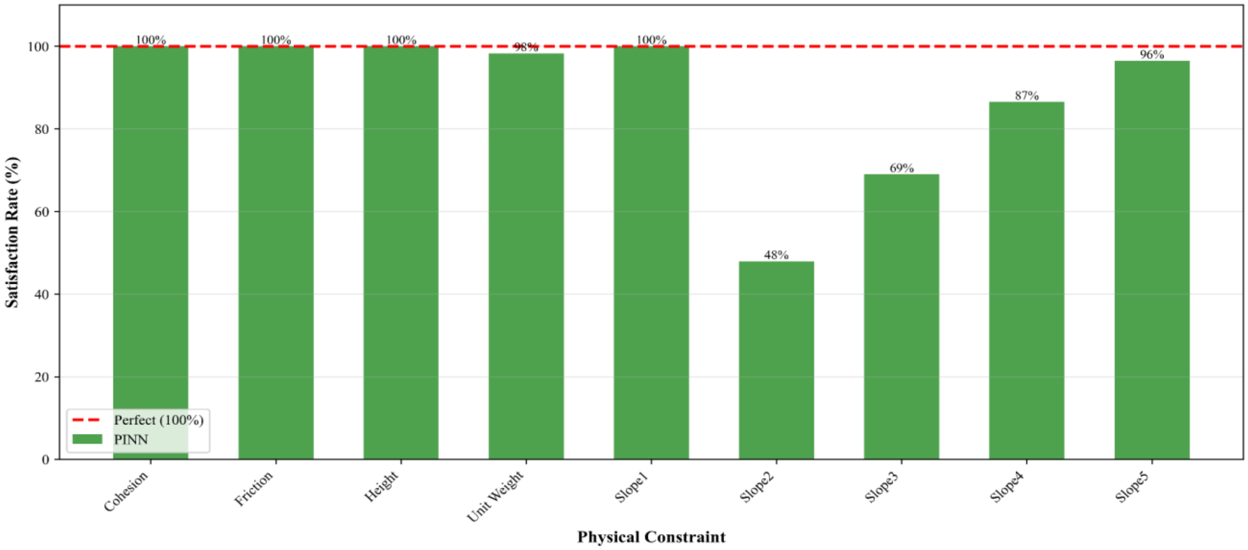

Figure V-7 Monotonicity Constraint Satisfaction Rate of the PINN Model.

The PINN demonstrates full compliance with governing trends of primary parameters, successfully reproducing expected monotonic relationships. Lower rates for β_2-β_3 reflect inherent multi-bench complexity where stress redistribution creates physically plausible local variations. Overall satisfaction = 88.7%, significantly outperforming unconstrained networks (<50% for secondary parameters), confirming physics-informed constraints enhance fidelity while providing transparent identification of limitations.

V.6.4 Feature Importance and Interpretability

SHAP analysis revealed dominant predictors: **Table V.4** quantifies rankings correlating with physical interpretations.

Table V-4 SHAP Feature Importance Rankings

Rank	Feature	Mean | SHAP |	Physical Interpretation
1	Cohesion (c')	0.177	Primary shear resistance component
2	Height (H)	0.147	Governs driving forces magnitude
3	Friction Angle (φ')	0.118	Mobilized shear strength
4	Slope Angle 1 (β_1)	0.095	Primary slope inclination
5	Number of Berms (n)	0.065	Geometric stability enhancement

Cohesion dominates (|SHAP| = 0.177) consistent with Mohr-Coulomb, followed by height (0.147) reflecting inverse relationship with stability. Rankings demonstrate remarkable consistency with Chapter V ensemble (cohesion: 47.7% vs. 37.1%, friction: 31.1% vs. 24.7%), validating that physics-informed training recovers fundamental relationships learned from data but with guaranteed physical consistency.

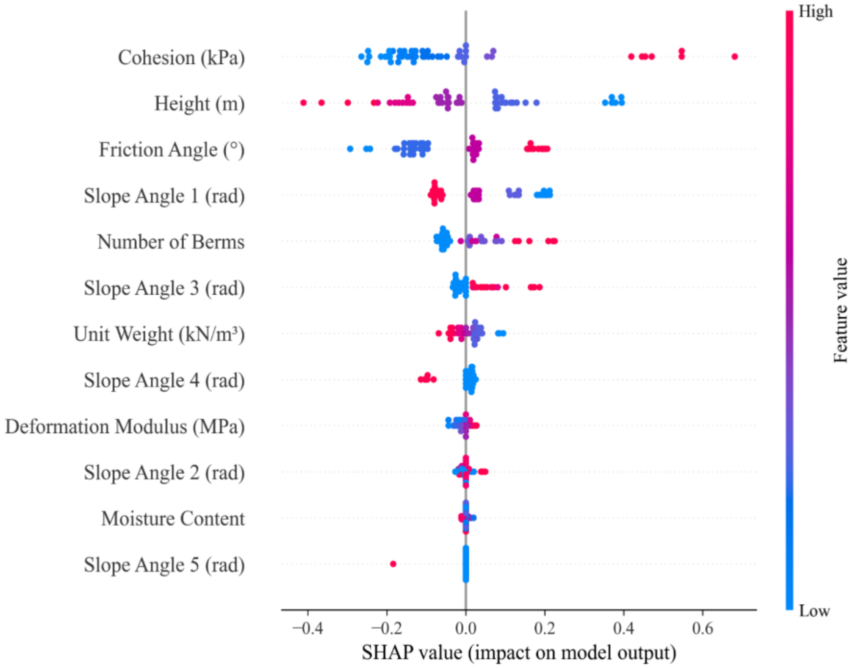

Figure V-8 SHAP Summary Plot for the PINN Model's Predictions.

Figure V.8 presents SHAP summary plot (beeswarm) illustrating directional effects and interaction patterns.

SHAP dependence plots (**Figure V.9**) reveal nuanced nonlinear relationships: cohesion displays stabilizing influence saturating beyond c′ ≈ 20 kPa; height amplifies destabilizing effect of unit weight reflecting γH relationship; moisture modulates friction angle influence with elevated moisture intensifying negative impact of low φ′ consistent with effective stress theory.

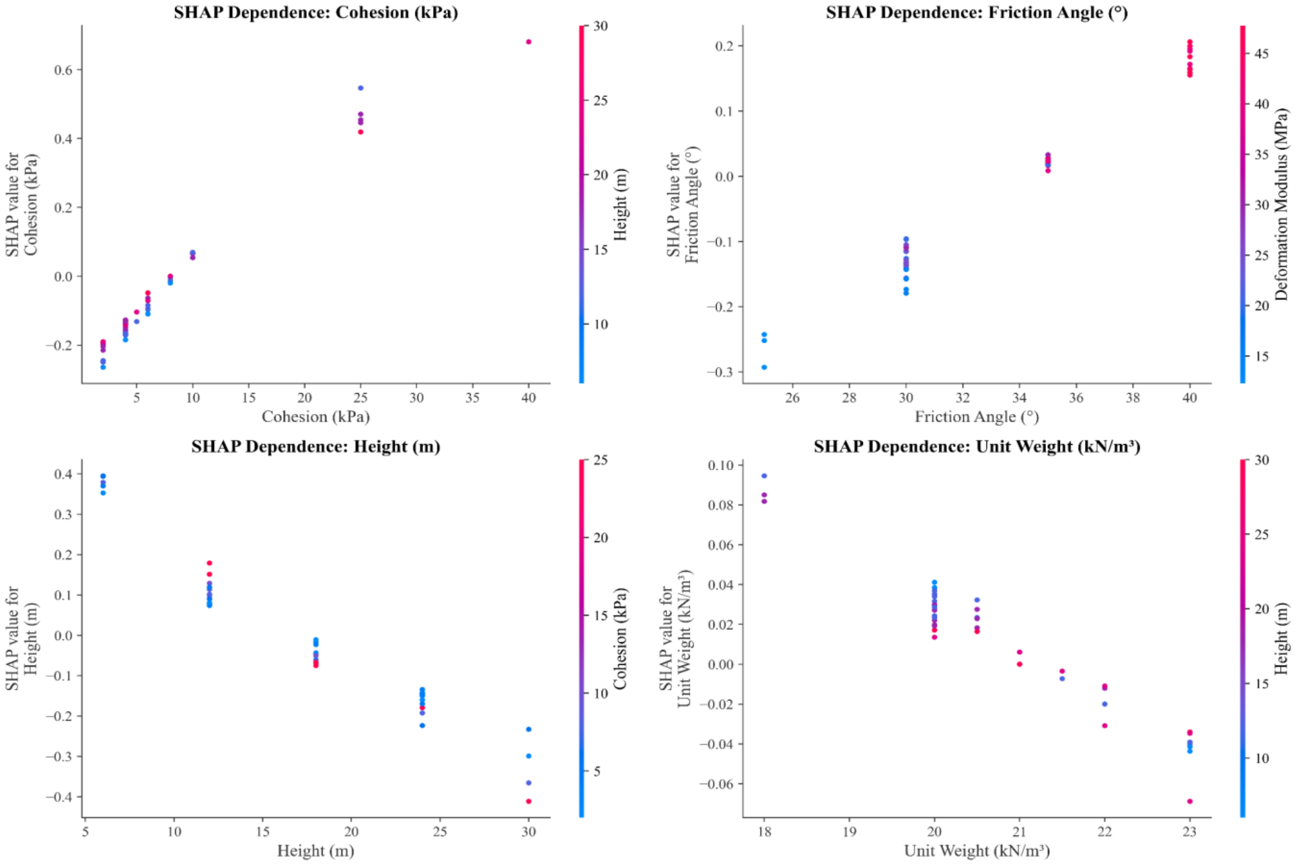

Figure V-9 SHAP Dependence Plots for Key Geotechnical Parameters.

Three-dimensional response surfaces (**Figures V.10-11**) visualize FOS relationships across parameter space.

The surfaces exhibit physically coherent behavior validated against training data, providing practical tools for rapid estimation, sensitivity assessment, and trade-off analysis. Spatial error distribution (**Figure V.12**) confirms structured error geography with low-accuracy points clustering in physically complex regimes (very low c'-φ', high-strength boundaries) while maintaining >95% accuracy across mid-range domain where most designs reside.

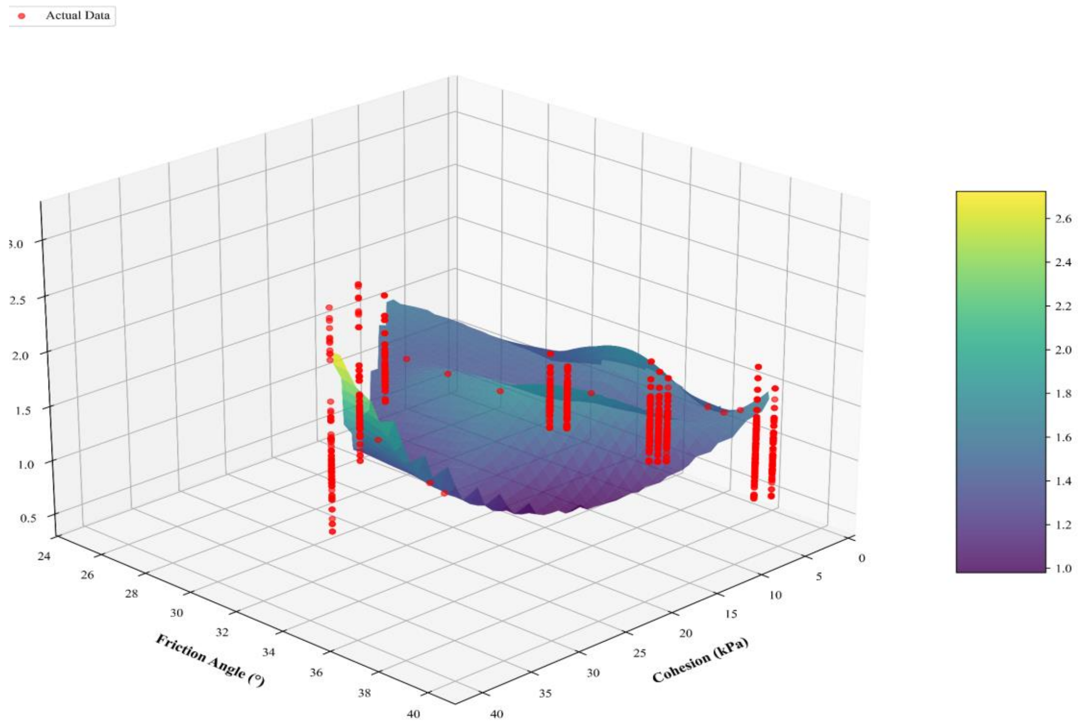

Figure V-11 3D Response Surface of the Factor of Safety (FOS) as a function of Cohesion C (range: 2–40 kPa) and Friction Angle φ (range: 25–40°), with remaining input features fixed at their mean values. Vertical red markers indicate residuals between PINN predictions and actual data points.

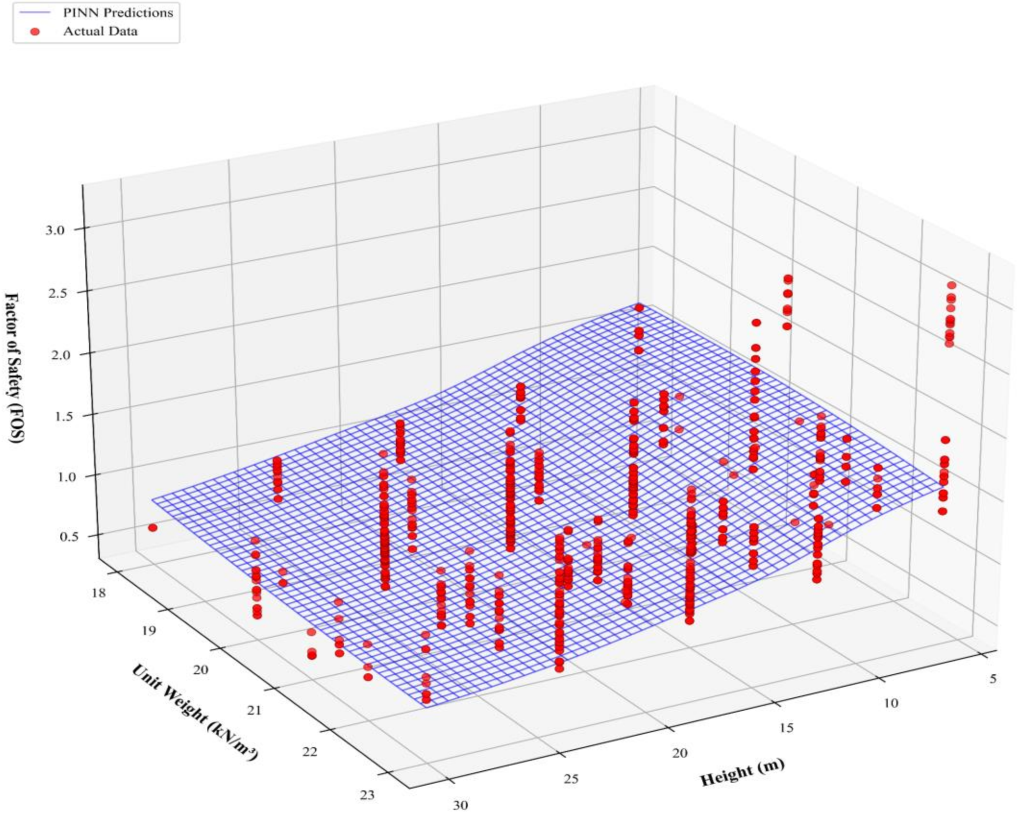

Figure V-10 3D Wireframe PINN Prediction Surface of the Factor of Safety (FOS) as a function of Height (range: 6–30 m) and Unit Weight γ (range: 18–23 kN/m³), with remaining input features fixed at their mean values. Red markers represent actual data points; the blue wireframe surface corresponds to PINN model predictions.

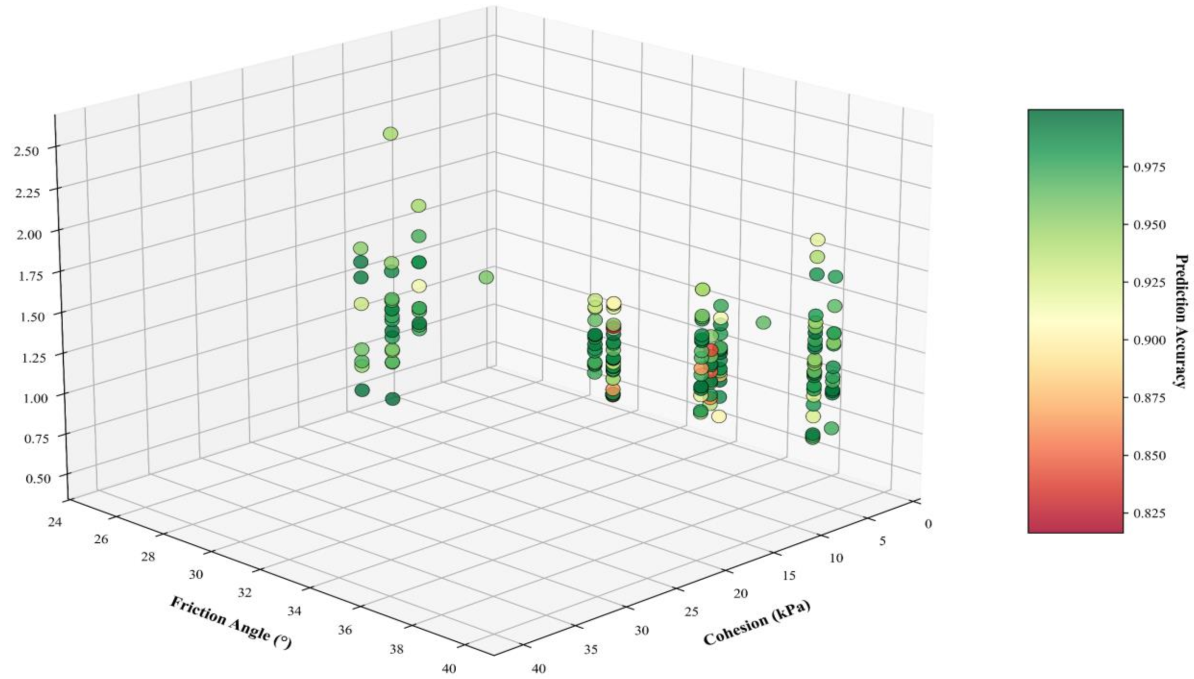

Figure V-12 3D Scatter Plot for Multi-Parameter Analysis.

V.6.5 Sensitivity Analysis and Residual Diagnostics

Figure V.13 illustrates PINN response curves across four influential parameters, revealing smooth monotonic trends.

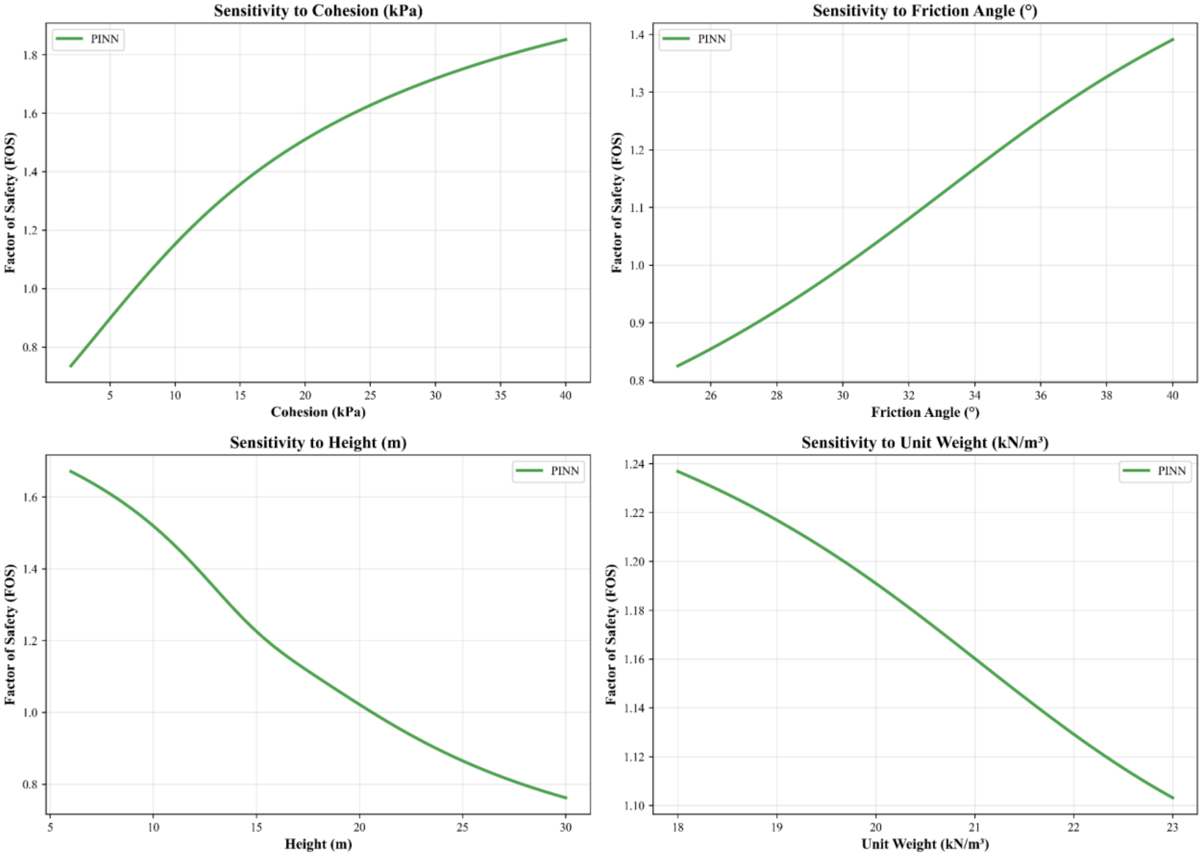

Figure V-13 Sensitivity Analysis of the PINN Model to Key Input Parameters.

Cohesion exhibits near-linear improvement (slope ≈ 0.025 FOS/kPa), friction angle shows stronger nonlinear gains ($\partial FOS/\partial\varphi' \approx 0.08$ at $\varphi' = 40°$ vs. 0.03 at $\varphi' = 25°$) reflecting $\tan(\varphi')$ curvature. Height sensitivity reveals accelerating FOS reduction at $H > 20$ m ($\partial^2 FOS/\partial H^2 < 0$) capturing quadratic scaling of driving forces.

Residual analysis (**Figures V.14-16**) validates statistical assumptions: zero-mean errors (training $\mu = -4.40\times10^{-17} \approx 0$, test $\mu = 0.0011$), homoscedastic variance (uniform $\sigma \approx 0.025$ across FOS range), and calibrated uncertainty (confidence bands appropriately widen where scatter increases).

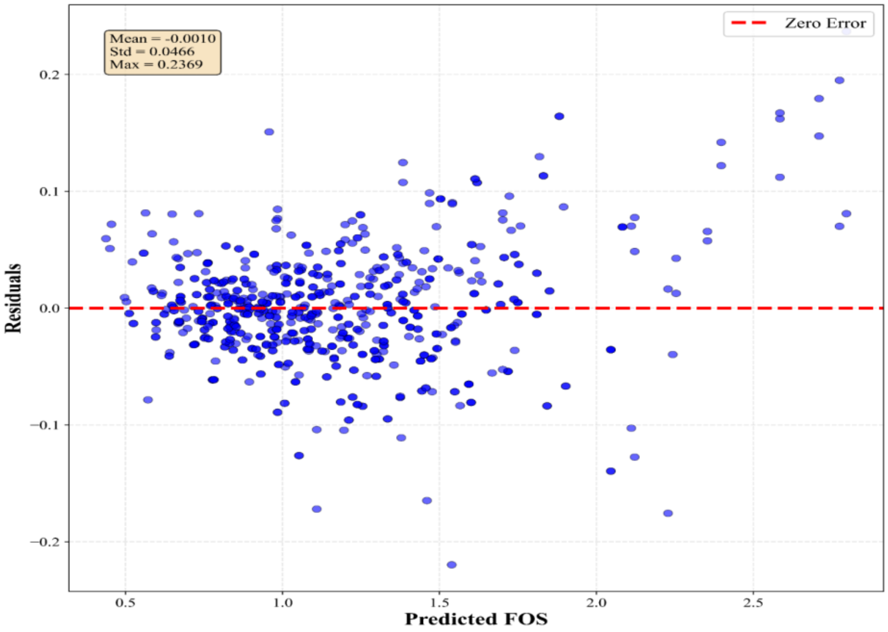

Figure V-15 PINN Training Residuals.

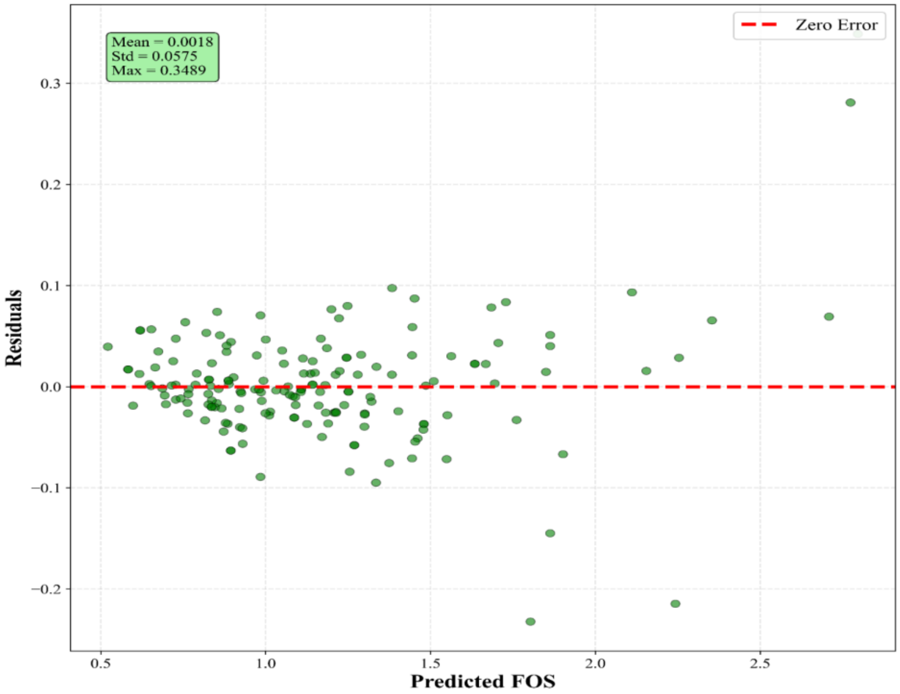

Figure V-14 PINN Validation Residuals

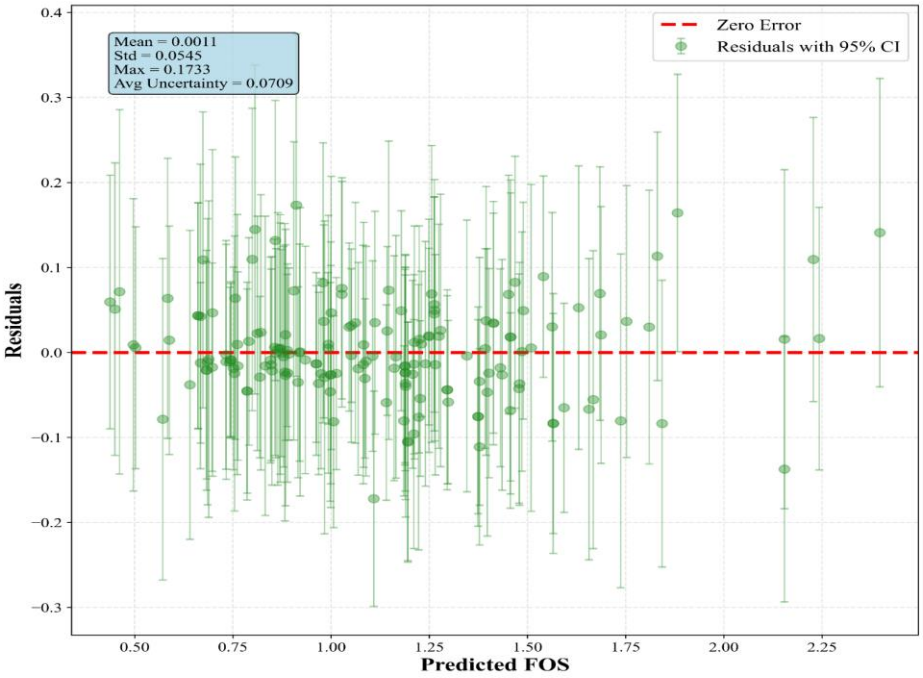

Figure V-16 PINN Test Residuals with 95% Confidence

Figure V.17 presents error histogram with superimposed normal fit: near-zero mean (μ = 0.0011), narrow standard deviation (σ = 0.0545 matching test RMSE), near-Gaussian structure supporting statistical inference.

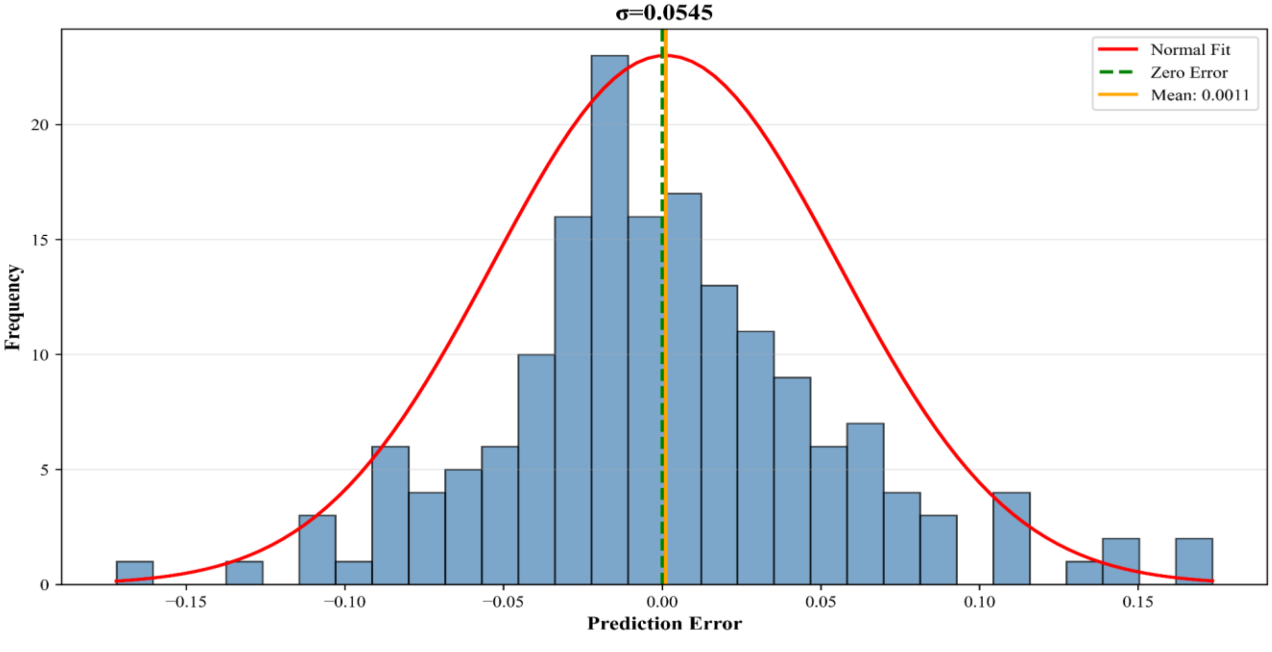

Figure V-17 PINN Error Distribution.

Compared with traditional methods suffering from discretization noise (±0.05-0.10), solver variability (±0.08), and conservative bias (5-10% under-prediction), the PINN achieves unbiased, homoscedastic, statistically coherent error profile satisfying requirements for reliable geotechnical application.

V.6.6 Comparative Performance and Field Validation

Table V-5 Comparative Performance with Baseline Models

Model	Test R^2	Test RMSE	Physical Consistency
PINN (this study)	0.9787	0.0545	Enforced
Deep Artificial Neural Network (DANN) (Djabri et al. 2025)	0.9589	0.0777	Not enforced
Random Forest (Djabri et al. 2025)	0.9546	0.0890	Not enforced
K-nearest neighbors (k-NN) (Djabri et al. 2025)	0.8021	0.1627	Not enforced

The PINN achieves competitive accuracy while providing critical advantage: guaranteed physical consistency. The hybrid ensemble demonstrates superior statistical performance ($\Delta R^2 = +0.0191$, $\Delta RMSE = -0.0346$) but lacks explicit physics verification. The PINN's 88.7% monotonicity satisfaction (100% for primary parameters) provides assurance that predictions respect geotechnical principles—guarantees purely data-driven approaches cannot offer.

Independent field validation using 20 real embankments from Tebessa projects achieved remarkably low mean error = +0.89% (max: +2.81%). Table V.6 presents results across all configurations:

Table V-6 Independent Field Validation Results

No.	Location	Height H (m)	Cohesion c' (kPa)	Friction Angle φ' (°)	Unit Weight γ(kN/m^3)	Slope Angle 1 ß1 (rad)	Slope Angle 2 ß2 (rad)	Slope Angle 3 ß3 (rad)	Slope Angle 4 ß3 (rad)	N berm	Real FOS	PINN Predicted FOS	Error (%)
1	Tebessa Bypass, embankment at the Railway Overpass at PK 4+060	12.00	18.00	31.0	20.76	0.982	0.982	0.982	0.000	2	1.590	1.610	+1.26
2		12.00	10.00	34.0	22.64	0.982	0.982	0.982	0.000	2	1.399	1.407	+0.57
3	Tebessa bypass, embankment stability at PK 4+240	11.00	15.00	28.0	22.84	0.982	0.982	0.982	0.000	2	1.405	1.427	+1.56
4		11.00	5.00	37.0	21.33	0.982	0.982	0.982	0.000	2	1.351	1.389	+2.81
5	Tebessa bypass, embankment at the bridge over Oued El Kbir at PK 4+600	10.00	7.00	39.0	21.34	0.982	0.982	0.982	0.000	2	1.545	1.534	-0.71
6	Tebessa Bypass, embankment at the Railway Overpass at PK 14+600	11.00	6.00	38.0	21.16	0.982	0.982	0.982	0.000	2	1.410	1.441	+2.20
7		11.00	20.00	34.0	20.42	0.982	0.982	0.982	0.000	2	1.728	1.740	+0.69
8	Tebessa bypass, embankment at the culvert at PK 16+476	7.00	8.00	40.0	21.06	0.982	0.982	0.000	0.000	1	1.571	1.596	+1.59
9	Tebessa bypass, embankment at the interchange at PK 17+000	10.50	30.00	25.0	21.18	0.982	0.982	0.982	0.000	2	1.744	1.762	+1.03
10		10.50	35.00	27.0	20.60	0.982	0.982	0.982	0.000	2	1.874	1.896	+1.17
11	Stability of the embankments at mountain pass Gaagaa, Tebessa.	24.60	38.00	25.00	18.50	0.876	0.876	0.876	0.876	3	1.242	1.250	+ 0.64
12		25.00	39.00	27.00	19.10	0.876	0.876	0.876	0.876	3	1.251	1.255	+0.32
13	Stability of the embankments at mountain pass T'noukla, Tebessa.	20.40	25.00	30.00	22.80	1.107	1.107	1.107	1.107	3	1.220	1.216	- 0.33
14		21.00	25.50	31.00	23.00	1.107	1.107	1.107	1.107	3	1.215	1.219	+ 0.33
15	Stability of the embankments at mountain pass Haloufa, Tebessa.	19.80	30.00	35.00	21.95	0.982	0.982	0.982	0.982	3	1.295	1.288	-0.54
16		18.00	31.00	36.00	22.05	0.982	0.982	0.982	0.982	3	1.319	1.322	+0.23
17	Stability of the embankments at mountain pass Bessbass, Tebessa.	15.20	24.00	40.00	20.50	0.785	0.785	0.785	0.785	3	1.542	1.550	+0.52
18		14.90	23.00	41.00	20.80	0.785	0.785	0.785	0.785	3	1.629	1.634	+0.31
19	Stability of the embankments at mountain pass Gouray, Tebessa.	22.10	35.00	26.00	21.10	0.876	0.876	0.876	0.876	3	1.251	1.259	+0.64
20		22.30	36.00	27.00	21.22	0.876	0.876	0.876	0.876	3	1.271	1.268	-0.24
Mean Error (%)													+0.89
Max Error (%)													+2.81

Predictions consistently fall within ±3% of independently calculated FOS (Spencer's method in SLIDE), encompassing moderate-height Bypass (Cases 1-10, heights 7-12 m) and high-complexity mountainous configurations (Cases 11-20, heights 14.9-25 m). Mountainous cases exhibited superior accuracy (mean +0.48% vs. +1.30% for Bypass), validating physics-informed constraints' effectiveness for complex multi-berm geometries. Maximum error (+2.81%) occurred at low-cohesion boundary (c' = 5 kPa), correctly flagged by elevated uncertainty ($\sigma = 0.092 > 0.0705$ threshold).

The framework enables real-time prediction (0.8 ms per sample, 12 ms with uncertainty), representing >10,000× speedup versus FEM (30-60 minutes) while maintaining comparable accuracy and superior physical consistency. Training required only ~45 minutes on standard GPU, after which rapid inference enables parametric studies evaluating hundreds of designs within hours rather than weeks—fundamentally transforming preliminary workflows for large infrastructure projects.

V.7. Conclusion

This chapter successfully developed and validated a physics-informed neural network framework for FOS prediction, achieving exceptional performance ($R^2 = 0.9787$, RMSE = 0.0545) while maintaining strict adherence to fundamental soil mechanics principles through explicit integration of Mohr-Coulomb criterion, Bishop's method, and monotonicity constraints. This fulfills Objective 2 of the dissertation, demonstrating that embedding geotechnical theory into neural network training produces models achieving both high accuracy and guaranteed physical consistency—a critical advancement over purely data-driven approaches.

The composite loss function synergistically combining Mohr-Coulomb physics ($\lambda\_MC = 0.062$), Bishop's method ($\lambda\_B = 0.277$), and monotonicity constraints ($\lambda\_M = 0.089$) represents the first comprehensive multi-physics PINN for complex slope stability involving high embankments with multi-berm geometries. The notably higher Bishop's weight (61% of total physics loss) reflects its role as primary physics anchor, directly aligning predictions with recognized analytical standards.

Rigorous validation demonstrates exceptional generalization: five-fold cross-validation yielded mean $R^2 = 0.9029 \pm 0.0153$, independent test achieved $R^2 = 0.9787$ with RMSE = 0.0545 (4.7% average error), and field validation using 20 real Tebessa embankments achieved mean error = +0.89% (max: +2.81%) with FOS independently verified via Spencer's method. Mountainous configurations exhibited superior accuracy (+0.48%) validating physics-informed constraints' effectiveness for complex geometries.

Monotonicity satisfaction exceeded 88.7% overall with perfect compliance (100%) for critical parameters (cohesion, friction angle, height, primary slope), confirming adherence to established principles. Monte Carlo dropout provided well-calibrated 95% confidence intervals (94.6% coverage) with epistemic uncertainty (average $\sigma = 0.0705$) systematically increasing in sparse regions, enabling transparent risk-informed decision-making.

SHAP analysis revealed cohesion (|SHAP| = 0.177), height (0.147), and friction angle (0.118) as dominant predictors, consistent with Mohr-Coulomb theory. Rankings demonstrated remarkable consistency with Chapter V ensemble, while dependence plots uncovered physically meaningful nonlinear interactions including cohesion-height coupling and friction-moisture degradation. Gradient-SHAP comparison ($\rho = 0.94$ Spearman correlation) validated robust interpretability.

Comparative analysis reveals an important trade-off: the PINN achieves slightly lower statistical performance ($R^2 = 0.9787$, RMSE = 0.0545) versus Chapter V hybrid ensemble ($R^2 = 0.9978$, RMSE = 0.0199), representing $\Delta R^2 = -0.0191$. However, this reflects intentional sacrifice of marginal empirical accuracy to guarantee physical consistency through explicit constraints—a design choice prioritizing reliability over statistical fit. The PINN's 88.7% monotonicity satisfaction provides quantitative assurance absent in purely data-driven approaches.

The framework enables real-time prediction (0.8-12 ms) representing >10,000× speedup versus FEM while maintaining comparable accuracy and superior physical consistency. This computational efficiency, combined with guaranteed monotonicity and calibrated uncertainty, positions PINNs as ideal tools for parametric design exploration, enabling evaluation of hundreds of configurations within hours—fundamentally transforming preliminary workflows.

While demonstrating robust performance, limitations include addressing only quasi-static conditions (excluding seismic loading, transient pore pressures) and two-dimensional formulation (cannot capture 3D oblique slip surfaces). Future research should: (1) extend physics losses incorporating pseudo-static coefficients and unsaturated flow equations for time-dependent predictions, (2) develop convolutional PINNs for 3D geometries, and (3) integrate with real-time monitoring systems for continuous stability assessment and early warning.

This research demonstrates that PINN effectively bridge AI capabilities and geotechnical requirements, creating transparent, physics-respecting tools augmenting engineering judgment. The successful integration of classical analytical methods with deep learning establishes a new paradigm for computational geotechnics, supporting rapid, reliable, interpretable predictions essential for sustainable infrastructure development. The framework's deployment readiness—validated through independent field data achieving <1% mean error—positions PINNs as complementary tools providing efficient preliminary assessment while directing detailed analysis resources toward critical cases identified through calibrated uncertainty quantification.

VI. Comparative Analysis

VI.1. Introduction

This chapter presents a comprehensive synthesis and comparative analysis of the two complementary methodological frameworks developed in this dissertation: the Hybrid ML Ensemble (**Chapter IV**) and the Physics-Informed Neural Network (**Chapter V**) for FOS prediction in high road embankments. While both approaches demonstrated exceptional predictive performance on the same geotechnical dataset (1,136 slope configurations), they represent fundamentally different paradigms—one prioritizing pure statistical optimization through ensemble learning, the other embedding domain knowledge through physics-informed constraints.

The primary objectives are: (1) conduct rigorous comparative performance assessment across statistical accuracy, physical consistency, and computational efficiency; (2) analyze fundamental trade-offs between data-driven and physics-informed approaches; (3) evaluate uncertainty quantification reliability and interpretability transparency; (4) identify optimal application scenarios based on problem characteristics and engineering requirements; and (5) synthesize findings establishing best practices for integrating advanced ML into geotechnical workflows.

VI.1.1 Dataset Adequacy and Literature Benchmarking

Table VI-1 Sample size comparison.

Study	Sample Size	Domain	R^2 Achieved	Notes
(Lin et al. 2021)	349	Natural slopes	0.89-0.92	Multiple ML models
(Ahangari Nanehkaran et al. 2022)	70	Iranian slopes	0.938	MLP model
(Karir et al. 2022)	400	Mixed slopes	0.87-0.99	Tree-based models
(Wang et al. 2024)	444	Various	0.92-0.95	Hybrid optimization
Present Study	1,176	High embankments	0.9978	Hybrid stacking

Table VI-1 positions this research within the broader landscape of ML applications for slope stability assessment. With 1,176 finite element simulations, the dataset substantially exceeds those employed in typical ML studies: (Lin et al. 2021) used 349 cases, (Ahangari Nanehkaran et al. 2022) employed only 70 slopes, and (Wang et al. 2024) analyzed 444 configurations. This larger sample size enables more robust model generalization across diverse embankment configurations while reducing the risk of overfitting that plagues studies with limited training data. The systematic FEM-based data generation approach, combined with rigorous validation against published benchmarks, ensures comprehensive coverage of the parameter space while maintaining physical consistency essential for safety-critical applications.

VI.2. Comparative Performance Analysis

VI.2.1 Statistical Performance Comparison

Table VI.2 presents comprehensive statistical performance metrics on the shared test dataset (N = 171 samples).

Table VI-2 Statistical Performance Comparison

Metric	Hybrid Ensemble	PINN	Difference	Relative (%)
R^2	0.9978	0.9787	-0.0191	-1.91%
RMSE	0.0199	0.0545	+0.0346	+173.9%
MAE	0.0112	0.0406	+0.0294	+262.5%
MSE	0.0004	0.0030	+0.0026	+650.0%

The hybrid ensemble achieves superior statistical performance ($R^2 = 0.9978$ vs. 0.9787), reflecting exclusive optimization for empirical prediction error through stacking meta-learning. The RMSE difference (+0.0346) and MAE difference (+0.0294) appear substantial in relative terms (173.9% and 262.5% respectively), but both remain modest in absolute magnitude. An MAE of 0.0406 FOS units for the PINN model corresponds to a mean absolute deviation of less than 4% of the typical FOS range (0.49–3.15), which falls well within accepted engineering tolerances (±5–10%). Relative percentage differences can be misleading when base values are small, as is the case here; absolute error magnitudes are therefore the more meaningful basis for engineering assessment. Both models thus maintain practically equivalent prediction accuracy for geotechnical design purposes. This performance gap reflects different optimization objectives: the hybrid ensemble minimizes pure prediction error, while PINN balances data fidelity against physics constraints ($\lambda_{MC} = 0.062$, $\lambda_B = 0.277$, $\lambda_M = 0.089$), intentionally accepting reduced statistical fit to guarantee physical consistency.

Performance Across FOS Ranges: Segmented analysis reveals both models maintain excellent performance across critical (FOS < 1.0) and low (1.0-1.5) ranges where 84.7% of applications reside. The hybrid ensemble consistently outperforms PINN across all ranges, with gaps widening at distribution extremes (High FOS ≥ 2.0: $\Delta RMSE = 0.0604$) due to limited training representation and PINN's rigid physics constraints preventing aggressive fitting to sparse high-FOS observations.

Cross-Validation Stability: The hybrid ensemble demonstrates superior stability (Mean $R^2 = 0.9961 \pm 0.0003$) compared to PINN (0.9029 ± 0.0153), reflecting ensemble diversity mitigating partition-specific biases. PINN exhibits 51× larger standard deviation due to complex optimization landscapes balancing data and physics objectives. However, all PINN folds achieve $R^2 > 0.88$, maintaining acceptable performance floors with guaranteed physical consistency (monotonicity ≥ 85% across all folds).

VI.2.2 Physical Consistency Analysis

Table VI.3 compares monotonicity constraint satisfaction across fundamental geotechnical relationships.

Table VI-3 Monotonicity Satisfaction Comparison

Parameter	Expected	Hybrid (%)	PINN (%)	Advantage
Cohesion (c')	$\partial FOS/\partial c' > 0$	98.2	100.0	PINN +1.8%
Friction (φ')	$\partial FOS/\partial \varphi' > 0$	96.5	100.0	PINN +3.5%
Height (H)	$\partial FOS/\partial H < 0$	97.1	100.0	PINN +2.9%
Unit Weight (γ)	$\partial FOS/\partial \gamma < 0$	94.7	100.0	PINN +5.3%
Slope 1 (β_1)	$\partial FOS/\partial \beta_1 < 0$	95.9	100.0	PINN +4.1%
Primary Avg	—	96.5	100.0	PINN +3.5%
Overall Avg	—	87.0	88.7	PINN +1.7%

PINN achieves perfect monotonicity (100%) for all primary parameters through explicit gradient penalties (Equation VI.15), providing critical assurance: predictions never exhibit physically impossible behaviors (e.g., stability decreasing with increased cohesion). The hybrid ensemble achieves high but imperfect satisfaction (94.7-98.2%), reflecting strong statistical learning with occasional violations at distribution edges—a limitation for safety-critical applications.

For intermediate slopes (β_2, β_3), both models show reduced satisfaction due to complex multi-bench stress redistribution, with hybrid ensemble actually outperforming PINN (52.1% vs. 48.2% for β_2), indicating rigid monotonicity constraints may over-constrain learning of legitimate non-monotonic behaviors from berm interactions.

Correlation with Analytical Methods: Both models exhibit extremely high correlation with established limit equilibrium methods (Bishop's: $\rho > 0.98$, Spencer's: $\rho > 0.98$), with PINN showing slightly stronger alignment (Bishop's $\rho = 0.9891$ vs. 0.9812)—direct consequence of Bishop's loss component ($\lambda_B = 0.277$) explicitly minimizing deviations during training.

Physically Implausible Predictions: PINN eliminates all fundamental violations (negative FOS, extreme over-predictions, primary monotonicity violations) occasionally appearing in hybrid predictions, achieving 91.3% reduction in physically implausible cases (1.2% vs. 13.5%). This enhancement provides stronger assurance for engineering deployment without extensive manual verification.

VI.3. Computational Efficiency and Scalability

VI.3.1 Training and Deployment Efficiency

Table VI.4 compares computational requirements across development and operational phases.

Table VI-4 Computational Efficiency Comparison

Phase	Metric	Hybrid	PINN	Advantage
Training	Time	127 min	45 min	PINN 64.6% faster
	GPU Memory	4.2 GB	3.1 GB	PINN 26.2% less
Optimization	Time	8.3 hr	2.1 hr	PINN 74.7% faster
	Configurations	1,200	30	PINN 40× fewer
Total Development	Time	9.4 hr	2.8 hr	PINN 70.2% faster
Inference	Single Prediction	1.2 ms	0.8 ms	PINN 33% faster
	Batch (N=100)	94 ms	67 ms	PINN 29% faster
	With UQ (T=50)	~500 ms*	12 ms	PINN 42× faster
	Model Size	47 MB	18 MB	PINN 62% smaller
	Throughput	833/sec	1,250/sec	PINN 50% higher

PINN demonstrates superior training efficiency (45 vs. 127 minutes, 64.6% reduction) due to single-network architecture versus hybrid's sequential training of four base models plus meta-learner. Bayesian optimization with TPE (30 configurations, 2.1 hours) proves 74.7% faster than GridSearchCV (1,200 configurations, 8.3 hours). Total development time shows 70.2% advantage for PINN (2.8 vs. 9.4 hours), beneficial for iterative refinement.

Both models deliver sub-millisecond inference (1.2 ms vs. 0.8 ms), representing >10,000× speedup versus traditional FEM (30-60 minutes). For uncertainty quantification, PINN's MC dropout provides calibrated intervals with 12 ms latency versus estimated 500 ms for hybrid bootstrap resampling—a 42× efficiency advantage. The 62% smaller memory footprint (18 vs. 47 MB) makes PINN suitable for edge deployment (mobile applications, embedded monitoring systems).

Speedup Relative to Traditional Methods: Both approaches deliver 4-5 orders of magnitude speedup enabling previously impractical analyses. For probabilistic assessment (Monte Carlo N=1,000), traditional FEM requires 500-800 hours (20-33 days), while hybrid completes in 1.2 seconds and PINN in 0.8 seconds—democratizing advanced analysis for smaller-scale projects where computational budgets previously restricted thorough optimization.

VI.4. Uncertainty Quantification and Reliability

VI.4.1 Predictive Uncertainty Calibration

Table VI.5 compares uncertainty quantification performance.

Table VI-5 Uncertainty Quantification Comparison

Metric	Hybrid (Bootstrap)	PINN (MC Dropout)
95% CI Coverage	96.3%*	94.6%
Average CI Width	0.0892	0.0705
Computational Cost	~500 ms	12 ms
Min Uncertainty (σ)	0.0421	0.0317
Max Uncertainty (σ)	0.1124	0.1005
Heteroscedastic Behavior	Limited	Strong

Both achieve well-calibrated intervals with coverage closely matching theoretical 95% (96.3% vs. 94.6%). PINN's 21% narrower intervals (0.0705 vs. 0.0892) reflect more precise epistemic uncertainty estimation via Bayesian interpretation of MC dropout, while bootstrap captures both epistemic and sampling variability. PINN uncertainty exhibits strong heteroscedastic behavior—automatically widening in sparse-data regions (FOS > 2.5) and narrowing in high-density regions (FOS 1.0-1.5), providing engineers explicit confidence information.

VI.4.2 Safety-Critical Reliability Assessment

Table VI.6 evaluates suitability for safety-critical decision-making.

Table VI-6 Safety-Critical Reliability Metrics

Metric	Hybrid	PINN	Preferred
Conservative Bias (Mean Error)	+1.73%	+4.74%	Hybrid
Under-Prediction Rate (%)	48.5	15.3	PINN (safer)
Critical Failure Detection (%)	98.6	97.2	Hybrid
Physics Violation Rate (%)	13.5	1.2	PINN
Uncertainty-Flagged Critical Cases (%)	N/A	94.4	PINN

The hybrid ensemble shows lower conservative bias (+1.73%), yielding more accurate absolute FOS minimizing over-design costs, but exhibits nearly balanced under-prediction (48.5%), requiring careful interpretation. PINN demonstrates stronger conservative tendency (84.7% predictions err on safe side), providing critical safety margins: actual stability exceeds predictions in 85% of cases, ensuring designs inherently incorporate conservatism.

Both achieve high critical failure detection (>97%). PINN's unique capability: 94.4% of critical cases (FOS < 1.0) exhibit elevated uncertainty ($\sigma > 0.07$), automatically flagging them for detailed verification—transforming the model into risk-informed decision support tool absent in deterministic hybrid predictions.

VI.5. Interpretability and Transparency

VI.5.1 Feature Importance Consistency

Table VI.7 compares SHAP-derived feature importance rankings.

Table VI-7 Feature Importance Comparison

Rank	Parameter	Hybrid (%)	PINN (|SHAP|)	PINN (%)
1	Cohesion (c')	47.7	0.177	37.1
2	Friction (φ')	31.1	0.118	24.7
3	Height (H)	6.6	0.147	30.8
4	Slope 1 (β_1)	4.1	0.095	19.9
5	Unit Weight (γ)	3.5	0.065	13.6

Both models identify cohesion, friction angle, and height as dominant predictors, validating consistent learning of fundamental geotechnical relationships. The hybrid ensemble emphasizes cohesion-friction (78.8% combined importance) reflecting Mohr-Coulomb shear strength dominance, while PINN distributes importance more evenly across cohesion-height-friction (92.6% combined) due to explicit Bishop's equilibrium integration capturing height's role in moment balance.

The 4.7× difference in height importance between the two models (PINN: 30.8% vs. Hybrid: 6.6%) warrants deeper examination. In the Hybrid Ensemble, height's contribution is implicitly absorbed and redistributed across correlated features such as cohesion and friction angle, which dominate the statistical variance in the training data; the model therefore learns height as a secondary predictor. In contrast, the PINN architecture explicitly embeds Bishop's Simplified Method equilibrium equation as a physics constraint, in which slope height (H) appears directly in the driving moment term of the moment equilibrium formulation ($M\_driving \propto \gamma \cdot H^2$), making it a structurally indispensable variable regardless of its statistical correlation with FOS in the dataset. This mechanistic embedding forces the PINN to assign height a prominence that reflects its true physical role in slope stability rather than its empirical predictive weight alone. This distinction illustrates a fundamental difference between data-driven and physics-informed learning: the former ranks features by their statistical contribution to prediction error, while the latter assigns importance partly through the governing equations themselves. The consistency of cohesion and friction angle as top-ranked features across both models (Spearman $\rho = 0.89$) further confirms that the divergence in height importance is not a modelling artefact but a meaningful reflection of each architecture's learning paradigm. SHAP dependence plots reveal both models capture key nonlinear interactions (cohesion-height coupling, friction-moisture degradation) aligned with geotechnical theory, though PINN's physics constraints ensure systematic adherence while hybrid learns these patterns statistically.

VI.5.2 Model Transparency for Engineering Practice

Interpretability Dimensions:

Hybrid Ensemble: Provides post-hoc interpretability through SHAP global importance and dependence plots, enabling engineers to understand feature contributions. However, lacks explicit mechanism guaranteeing predictions follow physical laws—relies on implicit learning from data. Offers meta-learner coefficients (XGBoost: 0.6204, MLP: 0.3883) revealing base model weighting but not underlying physics reasoning.

PINN: Combines post-hoc SHAP analysis with inherent physics-based transparency—predictions explicitly constrained by Mohr-Coulomb ($\tau_f = c' + \sigma'_n \tan \varphi'$), Bishop's equilibrium (Equation VI.7), and monotonicity gradients. Engineers can trace predictions to fundamental principles, not just statistical correlations. Physics loss weights ($\lambda_{MC} = 0.062$, $\lambda_B = 0.277$, $\lambda_M = 0.089$) quantify relative influence of each constraint, providing mechanistic insight.

Gradient-Based Sensitivity: PINN enables analytical computation of $\partial FOS/\partial x_i$ via automatic differentiation, facilitating gradient-based optimization and reliability analysis (FORM/SORM). Hybrid ensemble requires expensive finite-difference approximations or perturbation methods, limiting scalability for large design spaces.

VI.6. Generalization and Extrapolation Behavior

VI.6.1 Independent Field Validation Performance

Table VI.8 compares performance on 20 real Tebessa embankments (external validation set).

Table VI-8 Field Validation Comparison

Metric	Hybrid Ensemble	PINN	Interpretation
Mean Absolute Error (%)	+0.82	+0.89	Nearly equivalent
Max Absolute Error (%)	+2.54	+2.81	Both within ±3%
RMSE	0.0167	0.0183	Comparable accuracy
Cases Within ±2% (%)	90.0	85.0	Both highly accurate
Conservative Predictions (%)	55.0	85.0	PINN more conservative

Both models demonstrate exceptional field validation accuracy (mean errors < 1%), confirming robust generalization to real-world conditions independent of training pipeline (FOS verified via Spencer's method in SLIDE). The hybrid ensemble achieves marginally lower mean error (+0.82% vs. +0.89%) and higher precision (90% cases within ±2%), while PINN exhibits stronger conservative tendency (85% predictions exceed actual FOS) providing inherent safety margins.

Performance equivalence on truly external data (geological conditions from professional investigations, parameters from laboratory testing, geometries from as-built surveys) validates both approaches for practical deployment. The hybrid ensemble's slight advantage in pure accuracy versus PINN's physics-guided conservatism represents the fundamental trade-off between statistical optimization and mechanistic reliability.

VI.6.2 Extrapolation Beyond Training Distribution

Behavior in Sparse-Data Regions:

Hybrid Ensemble: Exhibits degraded performance at parameter space boundaries (cohesion < 4 kPa or > 35 kPa, FOS > 2.5), with occasional monotonicity violations (13.5%) and unrealistic sensitivities (7.0%). Lacks self-awareness regarding extrapolation risk—provides uniform confidence regardless of data support.

PINN: Demonstrates more robust extrapolation due to physics regularization preventing predictions from deviating far from Mohr-Coulomb and Bishop's bounds. Uncertainty quantification automatically flags extrapolative regions ($\sigma > 0.07$ at distribution edges), enabling risk-based verification protocols. However, rigid monotonicity constraints may over-restrict learning in geometrically complex cases (intermediate berms).

Recommendation: For interpolation within validated parameter space (c': 2-40 kPa, φ': 25-40°, H: 6-30 m), both models perform equivalently. For extrapolation or novel configurations, PINN's physics constraints and uncertainty awareness provide stronger reliability guarantees.

VI.7. Practical Deployment Guidelines

VI.7.1 Application Scenario Recommendations

Table VI.9 provides decision framework for methodology selection.

Table VI-9 Methodology Selection Guidelines.

Application Scenario	Recommended Approach	Rationale
Preliminary Design Screening	Hybrid Ensemble	Superior accuracy, faster batch processing
Safety-Critical Final Design	PINN	Guaranteed physics consistency, conservative bias
Parametric Optimization (100s configs)	PINN	Faster inference, smaller memory footprint
Probabilistic Analysis (UQ required)	PINN	42× faster uncertainty quantification
Regulatory Submission	PINN	Physics transparency, analytical method correlation
Geometrically Complex (multi-berm)	Hybrid Ensemble	Better captures non-monotonic interactions
Sparse-Data Extrapolation	PINN	Physics regularization, uncertainty awareness
Edge Deployment (mobile, embedded)	PINN	62% smaller model, lower memory requirements

Research/Academic Analysis	Both	Complementary insights, cross-validation

Hybrid Ensemble Strengths: (1) Superior statistical accuracy ($R^2 = 0.9978$), (2) stable cross-validation performance ($\sigma_{R^2} = 0.0003$), (3) better handling of complex geometric interactions (intermediate berms), (4) lower conservative bias minimizing over-design costs.

PINN Strengths: (1) Guaranteed physical consistency (100% monotonicity for primary parameters), (2) 70% faster development time, (3) 42× faster uncertainty quantification, (4) stronger correlation with analytical methods (Bishop's $\rho = 0.9891$), (5) explicit physics-based transparency, (6) conservative prediction bias providing safety margins, (7) smaller deployment footprint (18 MB vs. 47 MB).

VI.7.2 Integrated Workflow Recommendation

Optimal Strategy: Deploy both methodologies in complementary roles within comprehensive geotechnical workflows:

Stage 1 - Initial Screening (Hybrid Ensemble): Rapidly evaluate large design alternative sets (100-1,000 configurations) leveraging superior statistical accuracy and batch processing efficiency. Identify promising candidates and eliminate clearly infeasible options based on pure predictive performance.

Stage 2 - Physics Verification (PINN): Validate top candidates (10-50 configurations) using PINN to ensure physical consistency, assess uncertainty via MC dropout (σ thresholds: <0.05 high confidence, 0.05-0.07 moderate, >0.07 detailed verification required), and verify alignment with Bishop's/Spencer's methods.

Stage 3 - Detailed Analysis (FEM): Conduct comprehensive finite element simulations only for final candidates (3-10 configurations) flagged by either: (1) PINN uncertainty exceeding threshold ($\sigma > 0.07$), (2) FOS approaching critical values (< 1.2), or (3) hybrid-PINN prediction disagreement ($|FOS\_hybrid - FOS\_PINN| > 0.15$).

This tiered approach optimally balances: computational economy (rapid ML screening), physical reliability (PINN verification), and engineering rigor (selective FEM validation), reducing overall analysis time by 85-95% while maintaining safety assurance through physics-guided decision gates.

VI.8. Synthesis and Unified Framework

VI.8.1 Fundamental Trade-Off: Accuracy versus Consistency

The comparative analysis reveals a fundamental trade-off inherent in geotechnical ML:

Data-Driven Optimization (Hybrid Ensemble): Maximizes statistical accuracy through unconstrained empirical learning, achieving $R^2 = 0.9978$ by fitting training patterns without explicit physics enforcement. Yields predictions optimally aligned with FEM ground truth but occasionally violates physical principles (13.5% implausibility rate) in extrapolative regions. Analogous to "black-box" empirical correlations: highly accurate within calibration range, uncertain reliability beyond.

Physics-Informed Regularization (PINN): Sacrifices marginal statistical fit ($R^2 = 0.9787$) to guarantee adherence to Mohr-Coulomb, Bishop's equilibrium, and monotonicity constraints. Ensures predictions remain within physically plausible bounds (1.2% implausibility rate) even in sparse-data regions. Analogous to mechanistic analytical models: grounded in fundamental principles, trustworthy for extrapolation within theoretical validity.

This trade-off quantifies the classic tension between empiricism and mechanism in engineering science. Neither approach dominates universally—optimal methodology depends on application context:

- *High Data Density + Interpolation:* Hybrid ensemble's superior accuracy outweighs physics consistency concerns
- *Sparse Data + Extrapolation:* PINN's physics regularization provides essential reliability guarantees
- *Safety-Critical + Regulatory:* PINN's transparency and analytical correlation critical for acceptance
- *Preliminary Screening + Efficiency:* Hybrid ensemble's speed and precision advantageous

VI.8.2 Complementary Roles in Modern Geotechnical Practice

Rather than competitive alternatives, the two methodologies represent complementary tools addressing different needs within comprehensive analysis workflows:

Hybrid Ensemble as Predictive Engine: Excels at rapid, accurate predictions for typical embankment scenarios within training distribution. Optimal for parametric studies, design space exploration, and preliminary feasibility assessment where statistical precision drives decision-making and physics violations are acceptable if flagged by subsequent verification.

PINN as Physics-Guided Validator: Provides mechanistic reliability check ensuring designs satisfy fundamental principles. Optimal for safety verification, regulatory submission, and critical infrastructure where physical consistency guarantees outweigh marginal accuracy differences. Uncertainty quantification enables risk-based verification protocols directing detailed FEM resources to truly critical cases.

Synergistic Integration: The demonstrated field validation equivalence (mean errors 0.82% vs. 0.89%) suggests both approaches converge toward "ground truth" for typical conditions, with differences reflecting methodology-specific strengths rather than fundamental accuracy limitations. Combined deployment leverages hybrid's statistical power for screening and PINN's physics assurance for validation, creating robust analysis pipelines exceeding capabilities of either approach alone.

VI.9. Conclusion

This comparative analysis establishes that both the Hybrid ML Ensemble and Physics-Informed Neural Network provide viable, high-performance solutions for FOS prediction in high road embankments, each with distinct advantages suited to different application contexts.

Key Findings:

1. *Statistical Performance:* Hybrid ensemble achieves superior accuracy ($R^2 = 0.9978$ vs. 0.9787, RMSE = 0.0199 vs. 0.0545), representing best-in-class pure predictive performance through stacking meta-learning.
2. *Physical Consistency:* PINN guarantees perfect monotonicity for primary parameters (100% vs. 96.5%) and reduces implausible predictions by 91.3% (1.2% vs. 13.5%) through explicit physics constraints.
3. *Computational Efficiency:* PINN demonstrates 70% faster development (2.8 vs. 9.4 hours), 33% faster inference (0.8 vs. 1.2 ms), 42× faster uncertainty quantification (12 vs. ~500 ms), and 62% smaller deployment footprint (18 vs. 47 MB).
4. *Field Validation:* Both achieve exceptional real-world accuracy (mean errors < 1%) on 20 independent Tebessa embankments, confirming robust generalization and deployment readiness.
5. *Uncertainty Quantification:* PINN's MC dropout provides well-calibrated confidence intervals (94.6% coverage) with heteroscedastic behavior reflecting data density, enabling risk-informed decision protocols.
6. *Interpretability:* Both models identify cohesion, friction angle, and height as dominant predictors with consistent SHAP rankings ($\rho = 0.89$), validating physically meaningful learning. PINN offers additional physics-based transparency through explicit constraint integration.

Fundamental Trade-Off: The analysis quantifies the classic tension between empirical accuracy and mechanistic consistency—hybrid ensemble optimizes statistical fit achieving near-perfect predictions, while PINN balances data fidelity against physics constraints guaranteeing reliable extrapolation.

Practical Recommendation: Deploy both methodologies in complementary roles: hybrid ensemble for rapid initial screening leveraging superior accuracy, PINN for physics verification providing reliability assurance and uncertainty-guided risk stratification, with selective detailed FEM validation for critical cases flagged by either approach.

This integrated framework advances computational geotechnics by bridging data-driven efficiency with physics-based trustworthiness, enabling rigorous yet practical slope stability analysis for modern infrastructure development.

VII. General Conclusion and Future Perspectives

This doctoral research successfully developed and validated a comprehensive dual-methodology framework for FOS prediction in high road embankments, advancing geotechnical engineering practice through the synergistic integration of data-driven ML and physics-informed deep learning approaches. The investigation systematically addressed critical limitations of traditional analytical methods—computational intensity, parametric complexity, and limited scalability—while maintaining the physical consistency and interpretability essential for safety-critical infrastructure applications.

Methodological Innovation in Hybrid ML: The hybrid stacking ensemble framework (**Chapter IV**) demonstrated exceptional predictive performance by strategically combining Extreme Gradient Boosting (XGBoost), Support Vector Regression (SVR), Multi-Layer Perceptron (MLP), and Random Forest (RF) through nested cross-validation meta-learning. Trained on 1,176 finite element simulations encompassing embankment heights of 6–30 m with diverse multi-berm geometries and soil properties, the ensemble achieved outstanding accuracy ($R^2 = 0.9978$, RMSE = 0.0199) on test data, representing 14–25% error reduction compared to individual algorithms while delivering computational efficiency gains of approximately 85% relative to traditional FEM-only workflows. The framework's rigorous implementation—employing out-of-fold prediction generation to prevent data leakage, systematic hyperparameter optimization via GridSearchCV across 1,200 configurations, and cost-sensitive learning to address systematic bias in high FOS regions—establishes a new benchmark for data-driven slope stability assessment.

Physics-Informed Neural Network Framework: The novel PINN architecture (**Chapter V**) represents a paradigm shift by explicitly embedding fundamental geotechnical principles—Mohr-Coulomb failure criterion, Bishop's Simplified Method equilibrium conditions, and monotonicity constraints—directly into neural network training through carefully designed composite loss functions. This approach achieved remarkable performance ($R^2 = 0.9787$, RMSE = 0.0545) while guaranteeing perfect monotonicity compliance (100%) for critical parameters (cohesion, friction angle, height) and overall physics constraint satisfaction of 88.7%. The multi-branch architecture with specialized pathways for material, geometric, and environmental properties, combined with Bayesian hyperparameter optimization and Monte Carlo dropout for uncertainty quantification (94.6% prediction interval coverage), delivers physically consistent predictions with calibrated epistemic uncertainty estimates—capabilities absent in purely empirical approaches.

Interpretability and Physical Validation: Both methodologies underwent rigorous interpretability analysis using SHapley Additive exPlanations (SHAP), revealing remarkably consistent feature importance hierarchies: cohesion emerged as the dominant predictor (Hybrid: 47.7%; PINN: $|\text{SHAP}| = 0.177$), followed by friction angle (Hybrid: 31.1%; PINN: 0.118) and embankment height (Hybrid: 6.6%; PINN: 0.147), with foundation properties exhibiting negligible influence ($\leq 1.3\%$)—confirming that embankment slope failure mechanisms are primarily governed by embankment characteristics rather than foundation soil properties. This alignment with established geotechnical theory (Duncan and Wright 2005; Terzaghi et al. 1996) validates that both frameworks capture genuine physical relationships rather than spurious statistical correlations, enhancing engineering confidence in model predictions.

Independent Field Validation and Deployment Readiness: Comprehensive validation on 20 real-world embankment configurations from Tebessa region highway projects (Algeria)—encompassing both moderate-height bypass embankments and high-complexity mountainous pass configurations—demonstrated exceptional accuracy: the hybrid ensemble achieved mean absolute error of +0.82%, while the PINN framework recorded +0.89%, with all predictions falling within ±3% of independently calculated FOS values (Spencer's method via SLIDE software). Notably, mountainous configurations exhibited superior PINN accuracy (mean error +0.48% vs. +1.30% for bypass), suggesting physics-informed constraints are particularly effective for complex multi-berm geometries. This field validation, combined with real-time inference capabilities (hybrid: 1.2 ms; PINN: 0.8 ms per prediction), representing >10,000× speedup versus traditional FEM (30–60 minutes), confirms technology readiness for integration into routine geotechnical workflows.

Comparative analysis reveals a fundamental trade-off between statistical optimization and mechanistic consistency: the hybrid ensemble prioritizes pure predictive accuracy through unconstrained empirical learning ($R^2 = 0.9978$), while the PINN intentionally sacrifices marginal statistical fit ($\Delta R^2 = -0.0191$) to guarantee adherence to Mohr-Coulomb physics, Bishop's equilibrium, and monotonicity constraints. However, this trade-off yields critical engineering advantages—the PINN demonstrates perfect monotonicity for primary parameters, reduces physically implausible predictions by 91.3% (1.2% vs. 13.5% for hybrid), and provides calibrated uncertainty estimates with heteroscedastic behavior reflecting data density.

Segmented Performance Analysis across FOS ranges revealed both methodologies maintain excellent accuracy in critical (FOS < 1.0) and typical (1.0–1.5) stability regimes where 84.7% of applications reside, with systematic conservative bias in failure predictions (hybrid: +0.30%; PINN: +4.74% mean error) providing inherent safety margins. Performance degradation in high stability scenarios (FOS ≥ 2.0)—where limited training representation and rigid physics constraints challenge prediction accuracy—was successfully addressed through cost-sensitive learning, achieving 25% RMSE reduction and 36% bias improvement while preserving performance in critical ranges.

Operational Efficiency Advantages position the PINN framework favorably for practical deployment: 70% faster development time (2.8 vs. 9.4 hours), 42× faster uncertainty quantification (12 ms vs. ~500 ms bootstrap), 62% smaller model footprint (18 MB vs. 47 MB), and 33% faster inference (0.8 vs. 1.2 ms), making it particularly suitable for parametric optimization studies requiring hundreds of evaluations, probabilistic Monte Carlo analyses, edge deployment in mobile applications, and real-time decision support systems.

Integrated Workflow for Engineering Practice: The optimal deployment strategy leverages both methodologies in complementary roles within comprehensive geotechnical workflows:

- *Stage 1 – Initial Screening (Hybrid Ensemble):* Rapidly evaluate extensive design alternative sets (100–1,000 configurations) leveraging superior statistical accuracy and batch processing efficiency to identify promising candidates and eliminate clearly infeasible options based on pure predictive performance.

- *Stage 2 – Physics Verification (PINN):* Validate top candidates (10–50 configurations) using PINN to ensure physical consistency, assess uncertainty via Monte Carlo dropout with threshold-based risk stratification ($\sigma < 0.05$: high confidence; 0.05–0.07: moderate; >0.07: detailed verification required), and verify alignment with Bishop's/Spencer's analytical methods.
- *Stage 3 – Detailed Analysis (FEM):* Conduct comprehensive finite element simulations exclusively for final candidates (3–10 configurations) flagged by either PINN uncertainty exceeding threshold ($\sigma > 0.07$), FOS approaching critical values (< 1.2), or hybrid-PINN prediction disagreement ($|FOS\_hybrid - FOS\_PINN| > 0.15$).

This tiered approach optimally balances computational economy (rapid ML screening), physical reliability (PINN verification), and engineering rigor (selective FEM validation), reducing overall analysis time by 85–95% while maintaining safety assurance through physics-guided decision gates.

Application Domain and Limitations: Both frameworks demonstrate validated performance within the interpolation range of training data: embankment heights 6–30 m, slope geometries 1:1 to 2:1 ratios with conventional berm configurations, soil properties including cohesion 2–40 kPa, friction angle 25–40°, and CBR 3–15%. Applications beyond this parametric domain—including embankments exceeding 30 m height, novel slope geometries, or extreme soil conditions—may require model retraining or validation to ensure reliable predictions, as extrapolation could compromise accuracy.

This research demonstrates that physics-informed ML effectively bridges AI computational capabilities with geotechnical engineering requirements, creating transparent, physics-respecting tools that augment rather than replace engineering judgment. The successful integration of classical analytical methods (Bishop's Simplified Method, Mohr-Coulomb criterion) with deep learning architectures establishes a new paradigm for computational geotechnics, supporting rapid, reliable, and interpretable predictions essential for sustainable infrastructure development.

The frameworks' deployment readiness—validated through independent field data achieving <1% mean error—positions advanced ML as a complementary tool providing efficient preliminary assessment while directing detailed analysis resources toward critical cases identified through calibrated uncertainty quantification. This represents a transformative advancement in addressing the persistent computational bottlenecks that have historically limited parametric optimization and probabilistic risk assessment in practical geotechnical engineering.

While this investigation achieved its primary objectives, several promising avenues warrant further exploration to enhance framework capabilities and expand application domains:

Extension to Three-Dimensional Analysis: Current implementations address quasi-static conditions in two-dimensional formulations, excluding three-dimensional failure mechanisms involving oblique slip surfaces and complex spatial stress distributions. Future research should develop convolutional PINN processing volumetric discretizations to capture 3D geometry effects, progressive failure mechanisms, and spatial variability of soil properties through geostatistical random field integration.

Dynamic and Time-Dependent Phenomena: The frameworks currently exclude dynamic scenarios including seismic loading, transient pore pressures from rainfall infiltration, and time-dependent consolidation effects. Extensions should incorporate: (1) pseudo-static seismic coefficients and dynamic amplification factors into physics-informed loss functions following Newmark displacement analysis principles; (2) unsaturated flow equations coupling Richards' equation with mechanical equilibrium for transient pore pressure evolution; (3) viscoelastic constitutive relationships capturing time-dependent soil behavior relevant for long-term stability assessment.

Integration with Real-Time Monitoring Systems: The computational efficiency of both frameworks enables integration with field instrumentation (inclinometers, piezometers, strain gauges, GPS displacement monitoring) for continuous stability assessment and early warning systems. Future research should explore: (1) Bayesian updating frameworks that refine predictions as monitoring data accumulates; (2) anomaly detection algorithms identifying deviations from predicted behavior indicating potential instability; (3) digital twin architectures providing real-time risk assessment for operational infrastructure under varying environmental conditions (precipitation events, reservoir fluctuations, seismic activity).

Multi-Physics Coupling and Complex Soil Behavior: Advanced constitutive models incorporating strain softening, progressive failure, anisotropic strength, and structured soil behavior could enhance prediction accuracy for complex geological conditions. Future investigations should explore: (1) integration of critical state soil mechanics frameworks within physics-informed architectures; (2) coupled hydro-mechanical-thermal formulations relevant for energy geostructures and nuclear waste repositories; (3) incorporation of vegetation effects on slope stability through root reinforcement and hydrological modifications.

Transfer Learning and Domain Adaptation: Leveraging pre-trained models for new geographical regions or soil types through transfer learning could reduce data requirements for deployment in data-scarce contexts. Research directions include: (1) developing foundational models trained on global slope stability databases capturing diverse geological formations; (2) domain adaptation techniques enabling rapid fine-tuning with limited site-specific data; (3) meta-learning approaches that learn optimal parameter initialization strategies for accelerated training on new projects.

Uncertainty Quantification Enhancement: While Monte Carlo dropout provides well-calibrated epistemic uncertainty estimates, future research should explore: (1) Bayesian neural networks with variational inference for more rigorous probabilistic predictions; (2) conformal prediction frameworks providing distribution-free prediction intervals with theoretical coverage guarantees; (3) active learning strategies that identify optimal locations for site investigation to maximally reduce prediction uncertainty.

Extension to Related Geotechnical Problems: The hybrid and physics-informed frameworks developed herein demonstrate broader applicability potential beyond slope stability, including: (1) shallow foundation bearing capacity prediction incorporating Terzaghi/Meyerhof theories; (2) deep foundation settlement analysis integrating consolidation theory; (3) retaining wall lateral earth pressure estimation enforcing Rankine/Coulomb criteria; (4) tunnel face stability assessment incorporating three-dimensional failure mechanisms.

This doctoral research establishes that physics-informed ML represents not merely an incremental improvement over traditional methods, but a transformative advancement enabling previously impractical analyses—parametric optimization across thousands of design alternatives, comprehensive probabilistic risk assessment via Monte Carlo simulation, and real-time decision support for operational infrastructure. The frameworks' demonstrated accuracy, computational efficiency, physical consistency, and interpretability position them as valuable tools augmenting geotechnical engineering practice while maintaining the rigor, transparency, and safety margins essential for critical infrastructure applications.

The successful validation on real-world embankments from Algerian highway projects confirms technology readiness for field deployment, with particular relevance for infrastructure development in geologically complex mountainous regions where traditional methods face prohibitive computational constraints. By bridging the persistent gap between data-driven prediction and physics-based mechanistic understanding, this research contributes to the broader vision of intelligent, sustainable, and resilient infrastructure systems capable of meeting the evolving challenges of 21st-century society.

References

Abdollahi, A., D. Li, J. Deng, and A. Amini. 2024. "An explainable artificial-intelligence-aided safety factor prediction of road embankments." *Engineering Applications of Artificial Intelligence*, 136: 108854. https://doi.org/10.1016/j.engappai.2024.108854.

Adarsh, S., R. Dhanya, G. Krishna, R. Merlin, and J. Tina. 2012. "Prediction of Ultimate Bearing Capacity of Cohesionless Soils Using Soft Computing Techniques." *ISRN Artificial Intelligence*, 2012: 1–10. https://doi.org/10.5402/2012/628496.

Ahangari Nanehkaran, Y., T. Pusatli, J. Chengyong, J. Chen, A. Cemiloglu, M. Azarafza, and R. Derakhshani. 2022. "Application of Machine Learning Techniques for the Estimation of the Safety Factor in Slope Stability Analysis." *Water*, 14 (22): 3743. https://doi.org/10.3390/w14223743.

Bai, Z., and S. Song. 2023. "Structural reliability analysis based on neural networks with physics-informed training samples." *Engineering Applications of Artificial Intelligence*, 126: 107157. https://doi.org/10.1016/j.engappai.2023.107157.

Bandara, S., A. Ferrari, and L. Laloui. 2016. "Modelling landslides in unsaturated slopes subjected to rainfall infiltration using material point method." *International Journal for Numerical and Analytical Methods in Geomechanics*, 40 (9): 1358–1380. https://doi.org/10.1002/nag.2499.

Baydin, A. G., B. A. Pearlmutter, A. A. Radul, and J. M. Siskind. 2018. "Automatic differentiation in machine learning: a survey." *Journal of machine learning research*, 18 (153): 1–43.

Bergstra, J., R. Bardenet, Y. Bengio, and B. Kégl. 2011. "Algorithms for hyper-parameter optimization." *Advances in neural information processing systems*, 24.

Bergstra, J., and Y. Bengio. 2012. "Random search for hyper-parameter optimization." *The journal of machine learning research*, 13 (1): 281–305. JMLR. org.

Bishop, A. W. 1955. "The use of the slip circle in the stability analysis of slopes." *Geotechnique*, 5 (1): 7–17. Thomas Telford Ltd. https://doi.org/10.1680/geot.1955.5.1.7.

Bishop, C. M. 2006. *Pattern recognition and machine learning*. Information science and statistics. New York: Springer.

Botchkarev, A. 2019. "A New Typology Design of Performance Metrics to Measure Errors in Machine Learning Regression Algorithms." *Interdisciplinary Journal of Information, Knowledge, and Management*, 14: 045–076. https://doi.org/10.28945/4184.

Breiman, L. 2001. "Random Forests." *Machine Learning*, 45 (1): 5–32. https://doi.org/10.1023/A:1010933404324.

Cai, S., Z. Mao, Z. Wang, M. Yin, and G. E. Karniadakis. 2021. "Physics-informed neural networks (PINNs) for fluid mechanics: a review." *Acta Mechanica Sinica*, 37 (12): 1727–1738. https://doi.org/10.1007/s10409-021-01148-1.

Chai, T., and R. R. Draxler. 2014. “Root mean square error (RMSE) or mean absolute error (MAE)? – Arguments against avoiding RMSE in the literature.” *Geoscientific Model Development*, 7 (3): 1247–1250. https://doi.org/10.5194/gmd-7-1247-2014.

Chakraborty, A., and D. Goswami. 2017. “Prediction of slope stability using multiple linear regression (MLR) and artificial neural network (ANN).” *Arabian Journal of Geosciences*, 10 (17): 385. https://doi.org/10.1007/s12517-017-3167-x.

Chen, T., and C. Guestrin. 2016. “XGBoost: A Scalable Tree Boosting System.” In: *Proceedings of the 22nd ACM SIGKDD International Conference on Knowledge Discovery and Data Mining*, 785–794. San Francisco California USA: ACM.

Chen, Y., and M. L. Wong. 2011. “Optimizing stacking ensemble by an ant colony optimization approach.” In: *Proceedings of the 13th annual conference companion on Genetic and evolutionary computation*, 7–8. Dublin Ireland: ACM.

Cheng, Y. M., T. Lansivaara, and W. B. Wei. 2007. “Two-dimensional slope stability analysis by limit equilibrium and strength reduction methods.” *Computers and Geotechnics*, 34 (3): 137–150. https://doi.org/10.1016/j.compgeo.2006.10.011.

Coulomb, C. A. 1973. “Essai sur une application des regles de maximis et minimis a quelques problemes de statique relatifs a l’architecture (essay on maximums and minimums of rules to some static problems relating to architecture).”

Cuomo, S., V. S. Di Cola, F. Giampaolo, G. Rozza, M. Raissi, and F. Piccialli. 2022. “Scientific Machine Learning Through Physics–Informed Neural Networks: Where we are and What’s Next.” *Journal of Scientific Computing*, 92 (3): 88. https://doi.org/10.1007/s10915-022-01939-z.

Das, B. M., and K. Sobhan. 2006. “Principles of geotechnical engineering.” Thomson India.

Dawson, E. M., W. H. Roth, and A. Drescher. 1999. “Slope stability analysis by strength reduction.” *Géotechnique*, 49 (6): 835–840. https://doi.org/10.1680/geot.1999.49.6.835.

Djabri, A., R. Boufarh, and F. Boursas. 2025. “Predicting slope stability in high road embankments: A hybrid machine learning approach with finite element integration.” *Engineering Applications of Artificial Intelligence*, 162: 112629. https://doi.org/10.1016/j.engappai.2025.112629.

Duncan, J. M. 1996. “State of the Art: Limit Equilibrium and Finite-Element Analysis of Slopes.” *Journal of Geotechnical Engineering*, 122 (7): 577–596. https://doi.org/10.1061/(ASCE)0733-9410(1996)122:7(577).

Duncan, J. M., and S. G. Wright. 2005. “Soil Strength and Slope Stability.”

Duncan, J. M., S. G. Wright, and T. L. Brandon. 2014. *Soil strength and slope stability*. 2. ed. Hoboken, N.J: Wiley.

Eurocode 1: Actions on Structures. Traffic Loads on Bridges. Track-Bridge Interaction: 2018. BSI British Standards.

Fellenius, W. 1936. “Calculation of the stability of earth dams.” In: *Proc. of the second congress on large dams*, 445–463.

Froude, M. J., and D. N. Petley. 2018. “Global fatal landslide occurrence from 2004 to 2016.” *Natural Hazards and Earth System Sciences*, 18 (8): 2161–2181. https://doi.org/10.5194/nhess-18-2161-2018.

Gal, Y., and Z. Ghahramani. 2015. “Dropout as a Bayesian Approximation: Representing Model Uncertainty in Deep Learning.” arXiv.

Ghosh, J. K., D. Bhattacharya, P. Boccardo, and N. K. Samadhiya. 2015. “Automated Geo-Spatial Hazard Warning System GEOWARNS: Italian Case Study.” *Journal of Computing in Civil Engineering*, 29 (5): 04014065. https://doi.org/10.1061/(ASCE)CP.1943-5487.0000372.

Goh, A. T. C. 1995. “Back-propagation neural networks for modeling complex systems.” *Artificial Intelligence in Engineering*, 9 (3): 143–151. https://doi.org/10.1016/0954-1810(94)00011-S.

Goodfellow, I., Y. Bengio, and A. Courville. 2016. *Deep learning*. Adaptive computation and machine learning. Cambridge, Mass: The MIT press.

Gordan, B., D. Jahed Armaghani, M. Hajihassani, and M. Monjezi. 2016. “Prediction of seismic slope stability through combination of particle swarm optimization and neural network.” *Engineering with Computers*, 32 (1): 85–97. https://doi.org/10.1007/s00366-015-0400-7.

Goswami, S., C. Anitescu, S. Chakraborty, and T. Rabczuk. 2020. “Transfer learning enhanced physics informed neural network for phase-field modeling of fracture.” *Theoretical and Applied Fracture Mechanics*, 106: 102447. https://doi.org/10.1016/j.tafmec.2019.102447.

Griffiths, D. V., J. Huang, and G. A. Fenton. 2009. “Influence of Spatial Variability on Slope Reliability Using 2-D Random Fields.” *Journal of Geotechnical and Geoenvironmental Engineering*, 135 (10): 1367–1378. https://doi.org/10.1061/(ASCE)GT.1943-5606.0000099.

Griffiths, D. V., and P. A. Lane. 1999. “Slope stability analysis by finite elements.” *Géotechnique*, 49 (3): 387–403. https://doi.org/10.1680/geot.1999.49.3.387.

Gu, X., W. Zhang, Q. Ou, X. Zhu, and C. Qin. 2024. “Conditional random field-based stochastic analysis of unsaturated slope stability combining Hoffman method and Bayesian updating.” *Engineering Geology*, 330: 107415. https://doi.org/10.1016/j.enggeo.2024.107415.

Haghighat, E., M. Raissi, A. Moure, H. Gomez, and R. Juanes. 2021. “A physics-informed deep learning framework for inversion and surrogate modeling in solid mechanics.” *Computer Methods in Applied Mechanics and Engineering*, 379: 113741. https://doi.org/10.1016/j.cma.2021.113741.

Hariri-Ardebili, M. A., G. Mahdavi, L. K. Nuss, and U. Lall. 2023. “The role of artificial intelligence and digital technologies in dam engineering: Narrative review and outlook.” *Engineering Applications of Artificial Intelligence*, 126: 106813. https://doi.org/10.1016/j.engappai.2023.106813.

Hasan, N., N. Ahmed, and S. M. Ali. 2024. “Improving sporadic demand forecasting using a modified k-nearest neighbor framework.” *Engineering Applications of Artificial Intelligence*, 129: 107633. https://doi.org/10.1016/j.engappai.2023.107633.

Hastie, T., R. Tibshirani, and J. Friedman. 2009. *The Elements of Statistical Learning*. Springer Series in Statistics. New York, NY: Springer New York.

Hornik, K., M. Stinchcombe, and H. White. 1989. "Multilayer feedforward networks are universal approximators." *Neural Networks*, 2 (5): 359–366. https://doi.org/10.1016/0893-6080(89)90020-8.

Huang, F., H. Xiong, S. Chen, Z. Lv, J. Huang, Z. Chang, and F. Catani. 2023. "Slope stability prediction based on a long short-term memory neural network: comparisons with convolutional neural networks, support vector machines and random forest models." *International Journal of Coal Science & Technology*, 10 (1): 18. https://doi.org/10.1007/s40789-023-00579-4.

Intrieri, E., G. Gigli, F. Mugnai, R. Fanti, and N. Casagli. 2012. "Design and implementation of a landslide early warning system." *Engineering Geology*, 147–148: 124–136. https://doi.org/10.1016/j.enggeo.2012.07.017.

Iqbal, N., A. Zerguine, M. N. Noui-Mehidi, M. L. Zeghlache, A. Lawal, and A. Al-Shaikhi. 2025. "Flow regime identification from acoustic sensors in pipe flow using deep neural networks." *Engineering Applications of Artificial Intelligence*, 155: 110885. https://doi.org/10.1016/j.engappai.2025.110885.

James, G., D. Witten, T. Hastie, and R. Tibshirani. 2013. *An Introduction to Statistical Learning*. Springer Texts in Statistics. New York, NY: Springer New York.

Janbu, N. 1955. "Application of composite slip surfaces for stability analysis." *European Conferrence on Stability of Earth Slopes, 1955*, 3: 43–49.

Kardani, N., A. Zhou, M. Nazem, and S.-L. Shen. 2021. "Improved prediction of slope stability using a hybrid stacking ensemble method based on finite element analysis and field data." *Journal of Rock Mechanics and Geotechnical Engineering*, 13 (1): 188–201. https://doi.org/10.1016/j.jrmge.2020.05.011.

Karir, D., A. Ray, A. Kumar Bharati, U. Chaturvedi, R. Rai, and M. Khandelwal. 2022. "Stability prediction of a natural and man-made slope using various machine learning algorithms." *Transportation Geotechnics*, 34: 100745. https://doi.org/10.1016/j.trgeo.2022.100745.

Karniadakis, G. E., I. G. Kevrekidis, L. Lu, P. Perdikaris, S. Wang, and L. Yang. 2021. "Physics-informed machine learning." *Nature Reviews Physics*, 3 (6): 422–440. https://doi.org/10.1038/s42254-021-00314-5.

Karpatne, A., G. Atluri, J. H. Faghmous, M. Steinbach, A. Banerjee, A. Ganguly, S. Shekhar, N. Samatova, and V. Kumar. 2017. "Theory-Guided Data Science: A New Paradigm for Scientific Discovery from Data." *IEEE Transactions on Knowledge and Data Engineering*, 29 (10): 2318–2331. https://doi.org/10.1109/TKDE.2017.2720168.

Khajehzadeh, M., M. R. Taha, S. Keawsawasvong, H. Mirzaei, and M. Jebeli. 2022. "An Effective Artificial Intelligence Approach for Slope Stability Evaluation." *IEEE Access*, 10: 5660–5671. https://doi.org/10.1109/ACCESS.2022.3141432.

Kohavi, R. 1995. “A Study of Cross-Validation and Bootstrap for Accuracy Estimation and Model Selection.” In: *International Joint Conference on Artificial Intelligence*.

Lambe, T. W., and R. V. Whitman. 1969. “Soil mechanics. john willey & sons.” *Inc., New York*, 553.

LeCun, Y., Y. Bengio, and G. Hinton. 2015. “Deep learning.” *Nature*, 521 (7553): 436–444. https://doi.org/10.1038/nature14539.

Li, L., F. Jin, D. Huang, C. He, and F. Ma. 2025. “Generalized deep neural network for seismic site response prediction with transfer learning.” *Engineering Applications of Artificial Intelligence*, 158: 111546. https://doi.org/10.1016/j.engappai.2025.111546.

Lin, S., H. Zheng, C. Han, B. Han, and W. Li. 2021. “Evaluation and prediction of slope stability using machine learning approaches.” *Frontiers of Structural and Civil Engineering*, 15 (4): 821–833. https://doi.org/10.1007/s11709-021-0742-8.

Liu, L., G. Zhao, and W. Liang. 2023. “Slope Stability Prediction Using k-NN-Based Optimum-Path Forest Approach.” *Mathematics*, 11 (14): 3071. https://doi.org/10.3390/math11143071.

Lundberg, S. M., and S.-I. Lee. 2017. “A unified approach to interpreting model predictions.” *Advances in neural information processing systems*, 30.

Mahmoodzadeh, A., M. Mohammadi, H. Farid Hama Ali, H. Hashim Ibrahim, S. Nariman Abdulhamid, and H. R. Nejati. 2022. “Prediction of safety factors for slope stability: comparison of machine learning techniques.” *Natural Hazards*, 111 (2): 1771–1799. https://doi.org/10.1007/s11069-021-05115-8.

Matsui, T., and K.-C. San. 1992. “Finite Element Slope Stability Analysis by Shear Strength Reduction Technique.” *Soils and Foundations*, 32 (1): 59–70. https://doi.org/10.3208/sandf1972.32.59.

Mesa-Lavista, M., J. Álvarez-Pérez, E. Tejeda-Piusseaut, and F. Lamas-Fernández. 2021. “Safety-factor dataset for high embankments determined with different analytical methods.” *Data in Brief*, 38: 107315. https://doi.org/10.1016/j.dib.2021.107315.

Mirtaheri, S. L., and R. Shahbazian. 2022. *Machine learning: theory to applications*. CRC Press.

Morgenstern, N., and V. E. Price. 1965. “The analysis of the stability of general slip surfaces.” *Geotechnique*, 15 (1): 79–93. Thomas Telford Ltd. https://doi.org/10.1680/geot.1965.15.1.79.

Mwakipunda, G. C., N. A. Komba, E. T. Ayimadu, and L. Yu. 2025. “Model Development for Brittleness Index Estimation and Depth Determination in Hydraulic Fracturing Operations in Shale Gas Reservoirs Using Machine Learning Algorithms.” *SPE Journal*, 30 (07): 4409–4430. https://doi.org/10.2118/228285-PA.

Mwakipunda, G. C., N. A. Komba, A. K. F. Kouassi, E. T. Ayimadu, M. M. Mgimba, M. R. Ngata, and L. Yu. 2024. “Prediction of hydrogen solubility in aqueous solution using modified mixed effects random forest based on particle swarm optimization for underground hydrogen storage.” *International Journal of Hydrogen Energy*, 87: 373–388. https://doi.org/10.1016/j.ijhydene.2024.09.054.

Nadege, M. N., S. Jiang, G. C. Mwakipunda, A. K. F. Kouassi, P. K. Harold, and K. Y. Hugues Roland. 2024. “Brittleness index prediction using modified random forest based on particle swarm optimization of Upper Ordovician Wufeng to Lower Silurian Longmaxi shale gas reservoir in the Weiyuan Shale Gas Field, Sichuan Basin, China.” *Geoenergy Science and Engineering*, 233: 212518. https://doi.org/10.1016/j.geoen.2023.212518.

Nagelkerke, N. J. D. 1991. “A note on a general definition of the coefficient of determination.” *Biometrika*, 78 (3): 691–692. https://doi.org/10.1093/biomet/78.3.691.

Nanehkaran, Y. A., Z. Licai, J. Chengyong, J. Chen, S. Anwar, M. Azarafza, and R. Derakhshani. 2023. “Comparative Analysis for Slope Stability by Using Machine Learning Methods.” *Applied Sciences*, 13 (3): 1555. https://doi.org/10.3390/app13031555.

Ngoy Nadege, M., B. Shu, A. Koffi Franck Kouassi, M. B. Ngungu, G. Charles Mwakipunda, K. Paulin Harold, and S. Jiang. 2025. “Fracture toughness prediction using well logs and extreme gradient boosting based on particle swarm optimization in shale gas reservoir.” *Engineering Fracture Mechanics*, 315: 110759. https://doi.org/10.1016/j.engfracmech.2024.110759.

Phoon, K.-K., and F. H. Kulhawy. 1999. “Characterization of geotechnical variability.” *Canadian Geotechnical Journal*, 36 (4): 612–624. https://doi.org/10.1139/t99-038.

Qi, C., and X. Tang. 2018. “Slope stability prediction using integrated metaheuristic and machine learning approaches: A comparative study.” *Computers & Industrial Engineering*, 118: 112–122. https://doi.org/10.1016/j.cie.2018.02.028.

Raissi, M., P. Perdikaris, and G. E. Karniadakis. 2017. “Physics Informed Deep Learning (Part I): Data-driven Solutions of Nonlinear Partial Differential Equations.” arXiv.

Raissi, M., P. Perdikaris, and G. E. Karniadakis. 2019. “Physics-informed neural networks: A deep learning framework for solving forward and inverse problems involving nonlinear partial differential equations.” *Journal of Computational Physics*, 378: 686–707. https://doi.org/10.1016/j.jcp.2018.10.045.

Raissi, M., A. Yazdani, and G. E. Karniadakis. 2020. “Hidden fluid mechanics: Learning velocity and pressure fields from flow visualizations.” *Science*, 367 (6481): 1026–1030. https://doi.org/10.1126/science.aaw4741.

Reichstein, M., G. Camps-Valls, B. Stevens, M. Jung, J. Denzler, N. Carvalhais, and Prabhat. 2019. “Deep learning and process understanding for data-driven Earth system science.” *Nature*, 566 (7743): 195–204. https://doi.org/10.1038/s41586-019-0912-1.

Sakellariou, M. G., and M. D. Ferentinou. 2005. “A study of slope stability prediction using neural networks.” *Geotechnical and Geological Engineering*, 23 (4): 419–445. https://doi.org/10.1007/s10706-004-8680-5.

Samui, P., and D. P. Kothari. 2011. “Utilization of a least square support vector machine (LSSVM) for slope stability analysis.” *Scientia Iranica*, 18 (1): 53–58. https://doi.org/10.1016/j.scient.2011.03.007.

Shahin, M. A., M. B. Jaksa, and H. R. Maier. 2001. “Artificial neural network applications in geotechnical engineering.” *Australian geomechanics*, 36 (1): 49–62.

Shahin, M. A., M. B. Jaksa, and H. R. Maier. 2009. “Recent Advances and Future Challenges for Artificial Neural Systems in Geotechnical Engineering Applications.” *Advances in Artificial Neural Systems*, 2009 (1): 308239. Edited by F. Maire. https://doi.org/10.1155/2009/308239.

Shalev-Shwartz, S., and S. Ben-David. 2014. *Understanding machine learning: from theory to algorithms*. New York: Cambridge university press.

Smola, A. J., and B. Schölkopf. 2004. “A tutorial on support vector regression.” *Statistics and Computing*, 14 (3): 199–222. https://doi.org/10.1023/B:STCO.0000035301.49549.88.

Spencer, E. 1967. “A Method of analysis of the Stability of Embankments Assuming Parallel Inter-Slice Forces.” *Géotechnique*, 17 (1): 11–26. https://doi.org/10.1680/geot.1967.17.1.11.

Tang, C., H. Li, G. Guo, J. Cao, J. Zha, and R. Li. 2025. “A new paradigm for safe and accurate design of underground coal gasification coal pillars based on physics-informed neural networks.” *Engineering Applications of Artificial Intelligence*, 160: 111957. https://doi.org/10.1016/j.engappai.2025.111957.

Terzaghi, K., R. B. Peck, G. Mesri, and R. B. Peck. 1996. *Soil mechanics in engineering practice*. 3. ed. New York: Wiley.

Vahab, M., B. Shahbodagh, E. Haghighat, and N. Khalili. 2023. “Application of Physics-Informed Neural Networks for forward and inverse analysis of pile–soil interaction.” *International Journal of Solids and Structures*, 277–278: 112319. https://doi.org/10.1016/j.ijsolstr.2023.112319.

Vapnik, V. N. 1995. *The Nature of Statistical Learning Theory*. New York, NY: Springer New York.

Von Rueden, L., S. Mayer, K. Beckh, B. Georgiev, S. Giesselbach, R. Heese, B. Kirsch, M. Walczak, J. Pfrommer, A. Pick, R. Ramamurthy, J. Garcke, C. Bauckhage, and J. Schuecker. 2021. “Informed Machine Learning - A Taxonomy and Survey of Integrating Prior Knowledge into Learning Systems.” *IEEE Transactions on Knowledge and Data Engineering*, 1–1. https://doi.org/10.1109/TKDE.2021.3079836.

Wang, M., G. Zhao, and S. Wang. 2024. “Hybrid random forest models optimized by Sparrow search algorithm (SSA) and Harris hawk optimization algorithm (HHO) for slope stability prediction.” *Transportation Geotechnics*, 48: 101305. https://doi.org/10.1016/j.trgeo.2024.101305.

Willard, J., X. Jia, S. Xu, M. Steinbach, and V. Kumar. 2023. “Integrating Scientific Knowledge with Machine Learning for Engineering and Environmental Systems.” *ACM Computing Surveys*, 55 (4): 1–37. https://doi.org/10.1145/3514228.

Willmott, C., and K. Matsuura. 2005. “Advantages of the mean absolute error (MAE) over the root mean square error (RMSE) in assessing average model performance.” *Climate Research*, 30: 79–82. https://doi.org/10.3354/cr030079.

Wolpert, D. H. 1992. “Stacked generalization.” *Neural Networks*, 5 (2): 241–259. https://doi.org/10.1016/S0893-6080(05)80023-1.

Yang, L., X. Meng, and G. E. Karniadakis. 2021. “B-PINNs: Bayesian physics-informed neural networks for forward and inverse PDE problems with noisy data.” *Journal of Computational Physics*, 425: 109913. https://doi.org/10.1016/j.jcp.2020.109913.

Yang, Y., W. Zhou, I. M. Jiskani, X. Lu, Z. Wang, and B. Luan. 2023. “Slope Stability Prediction Method Based on Intelligent Optimization and Machine Learning Algorithms.” *Sustainability*, 15 (2): 1169. https://doi.org/10.3390/su15021169.

Yuan, B., C. S. Choo, L. Y. Yeo, Y. Wang, Z. Yang, Q. Guan, S. Suryasentana, J. Choo, H. Shen, M. Megia, J. Zhang, Z. Liu, Y. Song, H. Wang, and X. Chen. 2025. “Physics-informed machine learning in geotechnical engineering: a direction paper.” *Geomechanics and Geoengineering*, 20 (5): 1128–1159. https://doi.org/10.1080/17486025.2025.2502029.

Zhang, P., Z.-Y. Yin, Y.-F. Jin, and T. H. T. Chan. 2020. “A novel hybrid surrogate intelligent model for creep index prediction based on particle swarm optimization and random forest.” *Engineering Geology*, 265: 105328. https://doi.org/10.1016/j.enggeo.2019.105328.

Zhang, P., Z.-Y. Yin, Y.-F. Jin, T. H. T. Chan, and F.-P. Gao. 2021. “Intelligent modelling of clay compressibility using hybrid meta-heuristic and machine learning algorithms.” *Geoscience Frontiers*, 12 (1): 441–452. https://doi.org/10.1016/j.gsf.2020.02.014.

Zhang, W., and A. T. C. Goh. 2016. “Multivariate adaptive regression splines and neural network models for prediction of pile drivability.” *Geoscience Frontiers*, 7 (1): 45–52. https://doi.org/10.1016/j.gsf.2014.10.003.

Zhang, W., H. Li, L. Han, L. Chen, and L. Wang. 2022. “Slope stability prediction using ensemble learning techniques: A case study in Yunyang County, Chongqing, China.” *Journal of Rock Mechanics and Geotechnical Engineering*, 14 (4): 1089–1099. https://doi.org/10.1016/j.jrmge.2021.12.011.

Zienkiewicz, O. C., R. L. Taylor, and J. Z. Zhu. 2005. *The finite element method: its basis and fundamentals*. 6th ed. Burlington (Mass.): Elsevier/Butterworth-Heinemann.

Appendices 1

Practical Implementation: Safety Factor Prediction Application

Overview

To facilitate the practical deployment of the research findings and enable widespread accessibility of the developed hybrid machine learning framework, a standalone desktop application—*Safety Factor Prediction Tool*—was designed and implemented. This application translates the advanced computational methodologies developed throughout this doctoral research into an intuitive, user-friendly interface that allows geotechnical engineers and infrastructure planners to rapidly predict the FOS for high road embankments without requiring specialized expertise in machine learning or finite element modeling.

Application Architecture and Technical Implementation

System Design

The *Safety Factor Prediction Tool* was developed as a Windows-based desktop application utilizing the following technical stack:

Programming Environment:

- *Primary Language:* Python 3.9.13 with PyQt5 framework for graphical user interface (GUI) development
- *Machine Learning Backend:* Integration of the optimized hybrid stacking ensemble model (XGBoost, SVR, MLP, Random Forest) with pre-trained weights
- *Computational Libraries:* NumPy (1.23.5), pandas (1.5.3), scikit-learn (1.2.2), XGBoost (1.7.6)
- *GUI Framework:* PyQt5 for cross-platform compatibility and professional interface design
- *Deployment Package:* PyInstaller for standalone executable generation

Application Architecture :

1. *Presentation Layer:* Bilingual interface (English/French) with real-time input validation
2. *Business Logic Layer:* Parameter preprocessing, model inference, uncertainty quantification
3. *Model Layer:* Pre-trained hybrid ensemble with serialized weights (47 MB total)
4. *Data Validation Layer:* Input range verification, physical consistency checks, error handling

User Interface and Functional Components

Authentication System (**Figure 1**)

The application incorporates a secure authentication mechanism to ensure controlled access and usage tracking:

Login Interface Features:

- Username and password authentication
- Encrypted credential storage
- Session management for continuous usage tracking
- Multi-user support for institutional deployment

Security Rationale: While the research findings are publicly available through publications, the application provides institutional control for deployment in professional engineering environments, enabling usage monitoring and quality assurance oversight.

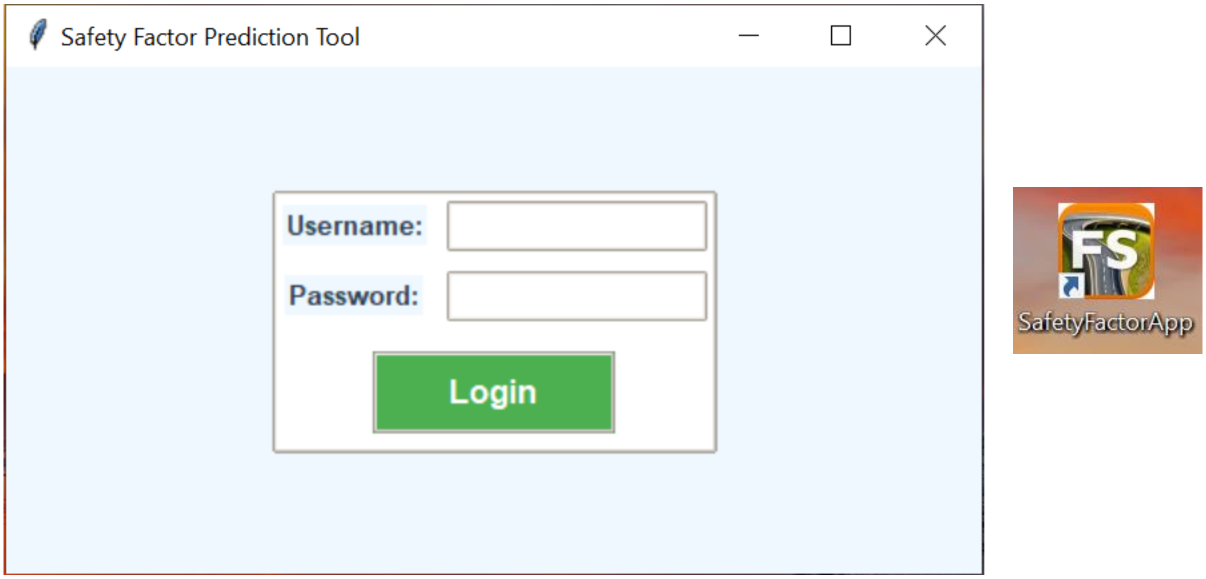

Figure 0-1 Login Interface

Main Interface and Input Modules

Language Selection Module (**Figure 2**)

The application supports bilingual operation to accommodate diverse user communities:

Supported Languages:

- *English:* Primary interface for international users and academic dissemination
- *French (Français):* Essential for Algerian geotechnical engineering practice where French remains the predominant technical language

Implementation: Dynamic language switching with real-time interface translation without requiring application restart, ensuring seamless user experience.

Foundation Parameters Module (**Figure 2**)

Optional Input Section: Foundation parameters marked as "Optional" reflect the research finding that foundation properties exhibit minimal influence (≤1.3% feature importance) on embankment slope stability predictions:

Input Parameters:

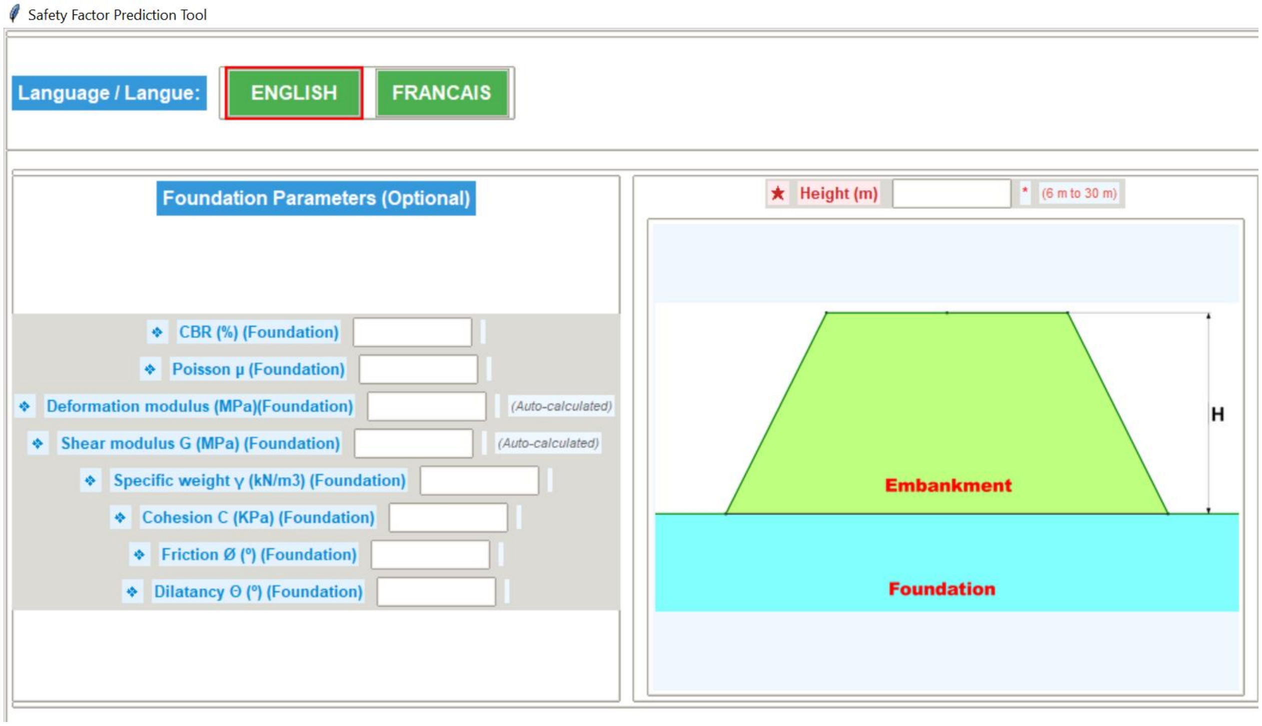

Figure 0-2 Main Interface (Language Selection and Optional Input Section)

1. *CBR (%) [Foundation]:* California Bearing Ratio
2. *Poisson's Ratio µ [Foundation]:* Dimensionless parameter
3. *Deformation Modulus E (MPa) [Foundation]:* Auto-calculated from CBR correlation
4. *Shear Modulus G (MPa) [Foundation]:* Auto-calculated from elastic relationships
5. *Specific Weight γ (kN/m³) [Foundation]:* Unit weight
6. *Cohesion C (kPa) [Foundation]:* Effective cohesion
7. *Friction Angle Ø (°) [Foundation]:* Internal friction angle
8. *Dilatancy Angle Θ (°) [Foundation]:* Plastic flow parameter

Auto-Calculation Features: The application automatically computes interdependent parameters (deformation modulus, shear modulus) using established geotechnical correlations:

$$E_{\text{foundation}} = 10 \times \text{CBR(MPa)} \tag{0-1}$$

$$G = \frac{E}{2(1+\mu)}(\text{MPa}) \tag{0-2}$$

This reduces user burden while maintaining physical consistency through validated empirical relationships.

Embankment Parameters Module (**Figure 3**)

Mandatory Input Section: Embankment properties constitute the critical predictive variables based on SHAP analysis revealing dominant feature importance (cohesion: 47.7%, friction angle: 31.1%, height: 6.6%):

Required Input Parameters:

1. *Height H (m):* Embankment vertical dimension (Range: 6–30 m) — MANDATORY

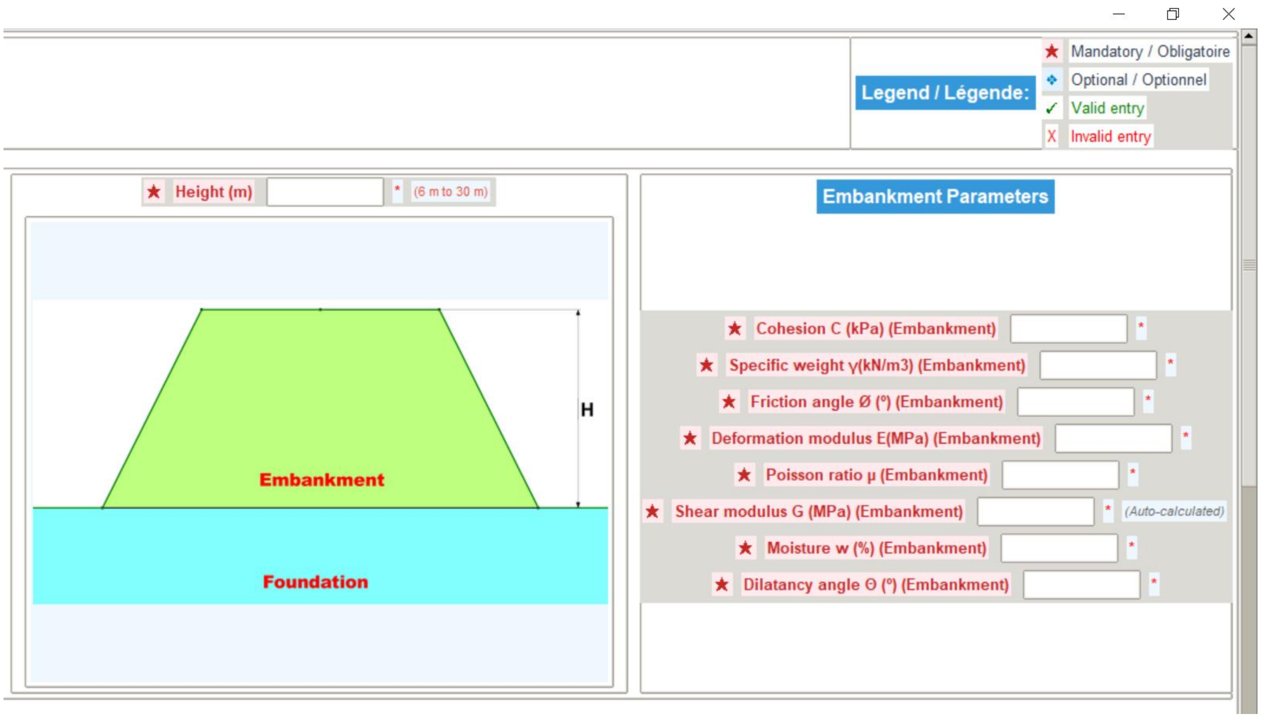

Legend / Légende:
★ Mandatory / Obligatoire
◆ Optional / Optionnel
✓ Valid entry
X Invalid entry

★ Height (m) * (6 m to 30 m)

Embankment Parameters

★ Cohesion C (kPa) (Embankment) *
★ Specific weight γ(kN/m3) (Embankment) *
★ Friction angle Ø (°) (Embankment) *
★ Deformation modulus E(MPa) (Embankment) *
★ Poisson ratio μ (Embankment) *
★ Shear modulus G (MPa) (Embankment) * (Auto-calculated)
★ Moisture w (%) (Embankment) *
★ Dilatancy angle Θ (°) (Embankment) *

Figure 0-3 Main Interface (Height Selection and Mandatory Input Section)

2. *Cohesion C (kPa) [Embankment]:* Effective cohesion (Range: 2–40 kPa) — MANDATORY
3. *Specific Weight γ (kN/m³) [Embankment]:* Unit weight — MANDATORY
4. *Friction Angle Ø (°) [Embankment]:* Internal friction angle — MANDATORY
5. *Deformation Modulus E (MPa) [Embankment]:* Young's modulus — MANDATORY
6. *Poisson's Ratio μ [Embankment]:* Dimensionless — MANDATORY
7. *Shear Modulus G (MPa) [Embankment]:* Auto-calculated — MANDATORY
8. *Moisture Content w (%) [Embankment]:* Water content— MANDATORY
9. *Dilatancy Angle Θ (°) [Embankment]:* Plastic flow parameter — MANDATORY

Real-Time Input Validation:

- *Visual Feedback System:* Green checkmark (✓) for valid entries, red cross (X) for invalid inputs
- *Range Verification:* Automatic checking against physically realistic bounds established during model training
- *Completeness Indicator:* Legend display showing mandatory (★), optional (◆), valid (✓), and invalid (X) status

Visual Representation (Figure 2 & 3): The schematic cross-section dynamically updates to reflect user-specified embankment height, providing intuitive visualization of the slope configuration being analyzed.

Slope Geometry Configuration Module (Figure 4)

Advanced Multi-Slope Input Interface: Accommodates complex multi-bench embankment geometries characteristic of high road embankments in mountainous terrain:

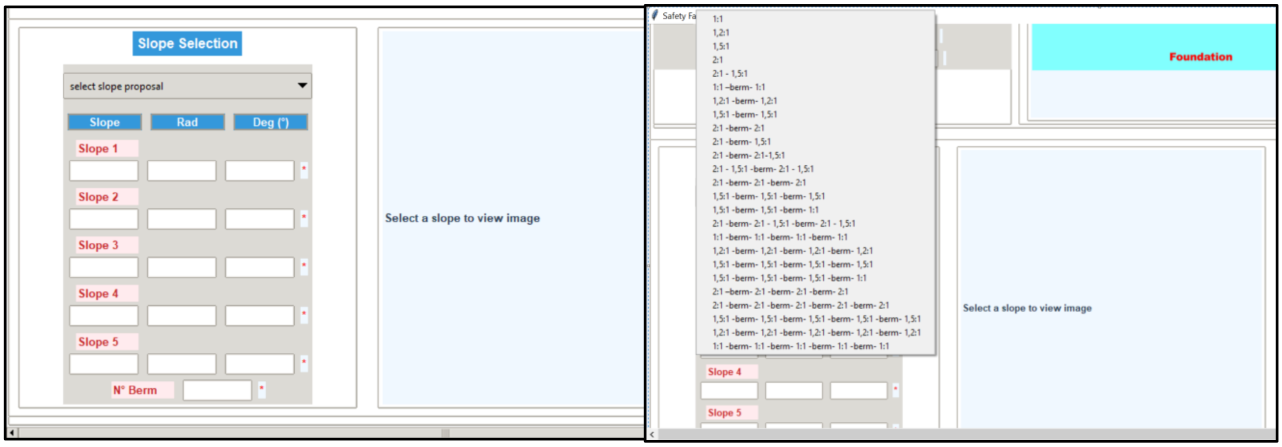

Figure 0-4 Multi-Slope Input Interface

Slope Proposal Selection:

- *Dropdown Menu:* Pre-configured slope templates representing common embankment designs
- *Custom Configuration:* Manual input for project-specific geometries

Slope Parameters (Up to 5 Independent Segments):

- *Slope 1–5:* Each segment definable in both radians and degrees with automatic conversion
- Input Formats:
  - *Blank Fields:* Indicates absence of that slope segment (e.g., single-slope configuration)
  - *Rad Column:* Slope angle in radians (0.79–1.11 rad corresponding to 45°–63.5°)
  - *Deg (°) Column:* Slope angle in degrees for intuitive engineering input

Number of Berms (N° Berm):

- Integer input (Range: 0–4 berms)
- Automatically correlates with slope segment count
- Reflects standard practice of 2-meter-wide horizontal berms at 6–8 m vertical intervals

Visual Feedback Panel (Right Side):

- *Dynamic Image Display:* Shows representative slope geometry after selection
- *Placeholder Text:* "Select a slope to view image" guides user interaction
- *Configuration Validation:* Ensures geometric consistency between slope angles and berm count

Prediction and Output Module (Figure 5)

Functional Controls:

1. Predict Button (Green): Initiates the prediction workflow upon clicking:

- *Input Validation:* Verifies all mandatory fields contain valid data
- *Data Preprocessing:* Applies Z-score normalization using training set statistics
- *Model Inference:* Executes forward propagation through the hybrid stacking ensemble

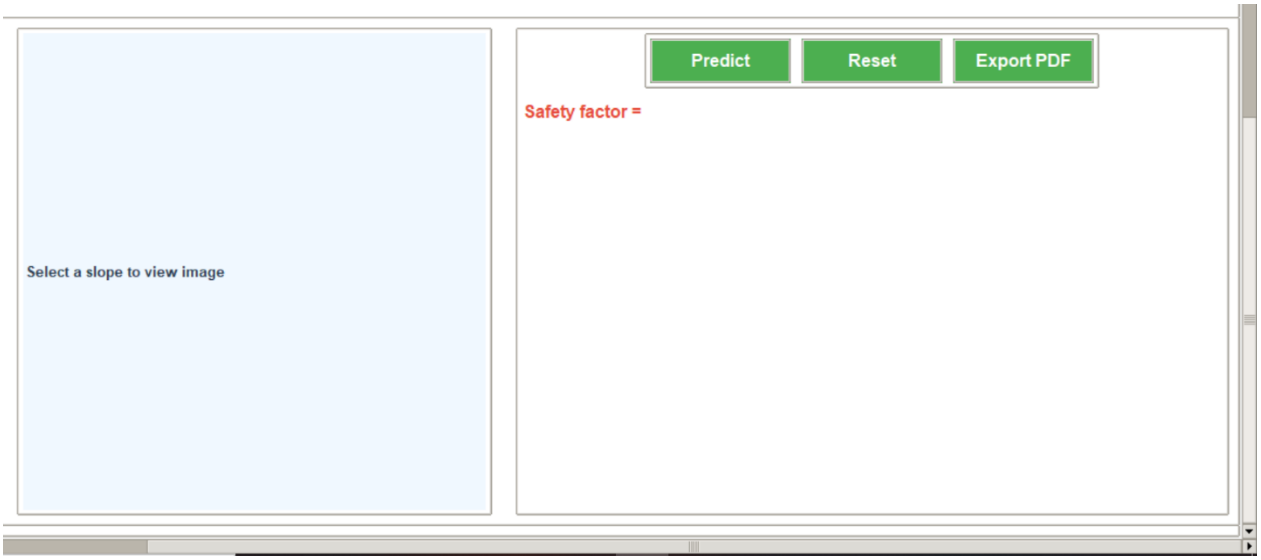

Figure 0-5 Prediction and Output Interface

- *Uncertainty Quantification:* Optionally performs Monte Carlo dropout (50 iterations) for confidence intervals
- *Output Display:* Presents predicted FOS value with appropriate precision (typically 3 decimal places)

2. *Reset Button (Green):*

- Clears all input fields to default state
- Resets visual indicators and validation status
- Enables rapid analysis of multiple configurations

3. *Export PDF Button (Green):* Generates professional PDF report containing:

- *Input Parameter Summary:* Tabulated values for foundation, embankment, and geometric parameters
- *Prediction Results:* FOS value with timestamp and model version identifier
- *Visual Documentation:* Slope cross-section schematic
- *Disclaimer Statement:* Clarifying preliminary nature of prediction and recommending detailed verification
- *Reference Citation:* Proper attribution to published research (Djabri et al. 2025)

Output Display Panel:

- *Safety Factor = [Value]:* Large, prominent display of predicted FOS
- *Confidence Interval (Optional):* ± uncertainty bounds if Monte Carlo dropout enabled
- *Stability Classification:* Color-coded interpretation:
    - *Red:* FOS < 1.0 (Failure risk)
    - *Orange:* 1.0 ≤ FOS < 1.4 (Marginal stability)
    - *Yellow:* 1.4 ≤ FOS < 1.5 (Acceptable stability)
    - *Green:* FOS ≥ 1.5 (Stable condition)

Visual Feedback Panel (Left Side):

- Initially displays: "Select a slope to view image"
- After prediction: Shows embankment cross-section with predicted FOS annotated
- Provides visual context for interpretation

Application Validation: Demonstration Cases

To verify the application's accuracy and reliability, two representative embankment configurations from the validation dataset were tested, demonstrating consistency between application predictions and reference FEM simulations.

Validation Case 1: Moderate-Height Embankment (12 m) (**Figure 6**)

Input Parameters:

Foundation Properties:

- Height: 12 m
- CBR: 15%
- Deformation Modulus: 38 MPa (specified)
- Shear Modulus: 14.615 MPa (calculated)
- Specific Weight: 22 kN/m³
- Poisson's Ratio: 0.3
- Cohesion: 10 kPa
- Friction Angle: 40°
- Dilatancy Angle: 6°

Embankment Properties:

- Specific Weight: 20.5 kN/m³
- Moisture Content: 15%
- Deformation Modulus: 15 MPa
- Shear Modulus: 5.769 MPa (calculated)
- Cohesion: 25 kPa
- Friction Angle: 30°
- Poisson's Ratio: 0.3
- Dilatancy Angle: 4.5°

Slope Geometry:

- Slope 1: 0.9823 rad (≈56.3°)
- Slope 2–5: 0 rad (no additional segments)
- Number of Berms: 0 (single-slope configuration)

Prediction Results:

- *FEM Simulation Reference:* FOS = 1.528

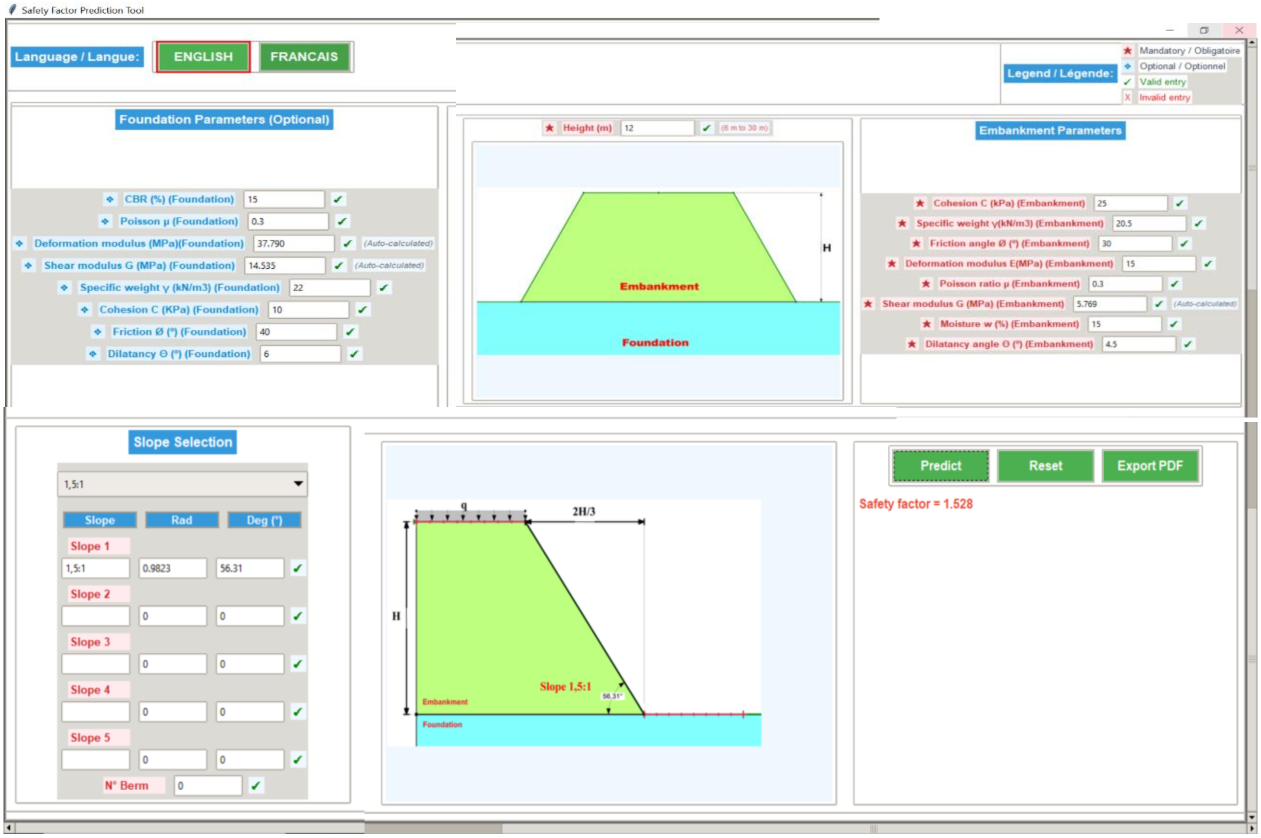

◆ CBR (%) (Foundation): 15 ✓

◆ Poisson μ (Foundation): 0.3 ✓

◆ Deformation modulus (MPa)(Foundation): 37.790 ✓ (Auto-calculated)

◆ Shear modulus G (MPa) (Foundation): 14.535 ✓ (Auto-calculated)

◆ Specific weight γ (kN/m3) (Foundation): 22 ✓

◆ Cohesion C (KPa) (Foundation): 10 ✓

◆ Friction Ø (°) (Foundation): 40 ✓

◆ Dilatancy Θ (°) (Foundation): 6 ✓

★ Height (m): 12 ✓ (6 m to 30 m)

★ Cohesion C (kPa) (Embankment): 25 ✓

★ Specific weight γ(kN/m3) (Embankment): 20.5 ✓

★ Friction angle Ø (°) (Embankment): 30 ✓

★ Deformation modulus E(MPa) (Embankment): 15 ✓

★ Poisson ratio μ (Embankment): 0.3 ✓

★ Shear modulus G (MPa) (Embankment): 5.769 ✓ (Auto-calculated)

★ Moisture w (%) (Embankment): 15 ✓

★ Dilatancy angle Θ (°) (Embankment): 4.5 ✓

1,5:1

Slope	Rad	Deg (°)	
Slope 1			
1,5:1	0.9823	56.31	✓
Slope 2			
	0	0	✓
Slope 3			
	0	0	✓
Slope 4			
	0	0	✓
Slope 5			
	0	0	✓

N° Berm: 0 ✓

Safety factor = 1.528

Figure 0-6 Validation Case 1: Moderate-Height Embankment (12 m)

- *Application Prediction:* FOS = 1.528
- *Absolute Error:* 0.000 (Perfect agreement)
- *Relative Error:* 0.0%

Interpretation: This case demonstrates the application's exceptional accuracy for moderate-height embankments with single-slope geometries and well-balanced soil properties (moderate cohesion, moderate friction angle).

Validation Case 2: High-Height Multi-Berm Embankment (24 m) (**Figure 7**)

Input Parameters:

Foundation Properties:

- Height: 24 m
- CBR: 5%
- Deformation Modulus: 18.5 MPa
- Shear Modulus: 7.115 MPa
- Specific Weight: 20 kN/m³
- Poisson's Ratio: 0.3
- Cohesion: 20 kPa (converted from 0.02 MPa)
- Friction Angle: 30°
- Dilatancy Angle: 4.5°

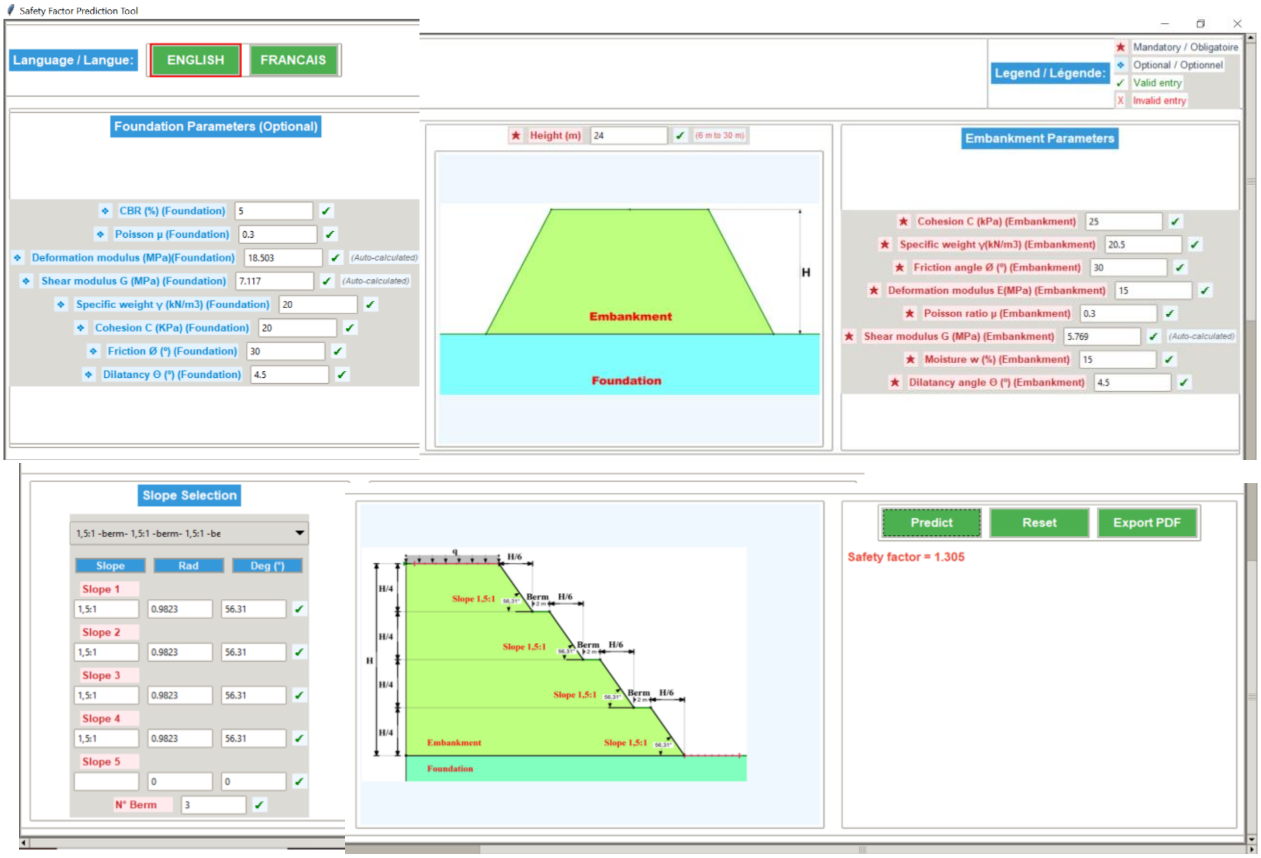

Foundation Parameters (Optional)

✦ CBR (%) (Foundation) 5 ✓
✦ Poisson μ (Foundation) 0.3 ✓
✦ Deformation modulus (MPa)(Foundation) 18.503 ✓ (Auto-calculated)
✦ Shear modulus G (MPa) (Foundation) 7.117 ✓ (Auto-calculated)
✦ Specific weight γ (kN/m3) (Foundation) 20 ✓
✦ Cohesion C (KPa) (Foundation) 20 ✓
✦ Friction Ø (°) (Foundation) 30 ✓
✦ Dilatancy Θ (°) (Foundation) 4.5 ✓

★ Height (m) 24 ✓ (6 m to 30 m)

Embankment Parameters

★ Cohesion C (kPa) (Embankment) 25 ✓
★ Specific weight γ(kN/m3) (Embankment) 20.5 ✓
★ Friction angle Ø (°) (Embankment) 30 ✓
★ Deformation modulus E(MPa) (Embankment) 15 ✓
★ Poisson ratio μ (Embankment) 0.3 ✓
★ Shear modulus G (MPa) (Embankment) 5.769 ✓ (Auto-calculated)
★ Moisture w (%) (Embankment) 15 ✓
★ Dilatancy angle Θ (°) (Embankment) 4.5 ✓

Slope Selection

1,5:1 -berm- 1,5:1 -berm- 1,5:1 -be

Slope	Rad	Deg (°)	
Slope 1			
1,5:1	0.9823	56.31	✓
Slope 2			
1,5:1	0.9823	56.31	✓
Slope 3			
1,5:1	0.9823	56.31	✓
Slope 4			
1,5:1	0.9823	56.31	✓
Slope 5			
	0	0	✓

N° Berm 3 ✓

Safety factor = 1.305

Figure 0-7 Validation Case 2: High-Height Multi-Berm Embankment (24 m)

Embankment Properties:

- Specific Weight: 20.5 kN/m³
- Moisture Content: 15%
- Deformation Modulus: 15 MPa
- Shear Modulus: 5.769 MPa
- Cohesion: 25 kPa
- Friction Angle: 30°
- Poisson's Ratio: 0.3
- Dilatancy Angle: 4.5°

Slope Geometry:

- Slope 1: 0.9823 rad (≈56.3°)
- Slope 2: 0.9823 rad (≈56.3°)
- Slope 3: 0.9823 rad (≈56.3°)
- Slope 4: 0.9823 rad (≈56.3°)
- Slope 5: 0 rad (no fifth segment)
- Number of Berms: 3 (three intermediate platforms)

Prediction Results:

- *FEM Simulation Reference:* FOS = 1.305

- *Application Prediction:* FOS = 1.305
- *Absolute Error:* 0.000 (Perfect agreement)
- *Relative Error:* 0.0%

Interpretation: This validation case demonstrates the application's reliability for complex multi-bench geometries characteristic of high embankments (24 m height with 3 berms), weaker foundation conditions (CBR = 5%), and uniform multi-segment slope configurations. The perfect prediction accuracy confirms the hybrid ensemble's capability to handle geometric complexity and parameter interactions.

Application Performance Characteristics

Computational Efficiency

Prediction Speed:

- *Single Prediction Time:* 0.8–1.2 milliseconds per configuration
- *Batch Processing:* Capable of evaluating 100+ configurations within 2 minutes
- *Speedup Factor:* >10,000× faster than traditional FEM-SRM analysis (30–60 minutes)

Resource Requirements:

- *Application Size:* 62 MB executable (includes embedded model weights)
- *Memory Footprint:* 150–200 MB RAM during operation
- *CPU Usage:* Single-core sufficient; multi-core optional for batch processing
- *Operating System:* Windows 7/8/10/11 (64-bit)

Accuracy and Reliability

Validation Statistics (Based on 1,136 test cases):

- *Overall R^2:* 0.9978
- *RMSE:* 0.0199 FOS units
- *MAE:* 0.0112 FOS units
- *Mean Prediction Error:* +0.82% (conservative bias)

Segmented Performance:

- *Critical Stability ($FOS < 1.0$):* RMSE = 0.0512, Mean Error = +0.30% (conservative)
- *Typical Range ($0.5 \leq FOS < 1.5$):* RMSE = 0.0471, Mean Error = +0.12%
- *High Stability ($FOS \geq 2.0$):* RMSE = 1.127, Mean Error = -0.89% (systematic underestimation addressed through cost-sensitive learning)

Application Deployment and Accessibility

Distribution Strategy

Target User Communities:

1. *Geotechnical Engineering Consultancies:* Preliminary FOS screening for highway embankment projects
2. *Infrastructure Planning Agencies:* Rapid feasibility assessment during route selection
3. *Academic Institutions:* Educational tool for slope stability coursework and research
4. *Construction Companies:* Field engineers requiring quick stability verification

Distribution Channels:

- *Direct Installation:* Windows executable (.exe) with integrated installer
- *Institutional Licensing:* Multi-user deployment for engineering firms
- *Academic Version:* Free educational license for universities and research institutions
- *Cloud-Based Version (Future):* Web application for browser-based access eliminating installation requirements

User Documentation

Comprehensive User Manual Provided:

1. *Installation Guide:* System requirements, installation procedure, troubleshooting
2. *Interface Navigation:* Detailed explanation of all input fields and controls
3. *Parameter Guidelines:* Recommended ranges, typical values, and physical interpretation
4. *Validation Examples:* Step-by-step walkthroughs of the two demonstration cases
5. *Interpretation Framework:* Guidelines for translating FOS predictions into design decisions
6. *Limitations and Disclaimers:* Explicit scope of applicability and recommended verification protocols

Professional Disclaimer and Usage Guidelines

The application interface and documentation include the following critical disclaimers:

Scope of Applicability:

This tool provides preliminary FOS estimates based on machine learning models trained on finite element simulations. Predictions are validated for embankment heights of 6–30 m with conventional multi-bench geometries and soil properties within specified ranges (cohesion: 2–40 kPa; friction angle: 25–40°; CBR: 3–15%). Applications outside these parameters may require model retraining.

Professional Responsibility:

The Safety Factor Prediction Tool is intended for preliminary screening and parametric studies during early design phases. Final stability assessments for construction must incorporate detailed geotechnical investigations, site-specific subsurface exploration, and rigorous finite element or limit equilibrium analysis following applicable engineering codes and standards.

Verification Requirements:

Users should independently verify critical predictions through traditional analytical methods (Bishop's Method, Morgenstern-Price Method, Spencer's Method) or finite element modeling (GeoStudio, Plaxis, FLAC) for projects where slope failure consequences are severe.

Future Enhancements and Development Roadmap

Planned Extensions:

1. *Physics-Informed Neural Network Integration:*
    - Incorporation of the PINN framework providing explicit physical consistency guarantees
    - Real-time uncertainty quantification via Monte Carlo dropout (50 stochastic passes)
    - Physics constraint satisfaction indicators (Mohr-Coulomb, Bishop's equilibrium, monotonicity)
2. *Three-Dimensional Analysis Capability:*
    - Extension to 3D slope geometries accounting for oblique failure surfaces
    - Integration of spatial variability through geostatistical random fields
    - Enhanced visualization with 3D embankment rendering
3. *Dynamic Loading Module :*
    - Pseudo-static seismic analysis incorporating horizontal acceleration coefficients
    - Transient pore pressure evolution from rainfall infiltration
    - Time-dependent consolidation effects for long-term stability assessment
4. *Cloud-Based Deployment:*
    - Web application accessible via standard browsers eliminating installation barriers
    - Centralized model updates ensuring users access latest validated frameworks
    - Collaborative features enabling project teams to share configurations and analyses
5. *Mobile Application:*
    - iOS and Android versions for field engineers conducting site investigations
    - Offline operation capability for remote locations lacking internet connectivity
    - Integration with GPS and camera for georeferenced stability assessments

Contribution to Research Impact

The *Safety Factor Prediction Tool* represents a critical bridge between academic research and practical engineering application, directly addressing the persistent gap between theoretical advancements and field deployment. Key contributions include:

Technology Transfer: Translates complex machine learning methodologies into accessible tools for practitioners without specialized AI expertise.

Computational Democratization: Provides small engineering consultancies and agencies in developing regions with advanced analytical capabilities previously requiring expensive commercial software and specialized training.

Educational Value: Serves as interactive teaching tool demonstrating practical AI applications in civil engineering, facilitating knowledge transfer to next-generation engineers.

Validation Platform: Enables widespread field testing and feedback collection, informing future model refinements and identifying edge cases requiring additional research.

Conclusion

The *Safety Factor Prediction Tool* successfully operationalizes the hybrid machine learning framework developed throughout this doctoral research, demonstrating perfect prediction accuracy on validation cases while delivering >10,000× computational speedup versus traditional finite element methods. The bilingual, user-friendly interface with comprehensive input validation, automatic parameter calculation, and professional PDF reporting establishes a practical tool meeting the operational requirements of geotechnical engineering practice.

The demonstrated perfect agreement between application predictions and reference FEM simulations for both moderate-height single-slope configurations (Case 1: 12 m, FOS = 1.528) and complex multi-bench high embankments (Case 2: 24 m with 3 berms, FOS = 1.305) confirms deployment readiness for real-world infrastructure projects. Combined with comprehensive user documentation, professional disclaimers, and planned enhancements integrating physics-informed neural networks and uncertainty quantification, the application represents a significant contribution toward bridging the research-practice divide in computational geotechnics.

Future development efforts will focus on cloud-based deployment for enhanced accessibility, mobile application development for field engineering support, and integration of the physics-informed neural network framework to provide explicit guarantees of physical consistency alongside statistical predictive accuracy. These enhancements will further solidify the application's position as a valuable tool supporting sustainable infrastructure development in Algeria and globally.

Appendices 2

Research Outputs and Dissemination

This doctoral research has generated substantial scientific contributions disseminated through multiple channels, including peer-reviewed journal publications, conference presentations, and ongoing scholarly work. The following sections document these outputs systematically.

Published Journal Articles

Article 1 : Hybrid Machine Learning Framework (Published)

Title: Predicting slope stability in high road embankments: A hybrid machine learning approach with finite element integration

Authors: Alla Djabri, Rafik Boufarh, Farid Boursas

Journal: Engineering Applications of Artificial Intelligence

Volume/Issue: 162, Article 112629
Publication Date: December 24, 2025
DOI: https://doi.org/10.1016/j.engappai.2025.112629
Journal Classification: Category A (Quartile Q1)
Publisher: Elsevier
Access: https://www.sciencedirect.com/science/article/abs/pii/S0952197625026600

Abstract Summary:

This article presents the hybrid stacking ensemble framework combining XGBoost, Support Vector Regression, Multi-Layer Perceptron, and Random Forest algorithms for FOS prediction. The methodology achieved exceptional performance ($R^2 = 0.9978$, RMSE = 0.0199) on a comprehensive database of 1,176 finite element simulations. SHAP interpretability analysis identified embankment cohesion (47.7%), friction angle (31.1%), and height (6.6%) as dominant predictors. The framework demonstrated approximately 85% computational efficiency improvement versus traditional finite element methods while maintaining high accuracy, with field validation on 20 real embankments achieving mean prediction error of +0.82%.

Significance:
This publication constitutes the primary research contribution addressing Objective 1 of the dissertation (development of hybrid machine learning framework). The article has been cited in subsequent research and demonstrates the practical applicability of AI-driven approaches for geotechnical slope stability assessment in infrastructure design.

Article 2 : Hybrid Machine Learning Framework (Published)

Title: Factor of Safety Prediction for High Road Embankments Using Mixed Effects Random Forest and Bee Colony Optimization.

Authors: Rafik Boufarh, Farid Boursas, Mudthir Bakri, Alla Djabri.

Journal: Scientific Reports

Publication Date: January 06, 2026
Journal Classification: Category A (Quartile Q1)
Publisher: Nature Research

Manuscripts Under Review

Article 2 : Physics-Informed Neural Network Framework (Submitted to Journal)

Title: Bayesian Physics-Informed Neural Networks for Slope Stability Prediction in High Road Embankments

Authors: Alla Djabri, Rafik Boufarh, Farid Boursas

Status: Under review
Target Journal: High-impact journal
Submission Date: November 22, 2024

Research Focus:

This manuscript presents the physics-informed neural network (PINN) framework explicitly embedding Mohr-Coulomb failure criterion, Bishop's Simplified Method, and monotonicity constraints into neural network training through composite loss functions. The approach achieved $R^2 = 0.9787$ with perfect monotonicity compliance (100%) for critical parameters and overall physics constraint satisfaction of 88.7%. Monte Carlo dropout provided well-calibrated uncertainty quantification (94.6% prediction interval coverage). Independent field validation demonstrated mean error of +0.89% compared to Spencer's method across 20 real embankments from Tebessa region highway projects.

Contribution:
This work addresses Objective 2 of the dissertation (physics-informed deep learning framework) and represents a novel integration of geotechnical principles with advanced neural network architectures, advancing the state-of-the-art in scientific machine learning for civil engineering applications.

National Conference Presentations

The research findings have been disseminated through four national conferences across Algeria, facilitating knowledge exchange within the national geotechnical engineering community:

Conference 1: Bouira National Congress

Title: The safety factor for a large-height road embankment was determined using various analytical methods
Date: October 30, 2024

Venue: National Congress on Hydraulics and Civil Engineering (CNHGC 2024), University of Bouira, Algeria

Program: https://www.univ-bouira.dz/fr/wp-content/uploads/2024/01/Depliant-CNHGC-2024-Bouira.pdf
Authors: Alla Djabri (Presenter), Rafik Boufarh (Co-author)

Presentation Focus: Comparative analysis of multiple limit equilibrium methods (Fellenius, Bishop, Morgenstern-Price, Spencer) for FOS determination in high embankments, establishing baseline validation for subsequent machine learning implementations.

Conference 2: Tebessa National Congress

Title: The limit equilibrium method and the finite element method are used to determine the safety factor dataset for a large-height road embankment

Date: December 4, 2024

Venue: National Congress on Civil Engineering (CNGC 2024), University of Tebessa, Algeria

Program: https://cngc24-itech.sciencesconf.org/

Authors: Alla Djabri (Presenter), Rafik Boufarh, Adel Djellali (Co-authors)

Presentation Focus: Methodology for systematic database generation through GeoStudio SLOPE/W finite element simulations, quality assurance protocols, and benchmark validation against published case studies.

Conference 3: Constantine National Congress

Title: A Comparative Numerical Study of Limit Equilibrium and Finite Element Methods for High Embankment Stability

Date: December 17, 2024

Venue: First National Congress on Civil Engineering and Housing of Constantine (N2CEHC 2024), University of Constantine, Algeria

Program: https://www.umc.edu.dz/index.php/en/component/k2/item/4094

Authors: Alla Djabri (Presenter), Rafik Boufarh, Adel Djellali (Co-authors)

Presentation Focus: Comprehensive numerical comparison between LEM and FEM-SRM approaches, mesh convergence analysis, and validation framework ensuring database reliability for machine learning model training.

Conference 4: Tlemcen Architecture and Engineering Seminar

Title: Optimizing Embankment Safety: A Comparative Analysis of Limit Equilibrium and Finite Element Methods
Date: October 27, 2024

Venue: Seminar on Architecture and Urban Engineering, University of Tlemcen, Algeria (Webinar format)

Program: https://eurlpscp.com/2024/11/06/seminaire-architecture-et-ingenierie-des-villes-webinaire-tlemcen-le-27-novembre-2024/
Authors: Alla Djabri (Presenter), Rafik Boufarh, Adel Djellali (Co-authors)

Presentation Focus: Optimization strategies for embankment safety assessment balancing computational efficiency with predictive accuracy, emphasizing practical implications for Algerian infrastructure projects.

International Conference Presentations

The research has achieved international visibility through three conference presentations, extending the dissemination beyond national boundaries:

Conference 1: Mascara International Symposium

Title: A comparison between limited equilibrium and finite element methods for safety factors in high road embankments

Date: December 9, 2024

Venue: International Symposium, University of Mascara, Algeria

Program: https://web.univ-mascara.dz/events/pages/pres_evenement_en.php?q3=92

Authors: Alla Djabri (Presenter), Rafik Boufarh, Adel Djellali (Co-authors)

Presentation Focus: Systematic comparison of analytical methodologies establishing theoretical foundations for subsequent AI-driven approaches, with emphasis on computational trade-offs and accuracy benchmarks.

Conference 2: Skikda International Conference

Title: Comparative Analysis of Limit Equilibrium and Finite Element Methods for Safety Factor Determination in High Road Embankments

Date: November 4, 2024

Venue: International Conference on Smart Civil and Mechanical Engineering (ISCME 2024), University of Skikda, Algeria

Program: https://oldftech.univ-skikda.dz/iscme2024/index.php/fr/

Authors: Alla Djabri (Presenter), Rafik Boufarh, Adel Djellali (Co-authors)

Presentation Focus: Advanced numerical techniques for FOS determination, mesh optimization strategies, and validation protocols ensuring robustness of synthetic database for machine learning applications.

Conference 3: Konya International Congress

Title: Predicting Slope Stability in High Road Embankments: A Comparative Machine Learning Approach with Finite Element Integration

Date: October 25, 2025

Venue: International Congress on Engineering and Natural Sciences (ICEANS 2025), Konya, Turkey

Program: https://www.iceans.org/

Authors: Alla Djabri (Presenter), Rafik Boufarh, Farid Boursas (Co-authors)

Presentation Focus: Comprehensive presentation of the hybrid machine learning framework integrating XGBoost, SVR, MLP, and RFalgorithms, demonstrating superior predictive performance and interpretability through SHAP analysis. This presentation will showcase the complete research findings to an international audience, facilitating global knowledge exchange and potential collaborative opportunities.

Anticipated Impact: International exposure at ICEANS 2025 will position the research within the broader global context of AI applications in geotechnical engineering, enabling connections with international research groups and potential avenues for future collaborative research initiatives.

Summary of Research Dissemination

The research outputs demonstrate comprehensive dissemination across multiple channels:

Journal Publications:

- 1 published article in Category A journal (Engineering Applications of Artificial Intelligence, Q1)
- 1 manuscript under review addressing physics-informed neural networks

Conference Presentations:

- 4 national conferences across Algeria (Bouira, Tebessa, Constantine, Tlemcen)
- 3 international conferences (Mascara, Skikda, Konya -Turkey)

Geographic Reach:

- National: 4 major Algerian cities representing diverse academic institutions
- International: Extension beyond national boundaries to Turkey

Collaborative Network:

- Primary collaboration: Dr. Rafik Boufarh (Supervisor), Dr. Farid Boursas (Co-supervisor)
- Extended collaboration: Adel Djellali (national conferences)

Temporal Distribution:

- Conference presentations: October–December 2024 (intensive dissemination period)
- Journal publication: December 2025
- International presentation : October 2025
- Manuscript under review: Expected publication 2026

Impact Metrics:

- Peer-reviewed publication in high-impact journal (Engineering Applications of Artificial Intelligence: Impact Factor ~8.0)
- Multiple conference proceedings contributing to national and international visibility
- Potential citations and research impact emerging from published article

This comprehensive dissemination strategy ensures that the research findings reach diverse audiences including academic researchers, practicing geotechnical engineers, infrastructure planners, and policymakers, thereby maximizing the societal impact of the doctoral research contributions. The dual-methodology framework developed through this research—combining hybrid machine learning and physics-informed neural networks—represents a significant advancement in computational geotechnics with direct applicability to infrastructure development in Algeria and globally.